Development and Optimization of Novel Morphing Wings for the Next-Generation Aircraft

by

Mir Hossein NEGAHBAN

MANUSCRIPT-BASED THESIS PRESENTED TO ÉCOLE DE TECHNOLOGIE SUPÉRIEURE IN PARTIAL FULFILLMENT OF THE DEGREE OF DOCTOR OF PHILOSOPHY
Ph.D.

MONTREAL, 31 July, 2025

ECOLE DE TECHNOLOGIE SUPÉRIEURE
UNIVERSITÉ DU QUÉBEC

© Copyright 2025 All rights reserved by Mir Hossein Negahban

© Copyright reserved

It is forbidden to reproduce, save or share the content of this document either in whole or in parts. The reader who wishes to print or save this document on any media must first get the permission of the author

BOARD OF EXAMINERS

THIS THESIS HAS BEEN EVALUATED

BY THE FOLLOWING BOARD OF EXAMINERS

Prof. Ruxandra Mihaela Botez, Thesis Supervisor
Department of Systems Engineering at École de technologie supérieure

Prof. Philippe Bocher, President of the Board of Examiners
Department of Mechanical Engineering at École de technologie supérieure

Prof. Tony Wong, Member of the jury
Department of Systems Engineering at École de technologie supérieure

Prof. Jeremy Laliberte, External Evaluator
Department of Mechanical and Aerospace Engineering at Carleton University

Prof. Rosario Pecora, Independent External Evaluator
Department of Aerospace Engineering at University of Naples, Italy

THIS THESIS WAS PRENSENTED AND DEFENDED

IN THE PRESENCE OF A BOARD OF EXAMINERS AND PUBLIC

ON 26th JUNE 2025

AT ECOLE DE TECHNOLOGIE SUPERIEURE

TO MY HEAVENLY MOTHER

ACKNOWLEDGMENT

Firstly, I am deeply appreciative of my supervisor, Prof. Ruxandra Mihaela Botez, for her exceptional technical support, leadership, professional guidance, encouragement, and mentorship throughout my research.

I am also very grateful to Jérémy Laliberté and Salman Shafi for the opportunity to join and receive funding from the CREATE UTILI program. This program significantly enriched my knowledge of Unmanned Aerial Systems. Additionally, it allowed me to engage with professionals from the drone industry through various meetings, workshops, and internships, which was highly rewarding.

My sincere gratitude goes to the Hydra Technologies team in Mexico for their consistent support, particularly Mr. Carlos Ruiz, Mr. Eduardo Yakin, and Mr. Alvaro Gutierrez Prado.

I also want to express my gratitude to my colleagues at LARCASE: Musavir Bashir, Simon Longtin-Martel, Seyed Mohammad Hashemi, Renan Sanches Geronel, Nicola Zonzini, and the internship students I worked with during this thesis: Victor Traisnel, Noe Del Aguila, Clovis Priolet, Gabriel Risse, Stanislas Mouret, Alexandre Hallonet, Marie Noupoussi-Woumeni, Constance Nguyen, and Tarek Saci.

Lastly, I want to thank all those who have provided me with moral support throughout my career and research. This journey would not have been possible without their encouragement. I especially mention my father, Mir Habib Negahban, my brother, Mir Sajjad Negahban; and my sister, Sima Negahban. Your unwavering support helped me complete this project on time.

Développement et optimisation de nouvelles ailes déformables pour l'avion de nouvelle génération

Mir Hossein NEGAHBAN

RÉSUMÉ

L’industrie aéronautique a pour objectif de réduire les émissions de carbone dans cette ère dangereuse de réchauffement climatique en adoptant diverses stratégies et technologies nouvelles. Réduire la consommation de carburant d’un avion pourrait considérablement contribuer à cet objectif au sens large. L'amélioration de la flotte d'avions de nouvelle génération grâce à l'utilisation de ces nouvelles technologies ouvre la voie à la réalisation des objectifs de l'aviation verte, à savoir d’une industrie aéronautique respectueuse de l'environnement. En utilisant la technologie prometteuse des ailes déformables, cette thèse explore les ailes de nouvelle génération visant à améliorer leur performance aérodynamique. Cette recherche porte sur des approches de innovantes et spécifiques qui pourraient être applicables sur le bord de fuite des ailes. Deux nouvelles approches pour des ailes déformables sont expliquées dans cette thèse, l'une étant le volet SMTE (Seamless Morphing Trailing Edge) et la seconde la conception d'ailerons et d'ailettes déformables par torsion. La première approche remplace les volets principaux conventionnels d'un avion, et la deuxième approche remplace par ailerons conventionnels au bout de l'aile.

À cette fin, une optimisation de la forme aérodynamique 3D est effectuée pour chaque approche d’aile déformable à l'aide d'un algorithme d'optimisation haute-fidélité. L'algorithme d'optimisation basé sur le gradient est programmé dans le solveur de flux haute-fidélité OpenFOAM. Le code Open Source adjoint orienté objet appelé DAFoam a été utilisé. La technique de paramétrage de déformation de forme libre (FFD), qui est une méthode efficace d'optimisation 3D a aussi été utilisé, Dans cette méthode, des centaines ou des milliers de variables de conception sont prises en compte lorsqu'on parle d'optimisation d'une aile complète ou d'un avion à grande échelle. Chaque approche d’aile déformable est spécifiée par une fonction objectif adaptée en fonction des objectifs de la mission et des conditions de vol. L'optimisation des volets déformables lisse du bord de fuite pour différentes conditions de vol, y compris la montée, la croisière et la descente planée, grâce à l'optimisation de la forme aérodynamique en régime permanent haute-fidélité et l'analyse comparative avec les volets articulés conventionnels démontrent la supériorité du volet déformable, montrant jusqu'à 3,8 % réduction de puissance et 6,13% d’augmentation de taux de montée. Le volet déformable lisse améliore également l'efficacité aérodynamique jusqu'à 17,8 % et étend l’écoulement laminaire sur la surface supérieure de l'aile. De plus, un gain d’endurance de 61,2 % a été réalisé par rapport à celle de la configuration de l’aile. Enfin, la configuration optimisée pour la descente en plané a permis d'obtenir une réduction remarquable de 43 % du taux de descente.

Une autre optimisation de forme aérodynamique basée sur un gradient haute-fidélité est effectuée pour améliorer l'efficacité de roulement et réduire la traînée induite en introduisant une nouvelle conception d'aileron et d'ailette déformable en torsion. L'aileron déformable par torsion a augmenté l'efficacité des ailerons par 34 % et a réduit la traînée induite par 61 % par rapport à leur conceptions conventionnelles. D'autre part, les ailettes déformables en torsion ont réduit la traînée induite par 25,7 % en vol de croisière et par 16,51 % en montée, ainsi elles ont réduit la traînée totale jusqu'à 7,5 % et ont amélioré l'efficacité aérodynamique jusqu'à 9%.

Après avoir obtenu des améliorations aérodynamiques prometteuses grâce au volet SMTE, l'étude a été développé en proposant le nouveau mécanisme de la trompe d'éléphant (ETM), un concept de bio-inspiré dérivé de la trompe flexible et polyvalente d'un éléphant. Une analyse structurelle et une optimisation de la topologie ont été effectuées pour examiner la faisabilité et le caractère pratique du mécanisme proposé. L'ETM utilise des éléments en forme de dents fixés à un caisson d'aile solide, actionnés par des câbles métalliques pour obtenir une déformation vers le bas du bord de fuite. L'analyse par des éléments finis et l'optimisation de la topologie garantissent la faisabilité structurelle et la stabilité de l'ETM, conduisant à un mécanisme de déformation fiable et léger. Enfin, l'analyse expérimentale est réalisée en prototypant le volet SMTE équipé du mécanisme en trompe d'éléphant pour valider les résultats obtenus à partir d'études aérodynamiques et structurelles. Cette étude a non seulement finalisé l'étude approfondie sur le développement d'un volet déformable de bord de fuite, mais plus important encore, elle a confirmé les avantages prometteurs du volet SMTE en termes de performances aérodynamiques et de faisabilité structurelle.

Ces études démontrent le potentiel des technologies d’ailes déformable pour améliorer considérablement les performances, l’efficacité et la maniabilité d’un avion, ouvrant ainsi la voie à leurs mises en œuvre pratiques dans les avions de nouvelle génération.

Mots clés: aile déformable, optimisation de la forme aérodynamique, volet de bord de fuite à déformation lisse, mécanisme de trompe d'éléphant, aileron déformable par torsion, efficacité de roulage, performances des ailerons, analyse structurelle, optimisation de la topologie, optimisation basée sur le gradient

Development and optimization of novel morphing wings for the next generation aircraft

Mir Hossein NEGAHBAN

ABSTRACT

The aeronautical industry has aimed to reduce its carbon emissions in this era of global warming by adopting various new strategies and technologies. Achieving reduced fuel consumption by aircraft would directly contribute to this goal. Improving the next-generation fleet of aircraft by using these new technologies paves the way for achieving green aviation's ultimate goal of an environmentally friendly aviation industry. This thesis explores next-generation wings in the framework of promising morphing wing technology, with the objective of enhancing aircraft aerodynamic performance and efficiency. This research focuses on innovative morphing approaches that could be applied on wings’ trailing edges. Two novel morphing approaches are introduced: the Seamless Morphing Trailing Edge (SMTE) flap, and the twist morphing ailerons and winglet design. The former replaces the conventional main flaps of an aircraft, and the latter replaces the conventional ailerons of a UAV.

For this purpose, 3D aerodynamic shape optimization is performed for each morphing approach using a high-fidelity gradient-based optimization algorithm with a high-fidelity flow solver, OpenFOAM. The framework is based on an object-oriented adjoint-based Open-Source code called DAFoam and uses the Free-Form Deformation (FFD) parametrization technique. FFD is an efficient method in 3D optimization, where 100s or 1000s of design variables are considered in a full wing or a full-scale aircraft optimization. A suitable objective function specifies each morphing approach according to the mission objectives and flight conditions.

Optimization of SMTE flaps for different flight conditions and regimes, including climb, cruise, and gliding descent is conducted using a high-fidelity steady-state aerodynamic shape optimization. A comparative analysis with the results from conventional hinged flaps demonstrates the morphing flap's superiority; indicating up to 3.8% power reduction and a 6.13% increase in climb rate. The SMTE flap also enhances aerodynamic efficiency by up to 17.8% and extends laminar flow on the wing's upper surface compared to a conventional hinged flap. In addition, a 61.2% gain was achieved for endurance improvement compared to that of a clean wing configuration. Finally, the optimized configuration for gliding descent achieved a 43% reduction in the descent rate.

Another high-fidelity gradient-based aerodynamic shape optimization is performed to improve rolling efficiency and reduce induced drag by introducing a novel twist morphing aileron and winglet design. The twist morphing increased the aileron efficiency by 34% and reduced induced drag by 61% compared to a conventional aileron design. In more detail, twist morphing winglets reduced the induced drag by 25.7% in cruise flight, by 16.51% in climb, total drag by up to 7.5%, and overall, enhanced aerodynamic efficiency by up to 9%.

After obtaining promising aerodynamic improvements for an SMTE flap, the study continues by proposing the novel Elephant Trunk Mechanism (ETM), a bio-inspired morphing concept derived from an elephant's flexible and versatile trunk. Structural analysis and topology optimization is performed to examine the feasibility and practicality of the proposed mechanism. The ETM employs tooth-like elements attached to a solid wing box, actuated by wire cables, to achieve smooth downward bending deformation of the trailing edge. Both Finite Element Analysis (FEA) and topology optimization ensure the structural feasibility and stability of the ETM, leading to a reliable and lightweight morphing mechanism.

Finally, an experimental analysis is performed by prototyping the SMTE flap equipped with an Elephant Trunk Mechanism to validate the results obtained from aerodynamic and structural studies. This study is orientated towards the development of morphing trailing edge flaps, but more importantly, it confirms the promising benefits of the SMTE flap in terms of aerodynamic performance and structural feasibility.

These studies demonstrate the potential of morphing wing technologies to significantly improve an aircraft's performance, efficiency, and maneuverability, paving the way for their practical implementation in next-generation aircraft.

Keywords: morphing wing, aerodynamic shape optimization, seamless morphing trailing edge (SMTE) flap, Elephant Trunk Mechanism (ETM), twist morphing aileron, rolling efficiency, aileron performance, structural analysis, topology optimization, gradient-based optimization

TABLE OF CONTENTS

Page

LIST OF TABLES

LIST OF FIGURES

LIST OF ABREVIATIONS AND ACRONYMS

ABC	Artificial Bee Colony
ACTE	Adaptive Compliant Trailing Edge
AD	Automatic Differentiation
AFRL	Air Force Research Laboratory
AFS	Artificial Fish Swarm
AFTI	Advanced Fighter Technology Integration
AIAA	American Institute of Aeronautics and Astronautics
AOA	Angle of Attack
AOD	Angle of Deflection
AR	Aspect Ratio
ATED	Adaptive Trailing Edge Device
BFGS	Broyden–Fletcher–Goldfarb–Shanno
BWO	Black Widow Optimization
CAD	Computer Aided Design
CFD	Computational Fluid Dynamics
CRM	Common Research Model
CST	Class Shape Transformation
CT	Computed Tomography
CWM	Continuous Wing Morphing
DA	Discrete Adjoint
DAFoam	Discrete Adjoint with OpenFOAM
DARPA	Defense Advanced Research Projects Agency
DLR	German Aerospace Center (Deutsches Zentrum für Luft- und Raumfahrt)
EBAM	Eccentric Beam Actuation Mechanism
EMC	Elastomeric Matrix Composite
ET	Elephant Trunk
ETM	Elephant Trunk Mechanism
ETS	École de Technologie Supérieure

FD	Finite Difference
FEA	Finite Element Analysis
FEM	Finite Element Method
FFD	Free-Form Deformation
FishBAC	Fishbone Active Camber
FOS	Factor of Safety
FWM	Flap Wing Morphing
GA	Genetic Algorithm
GND	Ground
GPIO	General Purpose Input Output
GT2	Gear Teeth 2
GUI	Graphical User Interface
IPOPT	Interior Point Optimizer
LABVIEW	Laboratory Virtual Instrumentation Engineering Workbench
LARCASE	Laboratory of Applied Research in Active Controls, Avionics and Aeroservoelasticity
LUSM	Linear Ultrasonic Motors
MAV	Micro Air Vehicle
MDO	Multidisciplinary Design Optimization
MTE	Morphing Trailing Edge
NASA	National Aeronautics and Space Administration
NGC	Northrop Grumman Corporation
NSERC	Natural Sciences and Engineering Research Council of Canada
NURBS	Non-Uniform Rational Basis Spline
OC	Optimality Criteria
OpenFOAM	Open Field Operation and Manipulation
PDE	Partial Differential Equations
PETSc	Portable, Extensible Toolkit for Scientific Computation
PIV	Particle Image Velocimetry
PLA	Poly Lactic Acid

PSO	Particle Swarm Optimization
PWM	Pulse With Modulation
RANS	Reynolds-Averaged Navier–Stokes
SA	Spalart Allmaras
SARISTU	Smart Intelligent Aircraft Structures
SIMP	Solid Isotropic Material with Penalization
SMA	Shape Memory Alloys
SMTE	Seamless Morphing Trailing Edge
SOA	Soft Object Animation
TE	Trailing Edge
TPU	Thermoplastic Poly Urethane
UAS	Unmanned Aerial System
UAV	Unmanned Aerial Vehicle
USAF	United States Air Force
USB	Universal Serial Bus
VCC	Common collector Voltage
VCCTEF	Variable Camber Continuous Trailing Edge Flap
VCTE	Variable Camber Trailing Edge

LIST OF SYMBOLS

A	Column section area
C_{mz_p}	Roll damping coefficient
$\vec{P}^{new}$	Object's vertices after deformation
$\mathrm{C_d}$	Drag coefficient
$\mathrm{C_l}$	Lift coefficient
K_e^0	Stiffness matrix
$\mathrm{x_{dv}}$	Design variables
$\mathrm{X_{pt}}$	Spatial coordinates
$C_{L_{\alpha_w}}$	Lift curve slope
$C_{mz_{\delta_a}}$	Aileron control power
$C_{D\mathrm{i}}$	Lift-induced Drag
C_{mz}	Roll moment coefficient
M_z	Roll moment
P_{req}	Required power
$Q_{i,j,k}$	Undeformed block
U_∞	Free-stream velocity
$\vec{V}$	B-spline volume
V^*	Minimum allowable volume of the material
V_e	Element's volume

W_1	Initial aircraft weight
W_2	Final aircraft weight
γ_p	Weight-specific fuel consumption
δ_a	Aileron deflection
η_p	Propulsive efficiency
ρ_e	Density each element
ω_z	Roll rate
$\Delta\overline{G}$	Geometric change
b	Span length
c	Chord
C	Structural compliance
C_p	Pressure coefficient
E	Young’s modulu
F	External forces
$\overline{g}$	Baseline geometry
h	Altitude
I	Second moment of inertia
K	Stiffness matrix
Kt	Factor of intensity
l	Effective length
L	Lift force
P_{av}	Available power
R	Residuals

S	Surface area
T	Thrust
T	Twist
u	Vector of nodal displacements
X_0	Initial variables
x_p	Parametrized FFD points
X_S	Surface coordinates
x_v	Volumetric deformed mesh
Y	Control points
Y+	Distance in wall coordinate
ε	Strain
ρ	Air density
σ	Stress
ϕ	Roll angle
AR	Aspect ratio
D	Drag force
E	Endurance
Q	Dynamic pressure
R	Range
V	Velocity
W	Weight
e	Efficiency factor
f	Function

p	Dimensionless roll rate
r	Fillet radius
x	Design variables
α	Angle of attack
γ	Angle of climb, Angle of descend
τ	Roll response time
ψ	Adjoint vector
ω	State variables
λ	Slender ratio

INTRODUCTION

Today, as climate change presents a growing threat to our everyday lives, the aeronautics industry is both a major contributor to the problem and a key player in finding solutions. Thousands of aircraft are flying daily, significantly impacting our environment with their carbon emissions. The effects of these emissions are significant, emphasizing the need for industry to adopt more sustainable practices. With the planet facing various climate-related challenges, including more extreme weather events, rising sea and lake water levels, and ecosystem disruptions, decisive action is more urgent than ever.

The aeronautic industry's role in addressing climate change is essential. The link between global air traffic and environmental damage underscores the necessity of overhauling current industry practices. Worldwide, industries and technology sectors are being called upon to align with sustainability goals. The commitment to reducing climate change's impact must be universal, involving every aspect of human activity, including aviation.

This focus on sustainability has driven significant advancements in aeronautical research, with organizations such as NASA leading the way. NASA's work in developing environmentally friendly aviation technologies highlights the potential for major reductions in greenhouse gas emissions. This fact is significant given the projected growth of the aviation industry. Before the COVID-19 pandemic, air traffic was expected to triple in a few years, necessitating around 9,000 new regional aircraft and potentially increasing global emissions.

However, there are considerable opportunities for improvements in the aeronautics industry. Enhancements in aerodynamic efficiency, for instance, can result in significant cost savings and reductions in gas emissions. A business jet with variable camber trailing edge technology can achieve a 5% reduction in fuel consumption, saving $7 billion annually (Huang & Ge, 2010). Beyond the financial benefits, such innovations are vital in lowering carbon dioxide (CO2) emissions, which is 70% of total aircraft emissions. These CO2 emissions represent crucial progress in combatting the effects of global warming.

By adopting sustainable practices and pioneering new technologies, industry can make substantial contributions to a more stable and healthier planet. The path to a sustainable future in aviation is more than preserving the skies, in which we fly; it's about ensuring the survival of the Earth we live on.

The morphing wing technology has been a transformative innovation in the aeronautics industry, promising significant advancements in aircraft performance through the modification (morphing) of wing configurations. Various morphing techniques have been applied and adopted on the trailing edge, camber, leading-edge, span, winglet, wing upper surfaces, and wingtip. These approaches have been analyzed for their aerodynamic and structural efficiencies and their morphing mechanisms. However, despite the promising research outcomes, their practical implementation on aircraft has been hindered by structural challenges.

The morphing wing technology broadly aims to replicate the flight patterns of birds, which have been finely tuned through millions of years of evolution. The objective is to continually adapt wings to enhance aircraft performance. This comprehensive field of study spans multiple disciplines, including aerodynamics, structural engineering, materials science, and control systems.

In the field of aerodynamics, morphing wing technology holds immense potential for next-generation environmentally friendly aircraft. This technology has significantly improved aircraft performance by reducing drag, fuel consumption, and weight. While many studies remain at the conceptual level due to structural limitations, ongoing research in aerodynamics and structural engineering continues to show a promising future for morphing wings.

The research on morphing wing technology has been accelerating, moving beyond the conceptual design phase to address manufacturing challenges. As these challenges represent the final phase before practical application, meticulous consideration is necessary to develop morphing wings for real aircraft. Concurrently, research continues to find additional promising capabilities of this technology. This interdisciplinary field encompasses aerodynamics, structures, materials, and control, necessitating strong links and interchangeability among these disciplines for its advancement.

Aerodynamic simulation is the main step needed to validate the advantages of a morphing design. Studies have shown that morphing wing designs that have undergone their manufacturing processes demonstrate their promising capabilities. Various morphing designs, tailored to specific mission objectives and aircraft maneuverability, have been proposed, including span morphing or telescopic wings, drooped nose wings, variable-sweep wings, upper surface morphing, variable thickness wings, and variable camber wings. Among these designs, variable camber wings and morphing trailing edge designs have garnered significant attention due to their potential to enhance flight performance.

CHAPTER 1

ORIGINALITY AND RESEARCH CONTRIBUTION

1.1 Problem statement

According to the Global Carbon Project, the drop in flights during the worldwide lockdown dramatically reduced carbon emissions compared to other sources, including surface transport and industry. Their findings indicate that during the peak of world-wide lockdown (March, April, and May 2020), the 75% reduction in air traffic accounted for 60% of the carbon emission reduction, while surface transport accounted only for a 36 % Carbon reduction (the second after aviation), which is nearly one half. Carbon emission reduction is, therefore, one of the highest-priority goals in the aeronautics industry due to its undeniable impact on the climate.

Given their unavoidable impact on the climate, aeronautical industries have agreed to revolutionize the aeronautics industry and to positively contribute, along with other industries, to achieve the common goal of protecting the Earth from global warming.

For decades, the aeronautical industry has been investing heavily in the improvement of airplanes, such as commercial jets, fighter aircraft, and unmanned aerial systems. With several decades of experience with conventional aircraft designs, it is now possible to have detailed information about the pros and cons of each aircraft part and the ways to implement it to make it more efficient. For wing design, the discontinuities on the wing body pose issues such as increased drag and turbulence, leading to more fuel burn and higher carbon emissions. To fight global warming, it is essential to deviate the conventional wing design into more efficient designs as a way to address the challenges mentioned above.

Regarding aircraft performance improvement, aerodynamic performance is the first objective, and it has remained the most popular and exciting research topic in the aeronautics industry for decades. However, aerodynamic improvement must be combined with aerodynamic optimization.

Morphing Wing Technology (MTW), one of the most promising technologies in the aeronautics industry, brings a solution for the significant improvement of modern aircraft technology. This technology is still mainly at the research level and must be applied to commercial jet airlines. Therefore, the implementation of MTW will be regarded as a turning point towards more environmentally friendly and bio-inspired aircraft.

Many morphing mechanisms have been proposed at the conceptual design level for different morphing configurations, such as a morphing leading edge and a trailing edge. However, few successful tests have been reported at the flight test level. Among these, the AFTI/F-111 Mission Adaptive Wing was a pioneering, joint project of the UASF, NASA and Boeing, in which a successful flight test was performed using an F-111 fighter aircraft equipped with active camber morphing. Unfortunately, the project was closed due to actuation system complexity and weight penalties. The Adaptive Complaint Trailing Edge (ACTE) project is another flight test-level project of the U.S Air Force Research Laboratory (AFRL), NASA and Flexsys. In the ACTE project, a Gulfstream III business jet equipped with morphing trailing edge wings was tested at an altitude of 40,000 ft; the only practical test of morphing wings in recent years.

The present research proposes two morphing configurations: on the wing trailing edge and on the wingtip. Trailing edge morphing is applied to the UAS-S45 wing using the Seamless Morphing Trailing Edge (SMTE) flap for the first configuration. Next, an optimization process is performed to find the optimum shape of the morphing wing configuration for the whole flight envelope of the UAS-S45. Subsequently, a morphing mechanism was proposed for the SMTE flap, called the “Elephant Trunk Mechanism (ETM)”. Structural analysis and topology optimization were performed on the proposed mechanisms to verify their feasibility. Finally, the UAS-S45 wing section equipped with ETM, and an actuation control system, was manufactured. The prototype wing section was tested in a wind tunnel to evaluate the proposed actuation mechanism (ETM), as well as to validate the numerical results obtained from the aerodynamic study.

In the second morphing configuration, novel twist morphing aileron and winglet are proposed with the aim to improve the rolling efficiency and reduce induced drag, respectively.

1.2 Research objectives

Two main objectives are studied in this research using the wing trailing edge. The first is applied to the flaps close to the wing root, and the second is applied on the flaps close to the wingtip or the ailerons. Each objective consists of sub-objectives.

1.2.1 Development of a Seamless Morphing Trailing Edge (SMTE) flap

The first objective of this research concerns the development of a Seamless Morphing Trailing Edge (SMTE) flap by establishing an interdisciplinary study. This objective consists of the following sub-objectives:

a) Aerodynamic shape optimization of the SMTE flap

This sub-objective is an aerodynamic study of the proposed morphing wing equipped with an SMTE flap. The morphing wing is optimized for different flight conditions (altitudes, airspeeds, and angles of attack). These flight conditions are chosen so that they cover the whole flight envelope, including climb, cruise, and descent. For each flight condition, an optimization is performed on the UAS-S45 to find the optimal flap configuration with the following objective functions:

- The climb phase objective is to increase the climb rate and reduce the required engine power;
- Two objective functions are considered for cruise flight:
    a) Increasing range
    b) Increasing endurance; and
- For the descent, the objective is to decrease the descent rate.

b) Comparison of the morphing wing with conventional wings

Following the successful optimization of the morphing wing for different flight conditions, a comparison is drawn between morphing and conventional wings. This comparison aims to evaluate the aerodynamic benefits gained by using the SMTE flap. It consists of evaluating the aerodynamic parameters, including flight range, endurance, and aerodynamic efficiency during cruise.

c) Structural analysis and topology optimization of the Elephant Trunk Mechanism (ETM) for the SMTE flap

After obtaining the morphing wing configurations for different flight conditions, the novel Elephant Trunk Mechanism (ETM) is proposed as an actuation mechanism for the SMTE flap. The structural analysis and the topology optimization have the following objectives:

- Analysis of the structural parameters, including the tension, factor of safety, and magnitude of deformation;
- Topology optimization of the ETM with the goal of reducing structural weight and improving structural parameters; and
- Comparison of the ETM before and after the topology optimization.

d) Prototyping the morphing wing equipped with an Elephant Trunk Mechanism (ETM) and an SMTE flap

After finalizing the SMTE flap aerodynamic and ETM structural analyses, their obtained results were used to prototype the UAS-S45 wing equipped with the SMTE flap and the internal ETMs. Finally, the prototyped wing section was tested in the wind tunnel. The objectives of this phase are:

- Examining the feasibility and practicability of the ETM;
- Providing a suitable control system for the ETM actuation containing a graphical interface;
- Examining the reliability and flexibility of the skin on the SMTE flap.
- Validating the numerical aerodynamic results using wind tunnel experimental data.

1.2.2 Design of a novel twist morphing wingtip

This twist morphing design is the second main objective of this research. This study aims to replace the conventional hinged ailerons and winglets of the UAS-S45 wing by twist morphing ailerons and winglets. The proposed morphing approach is analyzed in climb and cruise flight conditions by performing an aerodynamic optimization to find the optimum wingtip configuration corresponding to the specified objective function. This novel approach is aimed at improving the aerodynamic parameters on the wingtip with the following objectives:

- Improvement of aileron efficiency in a rolling maneuver using novel twist morphing ailerons; and
- Reduction of lift-induced drag and turbulence at the wingtip by use of novel twist morphing winglets.

1.3 Methodology

The morphing wing study is performed here on the full 3D wing. The aerodynamic optimization of this morphing wing is the main part of this study; therefore, establishing a reliable optimization framework is of paramount importance. This study uses a high-fidelity object-oriented optimization framework, DAFoam, based on an adjoint method. DAFoam is a discrete gradient-based optimization algorithm coupled with a high-fidelity flow solver, OpenFOAM. The optimization is proceeded by a reliable 3D wing parametrization called Free-Form Deformation (FFD), and ICEM-CFD meshing software is used for the generation of high-quality meshes. This optimization and these simulation tools are used for morphing wing aerodynamic optimization. The structural analysis part of this research is carried out using the Altair Inspire software for both the structural analysis and the topology optimization.

1.3.1 The Free-Form Deformation (FFD) parametrization technique

The parametrization technique selected for generating wing models significantly influences the outcomes of the optimization process. An effective parametrization can be achieved by encompassing a large design space with a few design variables. Free-Form Deformation (FFD), a part of the Soft Object Animation (SOA) algorithms, represents the deformative parametrization method. FFD has been continuously improved and is now used extensively in engineering applications, particularly for optimizing aerodynamic shapes. Early FFD models used tri-variate Bernstein polynomials to define control points, but more recent FFD models have adopted both tri-variate Bezier and NURBS polynomials. The studied object, such as an aircraft or its components, is embedded within an FFD block, with changes made to the block's control points, altering the shape of the embedded object. Traditional techniques, such as NURBS, Bezier-PARSEC, and CST are effective for 2D optimization, but they are impractical for 3D wing or aircraft optimization due to the high number of design variables. The FFD focuses on geometrical variations rather than on geometry itself, making the number of design variables almost irrelevant, and is thus suitable for complex optimization tasks. For instance, if $\overline{\mathrm{g}}$ is the baseline geometry and $\Delta\overline{\mathrm{G}}$ is its geometric change or variation, the morphing geometry can be represented as:

$$\overline{\mathbf{G}}_{morphing} = \overline{\mathbf{g}} + \Delta\overline{\mathbf{G}} \tag{1.1}$$

where $\Delta\bar{G}$ encompasses geometrical parameters variations, such as twist, camber, thickness, shear, and planform deformation, as outlined below:

$$\Delta\overline{\mathbf{G}} = \delta\overline{\mathbf{G}}_{twist} + \delta\overline{\mathbf{G}}_{camber} + \delta\overline{\mathbf{G}}_{thickness} + \delta\overline{\mathbf{G}}_{shear} + \delta\overline{\mathbf{G}}_{planform} \tag{1.2}$$

Depending on the morphing strategy, these variations are managed by specifying the degree of freedom to the FFD control points.

In this thesis, the tri-variate B-spline volume is used to describe the FFD block, as follows:

$$\vec{V}(u,v,w) = \sum_{i=0}^{N_u-1}\sum_{i=0}^{N_v-1}\sum_{i=0}^{N_w-1} N_{i,m_u}(u)N_{j,m_v}(v)N_{k,m_w}(w)Q_{i,j,k} \tag{1.3}$$

where m_u , m_v, and m_w are the degrees of freedom, $Q_{i,j,k}$ is the undeformed block, and N_{i,m_u}, N_{j,m_v}, and $N_{k,m_w}$are the basis functions (Ronzheimer, 2004):

$$\vec{P}(u,v,w) = \sum_{i=0}^{N_u-1}\sum_{i=0}^{N_v-1}\sum_{i=0}^{N_w-1} N_{i,m_u}(u)N_{j,m_v}(v)N_{k,m_w}(w)Q_{i,j,k} \tag{1.4}$$

The basic functions are calculated as follows:

$$N_{i,l_u} = \begin{cases} 0, & u_i \le u \le u_{i+1} \\ 1, & otherwise \end{cases} \tag{1.5.1}$$

and

$$N_{i,m_u}(u) = \frac{u-u_i}{u_{i+m_{u-1}}-u_i} N_{i,m_{u-1}}(u) + \frac{u_{i+m_u}-u}{u_{i+m_u-u_{i+1}}-u_i} N_{i+1,m_{u-1}}(u) \tag{1.5.2}$$

The original volume given in Eq. (1.4) is substituted with the new B-splines volume, which is computed using the updated coordinates of the embedded wing, as follows:

$$\vec{P}^{new}(u_0,v_0,w_0) = \sum_{i=0}^{n_u} N_{i,m_u}(u_0), N_{j,m_v}(v_0), N_{k,m_w}(w_0)Q_{i,j,k}^{new} \tag{1.6}$$

The coordinates of the control points after deformation are represented by $Q_{i,j,k}^{new}$, from which $\vec{P}^{new}$, the new coordinates of the embedded object, are determined. Figure 1.1 shows the wing morphing using the FFD technique.

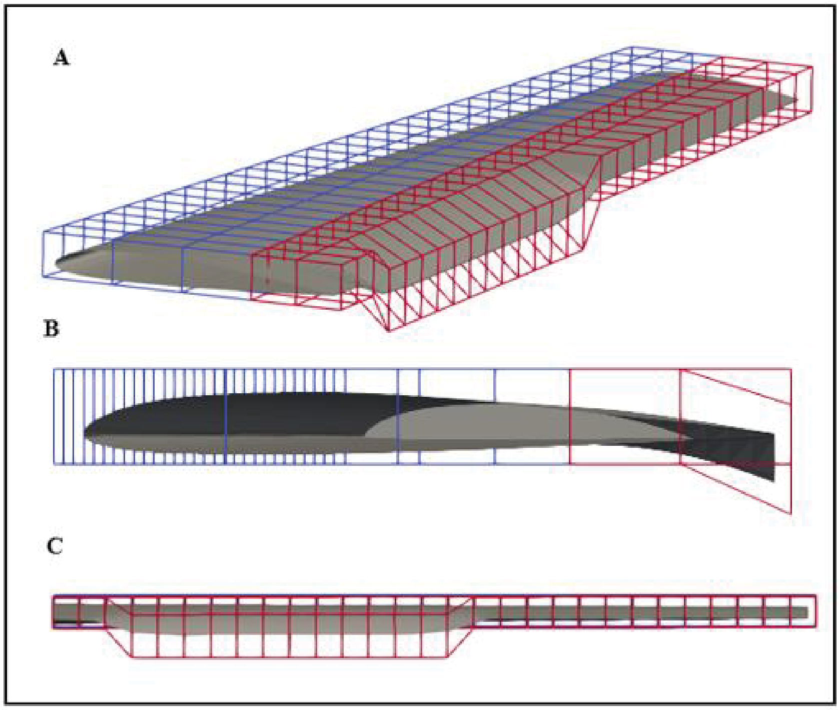

Figure 1.1 Wing morphing parametrization using the Free-Form Deformation technique: A) isometric, B) side view, and C) rear view

1.3.2 Gradient-based optimization algorithm using the adjoint method

The gradient-based method's solutions to optimization issues are typically stated as follows:

$$\min_{x \in R_n} f(x) \tag{1.7}$$

where the partial derivatives or gradients of the design variables are calculated to obtain the optimal value of f, which guides the search directions to obtain the best feasible values of *f(x)*. Although there are many gradient-based techniques, the best one depends on the optimization specifications, such as whether it is linear or nonlinear, bounded or unbounded, etc. In this research, a nonlinear constrained optimization problem needs to be solved. This study uses the Interior Point Optimizer (IPOPT) algorithm to tackle continuous and nonlinear constraint problems. The line searches in this strategy are predicted using filter techniques. The first and second derivatives of the objective function (Jacobian and Hessian, respectively) are found using the IPOPT optimizer with the Automatic Differentiation (AD) technique. Optimization problems with many design variables (wings or a whole airplane) can be solved thanks to the Discrete Adjoint (DA) method, which significantly decreases the number of iterations and, consequently, the calculation time.

Calculating the partial derivatives of the design variables is a difficult and expensive task in optimization situations, as it requires many design variables. By reversing this difficult job and considering the dependency of partial derivatives on the state variables rather than on the design variables, the DA approach can significantly reduce the computation time and expense. The adjoint terms are obtained using the Discrete Adjoint (DA) approach by differentiating the discretized Navier-Stokes equations. In other words, adjoint equation calculations, which rely on state variables, replace gradient computations, which depend on design variables. Significant computing time is saved because there are notably fewer state variables than design variables.

The objective function is represented by $f = f(x, \omega)$, where x and ω are the state and design variables, respectively. The following expression represents the computation of the total derivatives:

$$\frac{d\boldsymbol{f}}{d\boldsymbol{x}} = \frac{\partial \boldsymbol{f}}{\partial \boldsymbol{x}} + \frac{\partial \boldsymbol{f}}{\partial \boldsymbol{\omega}} \frac{\partial \boldsymbol{\omega}}{\partial \boldsymbol{x}} \tag{1.8}$$

Since $\mathbf{R}(x, \omega) = 0$ implies that the residuals of the governing equations must be satisfied, the derivatives of the residuals with respect to x must equal zero, which eliminates the residuals' dependency on the number of design variables, which is only present in the expression $\partial\omega/\partial x$.

$$\frac{d\mathbf{R}}{d\boldsymbol{x}} = \frac{\partial \mathbf{R}}{\partial \boldsymbol{x}} + \frac{\partial \mathbf{R}}{\partial \boldsymbol{\omega}} \frac{\partial \boldsymbol{\omega}}{\partial \boldsymbol{x}} = 0$$

that gives:

$$\frac{\partial \boldsymbol{\omega}}{\partial \boldsymbol{x}} = -\frac{\partial \mathbf{R}}{\partial \boldsymbol{x}} \left(\frac{\partial \mathbf{R}}{\partial \boldsymbol{\omega}}\right)^{-1} \tag{1.9}$$

Equations (1.8) and (1.9) are combined to obtain the following equation.

$$\frac{df}{dx} = \frac{\partial f}{\partial x} - \frac{\partial f}{\partial \omega}\left(\frac{\partial \mathbf{R}}{\partial \omega}\right)^{-1}\frac{\partial \mathbf{R}}{\partial x} \tag{1.10}$$

where $\frac{\partial f}{\partial \omega}\left(\frac{\partial \mathbf{R}}{\partial \omega}\right)^{-1}$ is the adjoint vector ψ, which is determined using the following equation (He et al., 2020):

$$\left[\frac{\partial \mathbf{R}}{\partial \omega}\right]^{T}\psi = \left[\frac{\partial f}{\partial \omega}\right]^{T} \tag{1.11}$$

Finally, after computing the $\frac{\partial f}{\partial x}$ and $\frac{\partial \mathbf{R}}{\partial x}$ in Eq. (1.10) as well as of the adjoint vector ψ in Eq. (1.11), the total derivative of f can be obtained as follows:

$$\frac{df}{dx} = \frac{\partial f}{\partial x} - \psi^{T}\frac{\partial \mathbf{R}}{\partial x} \tag{1.12}$$

1.3.3 The DAFoam optimization framework

This research is based on a high-fidelity optimization framework known as the object-oriented discrete adjoint (DA) approach with OpenFOAM, called “DAFoam”, developed at the Michigan University MDO laboratory, in which the optimization loop integrates the high-fidelity flow solver OpenFOAM. DAFoam gives more precise results than low-fidelity solvers such as XFOIL or XFLR5 that are commonly used in aerodynamic optimization.

To implement the DA approach in OpenFOAM for optimization problems, DAFoam uses the accelerated Finite Difference (FD) technique to compute the adjoint equation's partial derivatives, which differs from the Automatic Differentiation (AD) method. The discrete adjoint-based optimization in OpenFOAM is possible thanks to this method, even when dealing with a high number of design variables.

As described above, the OpenFOAM layer and Python libraries are connected through a high-level interface in this framework. The former is composed of the flow solver "simpleFoam,", while the latter is made up of three libraries for mesh deformation and optimization setup: "pyGeo" for surface geometry parametrization and geometric constraints computations, "pyWarp" for volume mesh deformation, and "pyOptSparse" for optimization. Figure 1.2 depicts the entire optimization procedure.

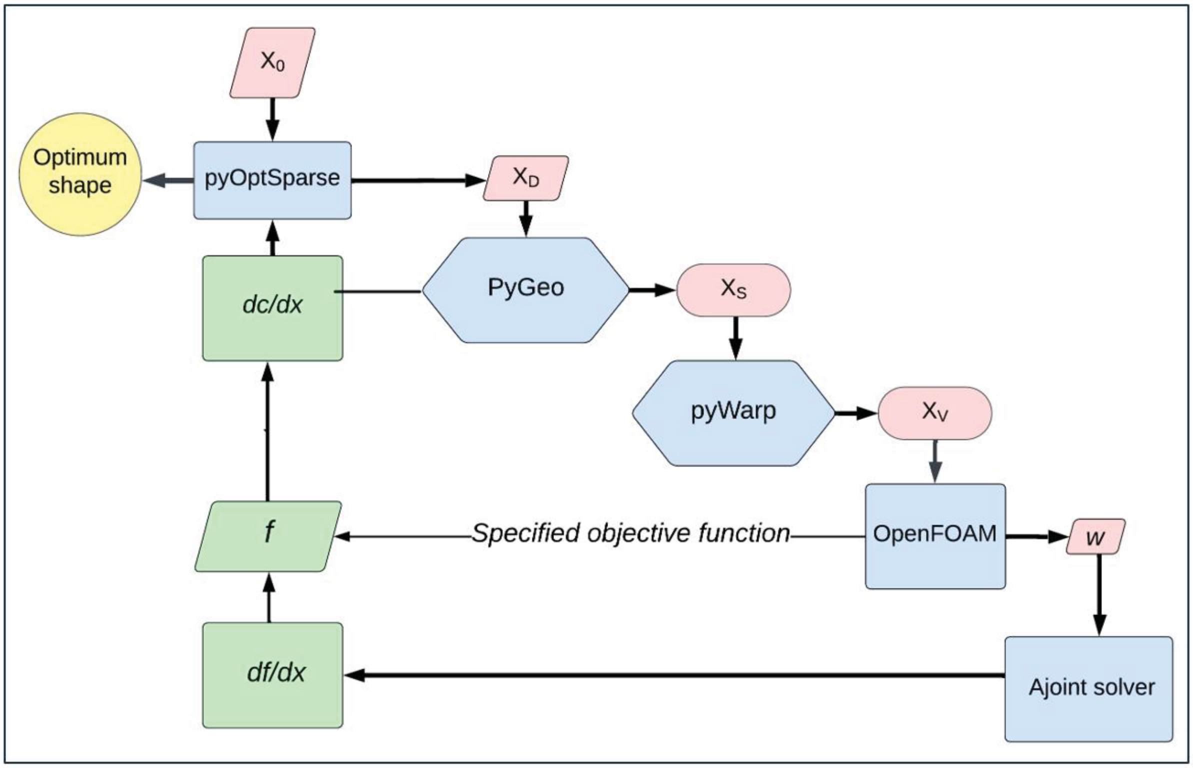

Figure 1.2 DAFoam optimization framework

1.3.4 Structural analysis and topology optimization of the Elephant Trunk Mechanism (ETM)

The Elephant Trunk Mechanism (ETM) is structurally analyzed utilizing Finite Element Analysis (FEA) in the Altair Inspire software. Several equations, including equilibrium, compatibility, and constitutive equations, are used, all derived from the laws of mechanics. The equations of equilibrium guarantee that the total sum of the forces and moments acting on the structure is zero. Three force equations and three moment equations, each corresponding to a coordinate direction, are used in the 3D FEA. The equilibrium equation in this paper is given by the static analysis:

$$K.\mathbf{u}=\mathbf{F} \tag{1.13}$$

where **u** is the vector of nodal displacements, F represents the external forces, and K denotes the stiffness matrix of the structure. The compatibility equations guarantee that the rotations and deformations of the elements match the displacements of their linked nodes. Thus, along the elements' boundaries, the continuity of their displacements is maintained.

A topology optimization is performed on the proposed mechanism for the SMTE flap; a multi-objective topology optimization conducted using Altair Inspire with the goal of reducing the structure's weight while maximizing its stiffness. Optimizing the topology improves material distribution by strengthening its important regions and cutting superfluous bulk to save weight.

Since the total structural compliance and stiffness are inversely correlated, the optimization aims to minimize structural compliance to maximize stiffness, which can be stated as follows:

$$C = \mathbf{F}^T\mathbf{u} \tag{1.14}$$

where the overall structural compliance is represented by C.

As stated in Equation (1.14), the stiffness or internal forces within a structure must be in balance with external forces to adhere to the equilibrium equation. Thus, we can rewrite Eq. (1.14) as follows in terms of stiffness by considering Eq. (1.13):

$$C = \mathbf{u}^T\mathbf{K}\,\mathbf{u} \tag{1.15}$$

Consequently, stiffness maximization, one of the objective functions, is satisfied by minimizing Eq. (1.15).

Weight reduction, the second objective here, depends on the material volume, V, in the design space, and the material density, ρ. Using the FE approach, the total volume is separated into finite element components and expressed as follows:

$$V(\rho) = \sum \rho_e V_e \tag{1.16}$$

where each element's volume and density are indicated by V_e and ρ_e, respectively.

1.4 Literature Review

Morphing wing design has emerged as a transformative approach in Aerospace Engineering, aiming to improve aerodynamic efficiency, flight adaptability, and to reduce fuel consumption across various flight conditions. Unlike conventional fixed-wing designs that are optimized for specific operational regimes, morphing wings enable real-time shape adaptation, facilitating a dynamic response to changing flight conditions. This versatility has shown advantages in enhancing lift, reducing drag, and achieving better performance, particularly for applications in Unmanned Aerial Vehicles (UAVs) and next-generation commercial aircraft. Numerous studies have explored the core components of morphing wing technology, including the development of adaptive materials that maintain wings’ structural integrity while enabling its flexibility, as well as innovative actuation systems that ensure efficient shape transformation. Additionally, recent work has advanced control methodologies to support these adaptations, allowing for more effective and reliable morphing capabilities. Together, these multidisciplinary studies contribute to advances in material science, structural mechanics, and control engineering to address the complex requirements of morphing wing systems.

1.4.1 Morphing Wing Reviews

In a comprehensive study, (Li et al., 2018) reviewed different types of morphing concepts applied on wing or airfoil models, from an aerodynamics, control and optimization perspectives. Their review included airfoil morphing, using variable camber (drooped nose leading edge and trailing edge morphing), variable thickness (upper-surface morphing), as well as wing morphing concepts, such as spanwise morphing, variable sweep, twist morphing, and folding wing. Different types of analyses and simulation tools that have been used in most of the earlier morphing studies were also presented in various disciplines. This review also highlighted that 2D morphing analyses were not as efficient as 3D morphing analyses.

In a recent review study, (Ameduri & Concilio, 2023) discussed the current aviation expectations on morphing wing technology and its limitations in applications on commercial jets. They focused on the weakness points in this technology. These applications on real aircraft include the load transmission of the moving parts to the supporting wing box, how the flexibility–rigidity paradox was addressed by specific critical components, such as the flexible skin, the scalability dependence of the morphing architectures, and the specific aeroelastic behavior of nonconventional architectures. They attempted to answer the questions of how soon morphing will become a practical application and what the main current challenges are. Four major weakness points, as the ones mentioned earlier, were identified: incorporation of load transmission modality from morphing subsystems into the structure, conflicting requirements between rigidity and flexibility, scalability of adaptive architectures, and aeroelastic response.

1.4.2 Morphing Wing Projects at LARCASE

In a three-years multidisciplinary CRIAQ 7.1 project, in a collaboration among ÉTS, Aerospace companies Bombardier and Thales, the research institute IAR-NRC and École Polytechnique, the morphing wing technology was analyzed by installing a flexible upper surface skin to the wing with the aim to analyse the aerodynamic performance. One objective was to identify and evaluate the laminar to turbulent flow transition towards the trailing edge and its effect on drag reduction. The inner mechanism of the morphing skin included two actuators using shape memory alloys, where both provided vertical displacements for the upper skin to control and thus to delay the flow transition point and obtain the optimized airfoil shape. By applying a genetic algorithm coupled with XFOIL flow solver on the morphing wing, the optimization process generated the optimum airfoil shape for 35 flight conditions, including five Mach numbers and seven angles of attack. The morphing wing equipped with sensors, actuators and control system was tested in the IAR-NRC wind tunnel to experimentally validate the numerical results. The SMA actuators were able to obtain 35 optimized aerodynamic skin shapes and to translate their displacements to the pressure sensors and control system (Popov, Botez, & Labib, 2008). A novel method was developed to determine the transition point. This method used two interpolation algorithms to calculate the second derivative of the pressure distribution, and to identify the maximum curvature location in the pressure distribution curve while accounting for the flow transition point. The final result of this project demonstrated that morphing upper skin could move the transition point towards the trailing edge by 40% , and thus could extend the laminar flow on the upper skin, and reduce the drag compared to the baseline wing for all 35 flight cases (Botez, Molaret, & Laurendeau, 2007).

As part of the CRIAQ MDO 505 project, a collaborative research project between Canadian and Italian partners, (R. M. Botez et al., 2018) conducted an exhaustive research on a new wing-tip morphing concept by using both upper surface morphing and an interchangeable aileron, with both conventional hinged and morphing configurations for different flight conditions. The morphing wing was also prototyped and tested at the NRC subsonic wind tunnel. The main purpose was to demonstrate the blended morphing concept and its influence on wing tip aerodynamic performance. They also performed a 2D aerodynamic optimization on both a morphing upper surface and a morphing aileron using the in-house genetic algorithm coupled with XFOIL solver. For the aero-structural optimization, the displacements of the internal actuators were determined at their optimum positions with the objective of controlling the laminar flow region on the wings' upper surface. In their study, 14 out of 22 cases obtained larger laminar flow regions, and a minimized turbulent region. The numerical results showed a very good agreement with the experimental results in terms of transition point detection. Finally, a blended morphing upper surface and a morphing aileron were found to be a suitable morphing configuration to both drag reduction by up to 9.5% and extension of laminar region by up to 9%.

1.4.3 Morphing Trailing Edge (MTE)

Using an internal compliant composite truss, (Wu et al., 2017) proposed a new morphing concept with an active trailing edge. They used an electric actuation system with Linear Ultrasonic Motors (LUSM) with the capability of performing for multiple degrees of freedom. The aerodynamics properties were extracted from both an XFOIL code and wind tunnel tests. The compliant morphing trailing edge was compared with a hinged flap airfoil to reveal the design's efficiency. The results, expressed in terms of lift-to-drag ratio, showed that the morphing trailing edge system, which had a smooth deflection, outperformed the conventional hinged flap airfoil. However, these results also demonstrated that the superiority of the morphing trailing edge occurred at small angles of attack, and for a lift coefficient smaller than 1.8, while the hinged flap showed a better performance for a higher angles of attack.

Another morphing trailing edge concept was introduced soon after, by (Dumont, 2018). He proposed a trailing edge morphing system by integration of two flexible surfaces at the upper and lower sides of the wing and with three rotational motors inside. This approach transfers the rotational motion of the motors to the bending of the flexible surfaces in a very smooth manner. A degree of rotation is translated as a degree of bending in both the upward and downward directions by preserving tangency and smoothness of the surface. Dumont applied this morphing approach to the main flaps and the ailerons. A gradient-based optimization was performed to find the best local position of the deflection. In this manner, a lift-to-drag ratio was chosen as the objective function. The results showed a 2.6% gain in the objective function and a 0.6-degree reduction in the angle of attack. The main flaps and ailerons had different optimization trends, so that, while the main flap camber was reduced, the ailerons camber was increased by its downward deflection, but the overall aerodynamic performance was improved. By performing another optimization with a different lift coefficient value as a constraint, Dumont showed that the morphing had a local impact on the aerodynamic performance. With a C_L of 0.42, the gain in the objective function was reduced to 1.3%; however, this case increased the lift to drag ratio for C_L values smaller than 0.45.

To design a trailing edge morphing system, (Li & Li, 2016) proposed a camber morphing wing model. They presented a mathematical model to verify the wing's ability to change its camber. The aerodynamics characteristics were investigated, and the relationship between the aerodynamic parameters and the tailing edge rotation angle was explored in a comparative analysis. Finally, they performed an optimization on the proposed mechanism to find its optimum linkage connections that would produce an optimum deformation along the trailing edge. An Artificial Fish Swarm (AFS) optimization algorithm was chosen for this task. The results indicated that this optimized mechanism could improve the aerodynamic characteristics; after optimization, both the lift and drag coefficients were decreased by 8.5% and 9.88%, respectively, thereby improving the lift to drag ratio by up to 1.5% .

Another morphing design concept was proposed by (You et al., 2019) – a gripper pin structure for an airplane wing, capable of decoupling the in-plane stiffness from out-of-plane stiffness. They analyzed the performance of a gripper wing skin for the variable camber-compliant wing morphing process. Structural analysis was conducted to examine the torsional and bending resistance mechanisms of the wing skin. Their results indicated that the gripper wing skin, compared with wing skin made of bulk materials, did not show excessive stress, a bulge effect, or irregular out-of-plane deformation, resulting in low actuation energy, desirable for downsizing an internal actuator power system. Nevertheless, considering actual production processes, they concluded that there could be limitations in the materials, fabrication processes, weight, fatigue performance, and size.

A variable camber morphing airfoil with compliant ribs and flexible composite skin was studied in a hierarchical modeling framework (Murugan, Woods, & Friswell, 2015). This work used a biologically inspired, internal structure, the Fish Bone Active Camber (FishBAC), to produce continuous camber morphing. They established a hierarchical computational model of the morphing airfoil to decouple the compliant ribs from the airfoil skin, and to decouple the aeroelastic simulation of the compliant 2D structure from the skin design optimization. First, a fluid-structure interaction was carried out with an homogenized beam model of the compliant rib structure and a 2D panel method. Next, they developed a Finite Element (FE) model of the camber morphing skin. A multi-objective optimization framework was then developed to find the optimal curvilinear fibers paths of the morphing skin to meet the airfoil geometric shape and actuation requirements. The results showed a significant camber variation, and significant changes in aerodynamic properties, as well as a multi-objective minimization of the actuation energy and out-of-plane skin deformation. These changes led to a considerable reduction in the elastic strain energy, and out-of-plane skin deformations.

In a comprehensive study, (Weishuang, Yun, & Peiqing, 2017) investigated the flexible variable camber trailing edge flap in three flight conditions: take-off, landing and cruise. They performed an optimization of the flap position on the main wing body, including overlap and gap distances, and also, they optimized the flap deflection for the specified flight conditions. The simulations were conducted in both 2D and 3D to compare their differences in the results. In the take-off and landing configurations, the objective function was the maximization of the lift coefficient as well as the lift-to-drag ratio. The results indicated that for the take-off configuration, there was a slight increase in camber, which led to an 8% gain in the lift coefficient, and a 7% gain in the lift-to-drag ratio; however, the stall angle was decreased by 1 degree. For the landing configuration, the variable camber trailing edge improved the lift coefficient at the stall angle by 1.5% while maintaining the stall characteristics. Finally, for the cruise flight condition, the lift increased by 40% at a cruise angle of 3 degrees in the 2D case, and the lift-to-drag ratio was increased by up to 30%. They proposed a variable camber mechanism with a corrugated structure as the stringer in the skin, with the eccentric beam as the deformation mechanism, so that the flap could bend with the rotation of the eccentric beam.

Structural analysis of the morphing trailing edge flap was conducted for a large aircraft wing (Di Matteo & Guo, 2011). The rear part of the trailing edge flap was modified to be integrated with a set of internal actuation mechanisms distributed along the span of the flap. The actuation system chosen to deflect the trailing edge flap structure was an eccentric beam actuation mechanism (EBAM), which was developed in the 1970s within the DARPA project. They performed a stress analysis to investigate the structural behavior of the flap under actuation and assessed its structural integrity during trailing edge deflection. They showed that under the internal actuation and external aerodynamic loads, the skin was made of composite and metallic materials; both materials were able to achieve the desired shapes subjected to the strength constraint. Finally, they studied the dynamic behavior of the morphing trailing edge flap and analyzed the effect of a transient dynamic load on the structure. The dynamic response results showed that the eccentric beam mechanism provided sufficient stiffness to the trailing edge flap to ensure a high degree of stability against gust loads.

(Barbarino, Dettmer, & Friswell, 2010) proposed an innovative flap architecture for a variable camber trailing edge based on a variable geometry truss concept. The compliant rib was based on a truss-like structure, in which its members were “active” rods made of Shape Memory Alloys (SMAs). These actuators were able to sustain the external loads while allowing controlled shape modification. An optimization process based on a genetic algorithm was established to optimize the topology of the internal truss structure. The performance of the structure was evaluated in terms of the achievable lift coefficient, and the required actuation temperatures for the SMAs. The lift coefficients for a morphed flap were compared with those of hinged flap for various angles of attack and higher lift coefficients were observed for the morphed flap, after deformation.

In an experimental study, (Nguyen et al., 2014) investigated the performance of a flexible wing with a Variable Camber Continuous Trailing Edge Flap (VCCTEF) to minimize drag in cruise flight by using low-cost aeroelastic model test techniques. They used a 10%-scaled model of a transport aircraft wing constructed with a woven fabric composite and a foam core. The VCCTEF design consisted of multi-segment flaps, each of them had three chordwise camber segments and five spanwise flap sections for a total of 15 flap sections. To cover the gaps between spanwise flaps, elastomeric material was used to create a continuous trailing edge. The elastic flap had three hinged sections, in which a combination of SMAs and electric actuators were utilized to bend the overall flap using the rotation of interior rods. They tested twelve different flap configurations to see the effect of various bending shapes on the lift to drag ratio and the lift and drag coefficients, all of which showed improvements in terms of drag reduction and aerodynamic performance, while two configurations lowered the aerodynamic efficiency compared to that of the baseline wing configuration. The wind tunnel test results revealed that a VCCTEF design could reduce drag by up to 6.31% and improve the lift to drag ratio by up to 4.85%.

Researchers also proposed and designed a continuous morphing trailing edge wing with a nano skin fabricated using a surface mechanical attrition treatment technology. Aerodynamics analysis was also performed to draw a comparison between a Flap Wing Morphing (FWM) and a Continuous Wing Morphing (CWM). The deflection point for the FWM wing was located at 30% of chord length, while it was at 50% of chord length for the CWM. Four different deflection angles were considered to find the specific range in which the morphing wings performed better. Longitudinal aerodynamic parameters, including the lift and the drag coefficient, as well as the lift to drag ratio were examined. The comparisons showed that lift enhancement for CWMs was higher for large deflection angles and the drag reduction of CWMs was remarkable, especially at lower deflection angles and small angles of attack compared to the FWM. It was also shown that with CWMs, the flow separation was suppressed, and its initiation was delayed. However, lift-to-drag ratio only increased for small angles of attack, which offered more choices to adapt to different flight conditions (Fengqian et al., 2021).

In a comparative study, (Abdessemed et al., 2018a) investigated the benefits of morphing trailing edge flaps versus those of conventional hinged flaps in a 3D analysis. They performed both a steady and an unsteady analysis to capture the aerodynamic performance in a real-time morphing process. The comparison was drawn for two flap angles: 0 and 14 degrees. They showed that the baseline wing with a hinged flap and zero deflection had an increase in drag and a reduction in lift due to the spanwise and chordwise gaps. The comparison of the morphing with the hinged flaps showed that a morphing trailing edge increased the lift by up to 40% at similar drag coefficients at angles of attack lower than 7 degrees compared to those of hinged flap, and the overall aerodynamic efficiency was improved by 45%. However, for angles of attack greater than 8 degrees there was a sudden increase in drag without any lift generation, which restricted the morphing trailing edge superiority to angles of attack smaller than 8 degrees, and the hinged flap performed better at higher angles of attack. This performance was due to the gaps around the flap, which assisted the flow control process by mixing pressure side flow with separated flow on the wing upper surface. Finally, the unsteady analysis results showed that the aerodynamic efficiency for the entire morphing time was smaller than that of steady-state morphing, which indicated the necessity of considering morphing motion in the design process.

In a joint project between NASA and Boeing, (Urnes & Nguyen, 2013) investigated a Variable Camber Continuous Trailing Edge Morphing Flap (VCCTEF) system for future transport aircraft. The VCCTEF improves aircraft performance in terms of lift and drag, as well as the weight and maneuverability of the aircraft, including its rolling performance. These researchers showed that a VCCTEF system could accomplish two performance objectives: 1-efficient high lift capability at take-off and landing, and 2- cruise drag reduction through the control of the twist shape of the flexible wing. This study was conducted on NASA's vortex-lattice code VORVIEW. The roll control analysis was performed to compare a flexible aileron system with a conventional one. This analysis was conducted on outer camber flap segments on the portion located away from the engines. By analyzing the roll control derivatives, they showed that a VCCTEF provided larger roll control derivatives than those of conventional ailerons. Hinge moment analysis, as well as aeroelastic analysis were also performed. Finally, the aerodynamic model was optimized to reduce the induced drag. The overall results indicated that a VCCTEF system had five important advantages with respect to a conventional system: 1- reduction of the cruise drag, 2-a high lift configuration with less drag, 3- better roll control, 4- stabilization of wing dynamic modes, and 5- weight savings for flap actuation components. A VCCTEF system thus had a very good potential to accomplish the energy goals for future N+3 aircraft transports.

In a joint project conducted by U.S. Air Force Research Laboratory (AFRL), NASA, and FlexSys Inc., a series of flight tests were conducted on a Gulfstream GIII business jet with variable geometry multifunctional control surfaces, with the purpose of eliminating the trailing edge flaps. The projects' title was the Adaptive Complaint Trailing Edge (ACTE). The test flights were conducted up to the Mach number of 0.75 and a maximum altitude of 40,000 ft. In this design, the control surface was bounded with left and right transition sections, through which all discontinuities on the wing body were eliminated. The main purpose of the flight tests was to demonstrate the robustness and feasibility of the FlexFoil material. It was found that an ACTE was structurally feasible, and it could perfectly sustain the maximum design loads of commercial aircraft for over 50 hours of flight tests without any failure. The test results showed that the ACTE design enhanced the lift coefficient without any drag reduction, thus improving the aerodynamic efficiency. On the other hand, unlike fowler flaps, the study showed that there was a possibility of air penetration at junction points, as well as the possibility of surface area extension. Therefore, at higher angles of attack, an ACTE required a flow augmentation device for maintaining good flow attachment at flap positions (Kota, Flick, & Collier, 2016).

In an experimental study, (Rivero et al., 2021) drew a comparison between FishBAC morphing wings and hinged trailing edge flaps in a quasi-2D wind tunnel to investigate the aerodynamic performance of the morphing flap by analyzing different criteria. The measurements were done by use of Particle Image Velocimetry (PIV). Three different wing configurations were tested, including a baseline NACA 23012, a plain flap and a FishBAC. The baseline wing performance was also validated with previous data in the literature. The test results showed that a plain flap gave a higher drag increment than that of a FishBAC configuration; however, the lift coefficient was similar for both configurations, which led to a greater lift to drag ratio (aerodynamic efficiency) for FishBAC morphing flaps for all tested angles of attack. This improvement was very noteworthy at moderate and high lift coefficients greater than one, ranging from 50% to 200%, but for lower lift coefficients, this improvement was only as high as 16%. These tests also revealed that aerodynamic loads restricted the FishBAC maximum deflection, and, as the angle of attack increased, this restriction became significant, leading to three times higher actuation power than that of hinged flaps.

(Woods et al., 2016) introduced a compliant morphing flap transition by addressing the side-edge gaps in the spanwise direction. With their proposed concept design, the gaps were sealed, and a smooth flow transition was accomplished, which lofted between the rigid wing and the morphing flap. They proposed a shape function for smooth deformation of the transition sections. They compared the morphing flap with and without transition sections to evaluate their impact on aerodynamic behavior, and found that in the absence of transition sections, a strong vortex was formed near the gaps, and the downstream rollup vortex disappeared. The CFD results also showed that by using transition sections, lift was increased, drag was reduced, and a 7% increase in lift-to-drag ratio was achieved.

To reduce lift-induced drag, researchers simulated and compared the trailing edge morphing flap with conventional wing flaps. The substantial difference in these designs was found in the transition sections; for the morphing wings, it was seamless, but for the conventional wings, there was a gap between the flap and the wing main body. First, they compared the non-optimized morphing wing with the conventional wing, and they found an increase in lift of up to 10.8% and an improvement in lift-to-drag ratio of up to 13.6% for the optimized morphing wing; however, as the angle of attack increased, the morphing effect decreased. Secondly, they added the optimized morphing wing results to the previous comparison, which revealed an increase in lift-to-drag ratio of up to 5.3% compared with the non-optimized morphing wing. The pressure coefficient variations were also compared and the results of the optimized morphing wing showed that the gaps elimination increased the pressure coefficient in the trailing edge section and reduced vortices in this area, which led to the reduction of the pressure drag of up to 5% in comparison to a conventional wing, and a reduction of up to 2.7% in comparison to a non-optimized morphing wing. Wind tunnel tests were also performed, which showed a good agreement with numerical results, with a 1.87% error for the lift and a 6.75% error for the drag. Finally, an experimental acoustic analysis was performed, and its results showed a noise level reduction of up to 50% for the morphing wing compared to the conventional wing (Ninian & Dakka, 2017).

A new morphing trailing edge design concept was introduced by Communier, Botez, & Wong, (2019). This morphing wing was designed and tested in the LARCASE's Price-Paidoussis subsonic wind tunnel and its performance was also compared to those of a rigid wing in the same wind tunnel. The deformation was performed by use of small vertical incisions. Based on the size and number of these incisions, the flexibility and amplitude of deformation were adjusted. A comparative study was performed between the morphing and rigid wings to identify the benefits of the morphing trailing edge in terms of aerodynamic efficiency. These comparisons of aerodynamic coefficients revealed that morphing wing generated a lower lift coefficient compared to that of a rigid wing; however, the drag coefficient was also lower than that of the rigid wing. Based on these results, the lift to drag ratio was obtained for both wing types, revealing that the morphing trailing edge had a higher lift-to-drag ratio and was more efficient than a rigid wing for angles of attack between -10° to 10°. Therefore, it was concluded that by using the morphing trailing edge, fuel consumption reduction could be achieved based on the results obtained from aerodynamic coefficients, while maintaining the same wing masses.

Gürses et al. (2017) designed and analyzed a hybrid morphing trailing edge for an Unmanned Aerial Vehicle (UAV). Both structural and aerodynamic analyses were performed. The wing trailing edge was morphed in both upward and downward directions to decrease and increase the camber (de-camber and camber), respectively. Target airfoil shapes were selected to match the morphed configuration to the target airfoils, and their aerodynamic property variations were analyzed. The final aerodynamic results indicated that the target morphed shape could be obtained with only a minimal deviation of the aerodynamic properties from the target shapes by considering lift, drag and pitching moment coefficients. Moreover, the structural integrity and safety were also ensured for the morphing control surface.

1.4.4 Gradient-based Optimization

An object-oriented framework to rapidly develop a discrete adjoint method based on OpenFOAM was developed in the MDO laboratory at Michigan University. Their framework had the potential of becoming useful tool for application in high-fidelity multidisciplinary design optimization problems. In this framework, the discrete adjoint method could be implemented on OpenFOAMs' steady-state primal solvers. They showed the benefit of rapidly implementation of the adjoint method on different primal solvers and turbulence models. Three aerodynamic shape optimizations were studied for incompressible, compressible, full turbulence, and transitional turbulence conditions. These three cases were: 1- Multipoint aerodynamic shape optimization for a low-speed UAV wing under full turbulence conditions; 2- Single-point aerodynamic shape optimization for the same UAV wing under transitional turbulence conditions; and 3- Single-point aerodynamic shape optimization for the Common Research Model (CRM) wing under subsonic conditions. The objective of all three optimization problems was drag minimization. The drag reduction obtained in these three cases were found to be 5.1%, 6.0%, and 5.0%, respectively, which confirmed the success of the proposed adjoint framework (He et al., 2019).

Another gradient-based aerodynamic optimization framework was performed by (Zhang et al., 2021). They investigated the optimum deformation of a transonic airfoil with morphing leading and trailing edges. Using an adjoint method, they studied optimum leading and trailing edge deformations with drag minimization as the objective function and control of the skin length as an optimization constraint. In this study, the CST method as parametrization method and the open-source SU2 flow solver were coupled for optimization purposes. First, the morphing leading and trailing edges were studied separately, then the combination of both morphing types was analyzed for their further evaluation. In the leading-edge morphing, there was a

16% reduction in drag and a 19% increase in aerodynamic efficiency. Moreover, the strong shock wave at about 50% of the chord length was replaced by a smoother one. In the second trailing edge morphing, the gain in drag reduction was up to 7%, which was lower compared to leading edge morphing. Finally, the results for synthetic leading and trailing edge morphing showed that the drag was reduced by 9.7%, and the angle of attack was decreased from 2.3° to 1° for constant lift.

Researchers investigated the multipoint aerodynamic shape optimization of an adaptive morphing trailing edge of a CRM wing by using a gradient-based optimization algorithm with an adjoint method. First, they optimized the baseline wing shape, and then they performed an optimization on the morphing wing and compared the results with a non-optimized wing. They kept the wing thickness constant by applying a thickness constraint and allowed aft of the 45% chord to move freely for specified flight conditions. The results showed that there was a 1% drag reduction for the non-optimized and a 5% reduction for the optimized morphing trailing edge. To show the gain achieved in fuel consumption by using a morphing trailing edge, they created a surrogate model of optimized trailing edge shapes to compute the cruise fuel burn for different fight missions and they observed that about a 1% fuel-burn reduction could be achieved (Lyu & Martins, 2015).

Different aspects of aerodynamic optimization realized by using gradient-based optimization were addressed in a joint project by ONERA and Airbus. Three cases were evaluated in this study, assessed by the AIAA Aerodynamic Design Optimization Discussion Group (ADODG). The first case was the drag minimization of an inviscid transonic airfoil with a constraint on its geometry; a comparison was drawn among several parametrization techniques and optimization algorithms. The second case addressed the drag minimization of a transonic airfoil using RANS equations, and finally, an optimization was performed on a 3D CRM wing with the objective of drag minimization using RANS equations. Several aspects of aerodynamic optimization were addressed, including the influence of parametrization, and the impact of the design space for achieving optimal performance. They showed that for 3D design spaces, gradient-based optimization had some difficulties; however, gradient-based optimizers demonstrated very good results for drag minimization problems with several nonlinear constraints. This study also found that parametrization of the deformation of the reference geometry is preferable than direct deformation of the geometry itself (Carrier et al., 2014).

A new open-source gradient-based optimization called DAFoam was developed by (He et al., 2020). DAFoam was introduced as an object-oriented adjoint-based framework to handle optimization problems with a large number of design variables by means of a rapid implementation of the discrete adjoint method. It coupled Python libraries for optimization algorithms, and their parametrization with steady-state primal solvers of a high-fidelity flow solver, OpenFOAM. This coupling was achieved by use of sub-classes in Python, which provided a high-level interface with OpenFOAM primal solvers. They described all the mathematical equations, optimization and coupling implementations for the DAFoam framework in detail and presented several examples of different optimization problems to show the capability of the framework, including multipoint aerodynamic optimization of a low-speed UAV, aerodynamic optimization of a transonic aircraft, aerothermal optimization of turbine internal cooling passage and aero structural optimization of an axial compressor rotor. The results showed drag reductions of 3.7% and 3.6% for UAVs and aircraft, respectively. For aerothermal optimization, a 20.5% reduction in aerodynamic loss and a 5.6% increase in heat transfer were obtained, and finally, a 3.2% torque reduction was obtained for the aero structural optimization of a rotor blade.

Performing a gradient-based optimization on the morphing trailing edge of a CRM wing, (Burdette & Martins, 2019) demonstrated that adding a trailing edge morphing device to the baseline wing model at aft 10% of the wing chord would reduce the fuel consumption. The purpose was to find the shape of the morphing section that provides the best performance at the specified conditions. They first performed the optimization in an aerodynamics-only manner with no structural optimization, and the results indicated a 1% reduction in fuel burn and a 5% reduction in drag for a long-range mission. In the next step, they performed a multipoint optimization on the baseline wing under nominal flight conditions, which reduced the drag by 10 counts, but it increased fuel consumption. However, after adding the trailing edge morphing device to the optimized wing, the fuel consumption was compensated, and it was equal to that obtained in the first case. They also performed a coupled aeroelastic analysis, in which the morphing shape of the wing was analyzed using an aerostructural analysis. The results showed a 1.72% reduction in fuel consumption, which was 0.72% higher than the aerodynamic-only optimization. They also found that without morphing, the aerodynamic performance of the wing was reduced. Finally, a clean sheet redesign of the wing with morphing trailing edge was performed, which included structural design variables as well as morphing capabilities. The results showed a 15.73% structural weight reduction, and a 2.72% lower fuel burn over the whole mission.

1.4.5 Overall Airfoil Shape Optimization

The overall airfoil shape optimization has been conducted by numerous researchers to obtain the best airfoil shape for different flight conditions. One of these optimizations was performed by (Secanell, Suleman, & Gamboa, 2006). They investigated six flight conditions: stall, takeoff run, climb gradient, rate of climb, cruise, and loiter conditions, and for each condition, the optimized airfoil shape was obtained through a high-fidelity aerodynamic optimization by using a gradient-based optimization framework. The results showed a significant drag reduction on the morphing airfoil. This reduction varied from 18.7% in the climb gradient condition to 48.9% in the cruise condition (79.6% in the stall condition) and the reduction in loiter condition was 35.2%. They also compared the engine power performance of a UAV to see the impact of the optimized airfoil on fuel consumption. They observed that, despite a reduction in the drag coefficient in all design conditions, there was an increase in the minimum installed power in the takeoff run and climb gradient conditions. They determined that this increase in installed power was nearly 2.6%. Nonetheless, at low speeds greater power improvements were achieved. Finally, it was concluded that optimal airfoils shared a common characteristic, meaning that they all had a similar thickness distribution, and that the main difference between the airfoils was their camber.

1.4.6 Wing Parametrization Techniques

(Samareh, 2000) presented a multidisciplinary shape parametrization approach by focusing on two main concepts: 1-shape parametrization of perturbations rather than the baseline geometry, and 2-Using soft object animation algorithms. This approach was simple, compact and efficient and it computed the analytic sensitivity derivatives for their use in gradient-based optimization. This algorithm was applied to both low-fidelity linear aerodynamics and high-fidelity nonlinear computational fluid dynamics analyses. Moreover, it could parametrize the planform, twist, dihedral, thickness, camber and free-form surfaces. This approach was implemented for the aerodynamic shape optimization using analytical sensitivity. This parametrization approach was clearly the best choice for three-dimensional structures with a high number of design variables, on an order of 10^3, while using other parametrization methods such as spline was not possible as it would require automatic grid generation for every deformation.

A survey of shape parametrization techniques for multidisciplinary optimization was conducted by (Samareh, 2001) with the aim of evaluating the stability of available parametrization techniques for the multidisciplinary optimization of aerospace applications of complex structures by using high-fidelity fluid and solid solvers, CFD and CSM. Eight different parametrization techniques were reviewed, including partial differential equations, discrete technique, analytical, polynomial and spline, free-form deformation, basis vector, and CAD-based techniques. The stability of these techniques was evaluated based on the efficiency, effectiveness, ease of implementation and the availability of analytical sensitivities for the geometry and grid. The authors concluded that the choice of shape parametrization technique depends on six main criteria:1) consistency and accuracy of the geometrical representation; 2) number of disciplines involved; 3) availability of automatic grid generation; 4) optimization algorithms and the availability of analytical sensitivity requirements, 5) development cycle time; and 6) direct connection to CAD.

1.4.7 Structural Analysis of the Morphing Trailing Edge

Considering the structural characteristics of the morphing trailing edge, (Arena et al., 2019) analyzed the finger-like rib mechanism with a hyper-elastic skin by a combination of soft and rigid parts to evaluate the effect of morphing skin on the adaptive structural system dynamic response by considering its damping increase and modal characteristics' deviation. The soft part was contributed in the trailing edge deflection for repetitive cycles, while the rigid part was used for preserving the shape under aerodynamic loads and for minimizing the actuation power required for morphing. They also performed a numerical sensitivity analysis to investigate the impact of mechanical properties of a multi-segment skin modal response of the whole system. To prove the adequacy of the design approach and quantify the dissipative effects induced by the rubber foam on the dynamic response, they carried out an experimental dynamic test. Their results showed that the morphing skin contributed to the modal damping of the entire structure by 3-3.5% compared to the 1-1.5% contribution of an aluminum-only structure.

(Qiu et al., 2014) proposed two morphing-potential skin structures, a trapezoidal corrugated and a honeycomb skin structures and a piezoelectric-hydraulic actuator. These structures were anisotropic to be consistent with high in-plane stiffness and low out-of-plane stiffness criteria for application in morphing structures. The honeycomb skin structure was sandwiched between two flexible sheets that adhered to the honeycomb. Finite element analysis was performed for different cell angles ranging from 0° to 60°. Equivalent tensile modulus, three-point bending stiffness and strain capacity were extracted for different cell angles, and then the fabricated prototype was tested and its results were compared with numerical results. In the second case, the trapezoidal corrugated structure was theoretically analyzed in terms of bending stiffness and tensile modulus. This skin structure was shown to be the best candidate for chordwise morphing, since it had a high stiffness parallel to the corrugated direction and a low stiffness perpendicular to the corrugated direction. The numerical results were compared with theoretical results. Finally, the piezoelectric hydraulic actuator was modeled, and the actuation speed was analysed for different frequencies. The overall results indicated that this actuator could be used for small-scale UAVs.

A one-dimensional flexible skin for a spanwise morphing wing of a UAV was presented by researchers for a morphing trailing edge. An elastomer-fiber-composite surface layer supported by a flexible honeycomb structure with a zero in-plane Poisson's ratio was proposed. This structure was designed for its use in span morphing UAVs with 1D morphing wingtips, so that the internal actuation system would stretch the skin to the desired shape and preserve that shape for a required morphing duration. Several substructure configurations were evaluated and tested, and the best one was chosen for prototyping. A silicone elastomer sheet with a highly anisotropic carbon fiber reinforcement and a zero-Poisson honeycomb structure were used, and they were able to preserve out-of-plane stiffness versus an aerodynamic pressure load without greatly increasing the in-plane stiffness. Both in-plane and out-of-plane stiffnesses were experimentally tested with an integrated actuation system, and the results showed that the proposed structure could extend 100% uniaxially and increase the surface area by 100%. The FEM analysis was also conducted, and it was shown that this structure could have a high strain with a good fatigue life, based on the fact that the global strain was found to be 20 times greater than the local strain (Bubert et al., 2010).

1.4.8 Morphing Ailerons

In an attempt to enhance the manoeuvrability of small-scale UAVs, inspired by the flying capabilities of birds, (Di Luca et al., 2017) proposed a morphing wing with artificial bird-like feathers at its outer wing edges, capable of turning into fully folded and fully deployed configurations for different aerodynamic requirements; fully folded (a 41% reduction in wing surface) had the advantage of drag reduction at high speeds, while fully deployed enhanced the manoeuvrability. Moreover, this design could control the rolling maneuver by the asymmetric folding of two wings. The prototype was tested in a wind tunnel and a drag reduction of 48% was achieved when it was fully folded, and a high lift generation of 32% was obtained, when fully deployed. The asymmetric morphing wing was compared with the conventional aileron deflection in terms of roll control. It was shown that unlike the aileron flaps, where the roll torque coefficient was only dependant on the deflection angle, the asymmetric morphing wing was dependant on both the lift coefficient and the deflection angle. However, the results showed that at lower lift coefficients, the ailerons generated higher torque than that of a morphing wing, confirming the fact that the ailerons perform better at high-speed conditions, but at higher lift coefficients, the trend was reversed, and the asymmetric morphing wing performance was much better than that of a conventional aileron.

CHAPTER 2

RESEARCH APPROACH AND THESIS ORGANIZATION

2.1 Research approach

This thesis investigates novel morphing approaches for their application in next-generation aircraft. The main objective of this research is to increase conventional wings' aerodynamic performance by utilizing morphing wings in different flight conditions. Two morphing approaches are presented: 1-Trailing edge morphing, and 2-Twist morphing wingtips.

2.1.1 Development of a Seamless Morphing Trailing Edge (SMTE)

The first morphing approach is studied by performing an aerodynamic study to analyze the SMTE flap performance on the whole flight envelope of the UAS-S45, including climb, cruise and descent regimes, thereby determining the optimum configuration of the SMTE flap for each flight condition by performing a high-fidelity aerodynamic optimization. Each flight condition has a specified objective.

For climb, the objective is to increase the climb rate and reduce the amount of power required, while for cruise conditions, there are two objectives: increasing both the flight range and the endurance. Finally, for descent, the objective is to find the optimum SMTE configuration that will decrease the descent rate in engine-out conditions, with the goal of obtaining a gliding descent. After obtaining the results for each flight condition, a comparison is made for the cruise flight condition in terms of range, endurance and aerodynamic efficiency to demonstrate how the morphing wing outperforms the conventional hinged flap configuration.

In the second phase, using the results obtained from the aerodynamic study, and after obtaining the optimum configuration of the SMTE flap for each flight condition, a novel trailing edge morphing mechanism is proposed, the “Elephant Trunk Mechanism” (ETM). Next, a structural analysis in conjunction with a topology optimization is performed to examine the feasibility and robustness of the proposed ETM by evaluating the structural parameters. A multi-objective topology optimization is then performed on the initial EMT to increase structural stiffness and reduce the required weight. Finally, the obtained results are compared with the parameters of the initial EMT in terms of structural stability and weight. Once the optimum ETM topology is found, four ETM ribs are installed on the SMTE flap section on UAS-S45 wing, respecting the flap geometry sizing that has been defined previously in aerodynamic studies.

In the third and final phase, having proven the superiority of the SMTE flap in an aerodynamic study, and the stability and reliability of the elephant trunk mechanism (ETM) in a structural study, a scaled prototype model of the morphing UAS-S45 wing is fabricated using 3D printing. This prototype wing consists of four ETM ribs on the flap section of the wing, with a specified distance in between, and a control system consisting of four actuation servomotors embedded in the wing box. The whole control system is connected to a power source with a graphical interface to control the flap deformation. In addition, this SMTE flap section is covered by a flexible skin on the upper and bottom sides to embed the ETMs. Finally, the prototyped wing is tested in a subsonic wind tunnel. This phase of the study aims to accomplish two main objectives: 1- to examine the results obtained from structural analysis in real-life, and to see if the real model could perform the intended deformations, that were determined from the aerodynamic study, as well as to examine the reliability and flexibility of the skin during its deformation, and 2- to validate numerical aerodynamic results with experimental data. This phase of the study finalizes the comprehensive study of a Seamless Morphing Trailing Edge (SMTE) flap, which was the first main objective of this research.

2.1.2 Twist morphing wingtip project

In this part of the research, a novel twist morphing wing is proposed with the goal of enhancing the aerodynamic efficiency of a wing. Two main objectives are studied using a twist morphing approach: enhancing the wing efficiency during rolling maneuvers and reducing the lift-induced wingtip drag.

2.1.2.1 Asymmetric Twist Morphing Wingtips (Twist Morphing Ailerons)

Novel twist morphing ailerons are developed in the first phase. Inspired by rolling maneuvers in birds, these morphing ailerons are intended to replace conventional hinged ailerons by twisting the wingtip and by maintaining the coherence of the wing body during the rolling maneuver by eliminating the gaps between the wings and ailerons. Twist morphing ailerons enhance the efficiency of the ailerons and their control power by increasing the rolling rate and the rolling moment, which improves the performance of the aircraft in a rolling maneuver. This study is performed under cruise flight conditions. A high-fidelity optimization is conducted to find the optimum configuration of the twist morphing ailerons. The optimum configuration of morphing ailerons is then compared to that of the conventional hinged ailerons in terms of rolling moment and induced drag.

2.1.2.2 Symmetric twist morphing wingtips (Twist morphing winglets)

In the second phase, another objective is accomplished using the same type of morphing concept, twist morphing, the reduction of lift-induced drag using twist morphing winglets. This study is performed at two flight conditions, cruise and climb. Unlike the twist morphing aileron, in which an asymmetric twist was established, symmetric twist is applied on both wings (left and right) in twist morphing winglets. The same high-fidelity optimization performed in the first phase is also applied on twist morphing winglets with a different objective: minimization of the lift-induced drag. The optimum configurations of the wingtips are found for cruise and climb flight conditions to achieve reduced induced drag.

2.2 Thesis organization

2.2.1 First journal paper: Free-Form Deformation Parameterization on the Aerodynamic Optimization of Morphing Trailing Edge

This study investigated the parametrization technique used in this study in detail. It employs Free-Form Deformation (FFD) parameterization to optimize the high-fidelity aerodynamic shape of the morphing trailing edge of an unmanned aerial system UAS-S45 wing.

In this study, the way in which parameterization flexibility affects optimization outcomes can be observed using five distinct cases, each with different numbers of FFD control points. The results showed that the number of control points had a major effect on the optimization results. The morphing capability was restricted when there were too few control points, which led to uneven deformations and small increases in the goal function. On the other hand, an excessive number of control points resulted in unfeasible wavy deformation.

To obtain the best outcomes, a balance was necessary between the number of control points and other criteria including computation time, solution optimality, and the improvement rate of the objective function. The best results were obtained in case 3, where a small number of control points was used, based on predetermined criteria such as the objective function value, deformation feasibility, convergence time, and optimality. A trial-and-error method was used to determine the optimum number of control points needed to obtain the best results. The study concluded that since it directly impacted the optimization process, obtaining the ideal number of FFD control points was very important and required careful attention.

2.2.2 Second journal paper: Seamless Morphing Trailing Edge Flaps for the UAS-S45 using High-Fidelity Aerodynamic Optimization

Using a high-fidelity gradient-based technique in combination with the Discrete Adjoint (DA) method, this study improved the seamless morphing trailing edge flap (SMTE flap) for the UAS-S45 over the whole flight envelope, including the climb, cruise, and descent phases. Finding the ideal SMTE flap configuration for every flight scenario was the main goal, with distinct objectives. The goal in the climb phase was to minimize the amount of required engine power by optimizing the SMTE flap to maximize the climb rate. The climb rate increased by 6.13% while engine power was lowered by up to 3.8%, according to the results. In the cruise flight, the objective was to increase both endurance and range. When compared to a hinged flap configuration, the SMTE flap demonstrated notable benefits. By sealing gaps in the transition portions, the SMTE flap enhanced the lift, stabilized the flow by lowering its turbulence, and extended laminar flow over the wings' upper surface. Accomplishing this gap sealing led to a 33% increase in the lift-to-drag ratio over the clean wing configuration and a 17.8% increase over the hinged flap wing configuration. It was also revealed that using an SMTE flap produced a 61.2% increase in endurance compared to the clean wing configuration. The SMTE flap was tuned to lower the descent rate. At a descent angle of -5°, an SMTE flap decreased the descent rate by as much as 43% compared to the baseline wing; the lowest descent rate was attained at $\gamma = -6°$.

2.2.3 Third journal paper: Structural and Topological Optimization of a Novel Elephant Trunk Mechanism for Morphing Wing Applications

This paper develops an innovative bio-inspired Elephant Trunk Mechanism (ETM), which was structurally investigated using topology optimization to assess its suitability for use in a Seamless Morphing Trailing Edge (SMTE) flap. This novel morphing concept features tooth-like elements that contract via a horizontal tensile force applied through cables to morph the trailing edge in the downwards direction. The best connection type between the cables and the holes was determined by static analysis using the Finite Element Method; a sliding contact arrangement was selected due to its higher stability than that of the no-contact configuration. Following this arrangement, the mechanism's structural analysis was performed. To enhance structural performance, geometrical changes were made, which resulted in a 0.4% stress reduction. In addition to increasing the trailing edge vertical displacement by 45.63% and reducing the maximum strain by 19%, these modifications improved structural flexibility. To decrease the weight, a topology optimization was then carried out within an appropriate design space. The maximum von Mises stress dropped by 10.43%, the factor of safety increased from 1.3 to 1.4, and the displacement was improved by 8.6%. The optimization resulted in an overall weight reduction of 4.2 N for the entire UAS-S45, with a mass reduction of up to 35.5% when compared to its original weight.

2.2.4 Fourth journal paper: Development and Experimental Study of a Seamless Morphing Trailing Edge Flap Equipped with an Elephant Trunk Actuation Mechanism

This paper represents the final stage in the development of the Seamless Morphing Trailing Edge (SMTE) flap, focusing on prototyping the wing section for wind tunnel testing. For this purpose, a prototype of the SMTE flap, including its Elephant Trunk Mechanism (ETM) and corresponding control system, were fabricated using 3D printing. The design satisfies all requirements established in earlier aerodynamic and structural studies.

The actuation of ETMs was achieved using four servomotors embedded in the leading-edge section of the wing. A graphical interface was also developed to control the morphing of the SMTE flap by adjusting the forces acting on the ETM. To ensure seamless coverage of the ETMs, the SMTE flap section was covered with a flexible silicon rubber skin. Following the assembly of the complete wing model, it was tested in a wind tunnel under the same flow conditions as those in the aerodynamic study to validate the numerical results. A total of 11 tests were conducted by varying both the angle of attack and flap deflection.

This study confirmed the stability and reliability of ETM and its practical functionality. Additionally, it revealed that the maximum deformation achieved exceeded the required value determined in the aerodynamic studies. The effectiveness of the silicon rubber flexible skin was also validated. To mitigate buckling on the lower surface of the wing, the lower skin was pre-tensioned and stretched before its attachment to the wing, eliminating any buckling after deformation. Furthermore, in the transition sections of the SMTE flap, the skin exhibited smooth deformation. Finally, a comparison between the wind tunnel test results and numerical aerodynamic predictions demonstrated a strong agreement between them, further validating the proposed design.

2.2.5 Fifth journal paper: Novel Twist Morphing Aileron and Winglet Design for UAV Control and Performance

This study, which uses twist morphing as its main morphing approach, emphasized another advantage of morphing wing technology. It effectively accomplishes its objectives, which included twist morphing analysis at the wingtip. Its two main goals are: 1) induced drag reduction at the wingtip by twist morphing wingtips, and 2) rolling maneuverability improvement by replacing twist morphing ailerons with hinged ailerons. For both goals, aerodynamic shape optimization was performed to identify the optimum configurations for the specified flight conditions.

The findings for twist morphing ailerons showed a 34% gain in the rolling moment of the UAS-S45. This gain not only improved the maneuverability but also enhanced the control power of the ailerons by increasing their roll rate compared to conventional hinged ailerons. Additionally, twist morphing ailerons reduced the induced drag by 61% by eliminating the gaps. The second objective—reducing induced drag with twist morphing wingtips—was also evaluated using the same optimization framework. Optimal wingtip designs were identified for both cruise and climb flight conditions by calculating total drag and the lift-to-drag ratio, with a focus on reducing induced drag. According to the findings, twist morphing wingtips decreased induced drag by up to 16.51% in climb and 25.7% in cruise flight compared to the baseline wing. They also improved aerodynamic efficiency by up to 9%, reduced total drag by up to 0.16% in cruise flight, and in climb by up to 7.5%.

CHAPTER 3

FREE-FORM DEFORMATION PARAMETERIZATION ON THE AERODYNAM OPTIMIZATION OF MORPHING TRAILING EDGE

Mir Hossein Negahban[1], Musavir Bashir[2], Ruxandra Mihaela Botez[3]

[1, 2, 3] LARCASE Laboratory of Applied Research in Active Controls, Avionics and Aeroservoelasticity, Department of System Engineering, École de Technologie Supérieure,
1100 Notre-Dame West, Montréal, Québec, Canada H3C 1K3

Paper published in Journal of Applied Mechanics, 28 February 2023
DOI : https://doi.org/10.3390/applmech4010017

Résumé

Chaque optimisation aérodynamique est précédée d'un paramétrage de l'objet aérien étudié, et en raison de son influence sur le processus d'optimisation final, une attention particulière doit être portée au choix de la méthode de paramétrage appropriée. Une optimisation aérodynamique d'un bord de fuite morphing est réalisée à l'aide d'une technique de paramétrage de déformation de forme libre dans le but d'examiner l'influence des conditions initiales du paramétrage sur les résultats d'optimisation, notamment sur le nombre de points de contrôle. L'optimisation haute fidélité basée sur le gradient utilisant la méthode adjointe discrète est établie par le couplage d'OpenFOAM et de Python dans le cadre d'optimisation DAFoam. Les résultats indiquent que le nombre de points de contrôle a un effet considérable sur le processus d'optimisation, en particulier sur la convergence, la valeur de la fonction objective et sur la faisabilité de la déformation.

Abstract

Every aerodynamic optimization is proceeded by a parameterization of the studied aerial object, and due to its influence on the final optimization process, careful attention should be made in choosing the appropriate parameterization method. An aerodynamic optimization of a morphing trailing edge is performed using a free-form deformation parameterization technique with the purpose of examining the influence of initial conditions of the parameterization on the optimization results, namely on the number of control points. High-fidelity gradient-based optimization using the discrete adjoint method is established by the coupling of OpenFOAM and Python within the DAFoam optimization framework. The results indicate that the number of control points has a considerable effect on the optimization process, in particular on the convergence, objective function value and on the deformation feasibility.

Keywords: Deformative parametrization, Gradient-based optimization, UAS-S45, Morphing flap, FFD control points, DAFoam optimization framework, OpenFOAM.

3.1 Introduction

Aerodynamic shape optimization has recently been the focus of many studies in the field of aeronautics due to its significant contribution in the improvement of aircraft and UAV performance. In the aerodynamic shape optimization, the choice of an adequate parameterization method to change the wing shape is of paramount importance before the start of the optimization process, meaning that the more realistically the wing shape can be parametrized, the more accurate and robust are the optimization results. The overall optimization process, including its computation time, robustness, and solution precision are strongly dependent upon the chosen parameterization technique (Khurana, Winarto, & Sinha, 2008).

Optimization process, whether one-objective or multi-objective (Huynh, Nguyen, & Nguyen, 2022; Wang et al., 2022) is always linked with how the optimizing model is defined or parametrized mathematically. A successful parameterization method is characterized by its ability to cover a large design space using a limited set of design variables (Masters et al., 2015). Shape parameterization methodology is divided into two categories: "constructive" and "deformative". In constructive methods, a wing is generated using a series of specified parameters, while in deformative methods, such as free-form deformation, a wing is generated by changing its initial shape.

In a comparative study, Sripawadkul et al. (Sripawadkul, Padulo, & Guenov, 2010) compared five constructive parameterization methods: the Ferguson method, B-Splines, CST, PARSEC and Hicks-Henne bump functions. Several desired characteristics were applied as criteria to find the best parameterization method. The comparative study showed that these metrics could be applied as a basis for objective function comparison, and that the best parameterization method is dependent upon the problem at hand. A survey of shape parameterization techniques for multidisciplinary optimization was performed by Samareh (Samareh, 2001), focused on the stability of available parameterization techniques for the multidisciplinary optimization of aerospace applications of complex structures. Eight different parameterization techniques were re-viewed: Partial Differential Equations (PDEs), discrete, analytical, polynomial and spline, Free-Form Deformation (FFDs), basis vector, and CAD-based. It was concluded that the choice of shape parameterization technique depends on six criteria: the parameterization accuracy, the disciplines involved, automatic grid generation, optimization algorithms, cycle time, and the CAD direct connection. In recent years, several aerodynamic optimization with different optimization algorithms and parametrization method have been per-formed in the Active Control, Avionics and Aeroservoelasticity Research Laboratory (LARCASE). Table 3.1 shows these studies in detail.

Table 3.1 List of research conducted at LARCASE using different optimization algorithms and parametrization methods

Year	Author	Morphing approach	Optimization process	method	Objective functions
2016	(Gabor et al., 2016)	Upper surface	ABC + BFGS	NURBS	Transition delay
2016	((O. Ş. Gabor, A. Koreanschi, & R. Botez, 2016)	Upper surface	ABC + BFGS	NURBS	L/D maximization
2016	((O. Ş. Gabor, A. Koreanschi, & R. M. Botez, 2016)	Upper surface	ABC	NURBS	Drag minimization
2017	(Koreanschi, Gabor, et al., 2017)	Upper surface+ aileron	GA	Cubic spline	Drag minimization. , transition delay
2021	(Bashir et al., 2021)	Leading + trailing edge	PSO	Bezier-PARSEC	Drag minimization, Endurance maximization
2022	(Bashir, Longtin-Martel, Botez, & Wong, 2022)	Leading edge	BWO	Class shape transformation (CST)	Drag minimization, Endurance maximization
2022	(Bashir, Longtin Martel, et al., 2022)	Trailing edge	BWO	Makima	L/D maximization
2023	(Mir Hossein Negahban, Musavir Bashir, & Ruxandra M Botez, 2023)	Combined chord and TE	Gradient	FFD	Drag minimization

In recent decades, morphing wing technology (Ameduri & Concilio, 2023; Dimino, Lecce, & Pecora, 2017; Pecora, 2021) has proven to be the main candidate to be applicable in the next generation aircrafts; therefore, many studies, have been performed on morphing wings, due to their unquestionable benefits in improving the aerodynamic efficiency. Numerous aerodynamic shape optimizations have been performed using different morphing wing approaches, including trailing edge, leading edge, upper surface and overall wing shape morphing. Secanell et al. (Secanell, Suleman, & Gamboa, 2006) investigated six flight conditions: stall, takeoff run, climb gradient, rate of climb, cruise, and loiter; and for each of these conditions, the morphing shape was studied through a high-fidelity aerodynamic optimization. The results showed a significant reduction in the airfoil drag coefficient on the morphing airfoil. Botez (Botez, 2018; Botez, 2022) presented recent studies conducted at the Laboratory in Active Controls, Avionics and Aeroservoelasticity (LARCASE), in which morphing wing optimization was performed with different parameterization methods and optimization algorithms. Using constructive parameterization, Koreanschi et al. (Koreanschi, Gabor, et al., 2017) applied three different optimization algorithms, including a Genetic Algorithm (GA), an Artificial Bee Colony (ABC) algorithm and a Gradient Descent algorithm for the optimization of the wings' upper surface using NURBS parameterization technique. Bashir et al. (Bashir et al., 2021) performed an aerodynamic shape optimization for the morphing leading edge (drooped nose leading edge) using the Bezier-PARSEC parameterization method and an evolutionary Particle Swarm Optimization (PSO) optimization algorithm. In another study (Bashir, Longtin-Martel, Botez, & Wong, 2022), the CST parameterization method was implemented on a morphing leading edge by adding local shape changes. However, in the optimization of the whole wing section, the whole aircraft or UAV, constructive parameterization methods may lose their efficiency, since in these problems, the number of design variables, unlike in two-dimensional cases, are of the order of one hundred or more. For this reason, deformative techniques, such as CAD-based models or the Free-Form Deformation (FFD) technique are recommended for the optimization of 3D wings or whole aircraft, based on (Burdette & Martins, 2019; Lyu, Kenway, & Martins, 2015; Lyu & Martins, 2015), as these techniques have been proven to be efficient because of their flexibility in solving problems with a high number of design variables of the order of 10^2.

Many optimization problems that use FFD technique in the optimization of the whole wing and aircraft are available. He et al. (He et al., 2019) applied the FFD parameterization technique on UAV and Common Research Model (CRM) wings, by the use 127 and 201 design variables, respectively. In another study (He et al., 2018), they applied the FFD parameterization method in the optimization of Ahmed body and of a full model car.

In (He et al., 2020), a CRM Wing-Body-Tail (whole aircraft) with a total of 227 design variables, a blended tube and a turbine blade were also parametrized with the FFD technique. Based on these studies, the FFD technique is the most feasible methodology for solving problems with a high number of design variables.

In the present study, an aerodynamic shape optimization is performed on the morphing trailing edge. Among the morphing configurations, the trailing edge morphing is the most commonly-studied, due to its conspicuous influence on flight performance, especially in cruise flight. Numerous studies from aerodynamic (Abdessemed, Bouferrouk, & Yao, 2022; Negahban, Botez, & Razavi, 2022), structural (Concilio et al., 2016; Pecora, Amoroso, et al., 2016) to aeroelastic (Pecora et al., 2014) aspects of this morphing configuration have been studied in recent years. In this study the optimization of morphing trailing edge of a UAS-S45 wing using the FFD parameterization technique. The UAS-S45 is a surveillance unmanned aerial system designed and manufactured by Hydra Technologies in Mexico. A complete aerodynamic model of this UAS-S45 is presented in (Kuitche & Botez, 2019; Kuitche et al., 2020). Figure 3.1 shows the UAS-S45 with different morphing configurations obtained from studies conducted at the LARCASE.

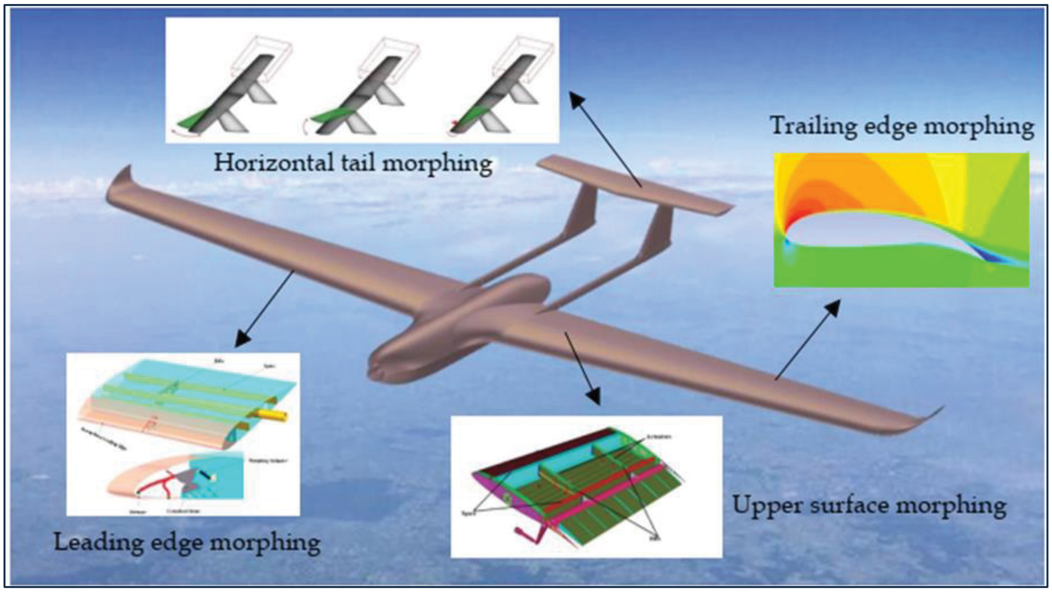

Figure 3.1 Morphing studies and optimizations conducted on the UAS-S45 at LARCASE

This study is performed using a high-fidelity optimization framework. To the best of the authors' knowledge, most of the optimization problems in the literature on morphing wings have been conducted using low-fidelity aerodynamic optimization tools, such as XFoil. This study utilizes a high-fidelity optimization tool, using the DAFoam optimization framework (He et al., 2020); however, the main focus of this study is on the parameterization using the FFD technique, with the objective of obtaining the optimization results by enhancing the accuracy of parameterization before the optimization process. In the FFD parameterization, the number of control points has a direct impact on the design of the optimization problem, meaning that it affects the fidelity of the final design. Therefore, in this paper, the FFD parameterization flexibility in terms of number of control points is considered. Too few control points (dependent on the case studied) will cause some parameters of the design space, such as displacement magnitude to be neglected and will also cause premature local convergence, and inaccurate mesh deformation, while too many design points will cause mesh overlap and longer optimization process, and thus, higher computation cost. Therefore, it is important to find the correct number of control points before starting the optimization problem. Basically, in FFD parametrization, the number of control points this is determined by trial-and-error, since there is no direct method to find the exact number of control points. This study is conducted to show the FFD control points flexibility and to compare the results obtained for different number of control points and their influences on the results obtained following the optimization process of a morphing airfoil. This study ensures the validation of the optimization results before starting the optimization; this process could be extended to any optimization problem conducted with the FFD parameterization technique.

3.2 Methodology

3.2.1 FFD Parameterization Technique

The FFD parameterization technique was first proposed by Sederberg and Parry (Sederberg & Parry, 1986). They introduced a new way to modify a solid model, so that its volume remains the same. Their mapping scheme was based on tri-variate Bernstein polynomials with control points being their coefficients. Since then, the mapping scheme has since evolved to use tri-variate Bezier, B-spline or NURBS polynomials. In this mapping technique, the geometry of any size is embedded inside a lattice, called FFD block, with its corresponding control points. The lattice consists of B-spline control points, which, when altered, deform the shape of embedded body. The number of control points and their displacements are dependent upon the geometry and the deformation zone. In Eq. (3.1), the Newton's method is used to map the parameter space into physical space, while the embedded object, which is inside a cartesian space, is mapped into the initial tri-variate B-spline volume (Ronzheimer, 2004):

$$\vec{P}(u,v,w) = \sum_{i=0}^{n_u} N_{i,m_u}(u), N_{j,m_v}(v), N_{k,m_w}(w) Q_{i,j,k} \tag{3.1}$$

where $\overrightarrow{P}$ are the vertices of the initial embedded object N_{i,m_u}, N_{j,m_v} and N_{k,m_w}, which are the B-spline basis functions of degree m_u, m_v, and m_w, and $Q_{i,j,k}$ is the initial deformation lattice. The basic functions are calculated in Eq. (3.2):

$$N_{i,l_u} = \begin{cases} 0, & u_i \leq u \leq u_{i+1} \\ 1, & otherwise \end{cases}$$

and

$$N_{i,m_u}(u) = \frac{u - u_i}{u_{i+m_{u-1}} - u_i} N_{i,m_{u-1}}(u) + \frac{u_{i+m_u} - u}{u_{i+m_u - u_{i+1}} - u_i} N_{i+1,m_{u-1}}(u) \tag{3.2}$$

After the deformation, the B-spline volume, calculated in Eq. (3.1), is substituted by a new B-spline volume with control points $Q_{i,j,k}^{new}$, which leads to Eq. (3.3):

$$\vec{P}^{new}(u_0, v_0, w_0) = \sum_{i=0}^{n_u} N_{i,m_u}(u_0), N_{j,m_v}(v_0), N_{k,m_w}(w_0) Q_{i,j,k}^{new} \tag{3.3}$$

where $\vec{P}^{new}$ represents the object's vertices after deformation.

FFD blocks parameterize the geometry variations rather than the geometry itself, it is therefore only necessary to use a set of design variables that span the desired geometry modification (Kenway, Kennedy, & Martins, 2010).

As the FFD blocks are represented by tri-variate B-spline volumes, the sensitivity of any point inside the volumes can be calculated according to Eq. (3.4).

$$\frac{\partial X_{pt}}{\partial x_{dv}} = \frac{\partial X_{coef}}{\partial x_{dv}} \frac{\partial X_{pt}}{\partial X_{coef}} \tag{3.4}$$

where $\mathbf{X_{pt}}$ are the spatial coordinates of the embedded points, $\mathbf{x_{dv}}$ are the design variables and $\mathbf{X_{coef}}$ are the spatial coordinates of the FFD block control points. In Eq. (3.4), $\frac{\partial \mathbf{X_{coef}}}{\partial \mathbf{x_{dv}}}$ shows the derivatives of control points' motion with respect to the actual design variables, and $\frac{\partial \mathbf{X_{pt}}}{\partial \mathbf{X_{coef}}}$ is the shape function. In this study, to examine the FFD parameterization, in terms of number of control points, five sets of FFD blocks with different numbers of control points for the same block topology and the same morphing configuration are examined. Figure 3.2 shows the S-45 airfoil embedded inside the FFD block. Two FFD blocks are used, one for the undeformed part (white block: 70% of the chord length) and one for its morphing trailing edge (red block: 30% of the chord length). As depicted in Fig. 3.2, the control points shown in green are the ones that are free to move in a vertical downward direction, while the rest of them (the ones without color) are constrained to zero movement in every direction.

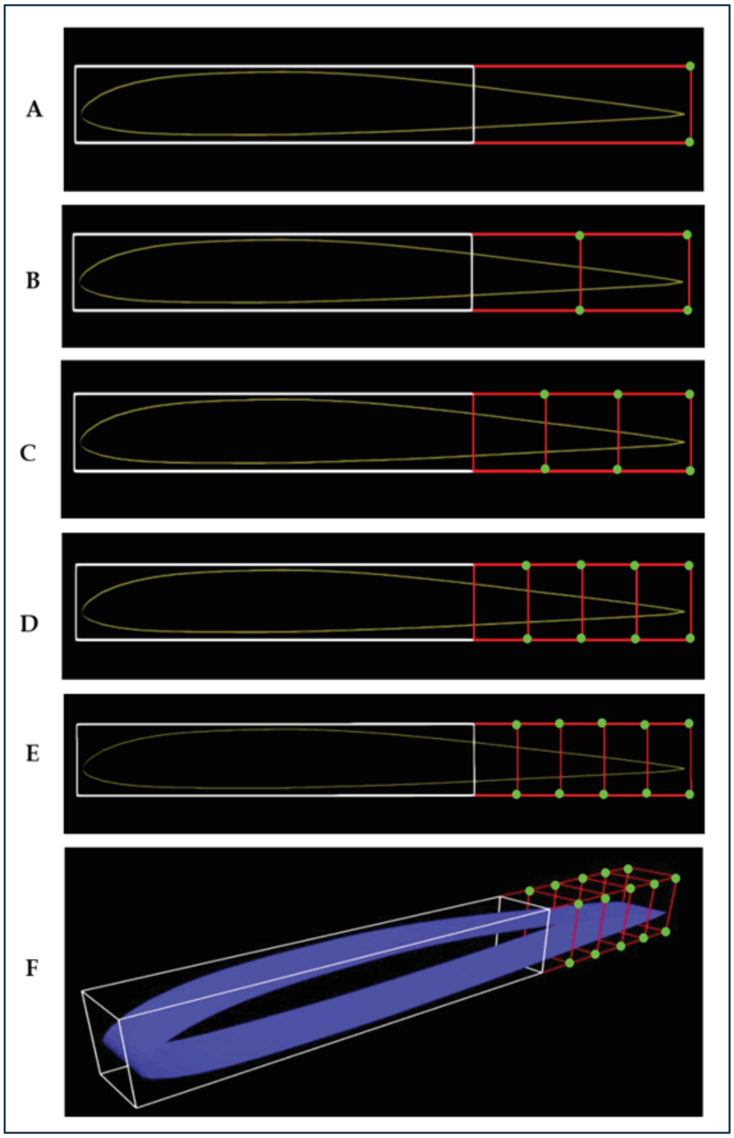

Figure 3.2 Embedded UAS-S45 airfoil in FFD blocks for five cases with A) 8, B) 12, C) 16, D) 20, E) 24 control points from a side view, and F) an isometric view of the FFD block with 24 control points

3.2.2 DAFoam Optimization Framework

For large-scale optimization problems on an aircraft's wing or a whole aircraft, gradient-based optimization is an efficient tool, as is capable of locally finding a set of design variables to maximize the aircraft performance. By using this optimization tool, DAFoam is capable of handling large-scale optimization problems in aerodynamics. Thus, its high-fidelity optimization framework ensures the reliability of the optimization results. In the field of aerodynamic optimization, most previous studies have used low-fidelity optimization approaches, in particular XFoil or XFLTR solvers, that solve the potential flow equations rather than the RANS equations. However, the DAFoam optimization framework, developed in 2019 by MDO Laboratory team in Michigan University (He et al., 2020), is capable of handling optimization problems with many design variables by using a high-fidelity solver, namely OpenFOAM. DAFoam uses an adjoint method to compute the derivatives of design variables, thereby making the computation cost independent on the number of design variables, but dependent on the number of functions of interest, which are the functions of design variables and the state variables (He et al., 2019). In this optimization framework, Open FOAM uses the RANS equations for calculating the aerodynamic parameters; the object-oriented discrete adjoint-based optimization process in Python, is coupled with OpenFOAM's steady-state solvers. For the computation of the adjoint equation, which contains the residual equations and function of interest, graph coloring is used to accelerate its calculus by dividing the Jacobian matrix into subgroups (of various colors), where the objective and residual computation routines are called only once instead of multiple times, (See (Burdyshaw & Anderson, 2005; Nielsen & Kleb, 2006)) for details regarding graph coloring).

Several benchmark studies have been performed using the DAFoam optimization framework in (He et al., 2018), (He et al., 2019), and (He et al., 2020) to solve different aerodynamic problems, all of which confirm its validity and efficiency.

3.2.3 Optimization numerical setup

This study was performed for the UAS-S45 cruise flight condition, in which, the speed was taken from its operation manual. Therefore, the corresponding cruise speed for the UAS-S45 is 70 knots (28.29 m/s) and the corresponding altitude is 15,000 ft. The turbulence model is Spalart-Allmaras, where the turbulence intensity is equal to 1%. To verify that the optimization results are independent of mesh density, three different number of elements (31598, 117068 and 198758) were chosen for numerical model studies, and it was found that the error between the lowest and highest number of elements results in terms of CL/CD was as low as 1.9%; therefore, the lowest number of elements was chosen for the optimization studies of all five cases. Figure 3.3 shows the density of elements around the airfoil with the chosen number of elements (equal to 31598). The surfaces to which the airfoil is attached are defined as the symmetry boundary, while the rest of the domain (inlet, outlet, upper and lower surfaces) have the InletOutlet boundary condition, a specific boundary condition in OpenFOAM. In this boundary condition, the boundary switches between “zero gradient” and “fixed value” condition, when the fluid flows out the domain and into the domain, respectively.

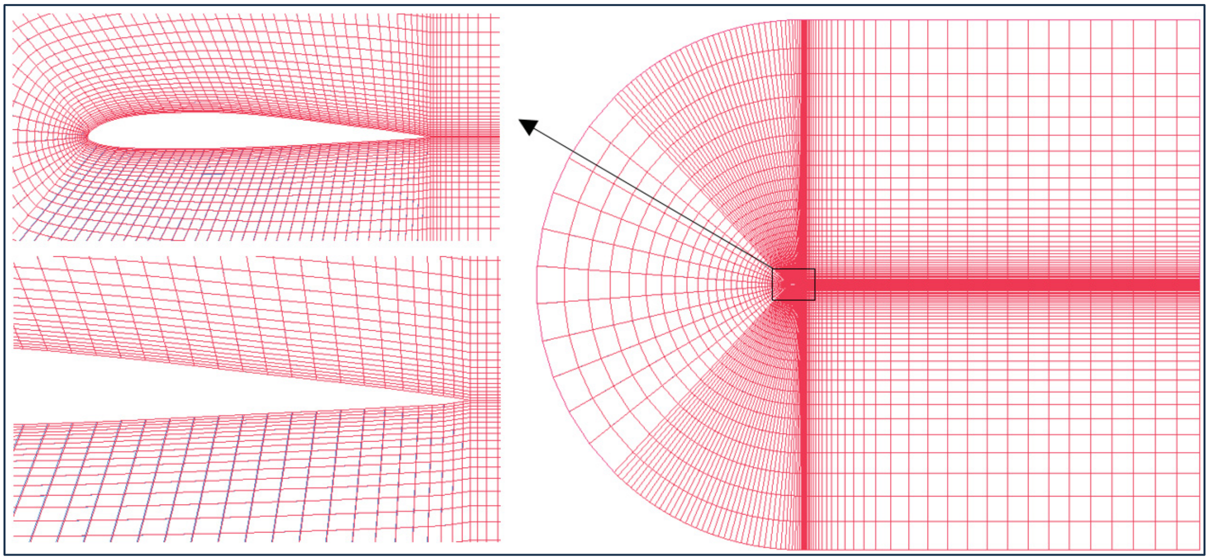

Figure 3.3 Illustration of the density of elements in the computational domain

The optimization is performed based on the above CFD setup, where the objective function is lift-to-drag maximization, where the lift coefficient is defined as an inequality constraint function ($C_{l\,min} \leq C_l$). The minimum lift coefficient is found before the optimization process and is used in the constraint function to prevent the lift coefficient from being lower than the minimum lift coefficient during the optimization. To have a linear deflection in the spanwise direction, a linear constraint is applied to have the same magnitude of deformation in the spanwise direction for each control point. The deflection is then constrained in a downward direction with a maximum value of 15 mm, while the deflection in the upward direction is confined to zero, therefore the flap is only deflected in a downward direction.

To compare the results obtained from different FFD parameterization setups, four criteria are considered: 1- optimality error, 2-convergence time, 3-objective function, and 4-deformation feasibility (realistic deformation in practice). Optimality error is a criterion for the evaluation of the optimization accuracy; it shows how well the objective function could be minimized or maximized, meaning that as its value approaches to zero, it shows that the objective function is optimized to the greatest or least value possible, which gives an idea of how well the solution is converged.

3.2.4 Optimization process for a morphing trailing edge flap

The optimization is performed in this research by using a gradient-based optimization that uses a discrete-adjoint method. OpenFOAM is used as the flow solver, while the generation of the FFD block and the optimization algorithm are conducted in Python. In this study, the optimization is performed to solve a nonlinear problem with continuous constraints. An Interior Point Optimizer (IPOPT) is used, as is suitable for solving non-linear programming problems with continuous constraints by minimizing or maximizing the objective function subjected to several constrained functions, as follows:

$$\begin{aligned} &min \quad f(x) \\ subjected\ to: \quad & LB \leq g(x) \leq UB \\ & LB \leq x \leq UB \end{aligned} \tag{3.5}$$

where $f(x)$ is the objective function, $g(x)$ is the constrained function, x are the design variables, and LB and UB represent the lower and upper bounds, respectively.

IPOPT uses filter methods with line search, and the first and second derivatives of the functions of interest, Jacobians, and Hessians, respectively, are obtained by use of Automatic Differentiation (AD) method; however, the Hessian matrix does not need to be calculated, since in case when the second derivatives are not available, the quasi-Newton methods are used, such as Broyden–Fletcher–Goldfarb–Shanno algorithm (BFGS). The approach used in this study is the trailing edge morphing for the UAS-S45 with the objective function of lift-to-drag maximization. FFD parameterization is applied to this morphing wing configuration and different criteria, as mentioned in the first section, are analyzed based on the results obtained from the optimization results. Figure 3.3 shows the overall optimization process needed to solve for this problem, while Table 3.2 shows the optimization setup for the UAS-S45 airfoil with morphing trailing edge (MTE). In this study, five cases were optimized, which were distinct in terms of the number of control points on the trailing edge. The minimum number of control point belongs to Case 1, with 8 control points and the maximum number belongs to Case 5 with 24 control point (Table 3.2). Figure 3.4 shows the overall optimization process in this study.

Table 3.2 Optimization setup for the morphing trailing edge of the UAS-S45

Function/variable	**Description**	**Case**				
Objective function		**1**	**2**	**3**	**4**	**5**
$max.\quad C_l/C_d$	Lift-to-drag ratio					
With respect to:						
y	TE FFD control points	8	12	16	20	24
α	Angle of attack	1	1	1	1	1
	Total design variables	9	13	17	21	25
Subject to:						
$C_l = 0.38514$	Constraint function					
$0 \leq \Delta y \leq 15\, mm$	Design variable bounds					
$\Delta y_{z=0}^{upper} = \Delta y_{z=1}^{upper}$	linear constraint					

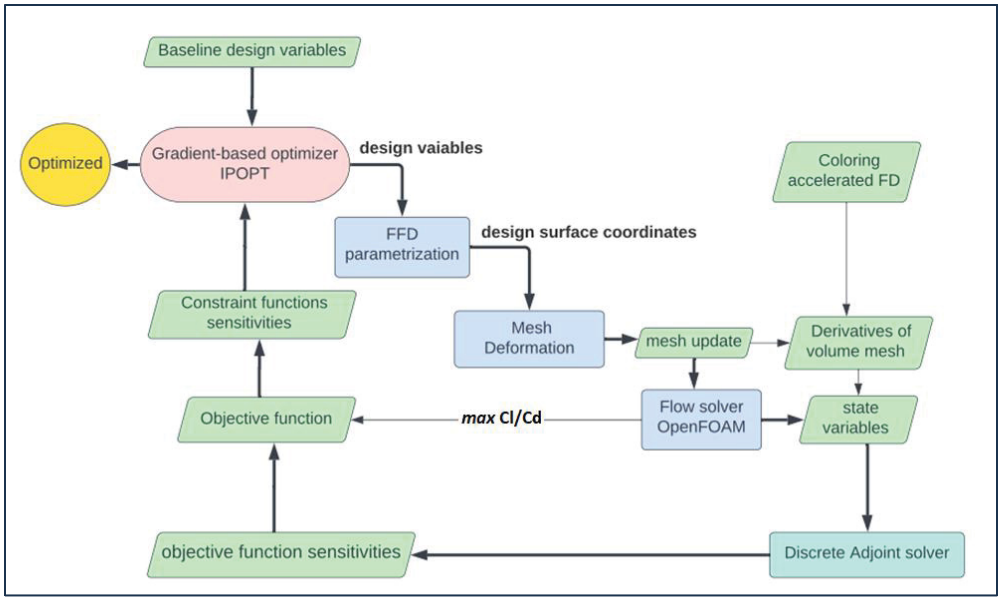

Figure 3.4 Overall optimization process of the UAS-S45 morphing wing trailing edge within the DAFoam optimization framework

3.3 Results and Discussion

The optimization results are compared for five cases, in which different number of control points are considered. Various criteria, including convergence time, number of iterations, optimality error and objective function values are compared for different number of control points. Figure 3.5 (A-B) show the optimality error of the optimization process for each case. In Fig. 3.4-A, it can be seen that for the cases 1 to 3, where the number of control points are lower than case 4 and 5, the convergence is reached with low number of iterations and is of the order of 10^{-6}. However, for the cases 4 and 5 (Fig. 3.5-B), a satisfactory convergence is not achieved even after 50 iterations and is of order of $10^{-2}$and $10^{-3}$for case 4 and 5, respectively. Table 3.3 shows the comparison of five cases in terms of the convergence time, number of iterations, optimality and C_l/C_d.

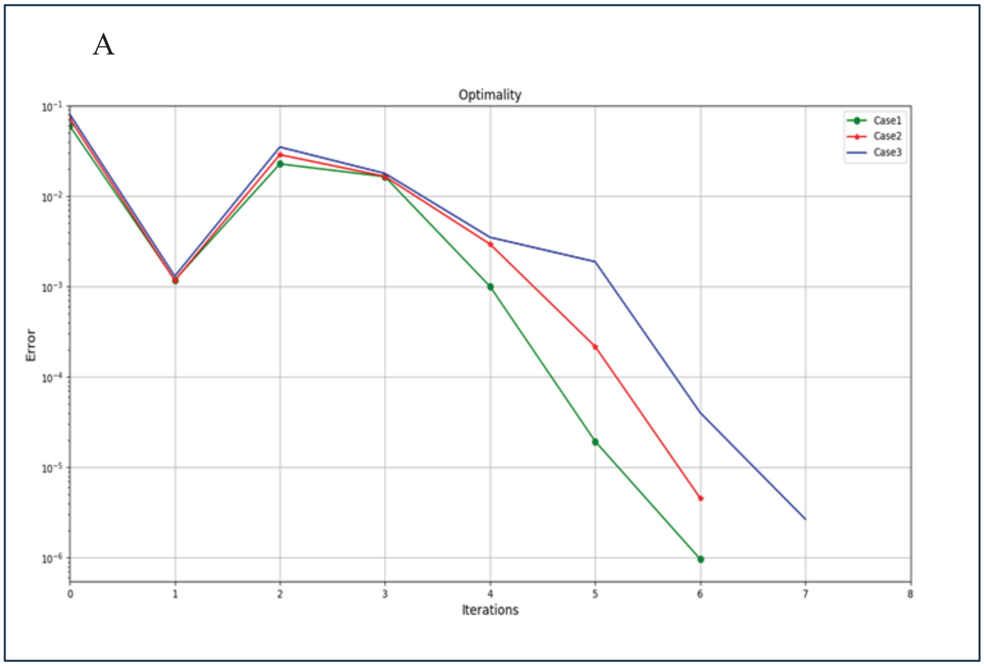

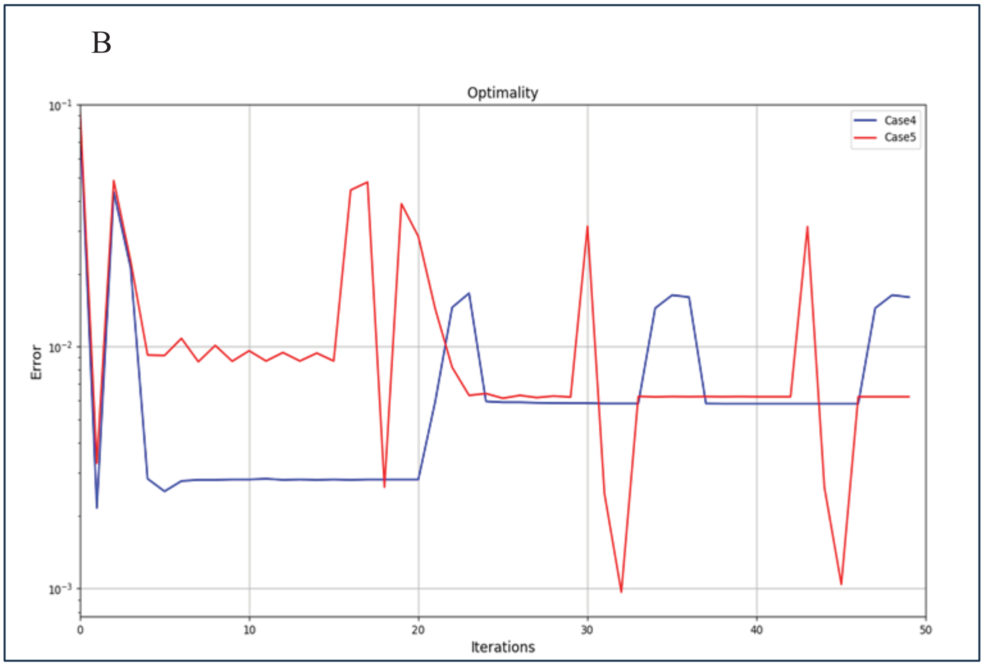

Figure 3.5 Optimality of the optimization process, A) Cases 1,2 and 3, B) Cases 4 and 5

Table 3.3 Comparison of the optimization results for five cases

Case	**Control points**	**Run time (sec.)**	**Itr. nr.**	**Optimality error**	**Initial Cl/Cd**	**Opt. Cl/Cd**	**Gain %**
1	8	218.732	6	9.63e-07	34.548	38.522	10.3
2	12	258.512	6	4.55e-06	34.532	39.547	12.7
3	16	504.096	7	2.67e-06	34.524	40.058	13.8
4	20	10925.43	50	1.60e-02	34.523	39.002	11.5
5	24	12203.12	50	6.20e-03	34.521	38.663	10.7

As shown in Table 3.3, as the number of control points increases, the number of iterations, computation time and optimality error increases, thus leading to inaccurate results. By considering the objective function, the maximum value of lift-to-drag ratio is obtained in case 3, which is correspondent to 13.8 % improvement. If all criteria are considered, it is obvious that case 3 with 8 control points gives the best results in terms of optimality error, convergence time, and Cl/Cd maximization (objective function).

Figure 3.6 shows the UAS-S45 airfoil after the morphing trailing edge optimization for all five cases. In case 1, the one with the least number of control points (6), there is a sharp bending of the trailing edge, similar to that of a hinged flap, but, as the number of control points increases, the deformation becomes smoother. However, when the control points' number exceeds 8 (cases 4 and 5), the trailing edge smooth deformation turns into a wavy type deformation (Fig. 3.6). Therefore, case 3 is the best case in terms of deformation feasibility.

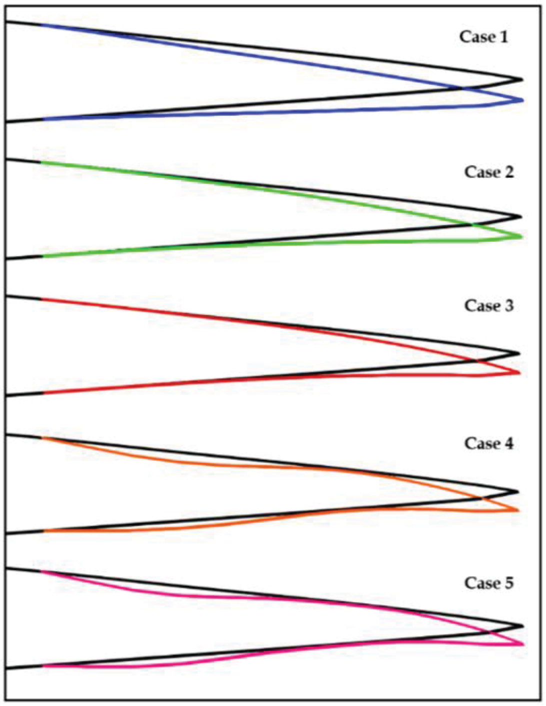

Figure 3.6 Illustration of the morphing trailing edge for the UAS-S45 airfoil for a) case 1, b) case 2, c) case 3, d) case 4, and e) case 5, after optimization

3.4 Conclusion

A high-fidelity aerodynamic optimization of a morphing trailing edge was performed in this study, using free-form deformation parameterization. The study was conducted for five different cases, distinct in terms of FFD number of control points. The main purpose of this study was to show the influence of FFD parameterization flexibility in terms of control points, and to show how it would affect the final optimization results. The study of five cases showed that the ultimate optimization results were directly influenced by the choice of the number of control points, where too few control points (less than 6) led to unsmooth deformation and less objective function improvement. This observation means that a low number of control points restricts the morphing capability, and the geometry becomes confined. On the other hand, higher number of control points (higher than 8) led to undesirable wavy deformations, which are impractical from the mechanism and manufacturing perspectives; moreover, higher number of control points did not show a very good optimization accuracy and a satisfactory convergence was not accomplished. We have shown the influence of the number of control points was substantial and it had a direct impact on the optimization results. There should be a trade-off to find the optimal number of control points prior to the start of the optimization by analyzing three parameters, including the computation time, solution optimality, and improvement rate of the objective function.

Therefore, the optimal solution was chosen based on the predefined criteria, including the objective function value, deformation feasibility, convergence time, and optimality. According to these criteria, case 3, which had a moderate number of control points, showed the best results out of five cases, with a 13.8% improvement obtained in terms of both higher optimization accuracy, and feasible deformation. Finally, it was concluded that obtaining the optimum number of control points in the FFD parameterization is of paramount importance, and that careful considerations should be made before starting the optimization process, as the number of control points directly influences the optimization results. So far, no direct mathematical formulation has been proposed for the choice of the number of control points in FFD parameterization, as it is a case-dependent, therefore, and trial-and-error procedure was used to find the most appropriate number of control points. The influence of FFD lattice topology will be studied for a three-dimensional wing to analyze its impact of lattice topology on the computation of the embedded body gradients.

CHAPTER 4

SEAMLESS MORPHING TRAILING EDGE FLAPS FOR UAS-S45USING HIGH-FIDELITY AERODYNAMIC OPTIMIZATION

Mir Hossein Negahban[1], Musavir Bashir[2], Victor Traisnel[3], Ruxandra Mihaela Botez[4]

[a, b, c, d] LARCASE Laboratory of Applied Research in Active Controls, Avionics and Aeroservoelasticity, Department of System Engineering, École de Technologie Supérieure, 1100 Notre-Dame West, Montréal, Québec, Canada H3C 1K3

Paper published in Chinese Journal of Aeronautics, 31 October 2023.
DOI : https://doi.org/10.1016/j.cja.2023.10.024

Résumé

Le volet morphing du bord de fuite sans soudure est étudié à l'aide d'une optimisation de forme aérodynamique en régime permanent haute fidélité afin de déterminer sa configuration optimale pour différentes conditions de vol, notamment la montée, la croisière et la descente planée. Une étude comparative est également menée entre une aile équipée de volet morphing et une aile à volet articulé classique. L'optimisation est réalisée en spécifiant une certaine fonction objective et l'objectif de performance de vol pour chaque condition de vol. Augmenter le taux de montée, étendre la portée de vol et l'endurance en croisière, et diminuer le taux de descente, sont les objectifs de performances de vol abordés dans cette étude. Diverses configurations optimales ont été trouvées pour l'aile morphing en déterminant la déviation optimale des volets morphing pour chaque condition de vol, en fonction de sa fonction objectif, chacune d'entre elles fonctionnant mieux que celle de l'aile de base. Il a été démontré qu'en utilisant une configuration optimale pour l'aile morphing en condition de montée, la puissance requise pouvait être réduite jusqu'à 3,8 % et le taux de montée augmenté de 6,13 %. L'étude comparative a également révélé que l'aile morphing améliore l'efficacité aérodynamique jusqu'à 17,8 % et étend l'écoulement laminaire. Enfin, la configuration optimale pour la descente planée a entraîné une réduction de 43 % du taux de descente.

Abstract

The seamless trailing edge morphing flap is investigated using a high-fidelity steady-state aerodynamic shape optimization to determine its optimum configuration for different flight conditions, including climb, cruise, and gliding descent. A comparative study is also conducted between a wing equipped with morphing flap and a wing with conventional hinged flap. The optimization is performed by specifying a certain objective function and the flight performance goal for each flight condition. Increasing the climb rate, extending the flight range and endurance in cruise, and decreasing the descend rate, are the flight performance goals covered in this study. Various optimum configurations were found for the morphing wing by determining the optimum morphing flap deflection for each flight condition, based on its objective function, each of which performed better than that of the baseline wing. It was shown that by using optimum configuration for the morphing wing in climb condition, the required power could be reduced by up to 3.8% and climb rate increases by 6.13%. The comparative study also revealed that the morphing wing enhances aerodynamic efficiency by up to 17.8% and extends the laminar flow. Finally, the optimum configuration for the gliding descent brought about a 43% reduction in the descent rate.

4.1 Introduction

The aeronautics industry has a significant impact on greenhouse gas emissions, as thousands of airplanes, ranging from personal aircraft to commercial and military jets, fly every day. This huge number of daily flights contributes to the emission of a large amount of CO_2 into the atmosphere. This situation was demonstrated during the COVID-19 pandemic, as satellite images show the CO_2 emissions before and during the pandemic; there was a considerable decrease in the CO_2 emissions (https://abcnews.go.com/International/severe-reduction-emissions-coronavirus-mitigate-climate-change-long/story?id=69334246). According to the Carbon Global Project (Le Quéré et al., 2020), the drop in flights dramatically reduced the Carbon emissions during the worldwide lockdown compared to the other sources, including surface transport and industry. Their findings indicate that during the peak of world-wide lockdown (March, April, and May 2020), the 75% reduction in air traffic accounted for 60% of the carbon emission reduction, while the surface transport accounted only for a 36 % reduction (being the second after aviation), which is nearly half. Carbon emission reduction is therefore one the highest-priority goals in the aeronautics industry due to its undeniable impact on the climate.

Following the main goal of green aviation, numerous projects both in industry and in academia, most of which are collaborative industrial-academics projects, have focused on reducing CO2 emissions. Among these, at the flight trajectory level, Airbus' UpNext (https://www.airbus.com/en/innovation/disruptive-concepts/biomimicry/fellofly) is one of the most recent projects. Their proposed "Fello'fly" concept offers a reduction of carbon emissions by at least 5% per trip according to operational evaluations. However, most of the studies in green aviation are at the level of aircraft design. These include aerodynamic, propulsive, and structural aspects of aircraft, all of which are inter-connected. For example, in aerodynamics, many studies have been conducted on drag reduction, which leads to a reduction in fuel and power consumption.

In aerodynamics, morphing wing technology has shown a great potential to apply to next-generation environmentally friendly aircraft , due to its success in improving aircraft performance by reducing drag and fuel consumption, as well as in reducing aircraft weight (Ameduri & Concilio, 2020; Dimino, Lecce, & Pecora, 2017). While most of these studies are still at the conceptual level due to structural limits, ongoing research in aerodynamics and at a structural level have shown a promising future for this technology. Many morphing approaches have been examined over the past few decades from sweep (Muhammad Umer et al., 2020), twist (Ismail et al., 2014; Segui & Botez, 2019), winglet (Liauzun et al., 2018; Segui et al., 2021), and span morphing (Ajaj et al., 2012), to camber (Communier, Botez, & Wong, 2020; Negahban, Botez, & Razavi, 2022; Razavi & Negahban, 2020; Yuzhu et al., 2022), chord (Mir Hossein Negahban, Musavir Bashir, & Ruxandra M Botez, 2023), leading edge (Bashir, Longtin-Martel, Botez, & Wong, 2022; Bashir, Longtin-Martel, Zonzini, et al., 2022; Zi et al., 2020), and upper surface (R. Botez et al., 2018; Botez, Molaret, & Laurendeau, 2007; O. Ş. Gabor, A. Koreanschi, & R. Botez, 2016; O. Ş. Gabor, A. Koreanschi, & R. M. Botez, 2016; Gabor et al., 2016; Koreanschi, Sugar-Gabor, et al., 2017; Koreanschi[a] et al., 2017; Popov, Botez, & Labib, 2008; Popov, Grigorie, Botez, Mamou, & Mébarki, 2010; Sugar Gabor, 2015) morphing. However, among these approaches, the trailing edge morphing (Carossa et al., 2016) has received considerable attention due to its substantial influence in improving flight performance and reducing fuel consumption. Beyond aerodynamic analysis, structural analysis (Pecora et al., 2014) as well as aerostructural analysis (Burdette et al., 2015) for the trailing edge morphing approach is developing more rapidly than other morphing approaches, due to the high number of studies in this area. Different types of morphing mechanisms have been proposed (Amendola et al., 2016; Dumont, 2018; Fengqian et al., 2021; Li & Li, 2016; Liu et al., 2013; Murugan, Woods, & Friswell, 2015; Pecora, 2021; You et al., 2019), some of which have been prototyped and successfully wind-tunnel tested (Arena et al., 2018; Communier et al., 2019; Nguyen et al., 2014; Takahashi, Yokozeki, & Hirano, 2016; Wu et al., 2017).

Numerous morphing mechanisms have been proposed at the conceptual design level for different morphing configurations, such as morphing leading edge, morphing trailing edge (Concilio et al., 2016; Pecora, Amoroso, et al., 2016), or morphing upper surface. However, few successful tests have been reported at the flight test level. Among these, AFTI/F-111 Mission Adaptive Wing (POWERS et al., 1992), is the pioneering project, a joint project of UASF, NASA and Boeing, in which a successful flight test was performed by F-111 fighter aircraft equipped with active camber morphing. Unfortunately, due to actuation system complexity and weight penalties, the project was closed. The Adaptive Complaint Trailing Edge (ACTE) project, among the U.S Air Force Research Laboratory (AFRL), NASA and Flexsys (Kota, Flick, & Collier, 2016; Kota et al., 2009a; Miller et al., 2016) is another flight test level project. In the ACTE project, a Gulfstream III business jet equipped with morphing trailing edge wings was tested at the altitude of 40,000 ft, and it was the only practical test of morphing wings in recent years. This work showed that this technology was dependable after over 50 hours of flight tests, and it documented its ability to improve aerodynamic performance.

The potential benefits of trailing edge morphing in terms of improving aerodynamic performance and thereby reducing fuel consumption have been illustrated in recent studies. Abdessemed et al. (Abdessemed et al., 2018a) compared morphing trailing edge flaps to conventional hinged flaps, both in steady and unsteady conditions to investigate the aerodynamic performance of real-time morphing. They showed that the baseline wing with a hinged flap and zero deflection caused an increase in drag and a reduction in lift due to the spanwise and chordwise gaps. The comparison of the morphing versus hinged flap showed that morphing trailing edge increased the lift by up to 40% at similar drag coefficients and improved the overall aerodynamic efficiency by 45%. In (Abdessemed et al., 2018b), the same authors evaluated this morphing configuration in a 2D transient study through dynamic meshing, and also analyzed the unsteady behavior of morphing flaps (Abdessemed, Bouferrouk, & Yao, 2022). They showed that 22% higher lift was generated and a 25% drag reduction was achieved for the morphing trailing edge flap, which led to a 40% improvement in aerodynamic efficiency for pre-stall angles of attack. In addition, the stall angle increased by 2 degrees compared to that of the hinged flap.

Several studies have been conducted on NASA's variable camber continuous trailing edge morphing flap (VCCTEF) system. In (Ting et al., 2018; Ting, Chaparro, & Nguyen, 2017), Ting et al. conducted aerodynamic and structural optimizations that found a gain of 2-16% in lift-to-drag ratio and up to a 8.4% in drag reduction for a range of flight conditions.

In a joint project between NASA and Boeing, Urnes et al. (Urnes & Nguyen, 2013) investigated the VCCTEF system for future transport aircraft, that improved aircraft performance in terms of lift and drag, while reducing aircraft weight and increasing its maneuverability, including rolling performance. Their work showed that a VCCTEF system could accomplish two performance objectives: 1-efficient high lift capability for take-off and landing, and 2- cruise drag reduction through the control of the flexible wing twist shape. A multidisciplinary optimization was also conducted on a VCCTEF system by Lebofsky et al. (Lebofsky, Ting, & Nguyen, 2015), through which the drag reduction was obtained by reducing the wing stiffness.

Woods et al. (Woods et al., 2016) introduced a compliant morphing flap transition section (sealing the gaps between wing main body and flap) by addressing the side-edge gaps in the spanwise direction. They showed that in the absence of transition, a strong vortex emerged near the gaps; however, with a transition section, the downstream roll-up vortex disappeared. CFD simulation results also showed that by using complaint transition section, lift was increased, drag was reduced and a 7% increase in lift-to-drag ratio was obtained.

To reduce lift-induced drag, Ninian and Dakka (Ninian & Dakka, 2017) simulated and compared the trailing edge morphing flap with a conventional wing flap. Their comparison of a non-optimized morphing wing with a conventional wing showed an increase in lift of up to 10.8% and a lift-to-drag ratio improvement of up to 13.6% for the optimized morphing wing. They also performed an experimental acoustic analysis and showed that using a morphing wing decreased the noise level up to 50% in comparison to using a conventional wing. The effects of deploying spanwise morphing trailing edges on wings were also studied in (Chae et al., 2017; Pankonien & Inman, 2014; Rodriguez et al., 2015).

Lyu et al. (Lyu & Martins, 2015) used the gradient-based optimization to perform a multipoint optimization for an adaptive trailing edge wing. Drag reductions of 1% in a morphing trailing edge wing at off-design conditions and of 5% at on-design conditions were obtained. They computed the cruise fuel consumption for different fight phases and found that by using the morphing trailing edge, nearly 1% fuel consumption reduction could be obtained.

A new morphing trailing edge design concept was introduced by Communier et al. (Communier, Botez, & Wong, 2019), in which the deformation was performed by use of small vertical incisions. The comparison of aerodynamic coefficients revealed that this morphing design achieved a lower drag coefficient than that of a conventional design. They also showed that the morphing trailing edge had a higher lift-to-drag ratio and outperformed a hinged flap for angles of attack ranging from -10° to 10°.

Bashir et al. (Bashir et al., 2021) investigated the shape optimization of an UAS-S45 airfoil by evaluating the morphing at the trailing edge at the leading edge. For the morphing leading edge, the lift coefficient was increased by 21% and the stall angle was delayed by 3 degrees. For the trailing edge morphing, by considering drag minimization as an objective function, they found a 26% gain in lift coefficient and an 8% gain in maximum lift coefficient, compared to the baseline airfoil. They also showed that trailing edge morphing improved the endurance by approximately 10.25% compared to that of the unmorphed airfoil.

Dumont (Dumont, 2018) proposed a trailing edge morphing mechanism that applied two flexible surfaces on the wings' lower and upper surfaces. This morphing approach was applied to both the flaps (inner wing) and the ailerons (outer wing). By performing a gradient-based optimization, Dumont obtained a 2.6% gain in the objective function as well as a 0.595-degree reduction in angle of attack.

To eliminate the gaps between flaps and the main wing configuration, Khorami et al. (Khorrami et al., 2014) patented an elastic morphing structure for the side edges of the trailing edge flap. This structure significantly reduced the aeroacoustic noises associated with the discontinuities of side edge gaps without compromising an aircraft's cruise efficiency. This innovative configuration was capable of elongation in a chordwise direction, bending and twisting as needed, and when not deployed, it conforms to the chordwise cross-section of the flap's side edge.

In an experimental study, Rivero et al. (Rivero et al., 2021) evaluated the FishBack morphing configuration with a hinged flap and the baseline airfoil; they found a lower drag penalty for the morphing configuration with a similar lift coefficient that led to a greater lift to drag ratio, that gave from 50% to 200% improvement over the baseline airfoil.

The above-mentioned studies are just some of the recent noteworthy studies on the morphing trailing edge. In this study, the aim is to achieve a high-fidelity optimization of the seamless morphing trailing edge (SMTE) flap for most of the flight conditions (climb, cruise, descent) of the whole flight envelope. To the authors knowledge, no optimization has been conducted on a morphing seamless flap to maximize the flight performance made possible by this morphing configuration. This present study is conducted on an UAS-S45, an unmanned aerial system that was designed and manufactured by Hydra Technologies, a Mexican company. This UAS is mainly designed for surveillance and reconnaissance missions. Multiple morphing studies have been conducted on this UAS at our Research Laboratory in Active Controls, Avionics and Aeroservoelasticity (LARCASE), as shown in Figure 4.1, and its aerodynamic model has been extensively studied (Kuitche & Botez, 2019).

In this paper, the seamless morphing flap was optimized using a high-fidelity gradient-based methodology that uses the discrete adjoint method on the three main flight phases of the whole flight envelope, including climb, cruise, and descent, with the specified objective functions for each flight condition. For the climb condition, the aim was to find the optimum deflection of the SMTE flap to maximize the climb rate, for the cruise flight, the main purposes were the range and endurance maximization, and for the descent flight, the main objective was to reduce the descent rate by the morphing of the SMTE flap.

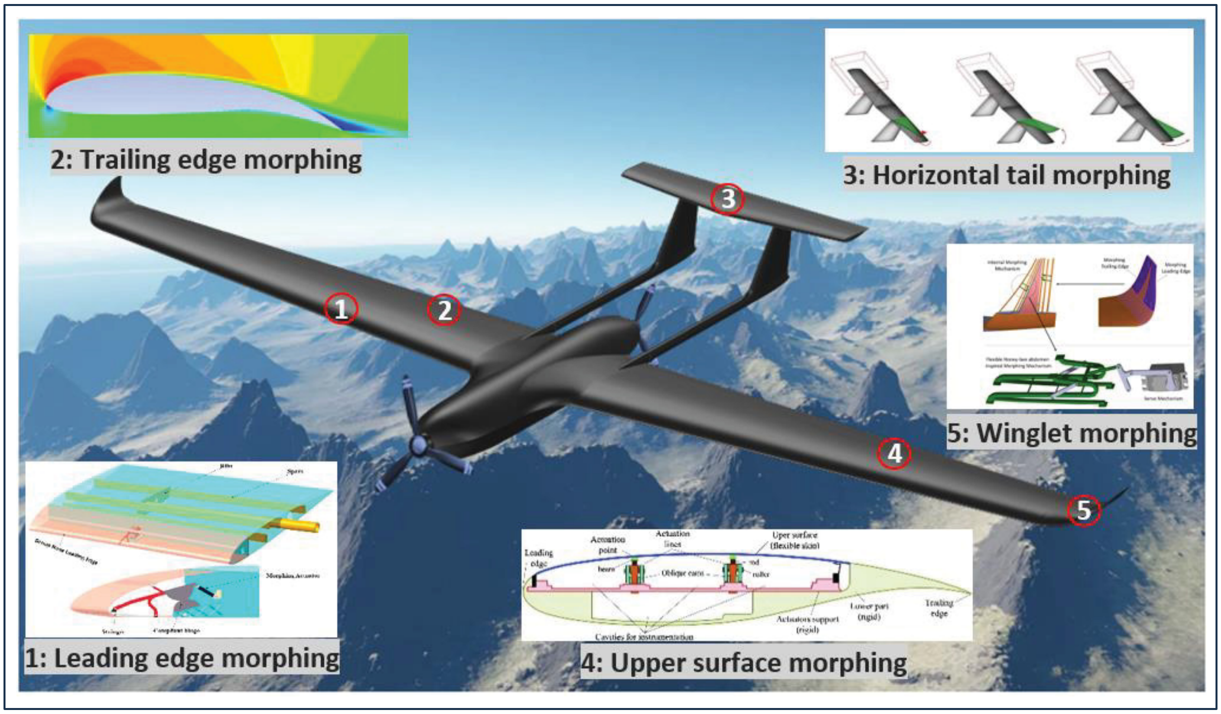

Figure 4.1 Morphing studies on UAS-S45 conducted at LARCASE

4.2 Methodology

Eliminating the gap between the wing and its edge flaps gave many advantages in terms of reducing the flow turbulence around the junctions by extending the laminar flow, reducing drag and noise, and thus, generating more lift force. Therefore, sealing the gaps in trailing edge flaps, which are considered the main control surfaces on a wing, and generating a smooth flap deformation will unquestionably improve the wings' aerodynamic performance. In this study, the SMTE flap is studied for the whole flight envelope for the UAS-S45 by finding the optimum deformation for each flight condition. Figure 4.2 illustrates the SMTE flap. As indicated, the SMTE flap covers 30% of the chord length and 41% of the wings' semi-span by including the transition sections.

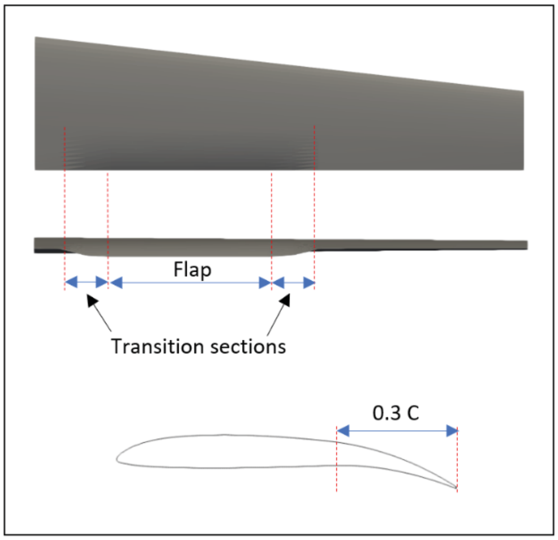

Figure 4.2 Schematics of a Seamless Morphing Trailing Edge Flap (SMTE)

Given that the main goal of this study is the aerodynamic optimization of the seamless morphing trailing edge (SMTE) flap, a high-fidelity optimization is conducted to obtain the optimum morphing configuration for SMTE flaps in different flight conditions, including climb, cruise, and descent. This optimization is performed separately for each flight condition with its specified objective function. Gradient-based optimization coupled with the discrete adjoint method in conjunction with the high-fidelity flow solver OpenFOAM. This process generates the UAS-S45 wing design using the Free-Form Deformation (FFD) parametrization method. The following sections describe the overall framework used in this paper.

4.2.1 Gradient-based optimization – IPOPT optimizer

The optimization problems solved by using the gradient-based method are generally expressed in the following form:

$$\min_{x \in R_n} f(x) \tag{4.1}$$

where the optimum value of $f(x)$ is found by calculating the partial derivatives or gradients of design variables, which leads the search directions to the optimum possible values of $f(x)$. Some algorithms, such as gradient descent, which is the basic algorithm of the gradient method, only requires the first derivatives of the function of interest (Jacobian matrix), whereas other algorithms also require the second derivatives (Hessian matrix). While there are many gradient-based algorithms, the most suitable algorithm is determined according to the optimization problem, including whether it is linear or nonlinear, constrained, or unconstrained, etc. In this study, the optimization problem is a nonlinear constrained problem that contains equality and inequality constraints. The algorithm established in this study is the Interior Point Optimizer (IPOPT), first developed by Wachter and Beiger in 2004 (Wächter & Biegler, 2006) and applied to solve nonlinear and continuous constraint problems. In this method, the line searches are based on filter methods. The IPOPT optimizer employs the Automatic Differentiation (AD) technique to find the first and second derivatives of the objective function (Jacobians and Hessians, respectively); however, quasi-Newton methods, such as the Broyden–Fletcher–Goldfarb–Shanno algorithm (BFGS) are used, when the second derivatives are not available. The general form of problems solved by the IPOPT method is (Ipopt Documentation):

$$\begin{aligned} & min \quad f(x) \\ subjected\ to: \quad & LB \leq g(x) \leq UB \\ & lb \leq x \leq ub \end{aligned} \tag{4.2}$$

where x are the design variables, $f(x)$ the objective function, $g(x)$ the constraint function, and LB and UB denote the lower and upper bounds for the constraint function, respectively. Likewise, lb and ub represent the lower and upper bounds for the design variables, respectively.

4.2.2 DAFoam optimization framework

The optimization methodology performed in this study takes advantage of a high-fidelity framework, known as the object-oriented discrete adjoint with OpenFOAM, in which the high-fidelity flow solver OpenFOAM is used in the optimization loop. This process produces results that are more accurate than those obtained by low-fidelity solvers, such as XFOIL or XFLR5, which are generally used in aerodynamic optimization. Discrete adjoint implementation in OpenFOAM was proposed by Towara and Naumann in (Towara & Naumann, 2013), where they have used an Automatic Differentiation (AD) for the computation of derivatives. However, the use of the AD considerably increases the computation cost for a simple problem, thus rendering the AD inappropriate for shape optimization. To extend the discrete adjoint (DA) implementation in OpenFOAM for solving optimization problems, the DAFoam optimization framework was developed by MDO laboratory team at Michigan University (He et al., 2020). In this optimization framework, the adjoint equation's partial derivatives were computed using the accelerated Finite Difference technique (FD) rather than an AD method, this is accomplished by making discrete adjoint based optimization in OpenFOAM a feasible process, even for optimization problems with a higher number of design variables. In this optimization framework, a high-level interface was established to compute the discrete adjoint derivatives by the solvers in OpenFOAM. For different solvers in OpenFOAM, the DA implementation differs in the: 1-residual and state variable vectors; 2- Jacobian matrix ; and 3- method for the calculation of residuals (He et al., 2020). Three child classes (sub-class) were therefore created to specify the above three variations, as well as another child class for specifying the turbulence state variables in OpenFOAM (He et al., 2020). This interface thus allows the adjoint derivative to be computed using any steady-state flow solver in OpenFOAM.

In this optimization framework, a high-level interface was established between the OpenFOAM layer and Python libraries, where the former consists of the flow solver “simpleFoam”, the adjoint and the graph coloring solvers, while the latter consists of three libraries for mesh deformation and optimization setup: “pyGeo” for the parametrization of surface geometry and geometric constraints computations, “pyWarp” for the deformation of volume mesh and “pyOptSparse” for the optimization (See (He et al., 2019; He et al., 2020) for details). Figure 4.3 illustrates the overall optimization process, where the OpenFOAM and Python layers are specified with different colors.

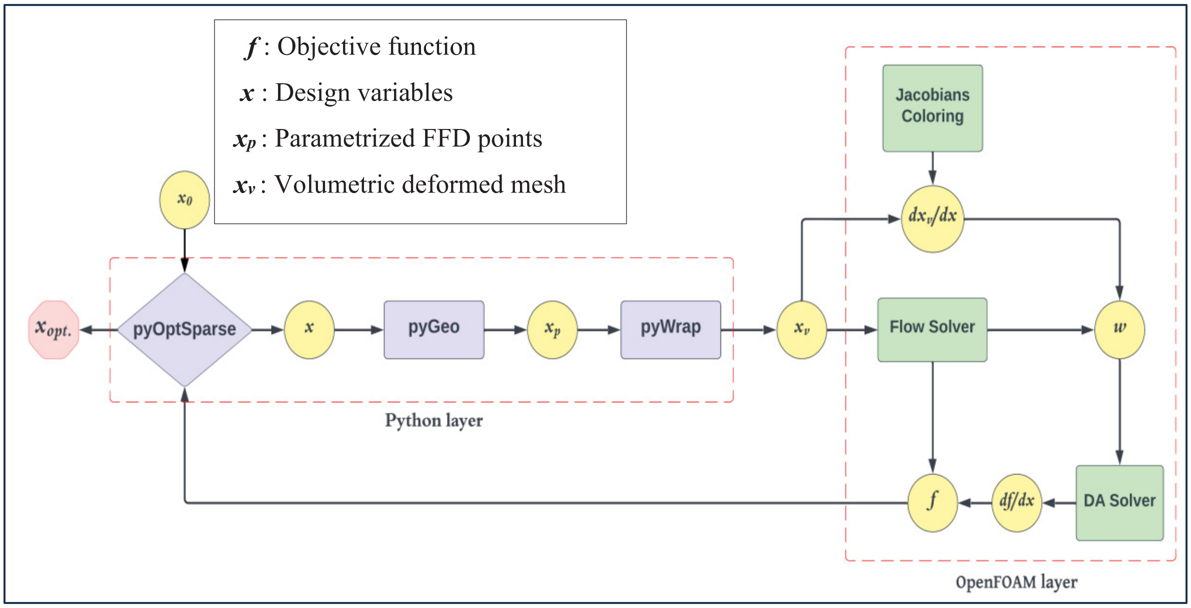

Figure 4.3 Overall optimization framework

4.2.3 Discrete Adjoint (DA) method

The Discrete Adjoint (DA) method uses discretized Navier-stokes equations to obtain the adjoint terms by differentiating the discretized equations. In optimization problems with high number of design variables, the computation of partial derivatives of the design variables is a very expensive and demanding task. The DA method is a reversed method, which can circumvent this demanding task and therefore, can highly reduce the computation time and cost by placing the dependency of partial derivatives on the state variables, rather than on the design variables. In other words, the most time-consuming part of gradient calculations, which are dependent on design variables, is replaced by adjoint equation calculations, which are dependent upon the state variables. The number of state variables is noticeably lower than the number of design variables, thereby a huge amount of computation time is saved.

Consider $f = f(x, \omega)$ as an objective function, where x and ω are the design and state variables, respectively. The computation of the total derivatives of f is expressed as follows:

$$\frac{df}{dx} = \frac{\partial f}{\partial x} + \frac{\partial f}{\partial \omega}\frac{\partial \omega}{\partial x} \tag{4.3}$$

where $\frac{\partial \omega}{\partial x}$ is the only term that depends upon the number of design variables; however, this dependency can be avoided by assuming that the residuals of governing equations must be satisfied, that *is* $\mathbf{R}(x, \omega) = 0$, and therefore the derivatives of residuals with respect to x are also equal to zero.

$$\frac{d\mathbf{R}}{dx} = \frac{\partial \mathbf{R}}{\partial x} + \frac{\partial \mathbf{R}}{\partial \omega}\frac{\partial \omega}{\partial x} = 0$$

or

$$\frac{\partial \omega}{\partial x} = -\frac{\partial \mathbf{R}}{\partial x}\left(\frac{\partial \mathbf{R}}{\partial \omega}\right)^{-1} \tag{4.4}$$

By combining equations (4.3) and (4.4) through the mutual term $\frac{d\omega}{dx}$, one obtains:

$$\frac{df}{dx} = \frac{\partial f}{\partial x} - \frac{\partial f}{\partial \omega}\left(\frac{\partial \mathbf{R}}{\partial \omega}\right)^{-1}\frac{\partial \mathbf{R}}{\partial x} \tag{4.5}$$

In Eq. (4.5), the term $\frac{\partial f}{\partial \omega}\left(\frac{\partial \mathbf{R}}{\partial \omega}\right)^{-1}$ is considered as the adjoint vector ψ, computed by solving a linear equation, called the adjoint equation (Eq. 4.6).

$$\left[\frac{\partial \mathbf{R}}{\partial \omega}\right]^T \psi = \left[\frac{\partial f}{\partial \omega}\right]^T \tag{4.6}$$

In Eq. (4.6), Finite Difference method (FD) is used for the computation of the partial derivatives; however, to accelerate the computation time, the graph coloring method (Gebremedhin, Manne, & Pothen, 2005) is used, in which the Jacobian matrix is divided into subgroups in specified colors so that at least one of the elements in adjacent rows is zero, and thus elements in multiple columns located in the same group are perturbed at the same time. The objective and residual computation is done only once (See (He et al., 2019) for details) in this graph coloring approach, in contrast to the regular FD method, which the number of iterations for the computation of the objective and residuals reaches to millions (approximately more than 10 million for 3D problems). After the computation of partial derivatives, the PETSc library (toolkit for advanced optimization in Python) is used to solve the adjoint equation to find the adjoint vector ψ. Finally, the last step is the computation of $\frac{\partial \boldsymbol{f}}{\partial \boldsymbol{x}}$ and $\frac{\partial \mathbf{R}}{\partial \boldsymbol{x}}$ in Eq. (4.5), which are obtained by using the Brute-Force FD approach. Ultimately, the total derivative of f can be obtained by replacing the partial derivatives of the objective function ($\frac{\partial \boldsymbol{f}}{\partial \boldsymbol{x}}$) and the residuals $\left(\frac{\partial \mathbf{R}}{\partial \boldsymbol{x}}\right)$ as well as of the adjoint vector ψ in Eq. (4.6), as follows:

$$\frac{d\boldsymbol{f}}{d\boldsymbol{x}} = \frac{\partial \boldsymbol{f}}{\partial \boldsymbol{x}} - \psi^{T} \frac{\partial \mathbf{R}}{\partial \boldsymbol{x}} \tag{4.7}$$

The DA procedure considerably reduces the number of iterations and thus, the computation time, making the optimization problems with high number of design variables (wing or full aircraft) feasible.

4.2.4 Free-Form Deformation (FFD)

Wing model is generated before the optimization process and the technique used for parametrization has a substantial impact on the final optimization results. Covering a large design space with a small number of design variables could lead to an effective parametrization (Masters et al., 2015). The FFD technique is part of the Soft Object Animation (SOA) algorithms (Sederberg & Parry, 1986), which are considered among deformative parametrization techniques. The FFD parametrization was developed by Sederberg and Parry (Sederberg & Parry, 1986) in 1986, since then, several modifications have been added to this algorithm, that are applied to real engineering problems (Coquillart, 1990; Lamousin & Waggenspack, 1994; Ronzheimer, 2004), in particular to aerodynamic shape optimization

(Samareh, 2004). In the earliest model, the control points on FFD block were defined through tri-variate Bernstein polynomials (Sederberg & Parry, 1986); however, subsequent models have introduced tri-variate Bezier, and NURBS polynomials (Coquillart, 1990; Lamousin & Waggenspack, 1994; Ronzheimer, 2004). In the FFD parametrization, the studied body (aircraft or its components, such as wing) is embedded inside the FFD block, and any modification in the control points of this block deforms the inner body shape. For 3D wing or aircraft optimization problems, in which the design variables are of the order of 10^2, constructive parametrization techniques, such as NURBS, Bezier-PARSEC, and CST, which are commonly used in 2D optimization problems, are not feasible due to the high number of design variables. However, since the FFD method considers the geometry variations rather than the geometry itself (Samareh, 2000), the number of design variables becomes almost irrelevant, thus making it the best technique for optimization problems with numerous design variables. For instance, let $\bar{\mathbf{g}}$ be the baseline geometry and $\Delta\bar{\mathbf{G}}$ the geometric change or variation, so that:

$$\bar{\mathbf{G}}_{defomed} = \bar{\mathbf{g}} + \Delta\bar{\mathbf{G}} \tag{4.8}$$

During the aerodynamic optimization, the geometric change $\Delta\bar{G}$ includes all types of variations, including twist, camber, thickness, shear, and planform deformation, as indicated below:

$$\Delta\bar{\mathbf{G}} = \delta\bar{\mathbf{G}}_{twist} + \delta\bar{\mathbf{G}}_{camber} + \delta\bar{\mathbf{G}}_{thickness} + \delta\bar{\mathbf{G}}_{shear} + \delta\bar{\mathbf{G}}_{planform} \tag{4.9}$$

Depending on the morphing approach, these variations are controlled by defining the degree of freedom to the FFD control points. For instance, in trailing edge morphing, the only required variation is the camber ($\delta\bar{G}_{camber} > 0$); therefore, all other variations are confined to zero deformation ($\delta\bar{\mathrm{G}}_{\mathrm{twist}} = \delta\bar{\mathrm{G}}_{\mathrm{thickness}} = \delta\bar{\mathrm{G}}_{\mathrm{shear}} = \delta\bar{\mathrm{G}}_{\mathrm{planform}} = 0$).

In this article, the FFD block is represented through the tri-variate B-spline volume, which is defined below:

$$\vec{V}(u,v,w) = \sum_{i=0}^{N_u-1} \sum_{i=0}^{N_v-1} \sum_{i=0}^{N_w-1} N_{i,m_u}(u) N_{j,m_v}(v) N_{k,m_w}(w) Q_{i,j,k} \tag{4.10}$$

where N_{i,m_u}, N_{j,m_v}, and $N_{k,m_w}$are the basic functions, m_u , m_v, and m_w are the degrees of freedom and $Q_{i,j,k}$ is the initial block. To map the parameter space (the FFD control points) to the physical space (the embedded geometry), the Newton search method (Ronzheimer, 2006) is applied to the initial embedded object given by $\vec{P}(u,v,w)$.

$$\vec{P}(u,v,w) = \sum_{i=0}^{N_u-1} \sum_{i=0}^{N_v-1} \sum_{i=0}^{N_w-1} N_{i,m_u}(u) N_{j,m_v}(v) N_{k,m_w}(w) Q_{i,j,k} \tag{4.11}$$

Using equation (12), the basic functions are calculated in all directions:

$$N_{i,l_u} = \begin{cases} 0, & u_i \leq u \leq u_{i+1} \\ 1, & otherwise \end{cases}$$

and

$$N_{i,m_u}(u) = \frac{u - u_i}{u_{i+m_{u-1}} - u_i} N_{i,m_{u-1}}(u) + \frac{u_{i+m_u} - u}{u_{i+m_u - u_{i+1}} - u_i} N_{i+1,m_{u-1}}(u) \tag{4.12}$$

By obtaining the new coordinates of the embedded body (wing), the new B-splines volume is calculated and is replaced by the initial volume given in Eq. (4.11).

$$\vec{P}^{new}(u_0,v_0,w_0) = \sum_{i=0}^{n_u} N_{i,m_u}(u_0), N_{j,m_v}(v_0), N_{k,m_w}(w_0) Q_{i,j,k}^{new} \tag{4.13}$$

In Eq. (4.13), $Q_{i,j,k}^{new}$ are the coordinates of the control points after deformation, through which the new coordinates of the embedded object are obtained, given by $\vec{P}^{new}$. The sensitivity of the points inside the FFD block can be obtained as follows (Kenway, Kennedy, & Martins, 2010):

$$\frac{\partial \boldsymbol{P}}{\partial x} = \frac{\partial \boldsymbol{Q}}{\partial x} \frac{\partial \boldsymbol{P}}{\partial \boldsymbol{Q}} \tag{4.14}$$

where x is the design variable, $\boldsymbol{P} = \vec{P}(u, v, w)$ are the coordinates of the embedded body, $\boldsymbol{Q} = \vec{Q}(u, v, w)$ are the coordinates of the FFD control points and $\frac{\partial \boldsymbol{P}}{\partial \boldsymbol{Q}}$ is the shape function. Two important factors should be noted before the optimization process. Firstly, the topology of the FFD block should be defined. The FFD block should be body-fitted, meaning that it should not be too large or far from the design surface, as the gradients received by the optimizer should be on the same order of magnitude during the optimization. Secondly, the number of control points is case-dependent, and it should be chosen depending on the studied case. In our previous work (Mir Hossein Negahban, Musavir Bashir, & Ruxandra Mihaela Botez, 2023), we showed how control points impacts the final optimization results and computation time. Therefore, this aspect should be considered before starting the optimization process. In this study, two types of FFD blocks are created, one corresponding to the trailing edge section (red block) and the other one corresponding to the rest of the wing (blue block) (see Fig. 4.3). Since we are studying trailing edge morphing, the deformation of the wing is confined to upward and downward deflections of the flap along the span. The number of control points for two blocks are 30 and 6 in the spanwise and chordwise directions, respectively, which corresponds to the total number of 360 FFD control points for the whole wing. Figure 4.3 shows the UAS-S45 wing embedded in FFD block. For a wing with SMTE flap, the control points on the flap section are free to move in the upwards and downwards directions, the rest of control points are confined to zero deflection, and thus only 52 out of the 360 control points are active (Fig. 4.4). Figure 4.5 shows the FFD block after morphing, in which the flap is morphed along with the block deformation.

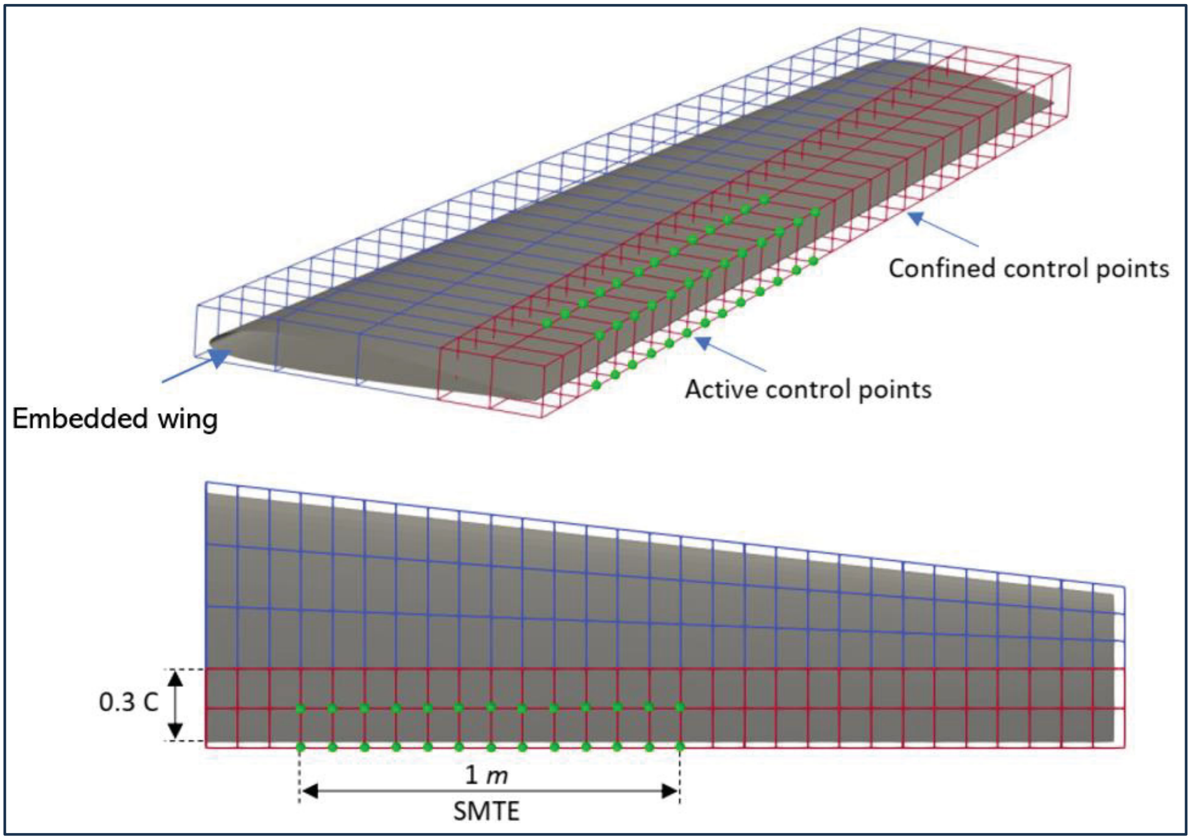

Figure 4.4 FFD blocks for the UAS-S45 wing

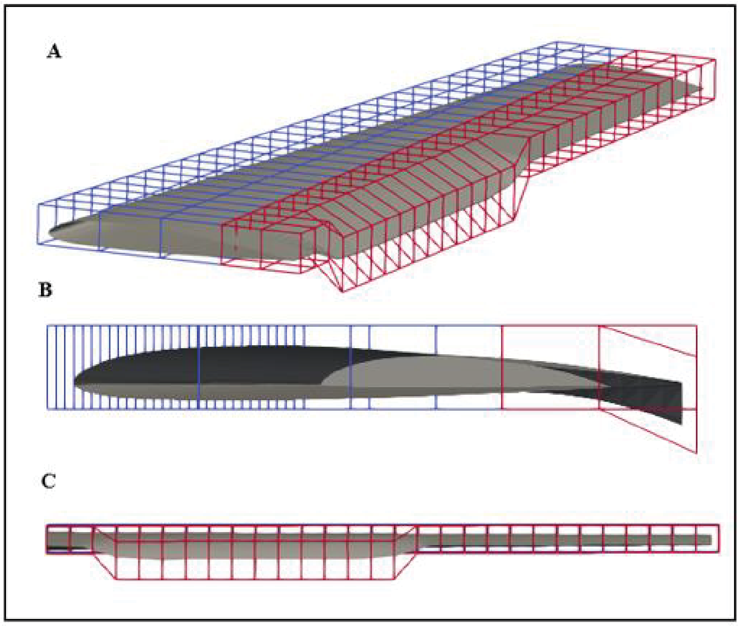

Figure 4.5 FFD blocks after deformation. A) isometric, B) side view, and C) rear view

4.2.5 Optimization methodology

4.2.5.1 Solver-agnostic setup

This study seeks the optimum configuration of the SMTE flap for the whole flight envelope, including climb, cruise, and descent. Therefore, each flight condition has different objective functions, that are characterized by specific goals, as summarized in Table 4.1.

Table 4.1 Specific goals and objective function for each flight condition

Flight condition	**Goal**	**Objective function**
Climb	Increasing climb rate	$min \quad {C_D}/{C_L^{3/2}}$
Cruise	Increasing range (flight distance)	$max \quad {C_L}/{C_D}$
	Increasing endurance (flight time)	$max \quad {C_L^{3/2}}/{C_D}$
Gliding Descent	Reducing descent rate	$min \quad {C_D}/{C_L^{3/2}}$

As indicated in Table 4.1, each flight condition has a different objective function, and in the cruise flight, the optimization process requires two different objectives, range, and endurance. Depending on the flight mission objective, the SMTE flap will have different configurations; for instance, if the UAV's mission objective relies on its long-distance flight, then the optimum wing configuration will be set according to the range maximization (Table 4.1), otherwise, if longer flight time is the mission objective, then the wing morphs to its optimum shape according to the optimum endurance configuration. Each flight condition is optimized according to its flight characteristics, including the angle of attack, altitude, and speed, and finally, the constraints and objective function. Table 4.2 indicates the details of each flight condition and Figure 6 illustrates the main flight envelope for the UAS-S45.

Table 4.2 Characteristics of each flight condition

Flight condition	**Speed (knot)**	**Altitude (ft)**	**Reynolds number $\times \mathbf{10^6}$**
Climb	65	0	1.2
Cruise - Range	55	15,000	0.7
Cruise - Endurance	55	15,000	0.7
Gliding Descent	55	15,000	0.7

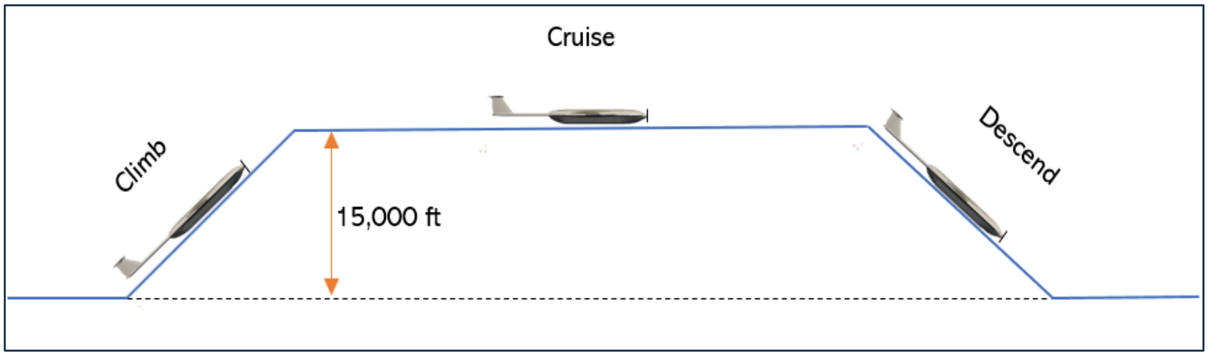

Figure 4.6 The whole flight envelope of the UAS-S45

Although the objective function for each flight condition is different, the overall optimization framework is the same for all of them. The number of geometric design variables (FFD block and control points) and geometric constraints remains the same for all optimization processes; however, the objective function is unique to each flight condition. Table 4.3 shows the overall optimization setup.

Table 4.3 Overall optimization setup for each flight condition

Function/variable	Description	Total number
Objective function		
max / min f	f: *Objective function for each flight condition (Table 1)*	4
w.r.t:		
Y	*FFD control points*	360
Subject to:		
$C_l \geq C_{l\,min}$	*Constant function*	1
AOA $_{\text{initial}}$=AOA $_{\text{final}}$	*Constant angle of attack*	1
$V \geq V_{initial}$	*Volume constraint*	
$-150mm \leq \Delta y \leq 150\ mm$	*Design variable bounds*	52
$\Delta y_{z=3}^{upper} = \Delta y_{z=15}^{upper}$	*Linear constraint*	52

The above optimization setup is used for each flight condition by simply changing the objective function according to Table 4.1. A total number of 24 optimizations are performed to find the optimum configuration of SMTE for the whole flight envelope of the UAS-S45.

4.2.5.2 Flow solver setup

As mentioned earlier, in this optimization framework, flow equations are solved using a high-fidelity solver, OpenFOAM, to extract the state variables and update the objective function in each iteration (Fig. 3). The whole flight envelope is in the subsonic regime. The incompressible

Navier-Stokes equations are solved with the steady state solver “simpleFoam”. The turbulence model chosen for this study is Spalart-Allmaras (S-A) model. The grid is generated in ICEM-CFD using a hexahedral structured grid (Fig. 4.7). Except for the boundary, to which the wing is attached and has “symmetry” boundary condition, the rest of the boundaries are defined as the “inletOutlet”. In this boundary condition, when the fluid flows into and out of the domain, the boundary condition alternates between “fixed value” and “zero gradient”, respectively.

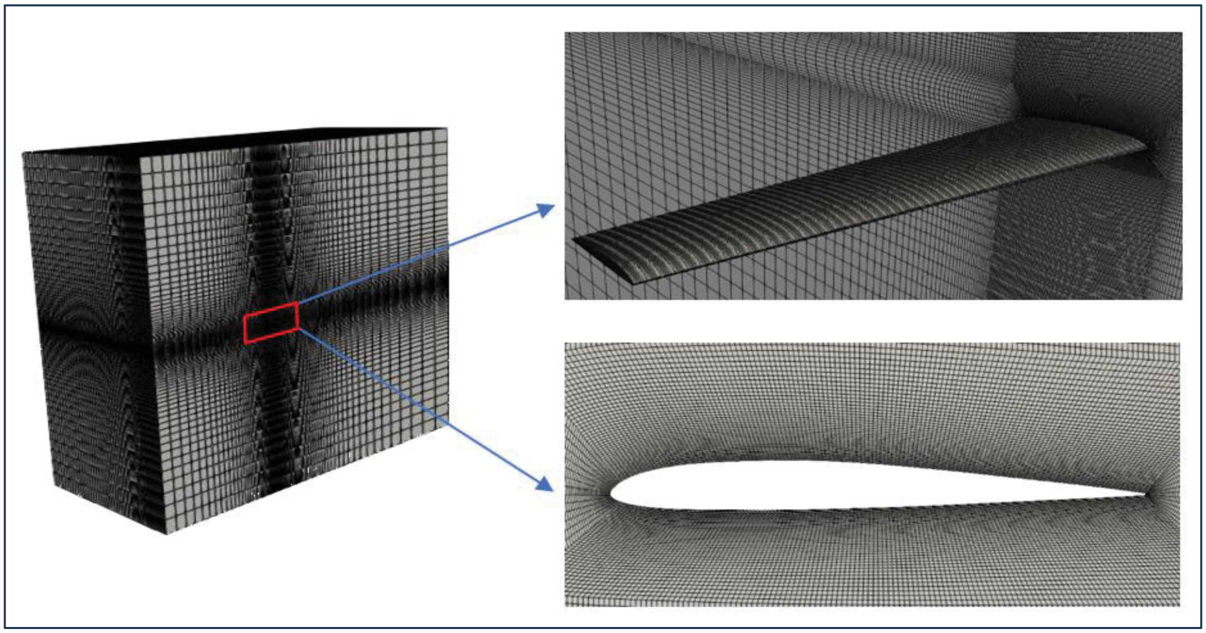

Figure 4.7 Illustration of the structured surface and volume mesh with hexahedral elements

4.3 Results and Discussion

The results obtained from the optimization are presented in four sections, each of which represents a set of flight conditions (climb, cruise, descent) with its specified objective function. For each flight condition, the aerodynamic properties of the wing with SMTE flap are compared with those of the baseline wing. A comparison is also drawn between an SMTE flap and a hinged flap on the full UAS-S45 in the cruise flight.

4.3.1 Climb condition

In a climbing flight, which accounts for the first phase of the whole flight envelope, the main goal is to increase the altitude, in other words, to turn the aircraft's kinetic and internal energy into potential energy to overcome the aircraft's weight. During a straight and level flight, the required energy is provided by the engines at a specified speed; however, to increase the potential energy (altitude) at the same speed, extra power is required; the amount of this added power determines the rate at which the altitude is increased (Marchman, 2004). The added power is the difference between the power required for level flight and the engine's available power. Figure 4.8 shows the balance of the aerodynamic forces for the UAS-S45 in climb condition.

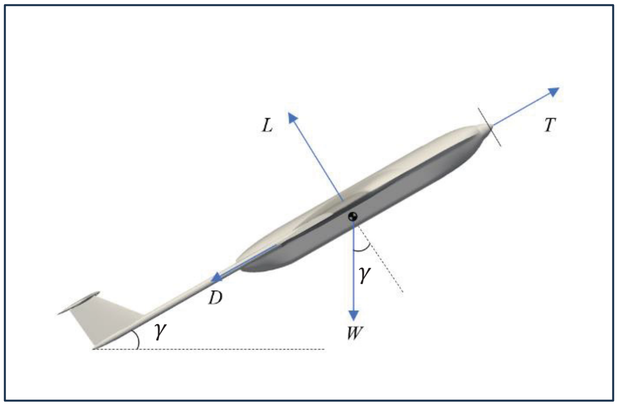

Figure 4.8 Aerodynamic force balance around the UAS-S45 in climbing flight condition

By assuming constant speed (no acceleration), summing these forces along the climb angle ($\boldsymbol{\gamma}$) gives:

$$\mathrm{T} - D = W sin\boldsymbol{\gamma} \tag{4.15}$$

To obtain the power, Eq. (4.15) is multiplied by the velocity as follows:

$$\frac{TV-DV}{W}=Vsin\boldsymbol{\gamma} \tag{4.16}$$

where TV and DV are the available power (P_{av}) and the required power (P_{req}), respectively. Therefore:

$$\frac{P_{av}-P_{req}}{W}=Vsin\boldsymbol{\gamma} \tag{4.17}$$

As shown in Fig. 4.9, $Vsin\,\boldsymbol{\gamma}$ is the vertical velocity of the aircraft and contributes to the rate of climb (dh/dt). As mentioned in Section 4.2, the main goal in climb phase is to increase the rate of climb, and, given that an aircraft's weight (W) and available power (P_{av}) are constant, the only variable is the required power (P_{req}) (as given in Eq. 4.17). Therefore, by reducing the required power (P_{req}), one can increase the rate of climb.

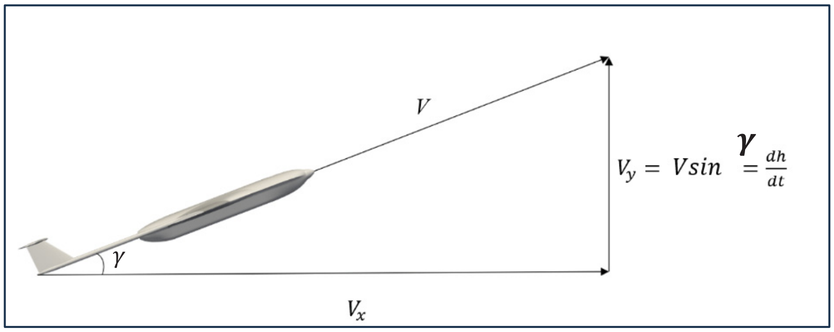

Figure 4.9 Illustration of the rate of climb as the vertical velocity

In level and straight flight, the required power is obtained from the Eq. (4.18) (Marchman, 2004):

$$P_{req}=\left(\frac{2W^3}{\rho S}\right)^{1/2}\frac{C_D}{C_L^{3/2}} \tag{4.18}$$

where, W is the aircraft weight, ρ the atmospheric density, and S the surface area.

In climb, due to the climbing angle, the lift force is equal to $W\cos\boldsymbol{\gamma}$; however, in this study, to use the level flight assumption (*L*=*W*), the small angle assumption (Marchman, 2004) is used, where the angles below 15° are considered, or where $\cos\boldsymbol{\gamma} \approx 1$. The minimum limit of this assumption is γ=5°, where $\cos\boldsymbol{\gamma} = 0.9962$, and its maximum limit is γ=15°, where $\cos\boldsymbol{\gamma} = 0.9659$, for which the maximum error is within 5%. In this study, the optimization of climb condition is performed for γ=5°, at which the level flight assumption has the least error, 0.38%.

In Eq. (4.18), to reduce the required power, one can simply minimize the $\frac{C_D}{C_L^{3/2}}$ term, through which the required power is minimized (Eq. (4.18)) and the climb rate is increased (Eq. 4.17). Therefore, the objective function to solve this optimization problem is defined as the minimization of $\frac{C_D}{C_L^{3/2}}$, leading to the goal in the climb condition, i.e., decreasing the P_{req} (Eq. 4.18) and increasing the climb rate. Table 4.4 shows the optimization results obtained for the UAS-S45 wing in the climb condition. Note that the deflection in the downward direction is assumed positive.

Table 4.4 Comparison of the UAS-S45 wing with and without an SMTE flap in climbing flight

Configuration	γ (°)	**Flap deflection (mm)**	C_L	C_D	$\frac{C_D}{C_L^{3/2}}$	**Required power (%)**	**Climb rate (%)**
S45+SMTE Flap	5	18.4	0.753	0.035	0.0534	-3.8	+ 6.13
Clean Wing	5	0	0.617	0.027	0.0555	-	

It is found that the required power (P_{req}) decreases 3.8% using the downward morphing of the flap, which leads to an increase in climb rate according to Eq. (4.17). In this case, where the weight of the UAS-S45 is nearly 49 kg and the $P_{av} = 8\ kw$, if we assume P_{req} is 5 kw, then the rate of climb becomes 61.2 m/s (Eq. (4.17)). However, by minimizing P_{req} by up to 3.8%, the climb rate for the S-45 wing equipped with an SMTE flap becomes 65.2 m/s, equivalent to a 6.13% increase in the climb rate (Table 4.4).

4.3.2 Cruise flight

In this study, the cruise flight objective function is divided into the optimization of range and of endurance. The optimization is performed according to the mission objective. If the mission objective is to cover a long-distance flight, then the SMTE flap will have the optimum shape according to the range objective function; and if the mission objective is to increase the flight time, the optimum shape will be based on the endurance objective function, as shown in Table 4.1.

4.3.2.1 Range optimization

For a propeller-engine aircraft, the range is calculated according to Eq. (4.19):

$$R = -\frac{\eta_p}{\gamma_p}\frac{C_L}{C_d}\ln\left(\frac{W_1}{W_2}\right) \tag{4.19}$$

where, η_p is the propulsive efficiency, γ_p weight-specific fuel consumption and W_1 and W_2 are initial and final aircraft weight, respectively.

According to Eq. (4.19), the only aerodynamic term that impacts the flight range is the lift-to-drag ratio, thus by increasing this ratio, the range will be increased. Therefore, the objective function in terms of range improvement is the maximization of the lift-to-drag ratio. Our results obtained from aerodynamic parameters, including lift, drag and lift-to drag-ratio show the need to deploy an SMTE flap, due to its substantial improvement of aerodynamic performance over clean wing and a wing with deflected hinged flaps (Fig. 4.10).

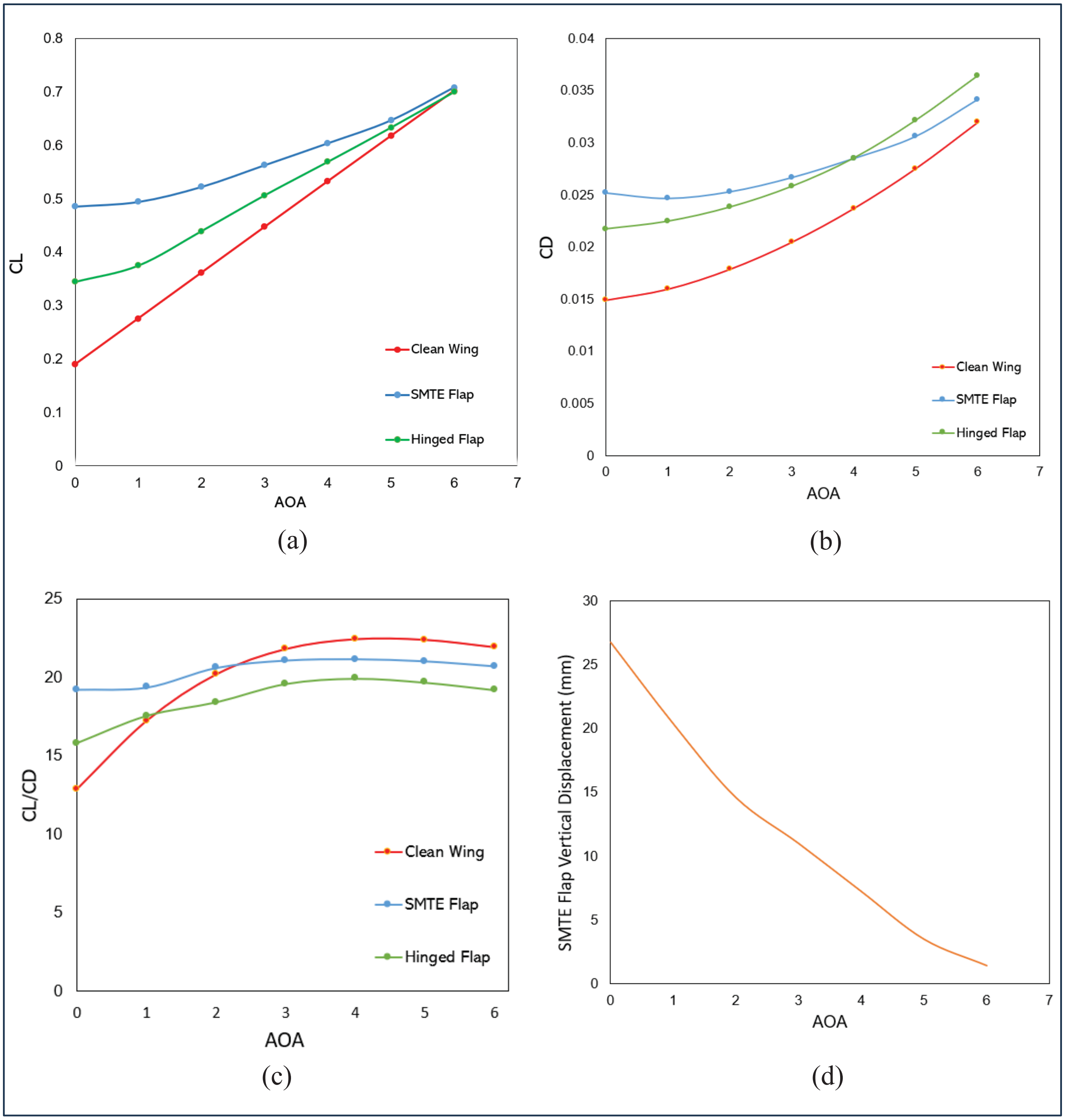

Figure 4.10 Comparison of the aerodynamic performance of the wing with SMTE flap, hinged flap, and baseline wing configurations for various angles of attack; a) lift coefficient, b) drag coefficient, c) lift-to-drag ratio, d) flap deflection magnitude

As shown in Figure 4.10-c, the overall aerodynamic performance of the wing with SMTE flap has increased compared to hinged flap configuration. By considering the diagrams of the lift and drag coefficients separately, it is evident that this improvement is mostly due to the excessive lift generation of the SMTE flap (Fig. 4.10-a). While the drag with SMTE flap is more than that of the hinged flap at some of the angles of attack (Fig. 4.10-b), this drag penalty is compensated by the excessive lift generation, which results in the overall improvement of the aerodynamic efficiency by up to 33% and 17.8% compared to clean wing and hinged flap, respectively (Fig. 4.10-c). It is also shown that by increasing the angle of attack, the optimized flap deflection decreases and approaches to zero deflection, becoming similar to the performance of the baseline wing configuration. Note that the angle of deflection of the hinged flap is taken from that of the optimized SMTE flap to draw a precise comparison ($AOD_{Hinged} = AOD_{Opt.\ SMTE}$).

In fact, a deflecting flap during cruise flight is not efficient at every angle of attack, hence the SMTE flap performance is only efficient for a limited range of angles of attack. As shown in Fig. 4.10-c, after AOA= 2.5°, the performance of the wing with SMTE flap degrades compared to that of the clean wing; however, for the wing with a hinged flap, the maximum best performance is only up to AOA=1°. This means that the morphing flap can perform in an extended range of AOAs (AOA=0° to 2.5°) compared to the hinged flap, for which better efficiency compared to baseline wing is limited to AOA=0 to 1°. Figure 4.11 compares the UAS-S45 wings with deflected SMTE and hinged flaps.

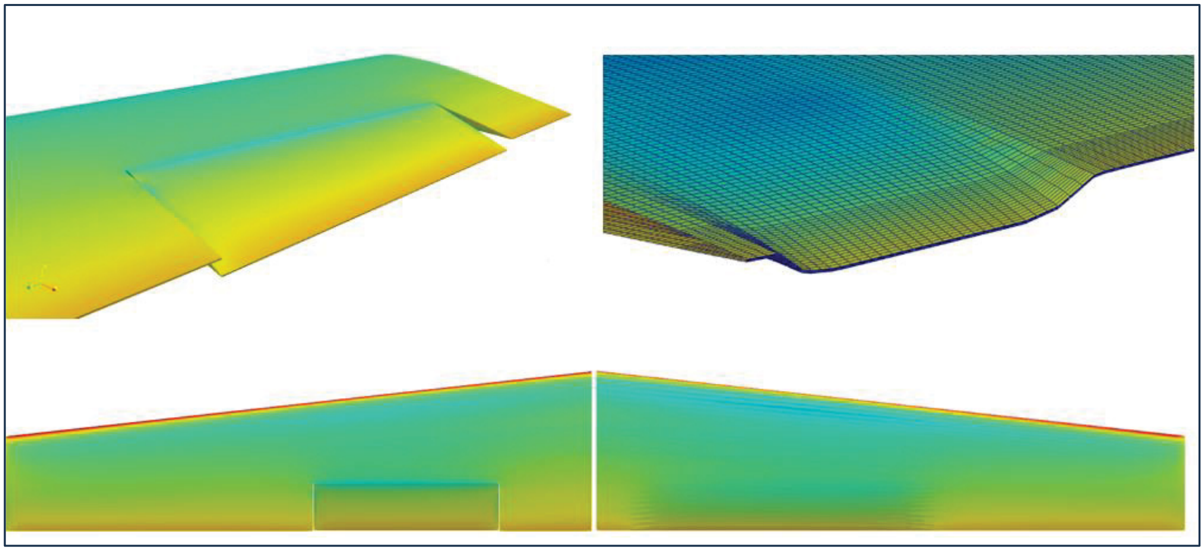

Figure 4.11 Comparison of SMTE flap (right) with hinged flap (left) for cruise flight

In addition, Figure 4.12 illustrates the whole UAS-S45 equipped with an SMTE flap on the right wing and a hinged flap on the left wing to obtain a good comparison in terms of the pressure variations, detailed in Figs 4.12 (a-c).

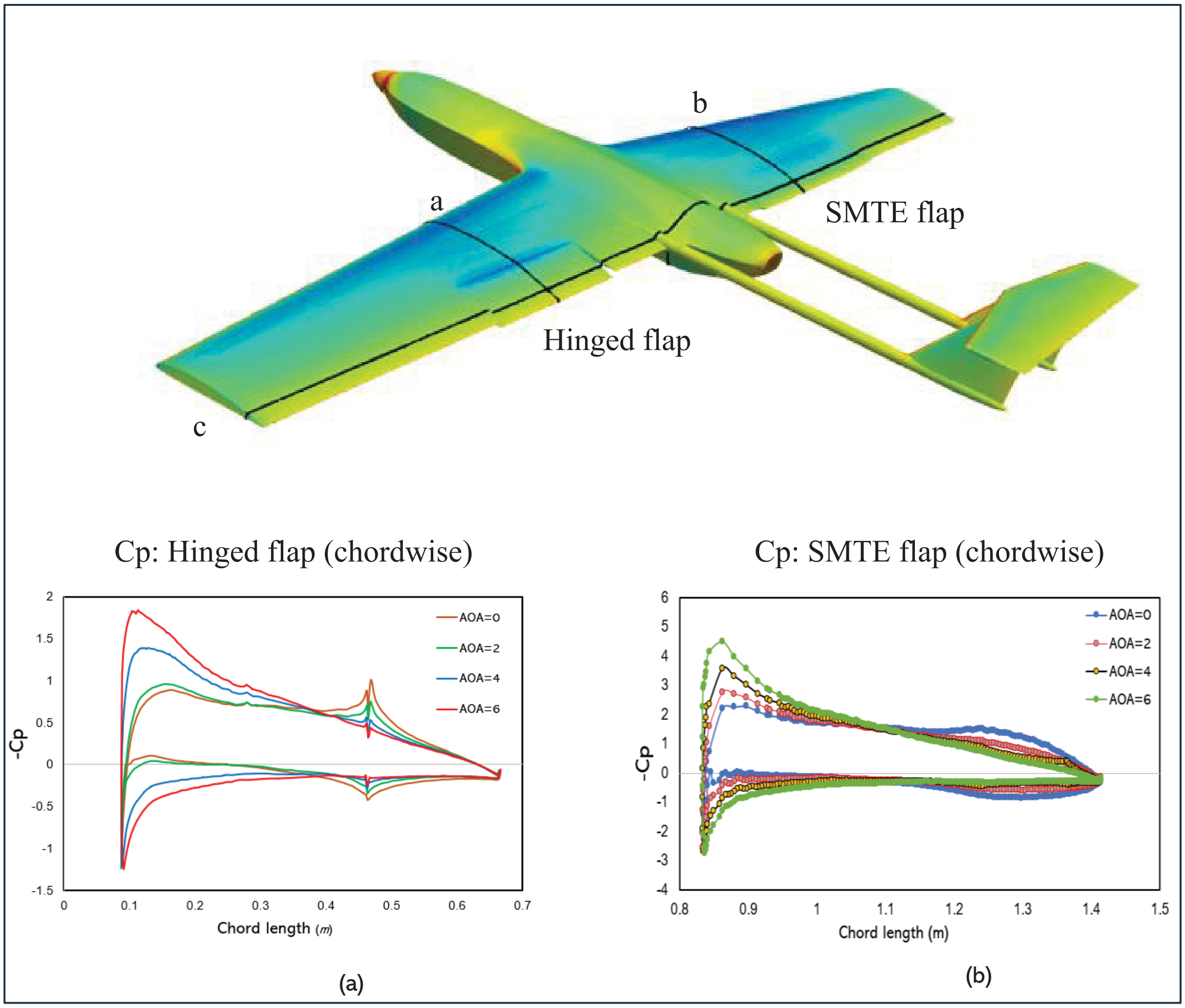

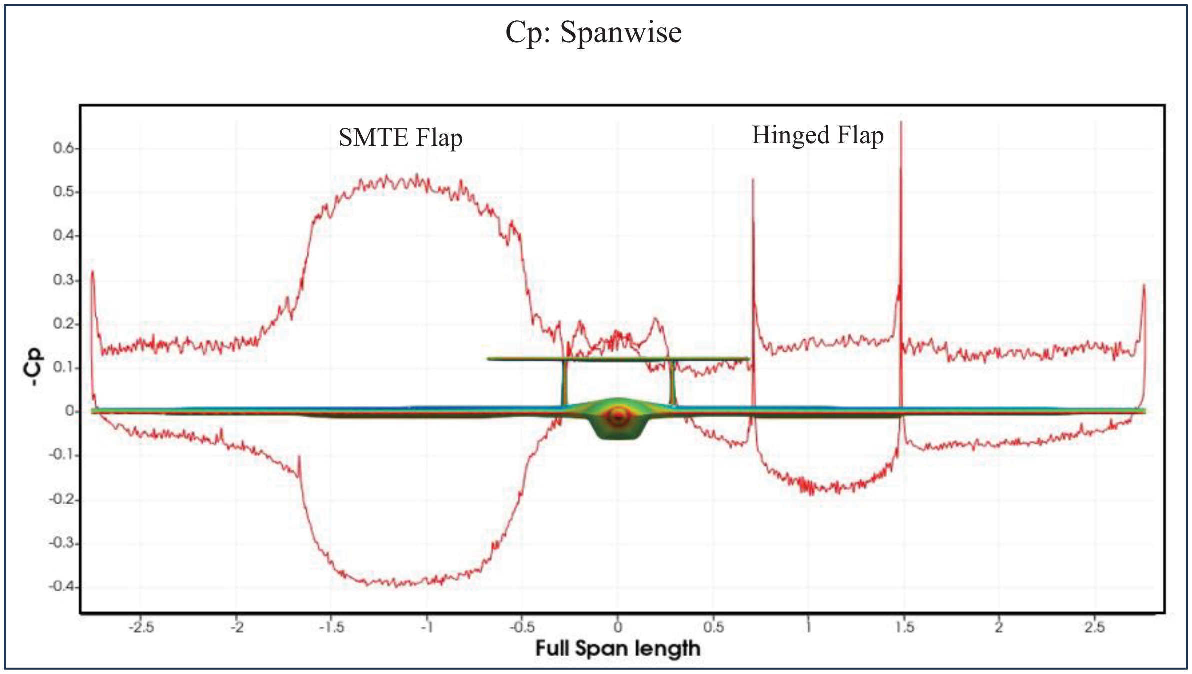

Figure 4.12 UAS-S45 equipped with an SMTE (right) and a hinged flap (left), with their pressure coefficient distribution presented in both chordwise (a and b), and c) spanwise directions

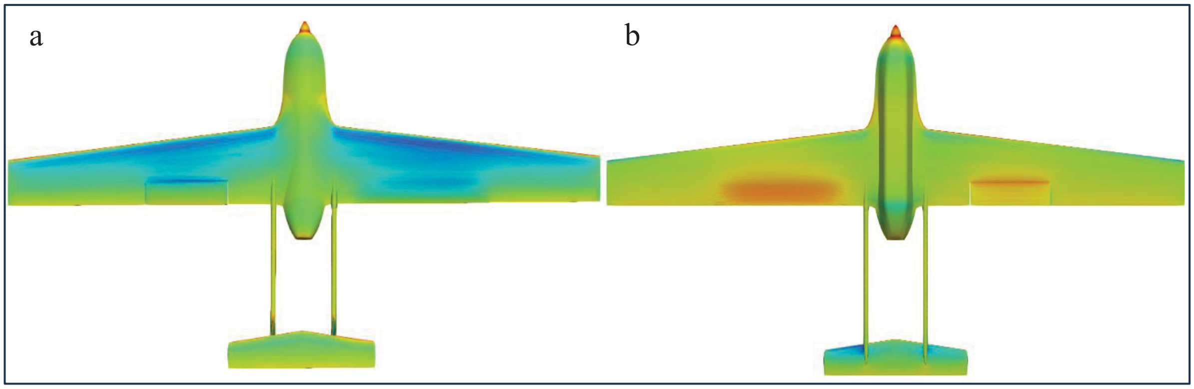

Figure 4.13 Pressure contours of a UAS-S45 with a hinged flap and an SMTE flap, from a) top view, and b) bottom view

The pressure coefficient distribution in both chordwise and spanwise directions in Fig. 4.12 (a, b, c) clearly show the pressure peaks around the gaps for the hinged flap, whereas for the SMTE flap, these pressure peaks have been eliminated, leading to very smooth pressure variations. These pressure peaks occur mainly because of the spillage of the flow from the pressure side to the suction side due to the presence of the gaps; for the hinged flap, this flow mixture acts as a flow control mechanism at higher angles of attack, where the flow on the pressure side mixes with the separated flow on the suction side and then reattaches to the separated flow.

In addition, both the chordwise and the spanwise pressure diagrams (Fig. 4.12 (a-c)) show that for the SMTE flap, the pressure gap between the upper and lower surface of the wing is more than that of the hinged flap, which leads to the increased lift generation. This increase in pressure coefficient is due to the seamless transition section, whose contribution in the flap deformation increases the lifting surface of the wing. In contrast, for the hinged flap, these sections are solid undeformed parts of the wing, which have no contribution to the flap deflection. Elimination of the gaps in the SMTE flap extends the laminar flow on the upper surface of the wing, whereas for the hinged flap, the low-pressure contour is stopped at the start of the gap (Fig. 4.13-a). The laminarity of the flow is preserved up to the tip of the trailing edge for the SMTE flap (Fig. 4.13-a). The bottom part of the pressure contours (Fig. 4.13-b) also illustrates the difference in the pressure gaps between the SMTE and the hinged flap. As shown, for the SMTE flap, the maximum pressure is concentrated on the bottom surface of the whole flap due to the elimination of the gaps and the flap's smooth deformations.

The seamless characteristic of the SMTE flap enhances the flow's steadiness and diminishes its turbulent behavior due to the elimination of the gaps. As shown in Figure 4.14-a, the gap in the hinged flap causes a downwash or spillage in the flow, similar to the wing tip downwash. Figures 4.14-b and 4.14-c clearly show the difference of the flow behaviors on these flaps, as the vorticity contours indicate the recirculation of the flow between the gaps in the hinged flap, while in the SMTE flap, this recirculation disappears, and the boundary layer is more stable. The creation of the downwash (by the hinged flap) decreases the effective angle of attack of the wing, and thus the lift, wherein the seamless effect of the SMTE flap eliminates both recirculation and downwash.

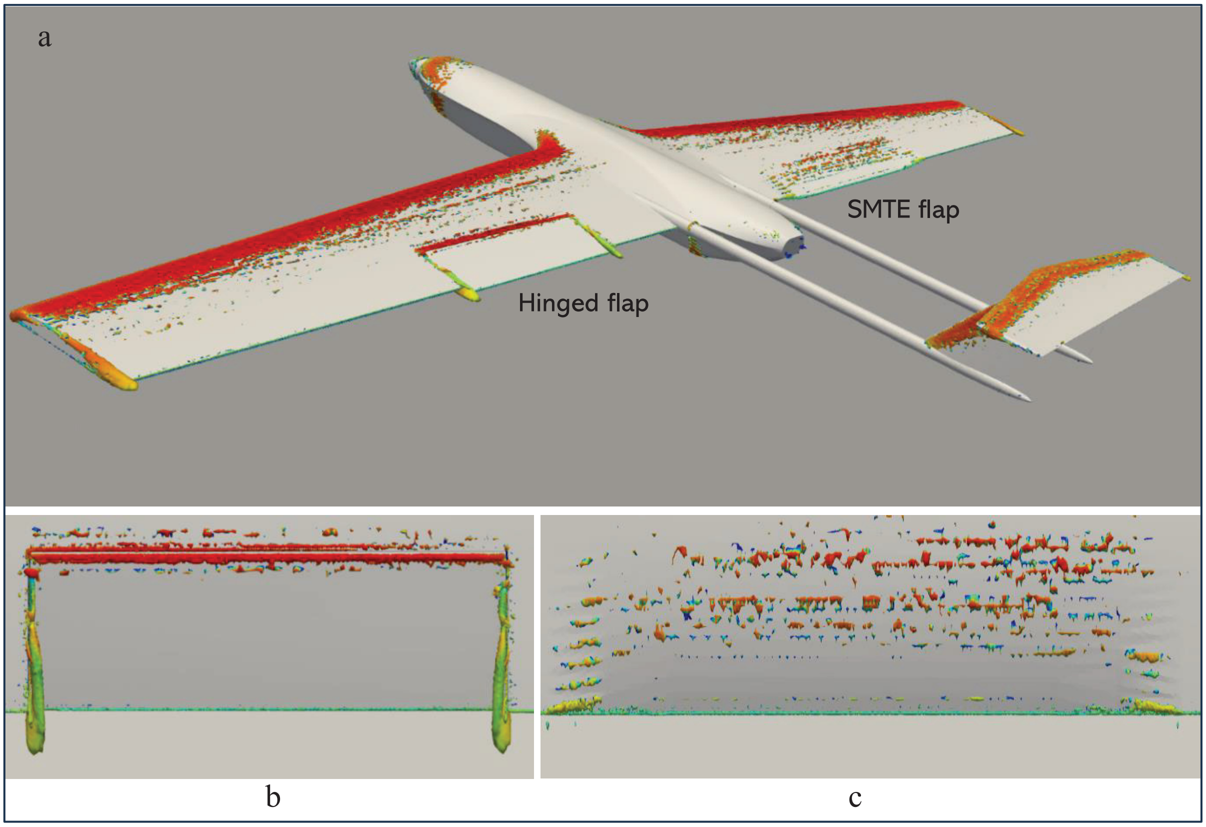

Figure 4.14 Vorticity contour comparison of the UAS-S45, with b) hinged, and c) SMTE flap

Therefore, by considering the aerodynamic advantages of the SMTE flap versus the hinged flap, the efficiency of the seamless morphing flap in improving aerodynamic performance is obvious.

4.3.2.2 Endurance optimization

As another objective function of the cruise condition, the endurance mainly concerns the flight time, as most of the flight time is dedicated to the cruise flight condition. Depending on the engine type, the relation of the endurance to the aerodynamic properties differs. For a propeller engine, the endurance equation is defined as follows:

$$E = -\frac{\eta_p}{\gamma_p}\sqrt{2\rho S}\,\frac{C_L^{\frac{3}{2}}}{C_d}\left(\frac{1}{\sqrt{W_2}} - \frac{1}{\sqrt{W_1}}\right) \tag{4.20}$$

where η_p is the propulsive efficiency, γ_p is the weight-specific fuel consumption, and the only aerodynamic term affecting the endurance is $C_L^{3/2}/C_D$, which is called endurance efficiency, where the lift generation is of higher priority than the drag reduction. By considering Eq. (4.20), the objective function for the endurance optimization of an SMTE flap is the maximization of the $C_L^{3/2}/C_D$ term. Having proven the superiority of the SMTE flap over the hinged flap in the previous section, here the purpose is to find the optimum configuration of an SMTE flap for maximum endurance.

Figures 4.15 (a-d) show the aerodynamic properties obtained with the SMTE flap after the optimization. These properties are compared to those of a clean wing, i.e., with no flap deflection.

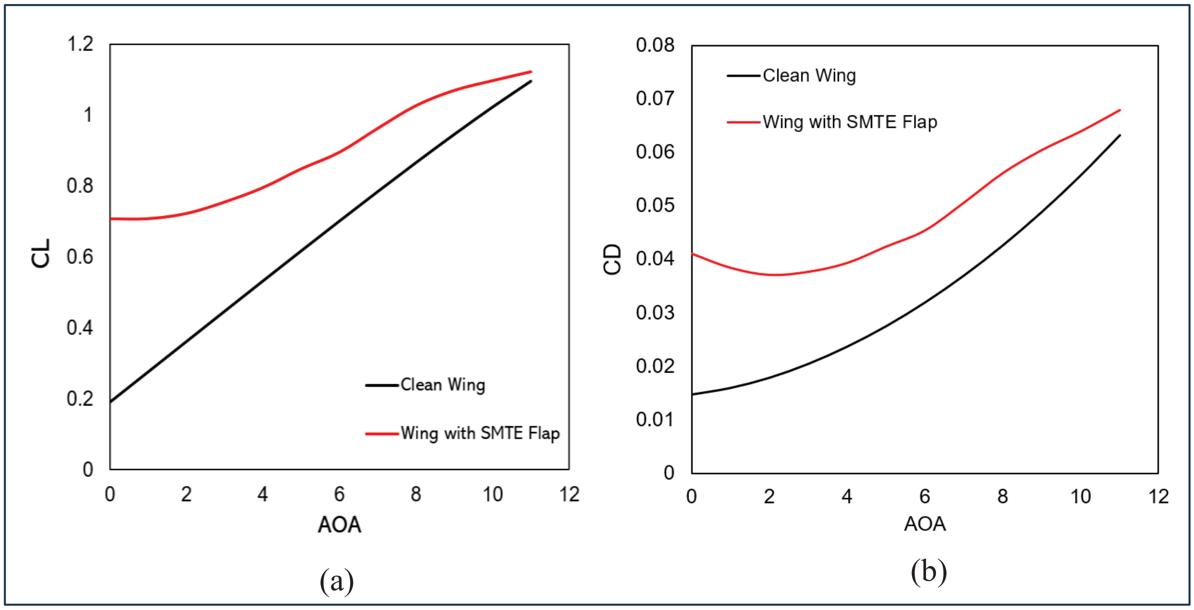

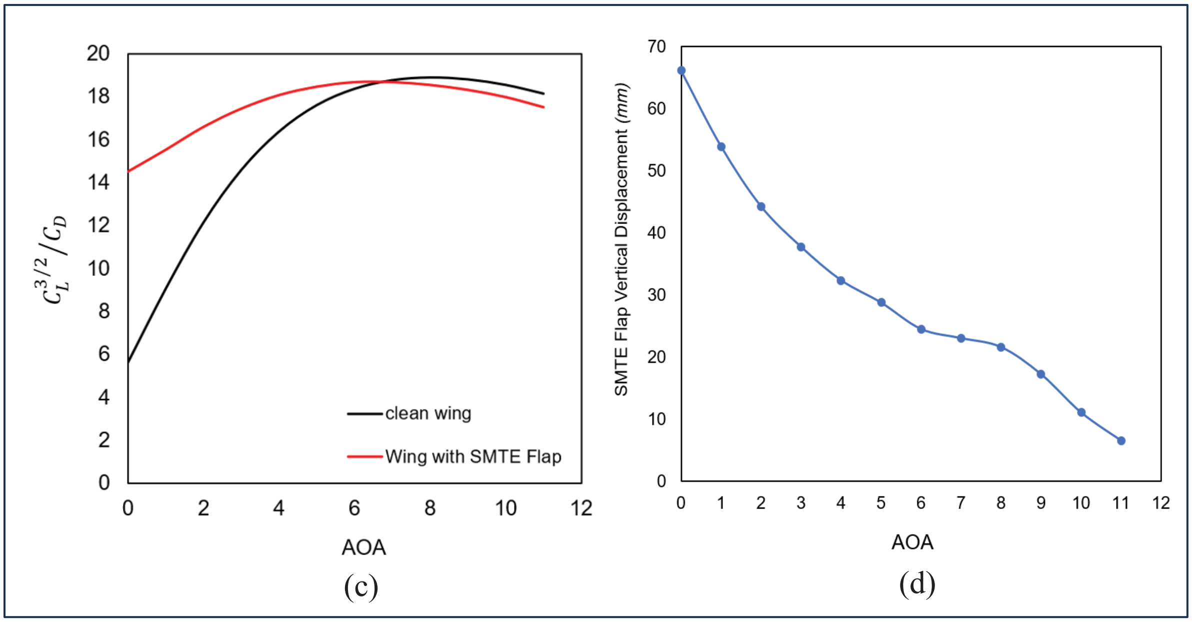

(c) (d)

Figure 4.15 Performance of the wing with an SMTE flap versus clean wing for different angles of attack; a) lift coefficient, b) drag coefficient, c) endurance efficiency, d) flap deflection magnitude

The optimum aerodynamic properties of an SMTE wing for maximum endurance are obtained for different angles of attack (Fig. 4.15). As shown in Fig. 4.15 (a and b), with flap deformation in the downwards direction, both lift and drag are increased; however, the increase in lift is more than that of the drag increase, and considering the endurance efficiency, $C_L^{3/2}/C_D$, the influence of lift is higher than that of drag; therefore, the final aerodynamic performance is improved compared to that of the clean wing. However, the endurance efficiency diagram (Fig. 4.15-c) shows that the morphing configuration loses its performance as the angle of attack increases up to the AOA= 7°, after which the performance of both wings becomes the same, and past this angle, the clean wing performs better than the wing with an SMTE flap. In other words, after AOA=7°, there should not be any flap deflection, since after AOA=7°, the retracted wing has its optimum endurance configuration. It should also be noted that since this is a cruise flight condition, smaller angles of attack are considered, and it is obvious that the maximum endurance occurs at the AOA=0, where it is 61.2% higher compared to the clean wing with retracted flaps. According to UAS-S45 manual, the cruise angle is almost 2 degrees, for which the endurance is increased by 26.78% with an SMTE flap (Fig. 4.15-c).

In the same way as range, in the endurance, the deformation of the SMTE flap also approaches zero deflection as the angle of attack increases (Fig. 4.15-d).

In addition, the spanwise pressure coefficient also shows a smooth variation trend near the SMTE flap, as shown in Fig. 4.16. At the AOA=11°, there is nearly no variation in the pressure coefficient, on both wings' upper and lower surfaces, thus indicating that the morphing wing performs like the baseline wing in terms of aerodynamic forces.

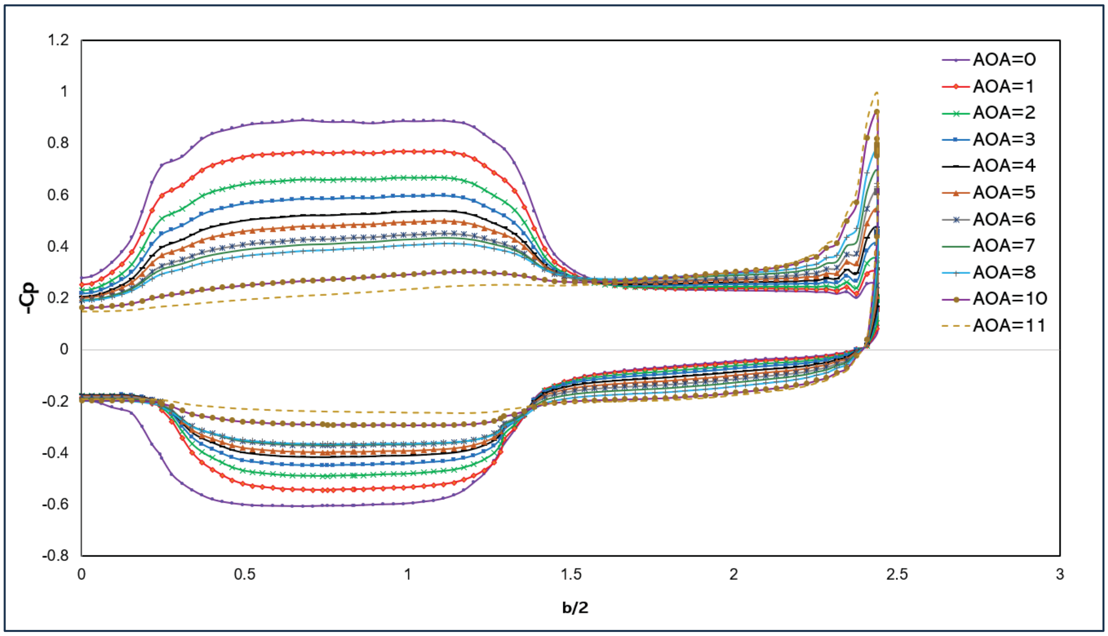

Figure 4.16 Spanwise pressure coefficient for the S-45 wing with SMTE flap

4.3.3 Gliding descent

The last flight condition studied in this paper is the non-powered gliding descent. In a space shuttle, non-powered or gliding descent is a normal flight condition, with no engine power involved in the whole distance from the orbit to the landing lane; a good equilibrium of the lift, drag and weight is used for landing the shuttle without any need for propulsive forces. Sailplanes are another example of gliding descent. Nonetheless, non-powered descent is not a normal flight condition for most aircraft, and it most often only occurs because of engine failure which calls for emergency measures. In this critical situation, the pilot's highest priority is to have more time to prepare for an emergency landing or to restart the engine; therefore, reducing the descent rate is the only option for extending the descent time.

In gliding descent, only the aerodynamic forces will guarantee the safety of the aircraft; therefore, establishing a suitable equilibrium among these forces is decisive. The only forces acting on the aircraft in the gliding descent are the lift, drag and weight, where the latter is almost non-variable (if overlooking the fuel weight), and only the lift and drag forces remain as crucial aerodynamic forces. This means that by choosing the optimum angle of attack and angle of deflection for the aircraft, the descent time can be extended, or in other words, the descent rate can be decreased as much as possible. In the same way as for the climb condition, in gliding descent, the small angle assumption is considered (angles between $-5°$ and $-15°$); however, since this is a descent condition, only the negative values in this range are considered. Figure 4.17 shows the UAS-S45 in gliding descent condition with the aerodynamic forces acting on it.

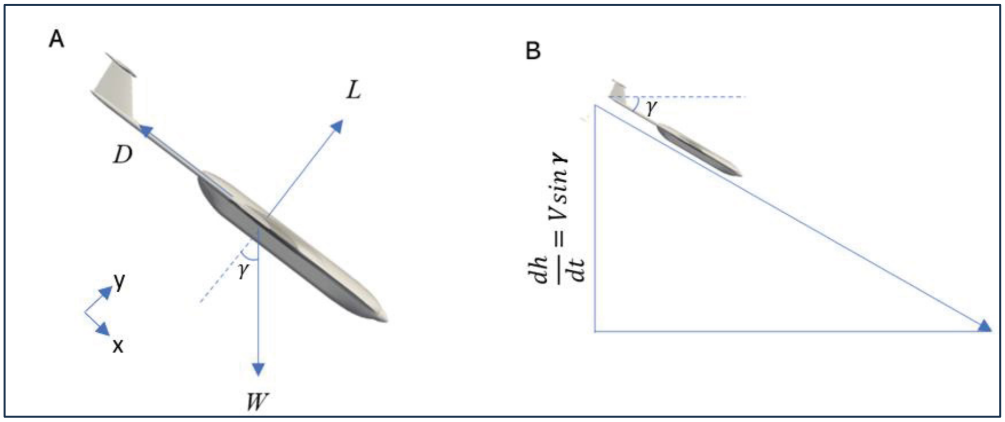

Figure 4.17 UAS-S45 in descent flight conditions with its aerodynamic forces (A) and descent trajectory (B)

The equilibrium of aerodynamic forces along the trajectory reflects the relationship between drag and weight (Eq. 21), and in the perpendicular direction, given the small angle assumption ($\cos\boldsymbol{\gamma} \approx 1$), we have $L = W$.

$$-D + W sin\gamma \ = 0 \tag{4.21}$$

By replacing W with L and multiplying all terms by velocity, the following equation is obtained.

$$V sin\gamma = \frac{DV}{L}$$

or

$$\frac{dh}{dt} = V\frac{C_D}{C_L} \tag{4.22}$$

Using the small angle assumption, the velocity becomes:

$$V = \sqrt{\frac{2W}{\rho S C_L}} \tag{4.23}$$

Finally, by replacing Eq. (4.23) in Eq. (4.22), the ultimate equation for the descent rate becomes:

$$\frac{dh}{dt} = \sqrt{\frac{2W}{\rho S}}\,\frac{C_D}{C_L^{3/2}} \tag{4.24}$$

Eq. (4.24) indicates that by minimizing the aerodynamic term $C_D/C_L^{3/2}$, which is the objective function, the descent rate is decreased; therefore, the objective function is defined as the minimization of $C_D/C_L^{3/2}$.

The values of $C_D/C_L^{3/2}$ are studied for a number of four different angles of descent, from $-5°$ to $-8°$ (all are within the small angle assumption range) to find the best angle of descent as well as the best angle of deflection for the SMTE flap versus the clean wing. Figure 18 shows the optimization results of the UAS-S45 wing with an SMTE flap, where the objective function ($C_D/C_L^{3/2}$) is minimized for different angles of attack.

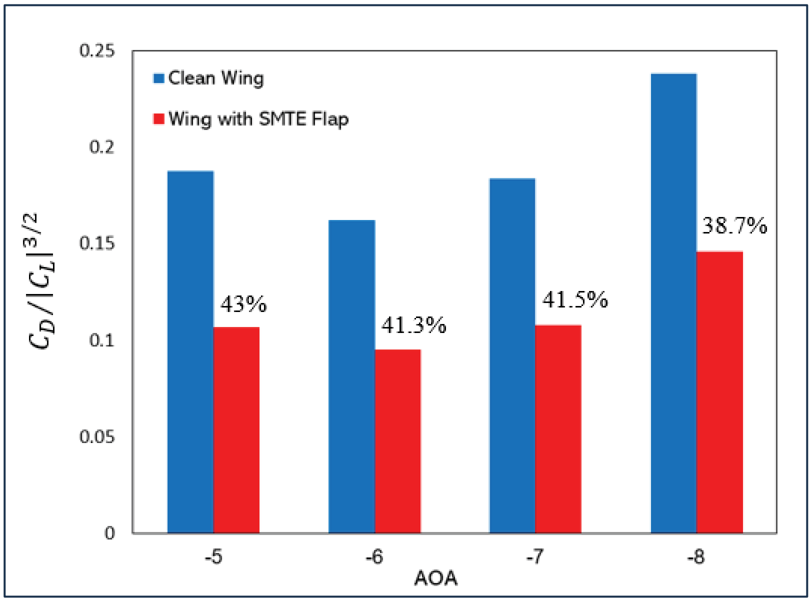

Figure 4.18 Comparison of the descent rate between a clean wing and a wing with an SMTE flap

As illustrated in Fig. 4.18, for all angles of attack the morphing flap deformation has minimized the descent rate compared to a wing with no flap. Evaluating the reduction of the rates of descent, the maximum reduction belongs to $\gamma = -5°$, with its 43% reduction in the descent rate, which is nearly half the normal descent rate. However, the minimum descent rate belongs to $\gamma = -6°$, where $C_D/\left|C_L^{3/2}\right| = 0.1$, meaning that, although the maximum minimization occurs at $\gamma = -5°$ (43%), it is not the minimum descent rate among the studied angles of attack ($C_D/\left|C_L^{3/2}\right| = 1.1$). Therefore, $\gamma = -6°$ is chosen as the optimum angle of descent, at which the minimum descent rate occurs. It can be deduced that by an optimum deformation of the SMTE flap in the gliding descent condition, an efficient equilibrium of aerodynamic forces is produced to reduce the descent rate as much as possible. Note that since the lift coefficient in descent is negative, the absolute value of the lift is used in Fig. 18. Unlike the previous flight conditions, e.g., climb and cruise, where the optimum deformation of the SMTE flap was in the downwards direction, in descending flight, due to the negative angle of descent, the optimal deformation of the flap is oriented in the upwards direction, and as the descent angle increases, the deformation also increases in the upwards direction (Fig. 4.19). Note that for better illustration, the absolute value of lift coefficient is represented, since in descent flight the generated lift is always negative.

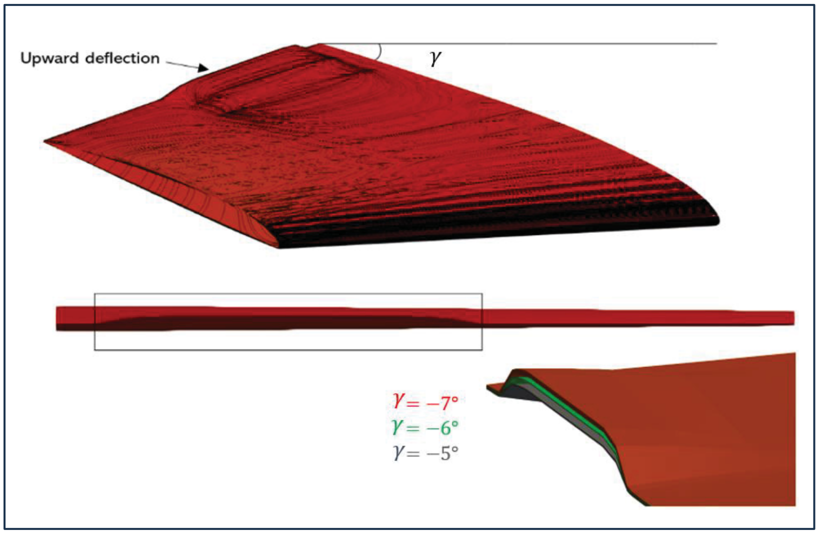

Figure 4.19 Optimum configuration of a UAS-S45 wing equipped with an SMTE flap for gliding descent flight

In addition, Figure 4.20 shows the pressure coefficient variations around a wing with an SMTE flap and for a clean wing at $\gamma = -7°$. The pressure coefficient variations indicate a pressure gap, through which the magnitude of negative lift force increases and since the variation of drag due to flap deflection is not high, the ultimate objective function, which is $C_D/C_L^{3/2}$, is decreased, thus accomplishing the goal of reducing the gliding descent rate.

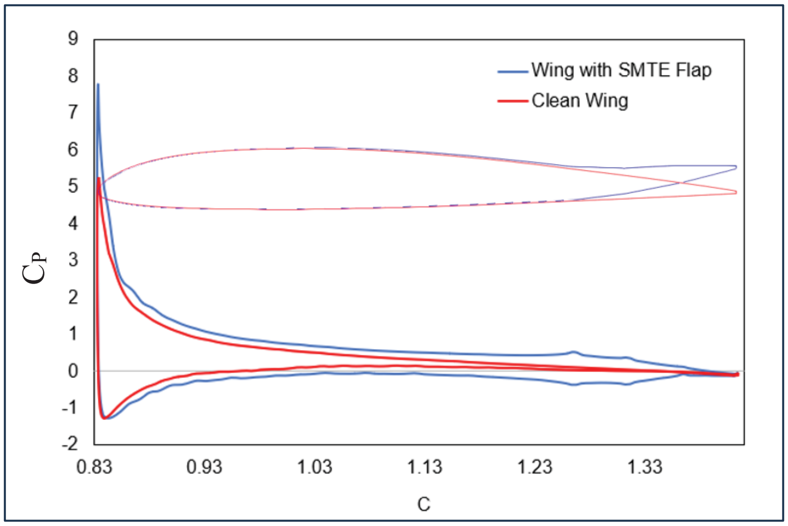

Figure 4.20 Pressure coefficient variations around a wing with an SMTE flap and around a clean wing at $\gamma = = -7°$

4.4 Conclusion

This study investigated the seamless morphing trailing edge flap (SMTE flap) for the whole flight envelope of a UAS-S45, including climb, cruise, and gliding descent, each of which have their unique specific flight characteristics. The main objective of this study was to find the optimum configuration of the SMTE flap for these three flight conditions with their corresponding objective functions and goals.

For the climb condition, the goal was to find an optimum configuration to increase the climb rate compared to that of the clean wing configuration, and this goal was accomplished by decreasing the required engine power to its minimum rate. The results showed that by decreasing the required power to a minimum rate by up to 3.8%, the climb rate could increase by 6.13 %.

The cruise flight condition had two objectives, range, and endurance improvement, depending on the flight mission objective. The goal was to increase both the range and endurance, and to find the optimum SMTE flap configuration for each of them. Regarding the range improvement, the SMTE flap was compared with the hinged flap configuration in terms of aerodynamic performance, and it was shown the SMTE flap out-performed the hinged flap in many aspects. These aspects included extending laminar flow on wing upper surface, improving the flow stability by restricting its turbulence behavior, and improving the aerodynamic performance by generating excessive lift by sealing the gaps in the transition sections, increasing the lift-to-drag ratio by up to 17.8% compared to the hinged flap, and by up to 33% compared to the clean wing configuration. Finally, the optimum angle of attack was determined for achieving maximum range. In the next step, the optimum configuration and angle of attack were found for maximizing the endurance; therefore, a 61.2% gain was achieved for endurance of the SMTE flap compared to that of the clean wing configuration.

In the final section, the gliding descent phase was studied with the purpose of reducing the descent rate by using an SMTE flap. Unlike the other flight conditions, where the optimum configuration of the flap was oriented in the downwards direction during the gliding descent, the optimum SMTE flap was deflected upwards, which minimized the descending rate for a number of four negative angles of descent. The maximum reduction of descent rate compared to baseline wing was up to 43% for $\gamma = -5°$, however, the minimum magnitude of the descent rate was achieved for $\gamma = -6°$, which was chosen as the optimum angle of attack for gliding descent.

This study showed the advantages of using SMTE flaps instead of conventional hinged flaps and found the optimum SMTE flap configuration for three flight phases of an UAS-S45, by which the aircraft could achieve its highest flight performance. In this study, only three main flight conditions are considered, while other phases such as cruise climb, loiter, and cruise descent will be presented in further studies. In addition, this study has considered only the aerodynamic aspects of the SMTE flap and other aspects such as actuation mechanism, structural weight and actuation control will be analyzed and presented in the future paper. For morphing aircraft, aerodynamics, structure, and control disciplines are coupled; therefore, in our next study, the structural and control aspects of an SMTE flap will be investigated by proposing a novel trailing edge actuation mechanism to analyze its structural feasibility and sustainability by utilizing the target optimized shapes of the SMTE flap obtained from this study. In addition, structural optimization will be performed in terms of structural weight minimization.

CHAPTER 5

STRUCTURAL AND TOPOLOGICAL OPTIMIZATION OF A NOVEL ELEPHANT TRUNK MECHANISM FOR MORPHING WING APPLICATIONS

Mir Hossein Negahban[1], Alexandre Hallonet[3], Marie Noupoussi Woumeni[4], Constance Nguyen, Ruxandra Mihaela Botez[5]

[1, 2, 3, 4,5] LARCASE Laboratory of Applied Research in Active Controls, Avionics and Aeroservoelasticity, Department of System Engineering, École de Technologie Supérieure, 1100 Notre-Dame West, Montréal, Québec, Canada H3C 1K3

Paper published in Aerospace Journal, 28 April 2025
DOI: https://doi.org/10.3390/aerospace12050381

Résumé

Un nouveau mécanisme de morphing sans couture des volets de bord de fuite est présenté dans cet article. Ce concept de morphing bio-inspiré est dérivé de la trompe d'un éléphant et est appelé mécanisme de trompe d'éléphant (ETM). La flexibilité structurelle de la trompe d'un éléphant et sa capacité à effectuer divers types de déformations en font un choix prometteur dans la technologie de morphing pour augmenter les performances de déformation continue et douce vers le bas au niveau d'un bord de fuite. Ce mécanisme se compose d'un certain nombre d'éléments en forme de dents attachés à un caisson d'aile solide ; les contractions de ces éléments en forme de dents par des forces d'actionnement externes modifient la forme du bord de fuite vers le bas. Les principales forces d'actionnement sont appliquées par l'intermédiaire de câbles métalliques passant à travers des éléments en forme de dents pour générer les contractions souhaitées sur les dents flexibles. Une analyse structurelle statique utilisant la méthode des éléments finis (FEM) est effectuée pour examiner ce nouveau concept de morphing et assurer sa faisabilité structurelle et sa stabilité. Une optimisation de la topologie est également effectuée pour trouver la configuration optimale dans le but de réduire le poids structurel. Le mécanisme optimisé est ensuite fixé à la section de volet d'une aile UAS-S45. Enfin, une analyse de la peau est effectuée pour trouver le matériau de peau optimal, qui correspond aux exigences du volet morphing. Les résultats de l'analyse structurelle et de l'optimisation de la topologie révèlent la fiabilité et la stabilité du mécanisme proposé pour une application dans le volet SMTE (Seamless Morphing Trailing Edge). Les résultats de l'optimisation ont conduit à des améliorations significatives des paramètres structurels, en plus de la réduction de poids souhaitée. Le déplacement vertical maximal ETM a augmenté de 8,6 %, tandis que la contrainte de von Mises a diminué de 10,43 %. De plus, le facteur de sécurité est passé de 1,3 à 1,5, indiquant ainsi une conception plus sûre. La masse de la structure a été réduite de 35,5 %, atteignant l'objectif principal de l'optimisation de la topologie.

Abstract

A novel mechanism for seamless morphing trailing edge flaps is presented in this paper. This bio- inspired morphing concept is derived from an elephant's trunk and is called the Elephant Trunk Mechanism (ETM). The structural flexibility of an elephant's trunk and its ability to perform various types of deformations makes it a promising choice in morphing technology for increasing the performance of continuous and smooth downward bending deformation at a trailing edge. This mechanism consists of a number of tooth-like elements attached to a solid wing box; the contractions of these tooth-like elements by external actuation forces change the trailing edge shape in the downwards direction. The main actuation forces are applied through wire ropes passing through tooth-like elements to generate the desired contractions on the flexible teeth. A static structural analysis using the Finite Element Method (FEM) is performed to examine this novel morphing concept and ensure its structural feasibility and stability. Topology optimization is also performed to find the optimum configuration with the objective of reducing the structural weight. The optimized mechanism is then attached to the flap section of an UAS-S45 wing. Finally, a skin analysis is performed to find its optimum skin material, which corresponds to the requirements of the morphing flap. The results of structural analysis

and topology optimization reveal the reliability and stability of the proposed mechanism for application in Seamless Morphing Trailing Edge (SMTE) flap. The optimization results led to significant improvements in the structural parameters, in addition to the desired weight reduction. The ETM maximum vertical displacement increased by 8.6%, while the von Mises stress decreased by 10.43%. Furthermore, the factor of safety improved from 1.3 to 1.5, thus indicating a safer design. The mass of the structure was reduced by 35.5%, achieving the primary goal of the topology optimization.

5.1 Introduction

Aerodynamic studies have shown that morphing wing technology (Ameduri & Concilio, 2023) was widely believed to be one of the ways to meet the goals of green aviation (Mrazova, 2014) by improving aircraft aerodynamic performance, in particular fuel consumption reduction, which directly leads to lower Carbon emissions. Morphing wing technology is a promising candidate for next-generation aircraft due to its numerous advantages. While the current hinged flaps used in the existing fleet have demonstrated reliable performance over the past decades, they have introduced discontinuities on the wing surface, that lead to several flight performance issues. These include increased turbulence, reduced functionality in hazardous climates, and increased drag due to the discontinuities on the wing body.

This innovative technology eliminates all discontinuities from the wing surface by integrating the main wing body with the flap sections, resulting in significant improvements in aerodynamic efficiency, fuel consumption reduction, and overall flight performance. This paper presents unique design challenges, particularly in developing the internal actuation mechanisms for morphing wings, which have been a focal point of research in recent decades. Over the last decade, several collaborative projects aimed at testing different morphing approaches have been launched. The DARPA/AFRL/NASA Smart Wing program, overseen by Northrop Grumman Corporation (NGC) as part of the DARPA Smart Materials and Structures initiative (Bartley-Cho et al., 2004), Flexsys and the US Air Force Research

Laboratory (Kota et al., 2009b), the CRIAQ MDO-505, a Canadian-Italian collaborative project (R. M. Botez et al., 2018), and Clean Sky 2 (Ameduri et al., 2018b) in Europe are some of these projects that have brought morphing technology up to the test level. This level of study requires researchers work in multiple disciplines, including aerodynamics, structure, and control.

Structural analysis concerns both the internal actuation mechanism and the external wing skin design, both of which are complimentary in the structural design. This phase of the design must comply with the aerodynamic design; any compromise in this phase could deteriorate the final wing design. Therefore, structural design, whether actuation design or skin design, should be treated meticulously. While a high number of morphing actuation designs have been proposed and then developed; however, most of these conceptual designs lack the desired feasibility at a practical level. Among various morphing designs, such as winglet (Eguea, Bravo-Mosquera, & Catalano, 2021; Liauzun et al., 2018), span (Ajaj et al., 2012), twist (Ismail et al., 2014), or leading-edge morphing (Fereidooni et al., 2021; Zi et al., 2020), trailing-edge morphing has demonstrated outstanding results over the past decades. Consequently, most research in mechanism design has concentrated on developing morphing trailing-edge mechanisms, while it needs to be tested in wind tunnel due to its promising advantages in the aircraft performance improvement. The research in morphing trailing edge actuation design has been also productive(Arena, Concilio, & Pecora, 2019; Concilio et al., 2016; Dimino, Flauto, Diodati, et al., 2014).

The Fishbone Active Camber (FishBAC) was an airfoil morphing structure presented by Woods et al. (Woods & Friswell, 2012) in 2012. Utilizing a compliant structure derived from biological inspiration, the FishBAC introduced significant, improvements in the aerodynamic qualities of an airfoil camber. The framework consisted of a thin, chordwise-bending beam spine connected to a pre-tensioned Elastomeric Matrix Composite (EMC) skin surface using stringers. Thus, several possible morphing configurations were presented. In their later study (Woods, Bilgen, & Friswell, 2014), Woods et al. compared the FishBAC structure to a conventional flap during wind tunnel tests, and they found that using the FishBAC, a significant drag reduction was obtained in the proposed morphing wing compared to the baseline configuration, while the lift remained the same. The Variable Camber Trailing Edge (VCTE), developed by Shi et al. (Shi et al., 2023), was another design for a morphing trailing edge. Based on a multi-block rotating rib, it consisted of three morphing blocks and one fixed block, hinged together; the actuation of any block was followed by the movements of other blocks. Their results showed a continuous and smooth deformation, ranging from 5° upwards to 15° downwards without damaging structural integrity. Cheng et al. (Cheng et al., 2023) proposed and developed a seamless morphing trailing edge with chord-wise camber variations, and a good capacity for load bearing. Finite Elements numerical simulations and experimental tests demonstrated that their proposed mechanism sustained the aerodynamic loads of 0.015 MPa and achieved deflections of 15° both upwards and downwards.

Within the European SARISTU project, an innovative actuation system for morphing trailing edges was developed by Dimino et al. (Dimino, Flauto, Diodati, & Pecora, 2014). They have modeled and analyzed a morphing actuation system composed of servo rotary actuators with the design objectives of supporting aerodynamic pressure loads and actuation forces. Their internal mechanism with a flexible outer skin was subjected to numerical, analytical, and experimental validations. In addition to its higher accuracy, the mechanism could significantly save weight and actuation power and withstand aerodynamic forces. A belt-rib morphing variable camber concept was developed at the German Aerospace Center (DLR) by Campanile and Sachau (Campanile & Sachau, 2000). This concept has been considered as one of the most successful designs for morphing wings, mainly due to its reliable structure and light weight. Its distributed flexibility allowed for a range of shape deformations. Through experimental tests on different prototypes, its stiffness properties were evaluated and then was followed by weight optimization. Another morphing trailing edge concept was also introduced at the DLR (Sinapius et al., 2014), called "Finger concept". In this concept, a flexible rib design combined from separate plate-like elements with revolute joints could generate arc-like deformation. A transmission beam was used to arrange the ribs, and five ribs were actuated with two actuators, leading to a reduced number of actuators. A smart-actuated trailing edge via smart materials was investigated by Wang et al. (Wang, Xu, & Zhu, 2013). Their mechanism could perform upward and downward deflections by using SMA wires. A control system was developed to assess the mechanism's accuracy; it indicated that this approach yielded accurate and stable results, with its maximum error less than 4%. However, the actuation response time reached 6.7sec. Wu et al. (Wu et al., 2017) introduced another innovative morphing concept featuring an active trailing edge, utilizing an internal compliant composite truss. They used an electric actuation system with Linear Ultrasonic Motors (LUSM) with the capability of performing multiple degrees of freedom. Dumont (Dumont, 2018) introduced an alternative trailing edge morphing concept, proposing a system with two flexible surfaces positioned at the upper and lower sides of the wing, each of them equipped with three internal rotational motors. The rotational motion of motors was transferred to the bending of the flexible surfaces in a very smooth manner. A specified degree of rotation was translated as a certain degree of bending both in the upwards and downwards directions by preserving surface tangency and smoothness. Bing Li and Gang Li (Li & Li, 2016) proposed a camber morphing wing model that could perform continuous camber morphing. Their proposed mechanism consisted of a planar linkage, in which the connection of the linkages was found through optimization. An aerodynamic study was performed to measure the airfoil's performance after its optimization; finally, a higher lift-to-drag ratio was achieved after optimization. In an experimental study, Nguyen et al. (Nguyen et al., 2014) investigated the performance of Variable Camber Continuous Trailing Edge Flaps (VCCTEF). Their design consisted of multi-segment flaps. To cover the gaps between spanwise flaps, they have used an elastomeric material. The elastic flap had three hinged sections; a combination of SMA and electric actuators was utilized to bend the overall flap using the rotation of interior rods. A structural analysis of the morphing trailing edge flap was conducted by Matteo et al. (Di Matteo & Guo, 2011) for a large aircraft wing. The actuation system selected to deflect the trailing edge (TE) flap structure was an Eccentric Beam Actuation Mechanism (EBAM), originally developed in the 1970s as part of the DARPA project. They performed a stress analysis to analyze the flap's structural motion during actuation, and to evaluate its integrity during its trailing edge deflection. Their findings revealed that, under internal actuation and external aerodynamic loads, both composite and metallic skin configurations successfully achieved the desired deflected shapes while meeting their strength constraints.

An Adaptive Trailing Edge Device (ATED) with rotatory segmented ribs was designed by Pecora et al. (Pecora, Dimino, et al., 2016). The structural analysis based on advanced FE analyses was performed, revealing that the proposed mechanism was reliable in terms of stress and maximum load conditions, as well as elastic stability. A novel concept of variable camber morphing leading and trailing edge sections was introduced by Takahashi et al. (Takahashi, Yokozeki, & Hirano, 2016). A prototype was manufactured, and both Finite Element structural analysis and an aerodynamic analysis were performed. The deformation of the leading and trailing edges was achieved by the corrugated structure embedded within the lower and upper surface of the wing; the deformation was induced on the corrugated structure by a wire connected to a servomotor. Finally, wind tunnel tests on the manufactured morphing wing prototype were performed, and a successful actuation at the speed of 20 m/s airflow was achieved. Barbarino et al. (Barbarino, Dettmer, & Friswell, 2010) proposed an innovative flap architecture for a variable camber trailing edges based on the variable geometry truss concept. The compliant rib was based on a truss-like structure, on which some of its parts were “active” rods made of shape memory alloys (SMA). These actuators were able to sustain the external loads while allowing controlled shape modification. An optimization process based on a genetic algorithm was established to optimize the topology of the internal truss structure. In a joint project called the Adaptive Compliant Trailing Edge (ACTE), conducted by the U.S. Air Force Research Laboratory (AFRL), NASA, and FlexSys Inc. (Kota, Flick, & Collier, 2016; Kota et al., 2009b), a series of flight tests were conducted on a Gulfstream GIII business jet with variable geometry multifunctional control surfaces, with the purpose of eliminating the trailing edge flaps. The test flight was conducted up to Mach = 0.75 and maximum altitude of 40,000 ft. In this design, the control surface was bounded with left and right transition sections, which eliminated all discontinuities on the wing body. The main purpose of the flight tests was to demonstrate the robustness and feasibility of the FlexFoil material; they confirmed that the ACTE was structurally feasible and could perfectly sustain the maximum design loads of commercial aircraft for over 50 hours of flight tests without any failure.

A morphing airfoil concept applicable to high lift devices such as flaps, ailerons(Negahban, Bashir, Priolet, & Botez, 2024), elevators, and rudders, was proposed by Du and Ang (Du & Ang, 2012). They have compared airfoils with a hinged flap with morphing airfoils with the aim to determine the influence of a morphing airfoil on the aerodynamic efficiency, and the flight dynamics of an airplane. In an attempt to passively eliminate discontinuities on the wing trailing edge flap, Khorami et al. (Khorrami et al., 2014) from NASA Langley Research Center patented the elastic deformable structure for the side edges of the trailing edge flap. This elastic structure was designed to minimize the aeroacoustic noise caused by discontinuities in the side edge gaps while maintaining the aircraft's cruise efficiency. This novel configuration could elongate in the chord-wise direction, bend, and twist, and when it was not deployed, it seamlessly conformed to the chordwise cross-section of the flap's side edge. Woods et al. (Woods et al., 2016) presented a compliant morphing flap transition to address the side-edge gaps in the spanwise direction. Their proposed concept design ensured that the gaps were sealed, and that the transition between the rigid wing and the morphing flap was smooth.

In the present study, a novel bio-inspired morphing trailing edge mechanism is introduced, called the “Elephant Trunk Mechanism (ETM). As indicated by its name, it is inspired by an elephant’s trunk, which has a very good bending flexibility. This type of deformation is analyzed with the objective of applying it to the trailing edge mechanism of the Seamless Morphing Trailing Edge (SMTE) flap, on which an aerodynamic optimization study was performed in a previous work (Negahban, Bashir, Traisnel, & Botez, 2024). Fewer movable parts contribute to the ETM unique design, making it simpler and lighter compared to other designs presented in the literature. Based on the results obtained in previous work , expressed in terms of geometric constraints and deformation range, in this study, the proposed mechanism is submitted to a complex structural analysis based on the Finite Element Method (FEM) with the aim of ensuring its robustness and functionality. To the authors' knowledge, the designs introduced in the literature may lack an optimization phase for further weight reduction. However, this study demonstrates that performing topology optimization in the final phase not only reduces unnecessary structural weight, but it also enhances the design from a structural perspective, particularly by increasing the factor of safety. Finally, once the ETM optimum configuration was found, the mechanism was installed on a UAS-S45 wing, and a skin analysis was conducted on the wing to identify a suitable skin material in terms of flexibility and stiffness. The UAS-S45 is a twin-engine tactical unmanned aircraft system with a range of 120 km, an operating ceiling of 17000 feet and 12 hours of autonomy; it is mainly used for surveillance, reconnaissance (See Appendix I for additional detail). Several studies have been conducted on the UAS-S45 at LARCASE in morphing wing technology (Communier, Botez, & Wong, 2020; Negahban, Bashir, & Botez, 2022; Mir Hossein Negahban, Musavir Bashir, & Ruxandra M Botez, 2023; Mir Hossein Negahban, Musavir Bashir, & Ruxandra Mihaela Botez, 2023); most of these studies were performed around aerodynamic optimization. However, in this study, the main purpose is to structurally evaluate the viability of the mechanism and its advantages.

5.2 Materials and Methods

5.2.1 Elephant Trunk Mechanism (ETM)

The motion of biological muscle hydrostats, such as octopus arms, squid tentacles, and elephant trunks, is remarkably versatile (Smith & Kier, 1989). Their lack of a skeletal structure, and a combination of muscle and soft tissue make them extremely complex. The biomechanics of their motions are based on the fundamental principle of volume conservation. For instance, a squid tentacle elongates when contraction occurs in transversely orientated muscle fibers (Liang, McMeeking, & Evans, 2006). Several industrial applications of the elephant trunk mechanism were analyzed, one of which is the elephant trunk robot used as a gripping mechanism(Yang et al., 2006), where its flexible rotational and bending motions were applied using a computer-controlled actuation system.

As an application in the aerospace industry, the bio-inspired Elephant Trunk Mechanism (ETM) is introduced in this paper for an application in morphing wing technology, utilizing the bending flexibility of the trunk in the morphing of a trailing edge, a complementary actuation mechanism for a Seamless Morphing Trailing Edge (SMTE) flap (Negahban, Bashir, Traisnel, & Botez, 2024). Figure 5.1 shows a CT scan of an elephant trunk mechanism in detail, clearly depicting its high degrees of freedom. Although contractions of the tooth-like muscles on the trunk facilitate its bending in every direction, in a trailing edge, it is important to mention that teeth contraction are limited to one side (the lower side of the trailing edge) to generate downward deformations. The initial inspired actuation mechanism is illustrated in Figure 5.2 with its geometric details.

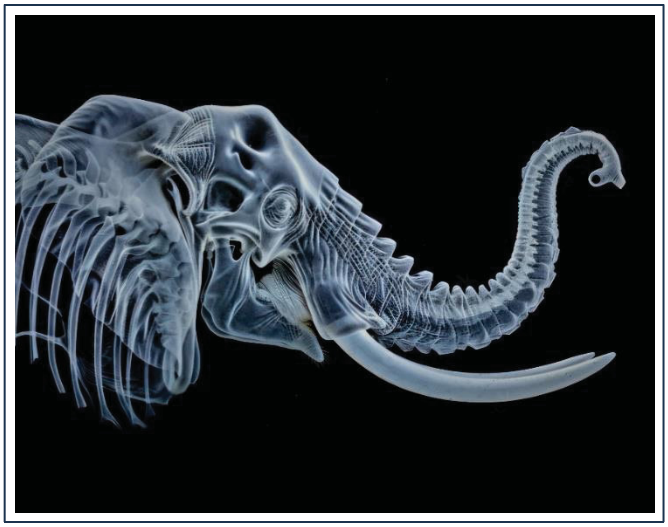

Figure 5.1 CT scan of an elephant's trunk mechanism (https://stock.adobe.com)

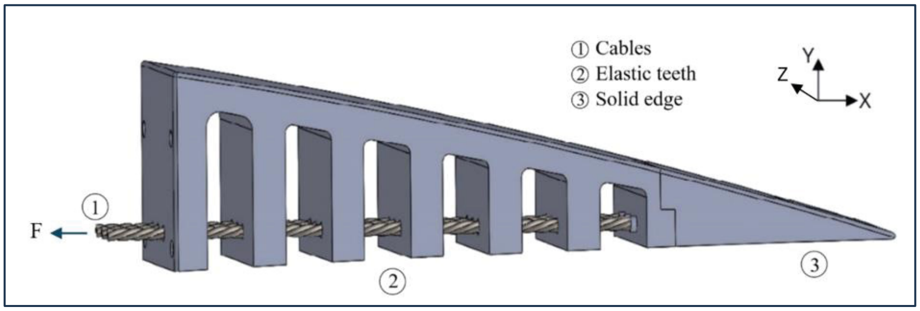

Figure 5.2 The bio-inspired elephant trunk mechanism for morphing trailing edge actuation

As shown in Figure 5.2, the proposed Elephant Trunk mechanism for a morphing trailing edge mimics the tooth-like structure of the actual elephant trunk, whose contraction generates the desired deformation in the trailing edge. Three major parts are differentiated in the structure in terms of material and elasticity: 1-cables, 2-elastic tooth-like part, 3-the solid edge part. The main part, where the deformation occurs, is the elastic tooth-like structure, whose contraction generates the desired deformation. It is screwed to the wing box from the one side, and to the solid edge part from the other side. Unlike an actual elephant's trunk, where the deformation occurs due to the contraction and expansion of muscles, in the proposed structure, the contraction of the teeth is obtained through tensile forces exerted on the cables. This preliminary system utilizes 3mm diameter cables that pass through the structure's teeth. Upon the exertion of the force to the cables in the negative *x*-direction (Figure 2), the tooth-like elements contract towards the direction of the applied force, causing the bending of the structure, and hence of the trailing edge of the wing. Using three cables in this mechanism facilitates the mechanical loads by distributing the total force equally among the three cables.

5.2.2 Aerodynamic Characteristics of the SMTE flap

The aerodynamic aspects of the SMTE flap were analyzed in a previous study (Negahban, Bashir, Traisnel, & Botez, 2024), where key characteristics such as aerodynamic efficiency, pressure distribution, and vorticity around the SMTE flap were analyzed. The entire flight envelope for the UAS-S45, including climb, cruise, and descent phases were considered. The optimal aerodynamic configuration of the SMTE flap was found for each flight condition. Additionally, a comparison was made between the SMTE flap and conventional hinged flaps aerodynamic performance.

The aerodynamic study covered entire flight envelope including climb, cruise, and gliding descent conditions. The following results were obtained from the aerodynamic study:

In the climb regime, the optimized SMTE flap achieved a 6.13% increase in climb rate and a 3.8% reduction in required engine power compared to the clean wing. In the cruise regime, the aerodynamic efficiency improved by 33% over the clean wing and 17.8% over a hinged flap due to smoother pressure distribution and extended laminar flow. Finally, in the gliding descent regime, the SMTE flap reduced the descent rate by up to 43%, enabling safer emergency glide paths. The comparison of the SMTE flap with a conventional hinged flap clearly demonstrated the aerodynamic advantage of the seamless design, primarily due to the elimination of flap side-edge gaps, which led to smoother pressure gradients, reduced drag, and enhanced lift generation (See (Negahban, Bashir, Traisnel, & Botez, 2024) for more detail).

The current study focuses on the actuation mechanism of the SMTE flap based on previous study findings that are utilized to define the aerodynamic and structural characteristics of the SMTE flap. For example, the proposed Elephant Trunk Mechanism (ETM) must adhere to certain requirements derived from the aerodynamic analysis. The first requirement involves geometrical constraints, ensuring that the SMTE flap dimensions in the current study match those used in the aerodynamic study. The second requirement refers to the maximum vertical deflection of the SMTE flap, to be achieved by the ETM. Additionally, achieving the desired vertical deflection must satisfy structural criteria, such as the factor of safety, mechanism stiffness, material selection, and structural weight. The aerodynamic loads acting on the wings' trailing edge, containing the SMTE flap, were incorporated in the material selection and adjusting the actuation forces acting on the ETMs. Figure 5.3 illustrates the geometrical dimensions of the SMTE flap that the proposed actuation mechanism must comply with.

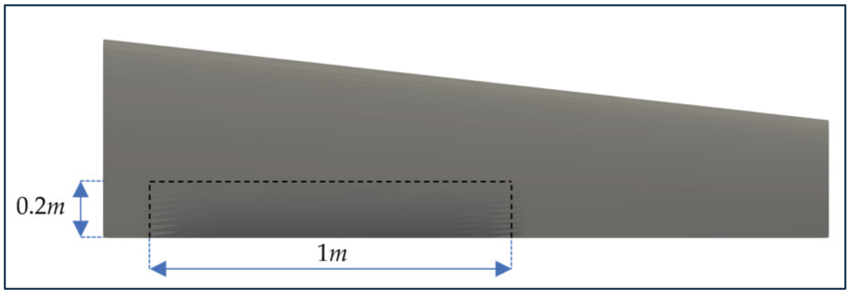

Figure 5.3 Geometrical dimensions of the SMTE flap on UAS-S45 wing in the aerodynamic study

Figure 5.3 depicts the dimensions of SMTE flap, that was used in aerodynamic study and will be also used in the present study. In Section 5.3.7, the orientation of the embedded ETMs will be discussed in detail. Regarding the second requirement, the maximum vertical displacement obtained from the aerodynamic study was found to be 66mm in the downward direction. Therefore, the proposed elephant trunk actuation mechanism should reach the maximum flap deflection of 66 *mm*.

5.2.3 Structural Analysis

A static structural analysis was performed in Altair using the FEM by considering the constraints and forces applied to the mechanism. Several model equations obtained using the fundamental principles of mechanics were considered during the analysis, including equilibrium, compatibility, and constitutive equations. Equilibrium equations ensure that the resultant of the forces and moments acting on the structure is zero. There are three equilibrium equations for forces and three equations for moments in the 3D Finite Element Analysis (FEM), each of which represents a direction in *xyz* coordinates. Given that a static analysis is performed, the corresponding equilibrium equation is given by:

$$\mathrm{K} \cdot \mathrm{u} = \mathrm{F} \tag{5.1}$$

where K represent the stiffness of the structure in a square matrix, which is based on the chosen material, u is the vector of nodal displacements, and F denotes the external forces.

The compatibility equations ensure that the displacements of connected nodes are consistent with the deformations and rotations of the elements; therefore, the continuity of displacements is preserved. Finally, the constitutive equations are expressed under the form of Hooke's law for linear elastic materials and is written as follows.

$$\sigma = \mathrm{E} \cdot \varepsilon \tag{5.2}$$

where σ denotes the stress, E is Young's modulus, and ε is the strain.

5.2.4 Material selection

Material selection is the first and most important phase in the FEA. Since the trailing edge is free at one end, and is located at least at 30% of chord length, it can bend easily under the gravity force if is made of a heavy material. However, the aerodynamic forces are stronger on the trailing edge; therefore, it should be stiff enough to not bend by any arbitrary force. By considering these observations, the chosen material should be flexible enough to generate desired bending deformations, stiff enough to bear strong aerodynamic forces, and light enough to not bend under the gravity force. To address these criteria, the aerodynamic loads on the SMTE flap, obtained from a previous study (Negahban, Bashir, Traisnel, & Botez, 2024), are considered. Based on the aerodynamic forces' values, and the required deflection obtained from aerodynamic study, nylon was selected as material for the elastic part of the ETM, while aluminum was selected for the solid edge. It was ensured that the selected material remained undeformed under pure aerodynamic loading, and it achieve the required maximum deflection exclusively under the applied actuation force.

The nylon is a polymer known for its excellent mechanical properties, and hence adaptable for several applications, including those of structural components. In our study, nylon is suitable for elephant trunks structures due to its high tensile strength and flexibility. The tensile strength of a material measures the ultimate stress that the material can resist before break when is undergoing a tension or a compression. The nylon equally allows a good flexibility within elastic deformation. This material property is thus suitable for our study, given that the intended mechanism should deform repeatedly in its elastic range during flight. Additionally, nylon has a low friction coefficient, making it especially suitable for this application, as the cables slide within the tooth-like elements. Its light weight equally reduces the overall weight of the mechanism.

For the cables, wire ropes are chosen, are they are strong, flexible, and durable structures made of twisted metal wires within each other. They are commonly used in various applications, in which strength, flexibility and load-bearing capacities are required. The wire ropes used in this study are made from high carbon steel which has excellent material properties. Wire ropes are equally known for their high tensile strength in case of heavy loads. Despite their high strength, wire ropes remain flexible, allowing them to comply to various structural shapes. Table 5.1 shows the material properties of the materials chosen for each part of the mechanism.

Table 5.1 Material properties for the Elephant Trunk Mechanism (ETM)

Part	**Material**	**Young's modulus (MPa)**	**Poisson's ratio**	**Density (kg/m^3)**	**Yield strength (MPa)**
Elastic tooth-like part	Nylon	2960	0.41	1140	75
Solid edge	Aluminium	70,000	0.33	2700	40
Cables	High Carbon Steel	200,000	0.29	7870	375

5.2.5 Boundary conditions

The fixation of the ET rib to the wing box is done with screws on the first solid tooth, which restricts any motion on the first tooth. Three cables pass through the interface (interface of the wing box and the ET rib), they pass through the holes in the teeth all the way to the aluminium solid edge, where they are firmly fixed. Two configurations are set up for the Finite Element analysis of the cables. In the first analysis, the cables have a "sliding contact" with the teeth's holes, so that equal forces are applied to all teeth simultaneously. In the second configuration, the cables move freely within the holes and "no contact" is defined between them and the teeth. In the sliding configuration, both the hole and the cable diameters are 3mm, while in the no-contact configuration, the diameters of the holes are 4mm and the diameters of cables are 3mm. Figure 5.4 shows the boundary conditions for both configurations.

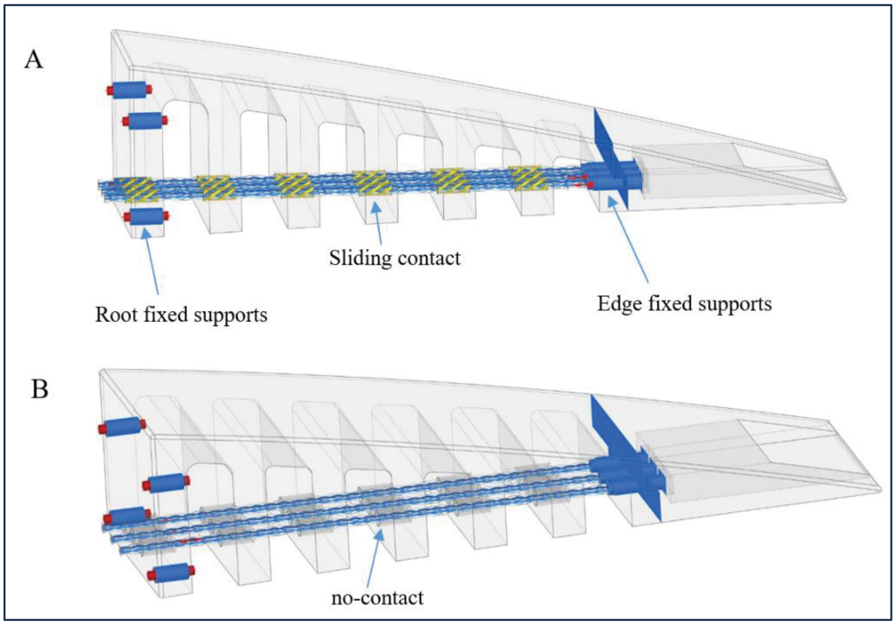

Figure 5.4 Illustration of boundary conditions for A) sliding contact, and B) no-contact between cables and holes

As shown in Figure 3, two fixed support are used for the boundary condition, the “root fixed supports” fix the first tooth (and the whole ET rib) to the wing box, while the “edge fixed supports” fix the elastic teeth to the solid edge part. These boundary conditions are the same for both sliding and no-contact configurations. However, the difference between the two configurations lies in the boundary condition between the cables and holes. The sliding contact and no-contact configurations are illustrated in yellow and gray colors, respectively (Figures 5.4-A and 5.4-B).

Once the fixation and interface contacts are determined, the final phase is the application of the desired forces. Each cable sustains a horizontal force of 250N in the negative x-direction; the total force of 750N is equally distributed among the three cables. The magnitude of the force was determined via our previous study (Negahban, Bashir, Traisnel, & Botez, 2024), where a maximum displacement of 66mm was found for SMTE flap. The effect of aerodynamic forces was incorporated into the calculation of the driving force, thus ensuring that the applied force was sufficiently high to overcome aerodynamic resistance. Note that, for any other deformation magnitude, the applied force could vary.

5.2.5.1 Sliding cable/hole configuration

By applying the force to the cables, the contours of structural parameters, including stress, strain, factor of safety, and displacement are presented in Figure 5.5, which also indicates the maximum value of each parameter.

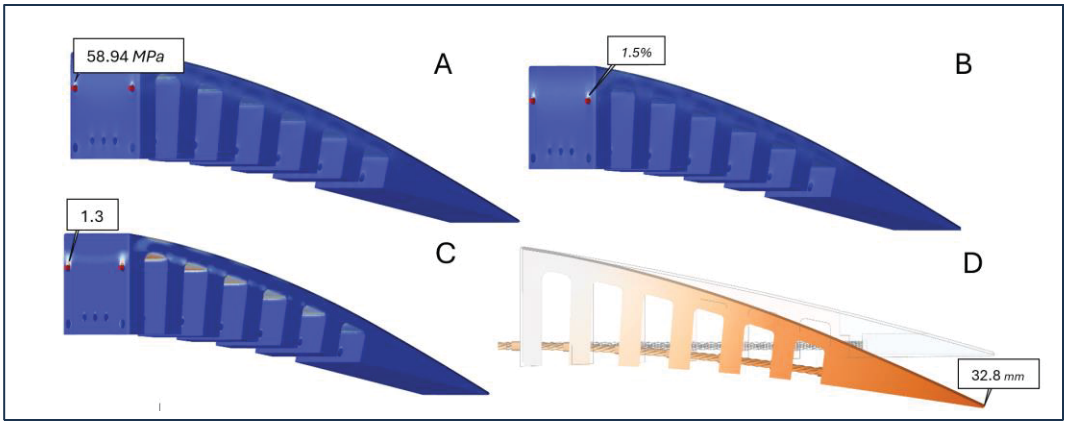

Figure 5.5 Contours of A) von Mises stress, B) strain, C) factor of safety, D) displacement for sliding configuration indicating maximum values for each parameter

As seen in Figure 5.5-A, the maximum von Mises stress on the ET rib reaches to 58.94 MPa, which is lower than the structure's tensile strength of 75 MPa (Table 1). The maximum local strain is equal to 0.01506 or 1.5% of its initial value, which occurs in the same area as the maximum von Mises stress as seen in the Fig. 5.5-B. The local strain value is less than 2%, which is within the elastic deformation limit. The safety level is calculated to ensure that the structure performs within the safety limits. The results show that the minimum Factor of Safety (FoS) is 1.3 at the place, where maximum stress and strain occur, (Fig. 5.5-C). This FoS is within the safety limits, which demonstrates the safety of the elastic structure.

In addition, the maximum attainable displacement of the edge can also be calculated, given the fact that it should respect the maximum displacement obtained from our previous study for increasing range (Negahban, Bashir, Traisnel, & Botez, 2024), which was found to be 26mm in the downward direction. The results show that using the given force (750N), a maximum deformation of 32.8*mm* in the downward direction is obtained (Fig. 5.5-D), which is higher than 26mm.

5.2.5.2 No-contact cable/hole configuration

An analysis like that of the sliding cable/hole configuration was conducted on the no-contact cable/hole configuration. It was found that for the no-contact configuration, the maximum von Mises stress reaches 105.3 MPa at the spot where the upper screws were located, and it was 44% higher than that of the sliding configuration. This increase was expected, as there was no contact or friction between the hole and the cable, and the inner teeth were not engaged in the deformation of the ET rib, since they had no friction against the cable and the applied force on the ET rib was directly exerted to the solid edge. Nevertheless, the results have shown similar values for the strain, which was equal to 0.01596 and only 5.6% higher than the sliding configuration strain. The minimum factor of safety is equal to 1.2, which guarantees the safety of the mechanism operation. Finally, considering the maximum vertical displacement of the ET rib after deformation, the no-contact configuration achieved higher vertical displacement than that of the sliding contact, reaching 39.53mm (17% higher than with sliding contact). Figure 5.6 shows the maximum values obtained for each parameter and Table 5.2 summarizes the results of both sliding and no-contact configurations.

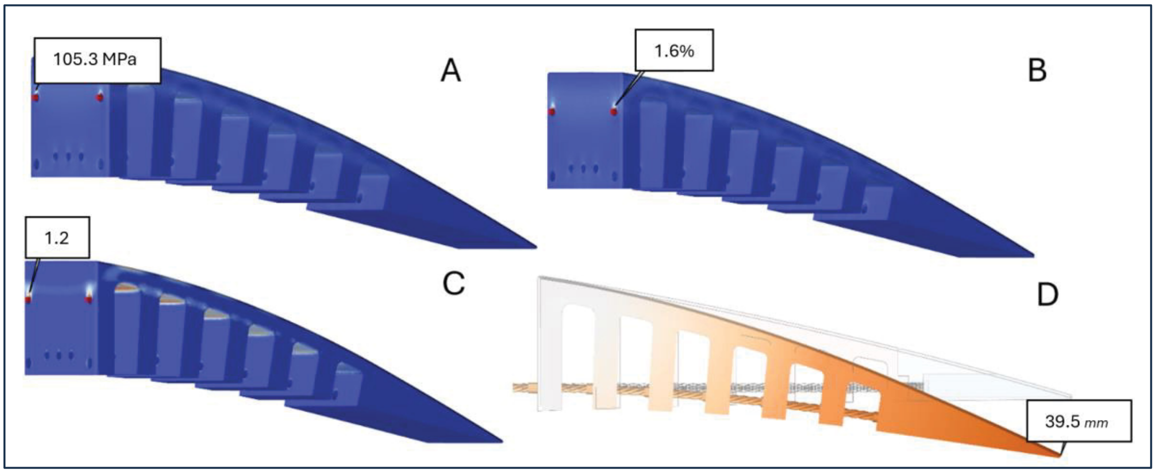

Figure 5.6 Contours of A) von Mises stress, B) strain, C) factor of safety, D) displacement for no-contact configuration indicating maximum values for each parameter

Table 5.2 Summary of the results of structural analysis for both types of cable/hole configurations

Cable/hole contact type	Max. von Mises stress (MPa)	Max. Strain %	Min. FoS	Max. displacement (mm)
Sliding	58.94	1.5	1.3	32.8
No contact	105.3	1.6	1.2	39.53

A comparison was drawn between the two configurations, as shown in Table 5.3, expressed in terms of their advantages and disadvantages.

Table 5.3 Advantages and disadvantages of the sliding and no-contact configurations

Contact type	Advantages	Disadvantages
Sliding	1- Higher stability 2- More uniform load distribution 3- Lower stress 4- No undesirable deformation due to frictional forces	1-Limited flexibility due to friction
No-contact	1- More flexibility and freedom 2- Reduced frictional forces on cables 3- More simple design	1- Less support and stability 2- Non-uniform load distribution 3- Undesired deformations of ET rib

As indicated in Table 5.3, when structural stability and equal load distribution are considered, the sliding motion was a more suitable choice than the no-contact configuration, despite having frictional force that introduced resistance; a resistance that acts as constraint against undesirable deformations. Therefore, the sliding configuration was selected for further study. To ensure numerical accuracy, a grid independence study was conducted. The details of this study, including mesh refinement levels and their corresponding results, are provided in Appendix II.

5.3 Results and discussion

5.3.1 Geometrical modifications

Some geometrical modifications on the sliding configuration were required to improve the robustness of the structure, based on the results obtained in a structural analysis (Fig. 5.4), especially to reduce the stress concentration around the screws, increase the reliability of ETM and to increase the maximum displacement of the elephant trunk (ET) rib. Two analyses are performed in this regard: 1- analysis of the teeth number and thickness, 2- analysis of the upper surface thickness. The first analysis aimed to find the optimum number of teeth for ETM along with their optimum thickness by considering the ETM weight and vertical displacement, and the second analysis was performed to improve the reliability and flexibility of the ETM by finding the best thickness for the upper surface. In the final step, the fixation of the ETM to the wing box was modified with the aim to reduce the stress concentration on the upper screws. Figure 5.7 depicts the initial ETM, in which the teeth thickness, upper surface thickness and the fixation to the wing box are specified.

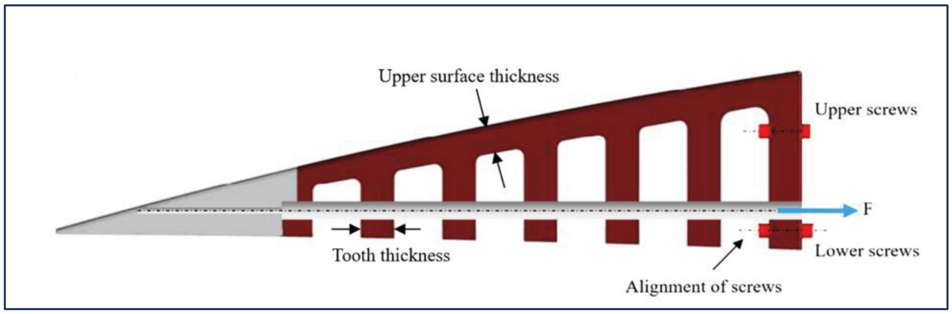

Figure 5.7 Initial ETM design

5.3.2 Analysis of the Teeth Number and their Thickness

The teeth number and thickness have an important role in improving the structural characteristics of the ETM in terms of weight and maximum vertical displacement. As indicated in Section 2.5, having chosen “sliding” over “no-contact” configuration, the maximum vertical displacement was smaller than 32.8mm. The analysis of the teeth number and thickness is aimed not only to increase the vertical displacement, but also to reduce structural weight. For this purpose, different number of teeth, ranging from 3 to 10 teeth are analyzed for three different thicknesses, ranging from 5 to 8 mm. The analysis is divided into two parts: 1-analysis of the teeth number, 2- analysis of the teeth thickness. In the first analysis, the best three teeth number was selected by considering the maximum force with the minimum factor of safety of 1.5. Table 5.4 shows the maximum force with the minimum factor of safety of 1.5 for different thicknesses and number of teeth.

Table 5.4 Maximum applied force for different thicknesses and number of teeth

	Maximum force with the Factor of Safety of 1.5 (N)		
Number of teeth	**Tooth thickness (mm)**		
	5	6	8
3	100.92	106.80	105.11
4	101.55	107.40	106.87
5	104.84	108.34	109.75
6	106.23	108.36	108.25
7	106.24	110.54	109.40
8	105.87	108.40	110.26
9	106.21	109.54	111.27
10	107.66	112.10	109.94

As seen in Table 5.4, by increasing the teeth number from 3 to 10, the force magnitude, which has the minimum FoS of 1.5, increases. The best three teeth numbers were selected for different thicknesses. For example, for teeth thickness of 5mm, the best three teeth numbers, which have the highest applicable force, are: 106.23 N ,106.24 N, and 107.66 N corresponding to the teeth number of 6, 7, and 10, respectively. The same criterion is used for the other teeth thicknesses (6 and 8 mm).

Once the best three teeth numbers are selected, the analysis is continued to find the best tooth thickness among 5, 6, and 8mm. In this analysis, two parameters, including structural weight and maximum vertical displacement are determined as the main criteria in obtaining the best tooth thickness. For this purpose, the weight and the vertical displacement of the three best tooth number (6, 7, 10) were calculated (Table 5.5).

Table 5.5 The structural weight and vertical displacement of ETM for three best teeth numbers

	Tooth thickness (mm)									
	5			**6**			**8**			**Weighting factor**
Number of teeth	6	7	10	6	7	10	6	7	10	
Structural Weight (g)	150	158	184	170	191	201	208	222	235	3
Score	27	24	18	21	15	12	9	6	3	
Vertical Displacement (mm)	51.4	50.1	47	50	46.4	45.9	43.5	41.8	39.3	2
Score	18	16	12	14	10	8	6	4	2	
Total score	45	40	30	35	25	20	15	10	5	
Ranking	1	2	4	3	5	6	7	8	9	

As depicted in Table 5.5, the structural weight has a higher weighing factor than that of the vertical displacement. Furthermore, Table 5.5 shows that the tooth thickness of 5 mm has the best ranking among the 9 cases, which corresponds to number of teeth equal to 6. Thus, for a 5 mm of thickness and 6 teeth, the modified ETM design has a lower structural weight, and a higher vertical displacement compared to its initial design. in which the number of teeth was 5 and the thickness was 8 mm.

5.3.3 Analysis of the Upper Surface Thickness

The thickness calculated in this paper, is the vertical component of the upper surface thickness, which connects the teeth to the ETM solid edge (Fig. 5.7). This thickness is independent of the teeth thickness, and a different analysis than that of the teeth thickness is established to find the optimum thickness of the upper surface. This analysis is performed in the absence of the teeth in the ETM flexible part with an aim to find the influence of the thickness of the bending part, and its best thickness with respect to ETM flexibility and reliability. Figure 5.8 shows the ETM without teeth for the analysis of the upper surface thickness. This thickness is aimed to be constant alongside the length of the elephant trunk rib.

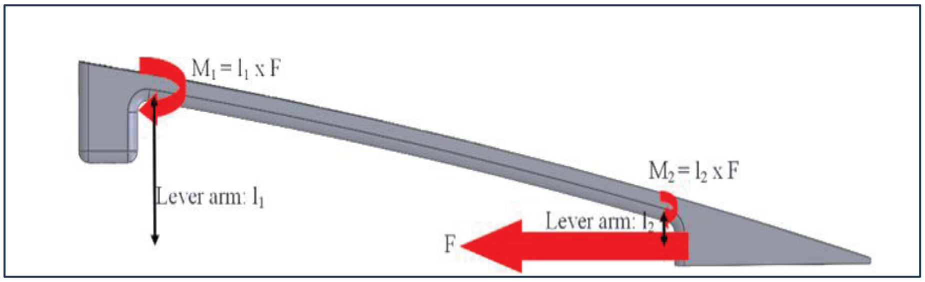

Figure 5.8 Schematics of the ETM without teeth for the analysis of the upper surface thickness

As illustrated in Fig. 5.8, a smaller moment (M_2) is generated by the shorter lever arm in the section connecting the bending and solid edge parts, resulting in reduced influence on ETM morphing. In contrast, the section linking the fixation and bending parts experiences a higher moment (M_1) due to its longer lever arm. Consequently, an appropriate upper surface thickness is necessary to compensate for this difference in moments (M_1 and M_2) and ensure the reliability and durability of the upper surface during ETM morphing.

Different thicknesses are studied, ranging from 4 mm to 16 mm. Their analysis requires the ETM to preserve its elastic deformation. With the elastic behavior being set, it is expected that both the displacement and the effort to be linearly proportional. For each thickness, the vertical displacement is set to be constant, while applying different force magnitudes. With this assumption, several structural parameters, including factor of safety, von Mises stress, and structural weight are calculated for each thickness. Table 5.6 indicates the values of these structural parameters for each thickness.

Table 5.6 Variations of structural parameters for different upper surface thicknesses

Thickness (mm)	**Force (N)**	**Displacement (mm)**	**FoS**	**von Mises stress (MPa)**	**Weight (g)**
4	35	62.49	2.2	33.6	81
	28	50.35	2.8	27.1	
	21	38.21	3.6	20.6	
	14	26.07	5.3	14.1	
	7	13.93	9.8	7.6	
8	300	62.39	0.9	80.1	122
	240	51.57	1.2	64.1	
	180	38.75	1.6	48.2	
	120	25.93	2.3	32.3	
	60	13.11	4.6	16.3	
12	1000	62.94	0.6	128.4	162
	800	50.37	0.7	102.8	
	600	37.81	1.0	77.1	
	400	25.24	1.5	51.5	
	200	12.68	2.9	25.9	
16	2500	63.48	0.4	208.2	201
	2000	54.00	0.5	166.6	
	1500	40.52	0.6	125.1	
	1000	27.03	0.9	83.5	
	500	13.55	1.8	42.0	

Table 5.6 indicates that by increasing the thickness, the force required to obtain the same magnitude of displacement also increases, which leads to an increase in the von Mises stress and weight of the whole ETM, and a reduction in the factor of safety. For example, for the

thicknesses of 4mm and 16 mm, to obtain a displacement of approximately 62 mm, the required force increases from 35N to 2500N, von Mises stress increases from 33.6 MPa to 208.2 MPa and the total ETM weight increase form 81g to 201g, while the factor of safety reduces from 2.2 to 0.4. To have a clear understanding of the values shown in Table 6, Figures 5.9 and 5.10 show the variations of the vertical displacement and von Mises stress with the forces for different upper surface thicknesses.

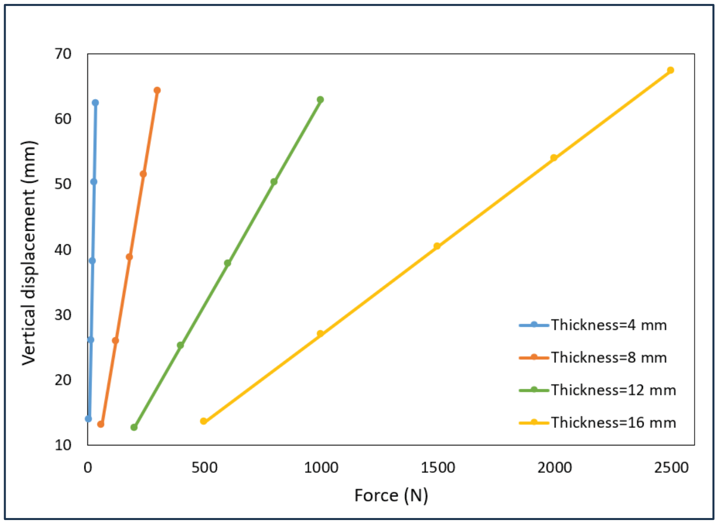

Figure 5.9 Variation of the vertical displacement with the force magnitude for different upper surface thicknesses

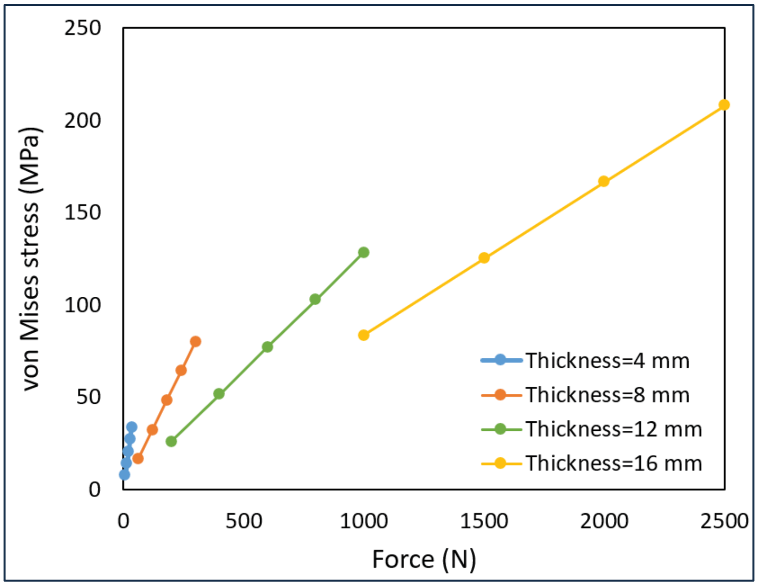

Figure 5.10 Variation of the von Mises stress with the force magnitude for different upper surface thicknesses

Figures 5.9 and 5.10 show that if displacement is constant, the increase in the von Mises stress and vertical displacement are linearly proportional to force magnitude and this linear variation is sharp for lower thickness values, while the thickness increases, the variation becomes mild. This linear variation could predict the force magnitude for each displacement and thickness.

In this study, the maximum desired displacement is 66 mm, which corresponds to the maximum vertical displacement obtained in our previous study (Negahban, Bashir, Traisnel, & Botez, 2024). To find the corresponding thickness for this vertical displacement, the ETM should meet the minimum factor of safety criteria, as mentioned in the Federal Airworthiness Regulation Part 25.303: “Unless otherwise specified, a factor of safety of 1.5 must be applied on the prescribed limit load which are considered external loads on the structure” (*Federal Aviation Administration. 1970*). For this purpose, for upper surface thicknesses, ranging from 4 mm to 16 mm, the maximum force for obtaining the minimum factor of safety of 1.5 was calculated, then the minimum required force for obtaining the 66 mm displacement was also calculated. Figure 5.11 shows the variations of these forces with the thickness.

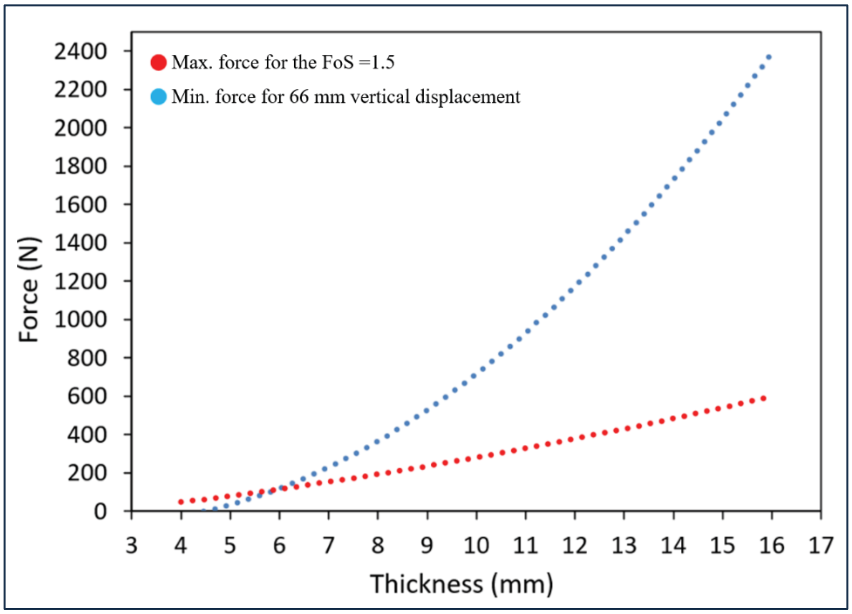

Figure 5.11 Force variation for different upper surface thicknesses

As shown in Fig. 5.11, the two diagrams intersect at the thickness equal to 5.93 mm. This thickness value means that the ETM can morph up to 66 mm by having the minimum factor of safety of 1.5. Therefore, the upper surface thickness analysis determines the best thickness value, by which both the flexibility and reliability of the ETM increased. Figure 5.12 depicts the contour of the von Mises stress for ETM after morphing.

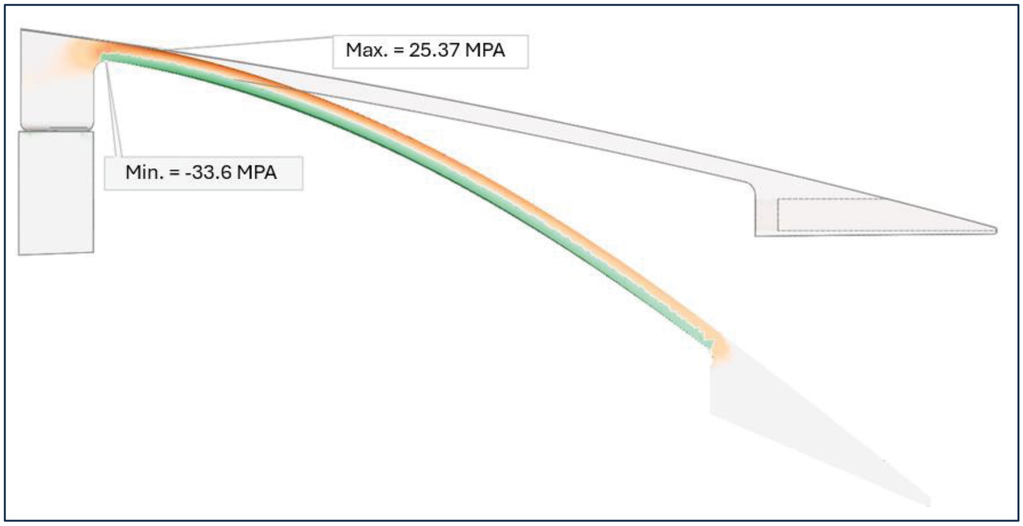

Figure 5.12 Maximum/minimum von Mises stress on the ETM after morphing with an optimum upper surface thickness

5.3.4 Modification of the ETM fixation to the wing box

As shown in the initial design of ETM (Fig. 5.7), due to the distance of the upper screws from the cables, when the ETM deforms in the downward direction, the upper screws sustain a higher force than that of the lower screws; therefore, higher stress concentrations are expected around upper screws, as shown in Figures 5 and 6. Therefore, instead of a horizontal fixation of the rib to the wing box, this rib was fixed using three screws at the top of the rib. This type of fixation reduces the stress concentration around the screws and moves it to another non-critical area. In the vertical fixation, no tensile force was expected to act on the screws, since the external force direction was perpendicular to the alignment of the screws.

Figure 5.13 shows the ETM modified design after finding the optimum number of teeth, their optimum thickness, the optimum upper surface thickness, and the suitable fixation to the wing box.

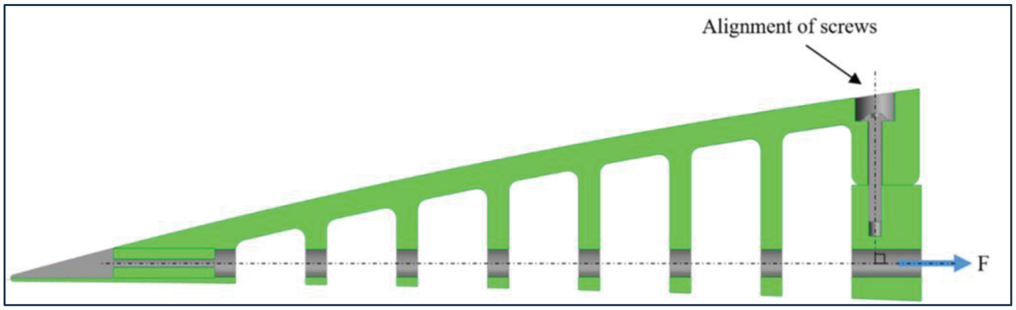

Figure 5.13 Modified design of ETM

To avoid errors created by the singularities present in the structural design, round fillets were added around the edges of the teeth of the ET ribs to create a smooth continuity on the structures' surfaces, which increases the safety of the structure by reducing stress concentration on the sharp edges. Stress concentration is related to the fillet radius by the following equation:

$$\Delta\sigma = K_t \frac{\mathrm{F}}{\pi r^2} \tag{5.3}$$

where K_t is the factor of intensity, r is the fillet radius, and F denotes the applied force on the fillet surface. According to Eq. (5.3), the smaller is the fillet, the higher is the stress concentration, which is detrimental to the structure's safety. Figure 5.14 shows the ETM after adding the fillets.

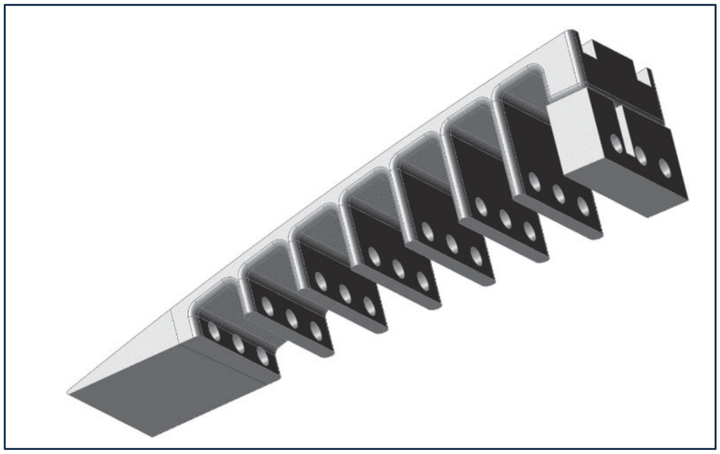

Figure 5.14 Elephant trunk rib with filleted edges

5.3.5 Results of the structural analysis

A structural analysis was performed for the modified structural design. Four parameters were analyzed: the von Mises stress, strain, factor of safety and displacement. Figure 5.15 shows the results obtained from this analysis, in which the maximum values for stress, strain, and displacement, and the minimum value for the factor of safety are indicated. These values indicate that the structural parameters have been improved compared to the initial design.

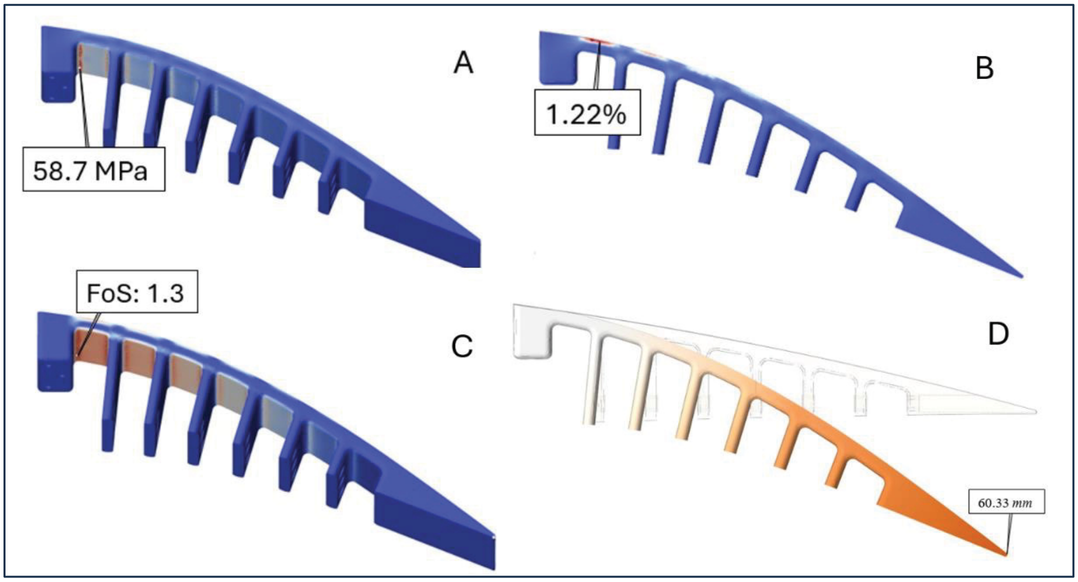

Figure 5.15 Contours of A) von Mises stress, B) strain, C) factor of safety, and D) displacement

Table 5.7 compares the results of structural parameters for the initial and modified structure. The results presented in Table 5.7 indicates that the maximum von Mises stress is reduced by 0.24 MP and moved to an area other than that around the screws; strain reduced by 19%, and vertical displacement by 45.63%; while the factor of safety remained unchanged. Therefore, the intended goals were accomplished by a geometrical modification, meaning that the stress concentration was both reduced and moved to a non-critical area, and the flexibility of the structure was increased. To further improve the structural parameters, particularly the structural weight, a topology optimization was performed and is described in the following section.

Table 5.7 Comparison of the structural parameters of the initial and modified structures

	Max. von Mises stress (MPa)	**Max. Strain %**	**Min. factor of safety**	**Max. displacement (mm)**
Initial model	58.94	1.51	1.3	32.8
Modified model	58.7	1.22	1.3	60.33

5.3.6 Topology optimization

A multi-objective topology optimization was performed to find the optimum ETM design while respecting its constraints. The optimization was conducted using Altair Inspire, with the objectives of minimizing the structure weight and maximizing the stiffness. In the topology optimization, the material distribution was improved by strengthening the design in critical areas, and by removing unnecessary mass to reduce the structural weight. In this process, multiple design spaces were considered, not only the solid edge, but also the interior of the upper surface and the space around the holes are included in these design spaces. Symmetric controls are also added to the design space to remove the mass symmetrically on each plane. There are eight symmetrical planes on the ETM in total, in which six symmetrical planes are located on the teeth (yz-plane), and two planes along the ETM length (xy-plane). Figure 5.16 shows the ETM with the specified design space (highlighted in red) and the symmetric control planes.

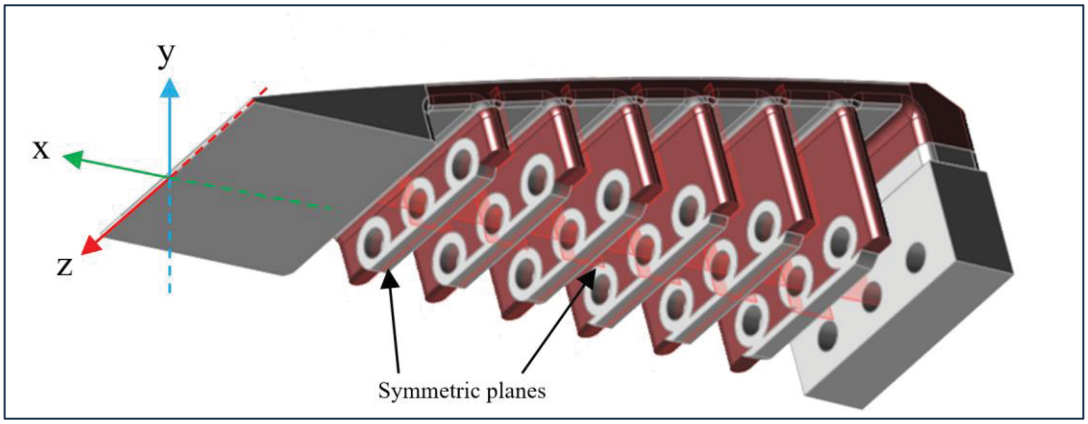

Figure 5.16 Illustration of the design space for topology optimization and the symmetrical planes

The stiffness is reversely proportional to the total structural compliance (Daynes, 2023); therefore, to increase the stiffness, the optimization tends to minimize the structural compliance, which is expressed as:

$$C = \mathrm{F}^T \mathrm{u} \tag{5.4}$$

where C denotes the total structural compliance, F is the external force vector, and u is the displacement vector.

To respect the equilibrium equation in Eq.(5.1), the stiffness or the internal forces within the structure should be in balance with external forces. Therefore, Eq. (5.4) is rewritten in terms of stiffness as follows:

$$C = \mathrm{u}^T \mathrm{K}\, \mathrm{u} \tag{5.5}$$

By minimizing Eq. (5.5), the objective functions of stiffness maximization is satisfied. The second objective function, that is the weight reduction, involves the material volume, $V,$ in the design space, which can be expressed as function of the material density, ρ. Since the analysis is using the FE method, the total volume is differentiated into finite elements, and it is written as:

$$V(\rho) = \sum \rho_e V_e \tag{5.6}$$

where ρ_e and V_e denote the density and volume of each element, respectively.

The optimization is subjected to several constraints that ensure the feasibility of the optimized topology. These constraints are: 1-material distribution constraints correspond to objective functions, in which the effective stiffness of each element is controlled as indicated in the following equation:

$$\mathrm{K}(\rho) = \sum \rho_e^p \mathrm{K}_e^0 \tag{5.7}$$

where p is the penalization factor that ensures the intermediate density penalization, and K_e^0 represents the stiffness matrix of each element when it is completely solid. 2-volume constraint, which limits the material removal to V^*, where V^* is the minimum allowable volume of the material, 3-density constraint, bounded between 0 and 1 ($0 \leq \rho_e \leq 1$), 4-symmetry constraint, which ensures symmetric material distribution in the design space, 5-the stiffness constraint that ensures the structure maintain its adequate stiffness by limiting it to a maximum allowable compliance, and finally, 6-equilibrium constraint function. Table 5.8 summarizes the entire optimization framework, including the objective functions and their corresponding constraints.

Table 5.8 Multi-objective topology optimization framework

Function/variable	Description
Objective functions	
Min. $C = \mathrm{u}^T \mathrm{K}\, \mathrm{u}$ Min. $V(\rho) = \sum \rho_e V_e$	*minimization of structural compliance* *minimization of weight*
Subject to:	
$\mathrm{K}(\rho)\mathrm{u} = \mathrm{F}$	*Equilibrium constraint function*
$\mathrm{K}(\rho) = \sum \rho_e^p \mathrm{K}_e^0$	*Material distribution constraint*
$\sum \rho_e V_e \geq V^*$	*Volume constraint*
$0 \leq \rho_e \leq 1 \quad \forall e$	*Density constraint*
$\rho_{ijk} = \rho_{ij(-k)} \quad \forall(i, j, k)$	*Symmetry constraint*
$C(\rho) \leq C_{max}$	*Stiffness constraint*

The optimization uses the combination of the Solid Isotropic Material with Penalization (SIMP) and the Optimality Criteria (OC) methods. The SIMP method distinguishes the solid from the void regions, while the penalization factor (p) modifies the material properties as function of the density. This penalization factor is especially useful in solving large scale problems. The combination of both algorithms ensures the robustness and efficiency of the optimization process.

The optimization started by initializing the design space with uniform material distribution ($\rho_e = 1$). The SIMP method was used to calculate the material properties by interpolation among element densities, where the penalization factor $\boldsymbol{p}$ was set to 3 to suppress intermediate densities and provide a clear material distribution. At each iteration, the structural compliance was computed using a Finite Element (FE) solver, and the displacement field (u) was obtained by solving the equilibrium equation (Eq (5.1)). The sensitivity analysis was performed to compute the derivative of the compliance with respect to the density variables (${}^{\partial C}/_{\partial \rho_e}$). Based on these sensitivities, the Optimality Criteria (OC) method updated the density values of each element using a heuristic update rule to satisfy the volume constraint. This iterative process continued until both convergence criteria—compliance and density field—were obtained below the prescribed thresholds (1% in this case).

Note that during the optimization, the cables were removed from the design space and only the tooth-like elastic part was optimized. Regarding the mass reduction, different target values are specified for each part. For the teeth, starting from solid edge part, 75, 73, 70, 66, 65, and 64% target mass reductions were specified, respectively. This percentage decrease was due to the relative proportion of the reference space in the total volume of the teeth. The fixation part and the bending part (upper surface) have a target value of 45% mass reduction. Figure 5.17 shows the ETM after topology optimization.

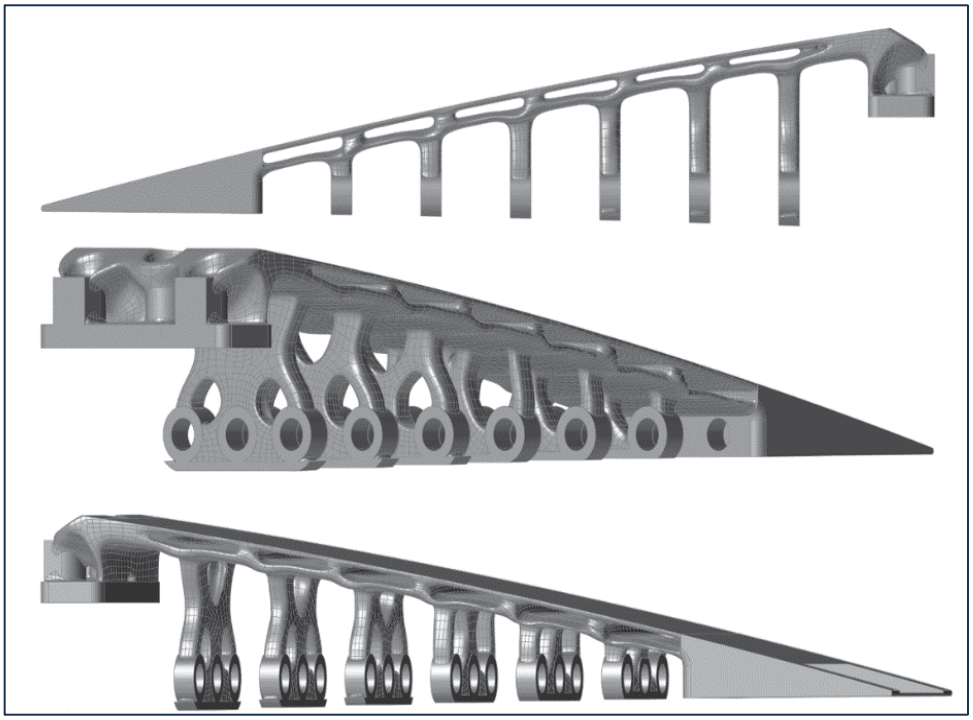

Figure 5.17 Schematics of the optimized topology of Elephant Trunk Mechanism (ETM) from different views

By expanding the design spaces to the ETM upper surface, unnecessary interior parts were removed from the structure. Moreover, more material was removed from the teeth, and the bulk shapes of the teeth were transformed into linkages supporting the holes, leading to even greater mass reduction. Figure 17 shows that unnecessary material has been removed from the ETM elastic bending part, which reduces the bending resistance, and the effort required for the deformation. Table 5.9 indicates the improvements obtained from the ETM topology optimization.

Table 5.9 Comparison of the structural parameters of the ETM before and after optimization

	Max. von Mises stress (MPa)	**Max. strain %**	**Min. FoS**	**Max. vertical displacement (mm)**	**Mass (kg)**
Initial ETM	58.7	1.2	1.3	60.33	0.155
Optimized ETM	52.58	1.63	1.5	66.02	0.100

The values presented in Table 5.9 show that most of the structural parameters were significantly improved. The maximum von Mises stress was reduced by 10.43%, the factor of safety was increased from 1.3 to 1.5, and the maximum vertical displacement increased by 8.6% (from 60.33 *mm* to 66.02 *mm*), thus indicating more structural flexibility on the optimized ETM. However, the maximum strain increased from 1.2 % to 1.63%, due to the hollow spaces on the upper bending part, created after the optimization. Finally, the results obtained for the mass reduction indicated that the initial mass of 0.155 kg was reduced to 0.1 kg, signifying a reduction of 35.5%. Figure 5.18 shows the deformation of the ETM before and after the optimization.

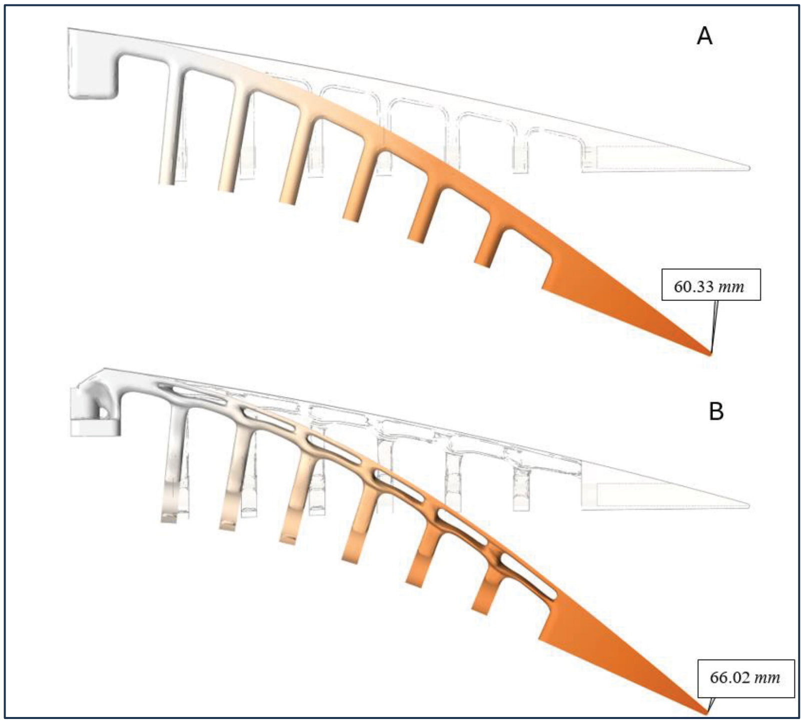

Figure 5.18 Maximum displacement of ET rib, A) before, and B) after topology optimization

A total number of four ETM ribs were used in the flap section of the UAS-S45 wing. These ETM were identical, except for small differences in their heights due to the tapered characteristics of the wing, which gave an infinitesimal difference in ETMs weight. Therefore, each ETM rib was optimized separately; and the mass reduction was unique for each ETM. Figure 5.19 shows the mass variations for each ETM rib.

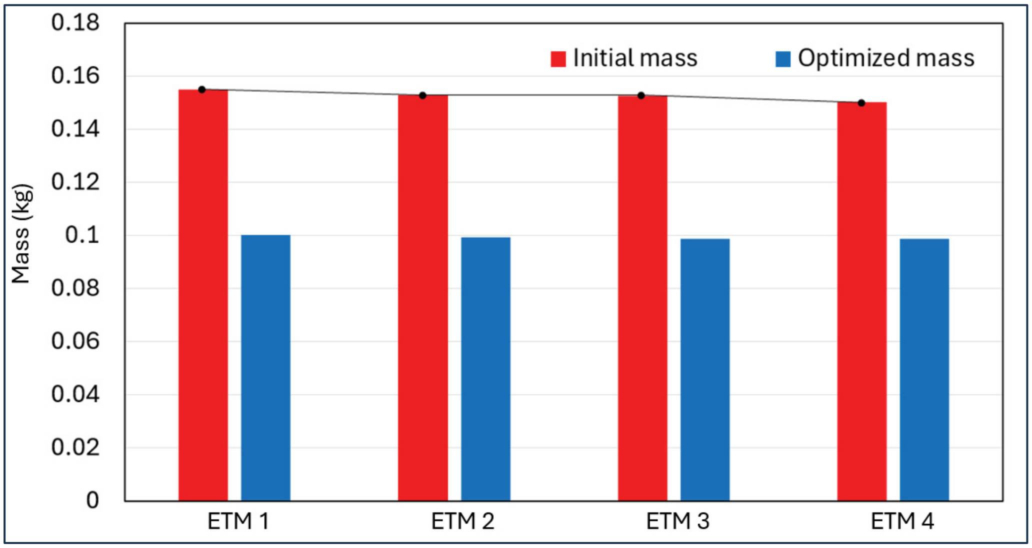

Figure 5.19 Mass variations for each ETM before (red) and after (blue) topology optimization

The mass was reduced for each ETM. Considering one wing, a total mass of 0.214 kg was removed from all four ET ribs after topology optimization, which would be equivalent to a 4.2 N weight reduction for the whole UAS equipped with two wings.

5.3.7 Elephant Trunk Mechanism Integration on the UAS-S45 wing box

After the structural analysis and topology optimization on the ETMs, a number of four ETMs were designed on the Seamless Morphing Trailing Edge (SMTE) flap section. The distance between these ribs corresponded to the flap length, which was defined in our previous study(Negahban, Bashir, Traisnel, & Botez, 2024). Figure 5.20 shows the SMTE flap and its geometrical details, in which the elephant trunk mechanism was used with the aim to generate the required deformation (Figure 5.20-B and 5.20-C). Therefore, the four ETM were located inside the morphing flap section and the transition sections on the right and left sides of the SMTE flap were used to follow the deformations obtained from the ETMs (Fig. 5.20-B). The total length of the SMTE was 1m, the section where the ETMs were embedded was equal to 0.735 of the total flap length (excluding transition sections), and 0.1325m was allocated to each transition section.

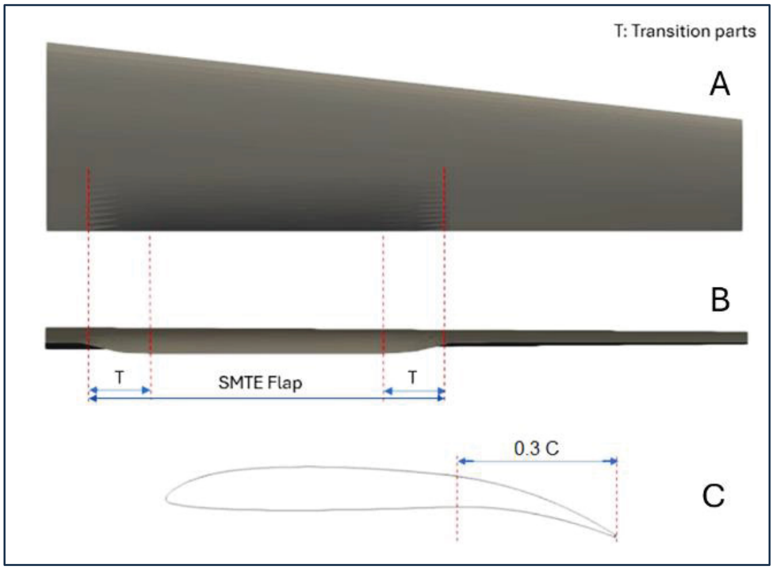

Figure 5.20 Schematics of the SMTE flap: A) top view, B) back view, C) side view after deformation

To fix the ETMs on the wing box, they were screwed from the top, as shown in Figure 5.21 The advantage of this type of fixation was its reduced stress concentration around the screws, as noted in Section 5.3.4.

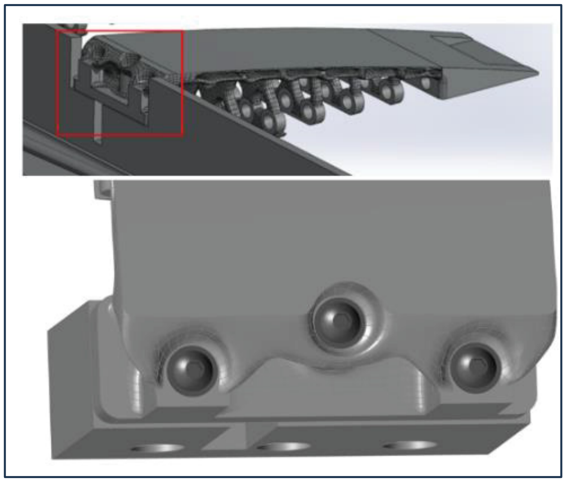

Figure 5.21 Schematics of the ETM fixation to the UAS-S45 wing box

Figure 5.22 illustrates the orientation of the ETMs inside the SMTE flap. Four ETMs were embedded inside the SMTE flap section, excluding the transition sections. They were fixed to the solid spar along the span. Respecting the symmetric orientation, ETM 2 and ETM 3 were fixed in the center of the flap, while ETM 1 and ETM 4 were fixed at the beginning of the transition sections, as shown in Fig. 5.22-B.

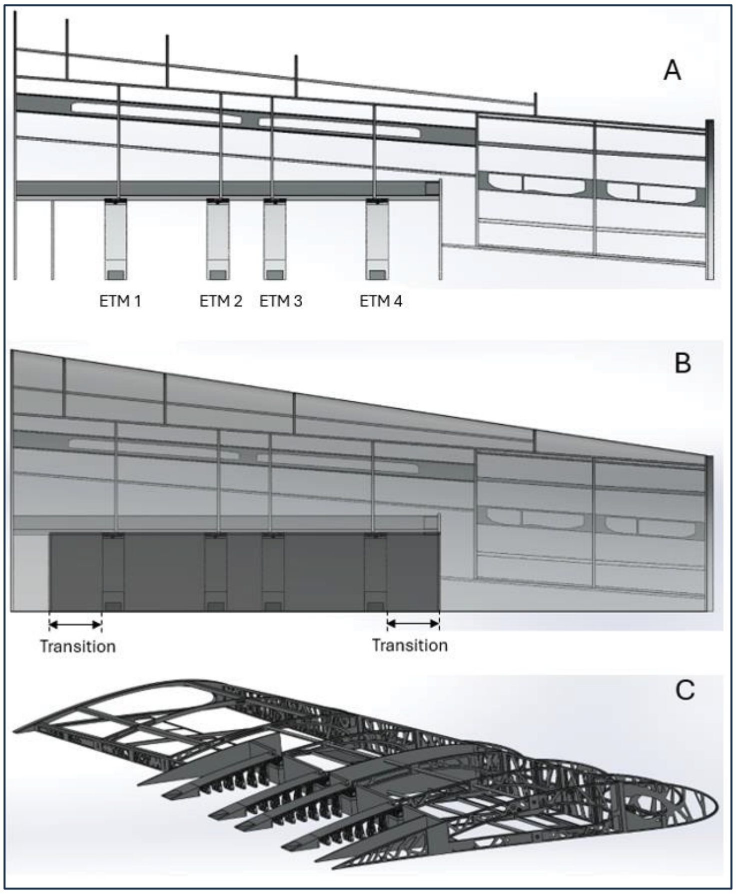

Figure 5.22 Installation of the four ETMs on the main wing box of the UAS-S45: A) top view, B) side view, C) isometric view

5.3.8 Skin analysis

In the final phase of this study, a skin analysis was performed with the aim to find the appropriate skin material, corresponding to the requirements of the Seamless Morphing Trailing Edge (SMTE) flap, which has high flexibility. Figure 5.23 shows a schematic of an UAS-S45 wing section with the STME flap, where the skin covers the whole flap section with the ETMs embedded within.

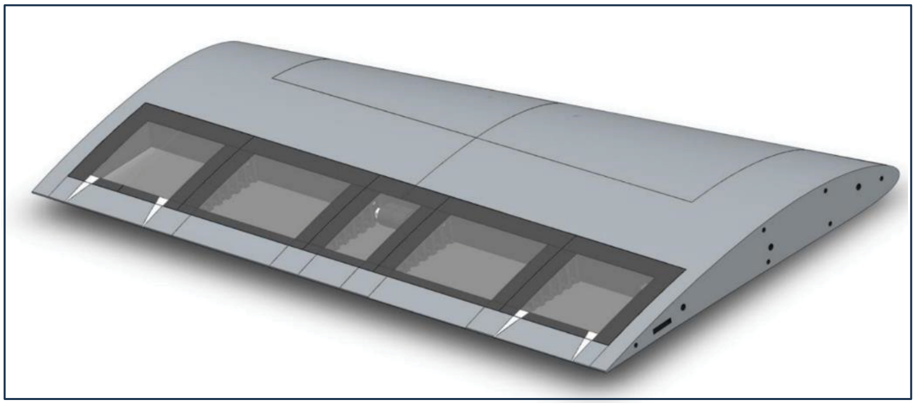

Figure 5.23 Schematics of an UAS-S45 wing section with the STME flap and skin

As seen is Fig. 5.23, the skin covers a rectangular area on both upper and lower surface of the wing. The analysis was performed by focusing on a section of the wing that contains the skin, which would reduce the computation time and cost. This approach requires establishing a suitable boundary condition corresponding to the actual constraints. The skin analysis was performed using the ANSYS software. Figure 5.24 shows the computational domain and the boundary condition for the skin analysis.

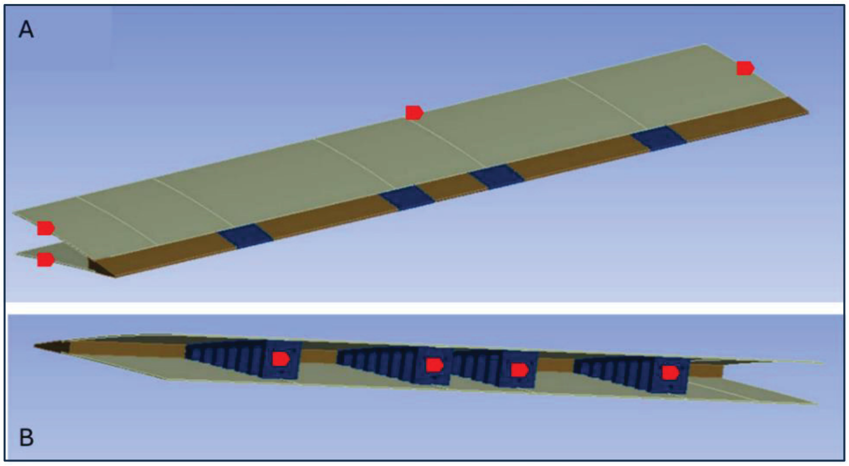

Figure 5.24 Computational domain and boundary conditions for the skin analysis, A) exterior view, B) interior view

As seen in Fig. 5.24, the wing sections, which have no impact on the skin analysis were eliminated, ETMs were considered as the supports for the upper and lower skins and were included in the analysis. Tho boundary condition used in this analysis requires the edges and surfaces specified in red color to have a fixed support during the analysis. In fact, in the actual wing, these areas (surfaces and edges) with fixed motion constraints are attached to the wing box. With these constraints, the only moving part of the wing was the trailing edge, where the downward morphing of the ETMs also deformed the skin.

To simulate the actuation of the morphing mechanism, a prescribed vertical displacement of 66 mm was applied at the trailing edge of the structure. This displacement corresponds to the maximum downward deflection produced by the Elephant Trunk Mechanisms (ETMs) during operation. The applied boundary condition was intended to replicate the deformation profile induced by the ETMs and assess the skin's flexibility and conformity to the target morphing shape.

For the skin analysis, silicon rubber (Silicon VMQ) was chosen due to its unique material properties in morphing wing applications. Table 5.10 depicts the silicon rubber properties, as follows.

Table 5.10 Material properties of the silicon rubber

Young's modulus (MPa)	**Poisson ratio**	**Tensile yield strength (MPa)**	**Density (kg/m^3)**
17	0.5	10.4	1230

Given the nonlinear deformation characteristics of silicone rubber, a hyper-elastic material model was used for the skin analysis. Silicon rubber is a very soft and flexible material in terms of elongation and stretchability. In addition, long fatigue resistance is one of the unique characteristics of silicon rubber, which makes it a suitable choice for morphing wing application, where frequent deformation during flight demands a material with high fatigue resistance. Therefore, by performing repeated morphing, it can maintain its flexibility without significant material degradation. Considering the temperature effect, silicon rubber performs very well at various temperatures ranging from -60 °C to $+200$ °C. For the UAS-S45 the ceiling altitude is 15,000 ft, where the temperatures could reach −20 °C at cruise flight; nevertheless, silicon rubber still performs very well at this temperature, as mentioned above.

By choosing silicon rubber as the SMTE flap skin material, a skin analysis was performed. In this analysis, the most important factor was the deformation smoothness, especially on the lower side of the flap, where wavy deformations were very likely to occur due to the downward deformation. Figure 5.25 shows the skin deformation contours after SMTE flap deformation.

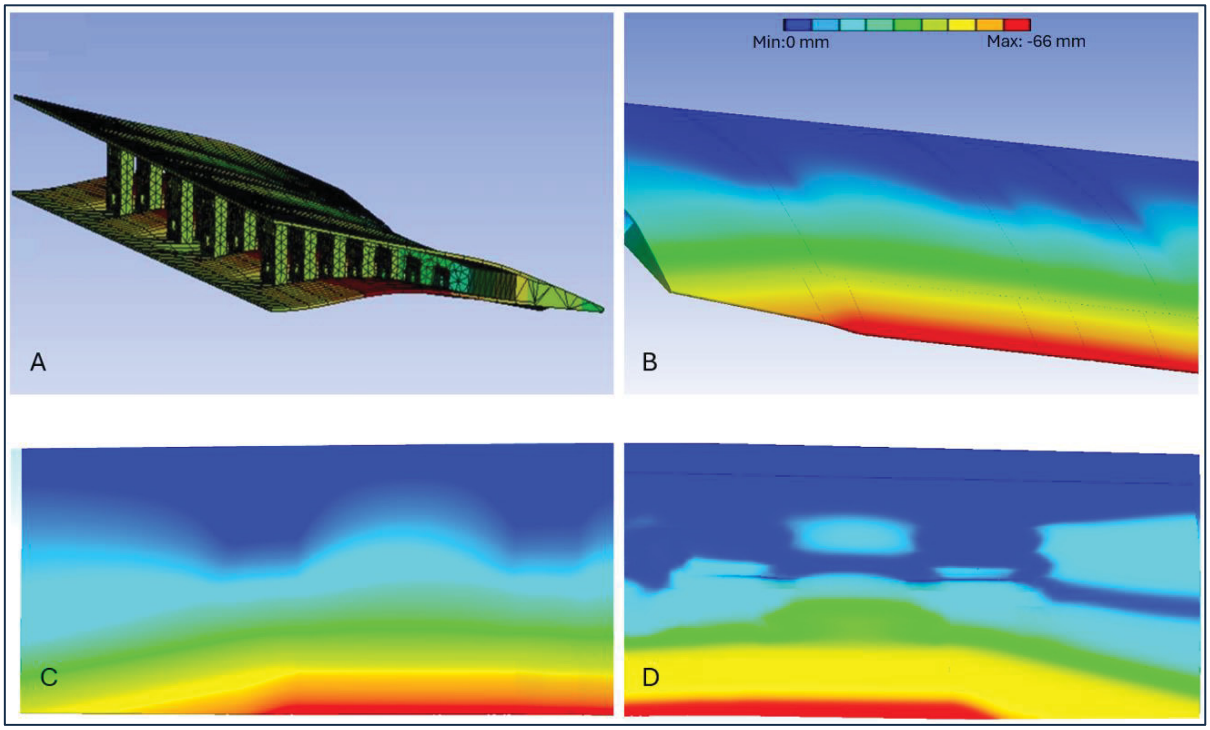

Figure 5.25 Deformation contours of the silicon rubber skin, A) isometric view, B) rear view, C) upper surface, D) lower surface

As shown in Figure 5.25, silicon rubber skin perfectly accomplishes the ETMs morphing, especially on the transition parts. It was found that the upper surface skin (Figures 5.25-B and 5.25-C), had a very good surface smoothness after morphing and there was no sign of distortion; however, Figure 5.25-C shows some distortions on the wing lower surface skin after morphing. This behavior was expected as the ETM downward deflection contracts the lower surface, and the skin contracts accordingly. This contraction issue on the lower surface could be easily solved by pre-tensioning the lower surface skin before attaching it to the ETMs, which means that the skin is stretched before attaching it to the ETMs and once the morphing occurs, the lower surface contraction preserves the initial state of the skin, thus the distortions will be eliminated on the lower surface.

5.4 Conclusion

This paper introduces the novel Elephant Trunk Mechanism (ETM) inspired by an elephant's trunk. This ETM was structurally investigated in conjunction with a topology optimization to examine its reliability and feasibility for its application on the Seamless Morphing Trailing Edge (SMTE) flap. The promising aerodynamic results of the SMTE flap from our previous study(Negahban, Bashir, Traisnel, & Botez, 2024) motivated us to perform this current study to further analyze it from a structural perspective. This novel morphing concept consisted of tooth-like elements whose contraction through a horizontal axial force by cables changed the trailing edge shape in the downward direction.

The static analysis was performed using the Finite Element Method (FEM). An analysis was first conducted to find a suitable connection type between the cables and the holes. A comparison between the two contact types revealed that the sliding contact configuration provided greater reliability in terms of stability, stress distribution, load transfer, and deformation feasibility.

Next, using the sliding contact boundary condition, the mechanism was structurally analyzed, and the results were further improved by geometrical modification. These modifications were analyzed in three ways: 1- analysis of finding the optimum number of teeth and their thicknesses, 2- upper surface thickness analysis, and finally, the analysis of the ETM fixation to the wing box. Following the ETMs' structural modifications, the stress was reduced by 0.4% and the stress concentration moved to a non-critical area, the maximum strain was reduced by 19%, and the ETM maximum vertical displacement increased by 45.63%, all of which improved the ETMs' structural flexibility.

Using a suitable design space, a topology optimization was conducted with the objective of minimizing the structural weight. The optimization results showed that not only was the weight reduced, but the structural parameters were also improved. The optimization results showed that the maximum von Mises stress was reduced by 10.43%, while the factor of safety increased from 1.3 to 1.5; and the ETM maximum vertical displacement was increased by 8.6%. The mass reduction, which was the main objective of the topology optimization, was reduced by up to 35.5% compared to the initial structure mass and a total weight reduction of 4.2 N was achieved for the whole UAS.

Finally, the four optimized ETMs were fixed on the SMTE flap to perform a skin analysis, in which silicon rubber was used as a base material due to its high fatigue life and flexibility. The results showed that the skin perfectly integrated with the ETM morphing, especially on the transition sections on the left and right side for the SMTE flap.

In our next study, the SMTE flap equipped with ETMs, and silicon rubber skin will be prototyped using a suitable actuation control system. The prototyped wing will be tested in a wind tunnel to validate the results obtained from this study.

CHAPTER 6

DEVELOPMENT AND EXPERIMENTAL STUDY OF A SEAMLESS MORPHING TRAILING EDGE FLAP EQUIPPED WITH AN ELEPHANT TRUNK ACTUATION MECHANISM

Mir Hossein Negahban[1], Tarek Saci[2], Ruxandra Mihaela Botez[3]

[1, 2, 3] LARCASE Laboratory of Applied Research in Active Controls, Avionics and
Aeroservoelasticity, Department of System Engineering, École de Technologie Supérieure,
1100 Notre-Dame West, Montréal, Québec, Canada H3C 1K3

Paper published in Applied Sciences Journal, 16 May 2025

Résumé

À la suite des performances prometteuses du volet à bord de fuite morphing sans discontinuité (SMTE) et de son système d'actionnement interne, le mécanisme de type trompe d'éléphant (ETM), analysés par des approches aérodynamiques et structurelles, cette étude présente une analyse expérimentale du volet SMTE équipé d'un mécanisme d'actionnement de type trompe d'éléphant. Le modèle d'aile morphing a été prototypé à l'aide d'une imprimante 3D. Quatre nervures morphing de type trompe d'éléphant ont été intégrées à l'intérieur de la section du volet, le tout recouvert d'une peau flexible. Le système de commande de l'actionnement du volet a été installé dans la boîte d'aile, en lien avec les quatre mécanismes de type trompe d'éléphant, à l'aide d'une interface graphique appropriée permettant de contrôler les déformations du volet SMTE. Le modèle finalisé a ensuite été testé en soufflerie subsonique afin de valider les résultats aérodynamiques numériques ainsi que la fonctionnalité du mécanisme de type trompe d'éléphant en conditions réelles. Les résultats confirment la fiabilité et la faisabilité du mécanisme proposé pour l'actionnement, et une très bonne concordance a été observée entre les données aérodynamiques numériques et les résultats expérimentaux en soufflerie.

Abstract

Following the promising performance of the Seamless Morphing Trailing Edge (SMTE) flap and its internal actuation system, Elephant Trunk Mechanism (ETM), investigated through aerodynamic and structural analyses, this study presents an experimental analysis of the SMTE flap equipped with an elephant trunk actuation mechanism. The morphing wing model was prototyped using a 3D printer. Four elephant trunk morphing ribs were embedded inside the flap section, all covered with a flexible skin. The control system for flap actuation was installed in the wing box corresponding to four elephant trunk mechanisms using an appropriate graphical interface to control the SMTE flap deflections. The completed model was further tested in a subsonic wind tunnel to validate the numerical aerodynamic results, as well as the functionality of the elephant trunk mechanism in real conditions. The results confirm the reliability and practicability of the proposed elephant trunk mechanism for actuation, and a very good agreement was obtained between numerical aerodynamic data and wind tunnel test results.

6.1 Introduction

Introducing a novel technology in Engineering, especially in the Aeronautics Industry, requires a comprehensive study of all related disciplines in an interchangeable manner to allow their real-life applications. Given this fact, morphing wing technology (Ameduri & Concilio, 2023; Barbarino et al., 2011), a novel wing technology designed for next-generation aircraft, has been the subject of meticulous studies over the past few decades. It has been evaluated through several disciplines, including aerodynamic design (Barbarino et al., 2011; Jo & Majid, 2022; Körpe, 2014; Wickenheiser & Garcia, 2007), structural analysis (Sicim Demirci et al., 2024; Soneda et al., 2020), flight dynamics (Liauzun et al., 2018; Obradovic & Subbarao, 2011; Xiao et al., 2019), actuation systems (Bourchak et al., 2015; Campanile & Sachau, 2000; Dimino, Flauto, Diodati, et al., 2014; Wang, Xu, & Zhu, 2013), and control (Fonzi, Brunton,

& Fasel, 2020; Moosavian, Xi, & Hashemi, 2013; Parancheerivilakkathil et al., 2024). The development of a morphing wing requires the contribution and integration of multiple disciplines. The promising advantages obtained from aerodynamic and structural studies in the past decades have encouraged further exploration of the practical application of morphing wings in the future. Considering the challenges concerning the practical applications of morphing wings (Jha & Kudva, 2004; Özel, Özbek, & Ekici, 2020; Sofla et al., 2010), comprehensive research covering all disciplines involved is needed. These studies include investigating the reliability of morphing wings in real flight, their manufacturing possibilities and their maintenance cost. A limited number of morphing wing technology applications in real flight have been tested in last decades: a joint project between Flexsys and the US Air Force Research Laboratory (Kota et al., 2009b); the CRIAQ MDO-505, a Canadian-Italian collaborative project (R. M. Botez et al., 2018); the CRIAQ 7.1, a Canadian collaborative project (Popov, Grigorie, Botez, Mamou, & Mebarki, 2010), SARISTU (Carossa et al., 2015) and Clean Sky 2 (Ameduri et al., 2018a) in Europe are just a few. Several studies conducted by testing different types of morphing wings in wind tunnels can be found in the literature.

6.1.1 Literature review

Recent advancements in morphing wing technologies have demonstrated significant potential for improving aerodynamic efficiency, flight control, and operational flexibility. A notable example is the Adaptive Compliant Trailing Edge (ACTE) project, a collaboration between the US Air Force Research Laboratory (AFRL), NASA, and FlexSys Inc. (Kota, Flick, & Collier, 2016). Using a Gulfstream GIII business jet equipped with variable-geometry multifunctional control surfaces, the project successfully validated the FlexFoil material at 40,000 feet and Mach 0.75, eliminating wing-body discontinuities through seamless transition sections.

Efforts to design morphing leading edges have also gained considerable attention. Zhigang (Zhigang et al., 2024) performed an experimental study by focusing on a morphing leading-edge concept. They developed a two-step design process, including the optimization of a variable-thickness composite compliant skin and an inner kinematic mechanism. The skin was optimized using a laminate continuity model with constraints and employed a genetic algorithm to handle discrete and continuous variables. The kinematic mechanism optimization involved a coupled four-bar linkage system, designed to achieve optimal aerodynamic airfoils. Experimental results validated the feasibility of this approach, confirming its effectiveness in achieving the desired morphing functionality.

Similarly, Communier (Communier et al., 2019) presented the design and wind tunnel testing of a Morphing Leading Edge (MLE) system for a medium-range unmanned aerial vehicle. The MLE prototype, made with a simple wooden construction, successfully modified the stall angle without affecting the slope of the lift coefficient versus the angle of attack. However, the servomotor required significantly more power compared to a traditional LE flap.

Beyond leading edge morphing, several studies have concentrated on trailing edge morphing concepts. Jia (Jia et al., 2022) presented the development and testing of a novel compliant morphing wing with a load-bearing morphing trailing edge. Optimized using a multidisciplinary approach, the wing demonstrated stall mitigation, with a 1° delay in stall angle and a 13% increase in post-stall lift. The maximum deflection reached 37.9°, and the wing showed strong load-bearing capability. Experimental and numerical results were in good agreement, although the wing's deformation was limited in the spanwise direction.

The integration of both leading and trailing edge morphing mechanisms has also been investigated for larger aircraft applications. Ricci (Ricci, De Gaspari, & Riccobene, 2016) described the experimental validation of a framework for designing morphing wings using in-house tools. This framework was applied to the design of morphing leading and trailing edges for a regional aircraft. A dedicated wind tunnel test campaign was conducted to validate the morphing devices, focusing on two phases: assessing the morphing shape and evaluating aerodynamic performance. The results showed good accuracy between predicted and measured morphing shapes, demonstrating the effectiveness of topology optimization methods, while the aerodynamic tests confirmed the potential benefits of the morphing surfaces and validated the design process.

Dimino (Dimino et al., 2022) extended these efforts by focusing on manufacturing strategies for compliant structures for a morphing wing with leading and trailing edges. Their study involved the development of a reduced-scale wind tunnel model to validate the proposed morphing concept and to correlate numerical models, emphasizing the importance of material selection and fabrication techniques in achieving successful experimental validations at a small scale. This study outlined the design, manufacturing, and wind tunnel test phases, highlighting the functionality of the morphing surfaces and the successful demonstration of the proposed concept in experimental wind tunnel conditions.

Several researchers have also explored combining multiple morphing strategies. Jeong and Bae (Jeong & Bae, 2022) investigated a morphing wing by combining variable span morphing and variable camber variable chord morphing mechanisms. Their study included wind tunnel and flight tests to evaluate the aerodynamic changes and operational stability of morphing mechanisms. The results confirmed increased lift coefficients and lift-to-drag ratios for morphing mechanisms, especially when morphing mechanisms were combined. However, challenges such as surface deformations of the latex skin during tests were noted, highlighting the need for further material optimization.

Investigations into local morphing applications, such as morphing ailerons, have further highlighted the potential for aerodynamic gains. Botez (Botez et al., 2017) designed, manufactured, and tested a wing-tip model featuring a morphing upper surface and interchangeable ailerons. The experimental results demonstrated that the morphing aileron extended the laminar flow over the wing surface by up to 9% of the chord length and achieved a drag coefficient reduction of up to 9%. These findings underscore the potential of morphing technologies to enhance aerodynamic efficiency by promoting laminar flow and reducing drag.

In addition to structural innovations, bio-inspired approaches have also emerged. Groves-Raines (Groves-Raines et al., 2022) explored the benefits of combining two bio-inspired technologies: wing morphing and distributed pressure sensing. A wind tunnel model was developed with an avian-inspired wing capable of sweep motion, and pressure sensors were distributed across the wing surface. The results showed that the wing sweep could be an effective method for pitch control, enhancing the aircraft's control authority at high angles of attack. Additionally, the pressure sensing system effectively detected the onset of aerodynamic stall, which could be used to implement an early warning stall system.

Finally, recognizing the broader environmental and economic benefits of morphing technologies, Salinas et al. (Salinas, Botez, & Gauthier, 2023) developed a validation methodology for morphing wing, aiming to enhance fuel efficiency and reduce environmental impact. They conducted aerodynamic simulations and wind tunnel testing to assess the wing’s morphing capabilities and optimize wing aerodynamic efficiency. The validation results confirmed that the morphing wing design performed as expected, with the experimental data. These findings validated the effectiveness of the morphing wing in achieving higher aerodynamic performance and lower fuel consumption.

6.1.2 Problem definition

This work presents the final phase of morphing wing development, building upon our aerodynamic analysis of the SMTE flap (Negahban, Bashir, Traisnel, & Botez, 2024). Previous study assessed the aerodynamic performance of the SMTE flap, followed by a structural analysis of the elephant trunk mechanism and flexible skin. With these results in hand, the present study aims to develop a prototype of the UAS-S45 wing, equipped with both the SMTE flap and the ETM to experimentally validate the previous results. To achieve this, a section of the UAS-S45 wing was prototyped. This section integrated the elephant trunk mechanism, flexible skin, and actuation control system within the wing box. The final model consisted of main components, including wing box, four elephant trunks, four actuation motors, and the flexible skin. Figures 6.1 and 6.2 illustrate the UAS-S45 wing equipped with an SMTE flap and the ETM actuation mechanism inside the SMTE flap, respectively.

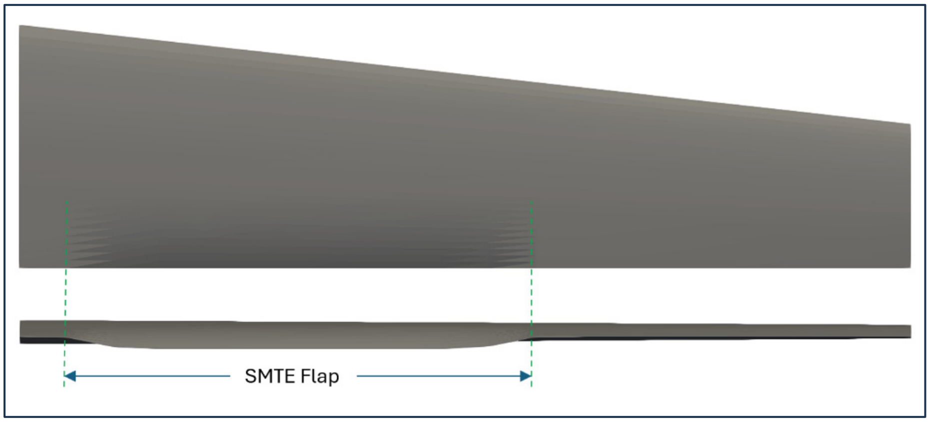

Figure 6.1 Schematic of the UAS-S45 wing equipped with a morphed SMTE flap

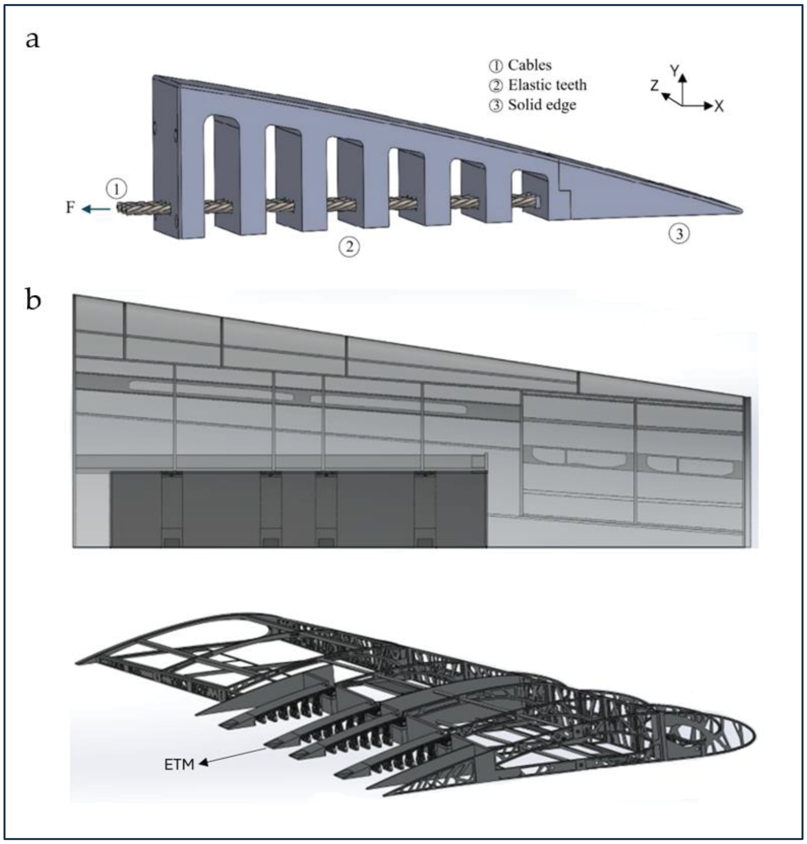

Figure 6.2 Illustration of the a) Elephant Trunk Mechanism (ETM), b) assembly of four ETMs inside the SMTE Flap

Figure 6.1 shows the SMTE flap after morphing. Since there are no discontinuities between the flap and the wing body, the flap was seamlessly integrated with the wing body. Figure 6.2 illustrates the internal wing structure in detail. As shown in Figure 6.2, four ETMs were incorporated inside the SMTE flap, oriented as specified above. Previous studies have conducted both aerodynamic and structural analyses of the SMTE flap and the ETM actuation mechanism (see (Negahban, Bashir, Traisnel, & Botez, 2024) and (Negahban et al., 2025) for more detail).

This study underscores the critical role of precise manufacturing processes and advanced structural innovations in the development of functional and scalable morphing wing systems. By incorporating detailed manufacturing processes into the development of morphing wing systems, this study highlights the critical role that precision in fabrication plays. The integration of manufacturing considerations not only enhance the structural integrity but also ensure that the morphing wing system is ready for real-world application.

In the present study, a section of the UAS-S45 wing was prototyped for its testing in a wind tunnel. The wing section was designed to conform to the dimensions of the wind tunnel. This prototype included the SMTE flap, the ETMs inside the flap, a flexible skin, and an actuation system embedded within the wingbox. Figure 6.3 displays the fully assembled wing section, showcasing all its components.

The assembled prototype underwent several tests in the LARCASE Price-Païdoussis subsonic wind tunnel. During the tests, the real-time actuation of the wing was evaluated at various angles of attack and flap deflections. These tests allowed a performance assessment of the actuation system under operational conditions and facilitated the validation of the experimental data with the numerical aerodynamic results obtained in previous studies.

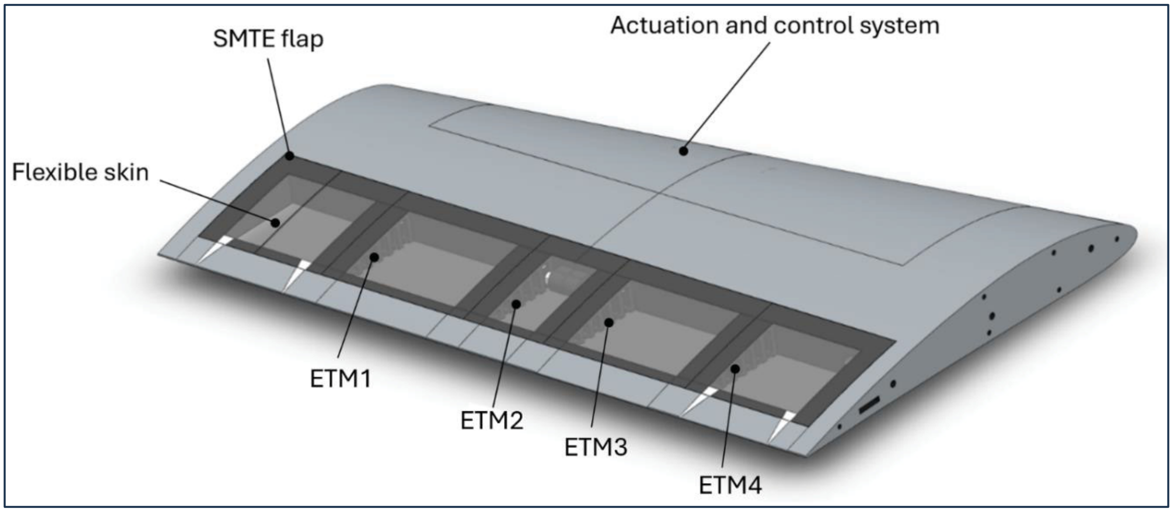

Figure 6.3 Schematic of the UAS-S45 wing section equipped with an SMTE flap, Elephant Trunk Mechanisms (ETMs), flexible skin, and an actuation system

6.2 Design of Experiment (DOE)

This section presents the comprehensive development process of the UAS-S45 wing section, highlighting not only its structural and aerodynamic design but also the integration of advanced prototyping and actuation technologies. Given that the objective of this study is the development of a seamless morphing trailing edge (SMTE) flap system, the manufacturing strategy, in particular the use of additive manufacturing plays a critical role in achieving the desired functional performance in the wind tunnel tests.

6.2.1 Prototyping the UAS-S45 wing section and its ETMs

Prototyping processes have advanced significantly with the advent of 3D printers. This manufacturing technology has revolutionized the industry, making prototyping more accessible, easier, and significantly less expensive than before. Most of the morphing wing prototypes in the literature have been fabricated using 3D printing (Jia et al., 2022; Moulton, 2021; Rivero et al., 2022). Three-dimensional printing is an additive manufacturing process that has offered a fast and cost-efficient approach to manufacturing models for wind tunnel testing. It creates a three-dimensional object by depositing melted polymer layer by layer. The process begins with designing the object in CAD software (SolidWorks 2021). The design is then processed by a slicer, a software that sets printing parameters and object orientations. The slicer divides the object into layers of defined thickness and generates G-codes, which are sent to the 3D printer (Ender 3 Max, Creality, China). The machine interprets these G-codes to control a heated nozzle that extrudes the polymer filament, “drawing” the object line by line and layer by layer.

The 3D printing parameters are critical for determining the mechanical properties and surface finish of the printed object, while the orientation of the object during printing is equally crucial. Similar to conventional composite materials, the mechanical properties of 3D-printed objects are anisotropic. In composite materials, fibers aligned in the direction of the applied load exhibit superior mechanical properties to those aligned in the perpendicular direction of the applied load. Likewise, 3D-printed objects, constructed layer by layer and line by line, display mechanical behavior resembling that of composites. In this case, the melted filament serves simultaneously as a fiber, as well as a matrix. Forces applied perpendicular to the layers can cause delamination, as the interface between layers, rather than the continuous fibers, must bear the load. This fact highlights the importance of optimizing printing parameters and arrangements to achieve desired mechanical performance. Figure 6.4 shows the vertical and horizontal arrangements.

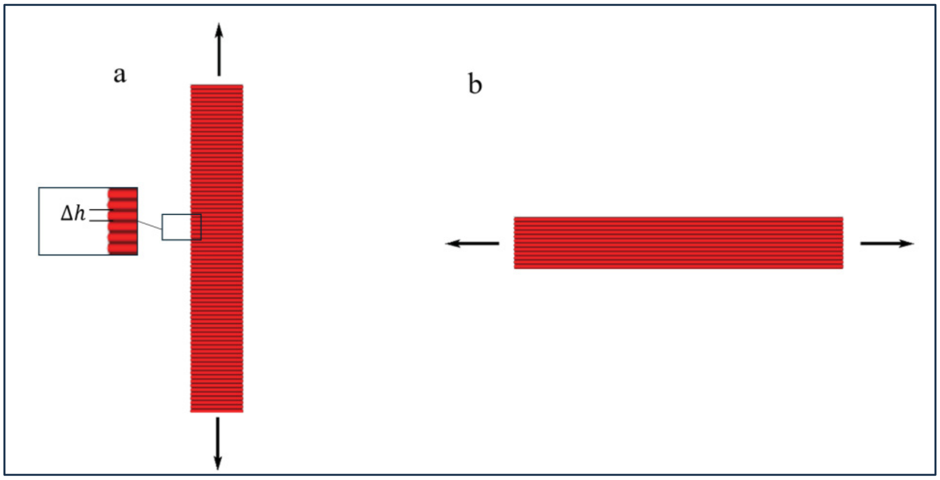

Figure 6.4 Three-dimensional printing layer arrangements, a) vertical, b) horizontal

As shown in Figure 6.4, each layer in 3D printing has a specific height (Δh), representing a 2D slice of the studied object. Each layer is supported by the layer directly beneath it. However, if an object contains a cantilever or an overhanging part, the first layer of the cantilever will lack underlying support. To address this issue, the slicer automatically generates a block of support material beneath the overhang part. These supports are typically considered as waste material and are removed during post-processing. Optimizing the orientation and positioning of the object can significantly improve its mechanical properties while reducing printing costs and time by minimizing the need for support structures.

In this study, the vertical arrangement is chosen for printing due to the wing's curved upper and lower surfaces. Printing these surfaces with greater accuracy is more easily achieved using the vertical orientation than with a horizontal arrangement. Figure 6.5 shows the vertically arranged wing section during its 3D printing.

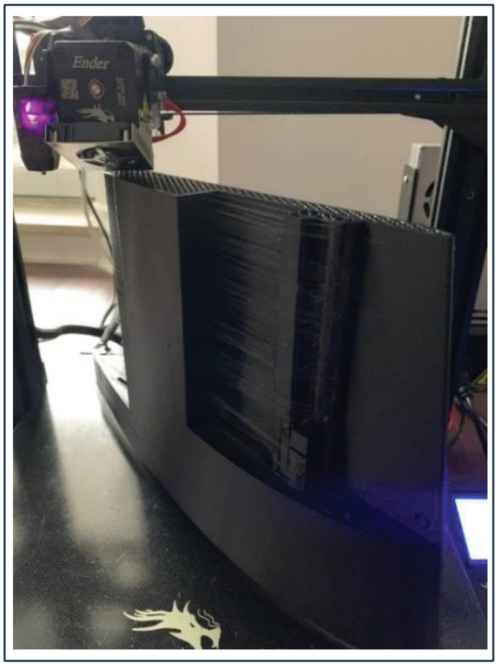

Figure 6.5 Three-dimensional printing of the wing section with vertical arrangement

The material used for the wing section is PLA+, an enhanced version of regular PLA with additives that improve surface finish and simplify the printing process. The primary properties of PLA+ are provided in Table 6.1, as specified by the filament manufacturer (Farnell, 2025).

Table 6.1 Physical and mechanical properties of the PLA+

Property	**Value**
Density (g/cm^3)	1.23
Melt Flow Index (190°C/2.16kg)	5
Tensile Strength (MPa)	63
Elongation at Break (%)	20
Flexural Strength (MPa)	74
Flexural Modulus (MPa)	1973
Heat Distortion Temperature (°C)	53

Based on the results obtained from the structural analysis in the previous work (Negahban et al., 2025), the material selected for the ETMs was nylon. Nylon's exceptional mechanical properties made it an ideal material for structural components in the elephant trunk mechanism. Its high tensile strength and flexibility support material elastic deformation during flight, while its low friction coefficient ensures smooth cable motion within its tooth-like components. Additionally, nylon's light weight reduced the mechanism's overall mass, enhancing energy efficiency and minimizing aerodynamic loads (Negahban et al., 2025). Table 6.2 depicts the nylons' material properties.

Table 6.2 Material properties of nylon

Young's modulus (MPa)	**Poisson's ratio**	**Density (kg/m^3)**	**Yield strength (MPa)**
2960	0.41	1140	75

The ETMs were printed in vertical direction in the same way as for the wing box, to ensure the highest level of precision. They were produced in batches (containing 6 ETMs) to enhance printing accuracy and maintain material uniform shapes. Figure 6.6 illustrates the printed ETMs.

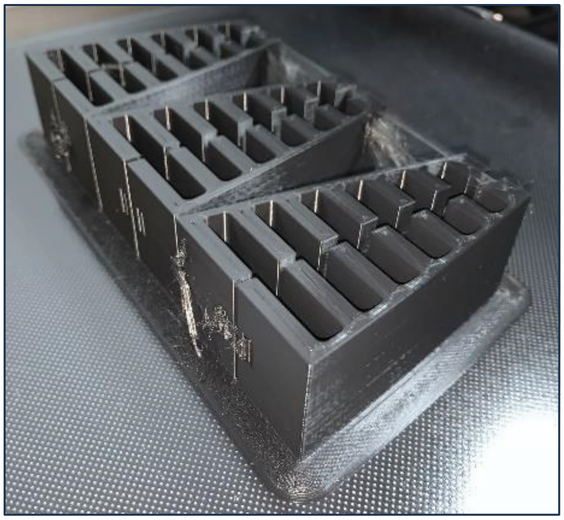

Figure 6.6 A batch of 3D printed EMTs

6.2.2 Printing setup

The final part's quality and functionality are greatly influenced by the printing parameters. The surface smoothness, dimensional accuracy, and mechanical characteristics of the printed product are directly impacted by variables such as layer height, nozzle temperature, printing speed, infill density, and cooling parameters. For example, higher nozzle temperatures can improve layer adhesion at the expense of possible material deterioration, whereas lower layer heights produce smoother surfaces but increase the printing times. Optimizing the infill pattern and density according to its intended use is crucial because these factors also affect the part's weight and structural integrity. Adjusting these factors not only guarantee excellent part quality, but it also minimizes material waste, and production time. The main printing parameters used in this study are presented in Table 6.3.

Table 6.3 Printing parameters

Property	**Value**
Layer height (mm)	0.2
Line width (mm)	0.4
Wall thickness (mm)	2
Top/bottom thickness (mm)	2
Infill density (%)	30
Printing temperature (°C)	200
Build plate temperature (°C)	60
Print speed (mm/s)	50
Wall print speed (mm/s)	15
Build plate adhesion type	Brim

To reduce weight, cost, and printing time, slicer software offers an infill feature that hollows out the interior of the part and replaces it with a geometrically and mechanically stable structures, such as cubic grids, triangles, or honeycomb patterns. This technique significantly decreases the number of printed lines per layer, reducing printing time and, most importantly, minimizing structural weight. Additionally, the infill structure enhances the part's stiffness, ensuring that the part maintains its strength while using less material. In this study, a triangular infill pattern was used for the wing box, as shown in Figure 6.7. By optimizing the printing parameters, the printing process was completed in a total time of 21 days, and consumed approximately 2 kg of PLA+ material.

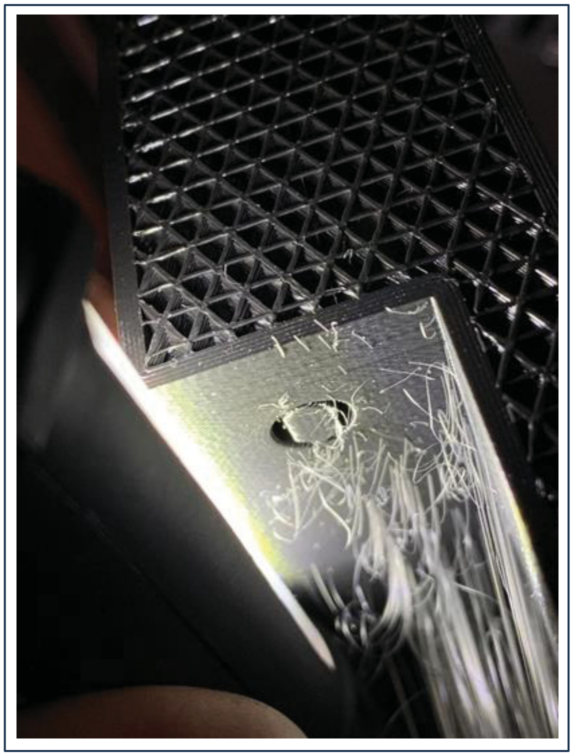

Figure 6.7 Triangular infill pattern of the UAS-S45 wing box

6.2.3 Post-printing

After printing the main wing section and the ETMs, they were installed in the SMTE flap section. Subsequently, the wing section prototype underwent a meticulous post-processing phase to enhance its surface quality. Sanding was done to remove the visible demarcations and irregularities created by the layering effect of the 3D printing process. This step ensured a seamless and smooth surface, critical for reducing surface roughness, and avoiding any unintended aerodynamic effects during testing. Once the sanding was completed, the wing section was painted with two layers of automotive-grade spray paint to reach this gloss finish. This final step ensured the prototype's readiness for wind tunnel testing, as surface smoothness is crucial for accurate aerodynamic measurements and performance evaluation. Figure 6.8 shows the wing section before and after painting.

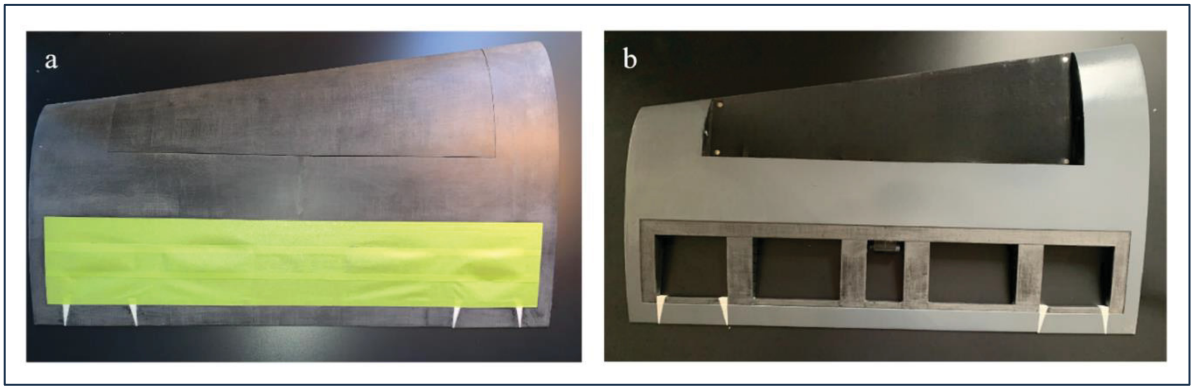

Figure 6.8 Schematics of UAS-S45 wing section, a) before, b) after painting

As shown in Figure 6.8-b, the surface exhibits a smooth, polished finish, making it suitable for subsequent wind tunnel tests. Additionally, Figure 6.8-b illustrates the allocated space for the actuation system located at the leading edge of the wing, covered by a magnetic fairing designed to embed the wiring and actuation servo motors. This fairing ensures a smooth aerodynamic surface by eliminating external fasteners, which is particularly critical for preserving flow integrity during wind tunnel testing. The localized magnetic field prevents interference with the servo motors, maintaining both mechanical stability and electronic reliability.

6.2.4 Actuation control system

The wing section was fully assembled with its four servo motors, cables, Gate Tooth 2 (GT2) pulleys, and wiring harness. The wiring harness was carefully arranged and secured to manage the bulkiness within the actuation housing, ensuring an organized layout. Figure 6.9 shows the assembled wing section, highlighting the placement of the servo motors, GT2 pulleys, cables, wiring, and their fixed positions.

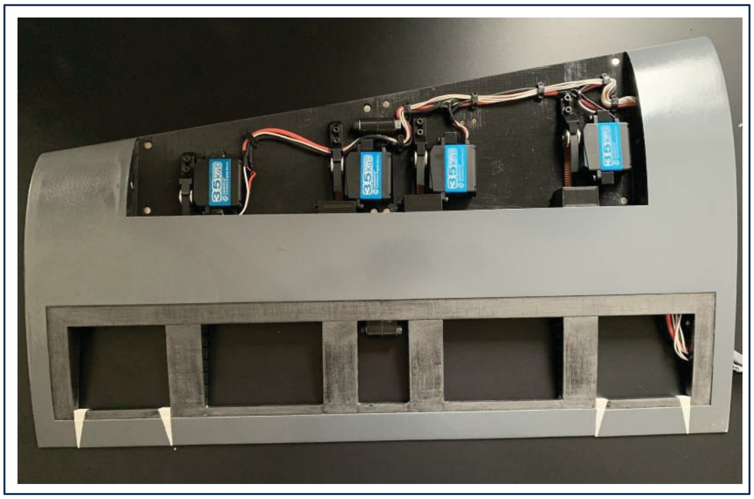

Figure 6.9 The final assembly of the actuation system inside the wingbox

The SMTE flap actuation with ETMs was achieved by applying a horizontal tensile force to the cables using four servo motors, one for each of the four ETMs. These motors are highly precise and strong, capable of applying and maintaining adequate torque. Each servo motor typically has three terminals: Common Collector Voltage (VCC), Ground (GND), and Pulse With Modulation (PWM). The PWM terminal receives a 50 Hz square wave signal (ranging from 0V to 5V in this study) sent every 20 milliseconds, where the pulse width represents the input data (Figure 6.10).

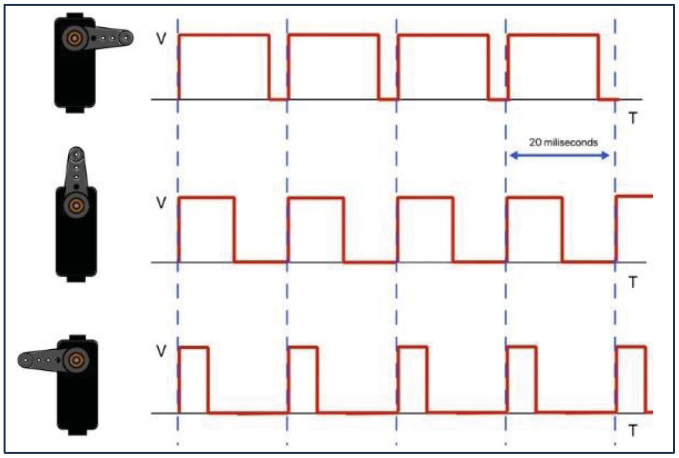

Figure 6.10 The correlation between the pulse width and the position of the servo motor

The larger the pulse is, the more the shaft rotates counterclockwise and vice-versa. Therefore, to obtain a certain shaft position and maintain it, a constant PWM signal should be provided continuously. To transfer the shaft torque into a linear force, GT2 pulleys are used. Figure 6.11 shows the pulleys embedded in the wing box.

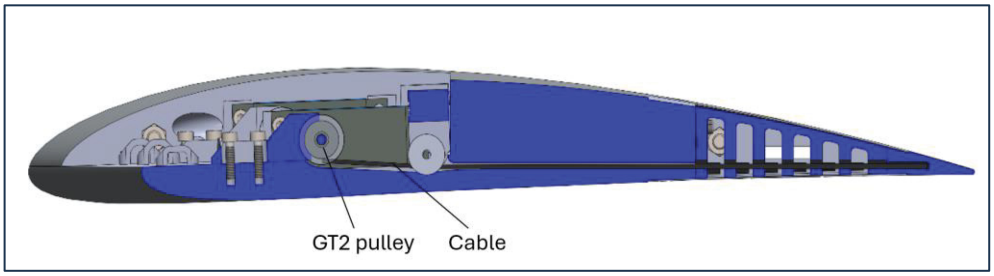

Figure 6.11 Cross-section view of the control system in the wing box with GT2 pulley

6.2.5 Implementation of flexible skin

The SMTE flap is composed of two main components: (1) the middle flap section, which undergoes upward and downward bending deformations; and (2) the transition sections on the right and left sides, which adapt to the deformation of the middle flap. The transition sections experience twist deformation due to their attachment to both rigid wing structure and the SMTE flap. Consequently, these sections require enhanced flexibility of the skin material. To accommodate complex deformation patterns, a flexible skin material with suitable mechanical properties was selected to allow elasticity for tension in the upper skin and compression in the lower skin.

In previous work (Negahban et al., 2025), two materials were tested for the skin: (1) Thermoplastic Polyurethane (TPU), an elastic polymer widely used in 3D printing; and (2) silicone rubber. A preliminary skin analysis was conducted in ANSYS 2021 R2 to evaluate the suitability of these materials (see (Negahban et al., 2025) for more details). The TPU exhibited yielding under tension in long runs, likely due to stress relaxation. This behavior was attributed to the release of residual stresses induced during manufacturing when subjected to a constant constraint over time, even within the elastic limit. In contrast, in terms of stretchability and elongation, silicone rubber was an extremely soft and flexible material. Its extended fatigue resistance made it a very good option for morphing wings, as repeated deformations during flight require a material with a very strong fatigue resistance. As a result, it retained its flexibility through repeated morphing without a noticeable material deterioration. Therefore, it demonstrated an excellent performance in supporting the morphing capabilities of the transition sections. Based on these findings, the TPU was replaced with silicone rubber for the skin material. Table 6.4 summarizes the material properties of silicone rubber.

Table 6.4. Material properties of silicon rubber (Negahban et al., 2025)

Young's modulus (MPa)	**Poisson ratio**	**Tensile yield strength (MPa)**	**Density (kg/m^3)**
17	0.5	10.4	1230

However, even with silicone rubber, the buckling contraction on the wing lower surface remained unchanged, and the creation of waves on the lower skin was observed. This buckling of the skin was due to its low stiffness and high slenderness ratio. In the structural analysis, for a longitudinal compression of a column, slenderness is defined as the ratio between the section and the length of the column. The higher this ratio is, the more the structure tends to buckle. The slender ratio is given by:

$$\lambda = \frac{l}{\sqrt{I/A}} \tag{6.1}$$

where l is the effective length, I denotes the second moment of inertia, and A is the section of the column.

To address the buckling issue on the wing lower surface, a solution was obtained without altering the skin material. Since buckling occurs only under compression, the solution was to maintain tension within the working range of the skin. To ensure uniform tension across the entire skin and to maintain consistent tension across all skin panels, a screw-driven pre-tensioning device was designed and 3D-printed. This device securely grasps both sides of the skin panel, and by turning two long screws, the distance between the jaws increases, thereby applying uniform tension along the panel. The applied tension can then be accurately measured using a caliper. Figure 6.12 illustrates the pre-tensioning device.

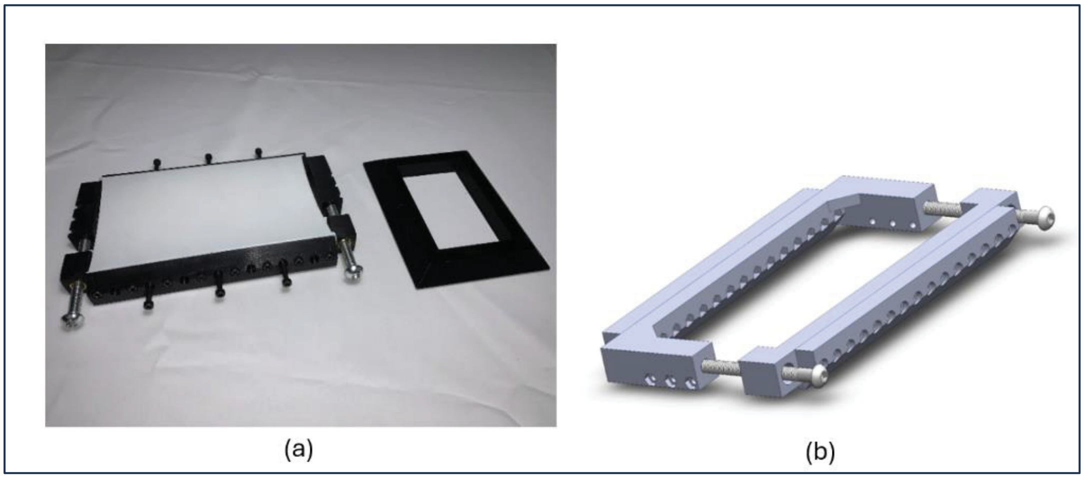

Figure 6.12 Schematics of pre-tensioning device for flexible skin. a) fabricated model, b) CAD design model

As shown in Figure 6.12, the skin was first laid down using the pre-tensioning device. It was clamped between the two jaws and then tensioned by tightening the long screws. An elongation of 40% was applied, which corresponded to 32mm for a 75mm skin panel at rest. After applying the intended tension to the skin, it was secured in its designated position using cyanoacrylate glue, which was precisely applied with surgical syringes equipped with non-sharp needles. Figure 6.13 shows the procedure for attaching the SMTE skin to the flap.

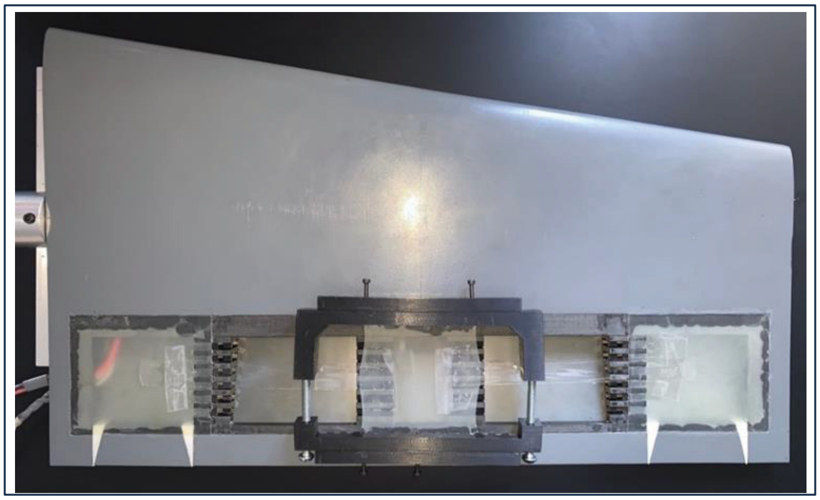

Figure 6.13 Attachment of the flexible skin on the lower surface of the SMTE flap using the pretension tool

6.2.6 Graphical User Interface (GUI)

To control the deformation of the morphing wing, the LABVIEW 2021 software was used that allowed for the design of a Graphical User Interface (GUI) and communication with external devices via USB or serial ports. LABVIEW is typically used with data acquisition cards provided by National Instruments. However, in this study, an Arduino Uno was utilized, which had a resolution of 10 bits, suitable for this case, and which can handle PWM signals on certain GPIO (General Purpose Input Output) pins. The LINX library was utilized to control the Arduino with the LabVIEW interface.

Since each elephant trunk mechanism is independent and therefore has its own servo motor, the tension between the cables cannot be the same without calibration. The program includes an adjustment section with which each motor can be controlled separately, while the flap is managed via the Global Angle Control section. The serial port setting allows the selection of the communication port for the Arduino board. Finally, the servo pin number option allows the selection of the PWM GPIO terminals where each motor is connected. Figure 6.14 illustrates this GUI.

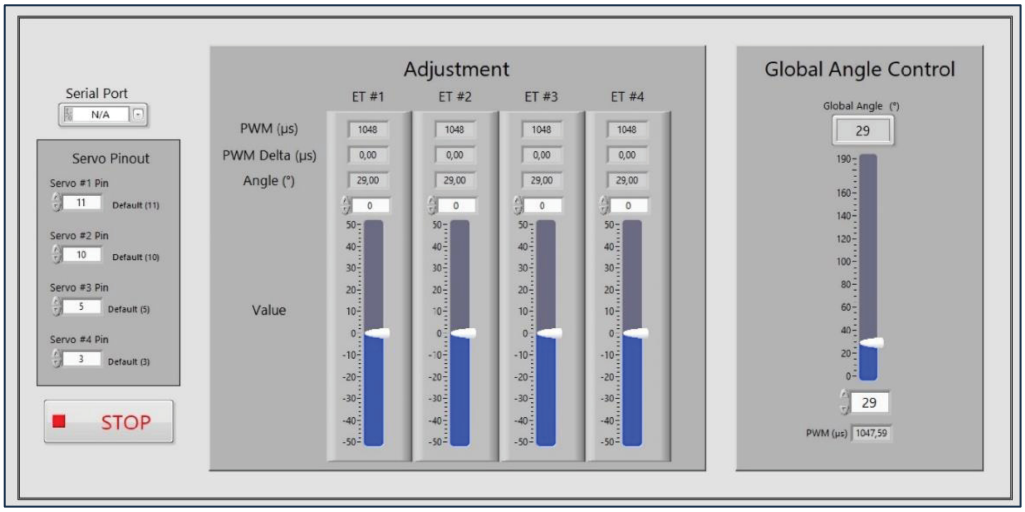

Serial Port: N/A

Servo #1 Pin: 11 Default (11)
Servo #2 Pin: 10 Default (10)
Servo #3 Pin: 5 Default (5)
Servo #4 Pin: 3 Default (3)

	ET #1	ET #2	ET #3	ET #4
PWM (µs)	1048	1048	1048	1048
PWM Delta (µs)	0,00	0,00	0,00	0,00
Angle (°)	29,00	29,00	29,00	29,00
Value	0	0	0	0

Global Angle (°): 29
29
PWM (µs): 1047,59

Figure 6.14 Graphical user interface for controlling the deflection of the SMTE flap

A precision dial indicator was used to calibrate the ETMs. The calibration process was the following:

- The wing was placed flat on the lower skin on a flat surface (measuring marble), with the flap section extended on a cantilever.
- It was then clamped to the marble, and the precision dial was positioned vertically on the trailing edge.
- The wing was then connected to the Arduino board and the power supply, and the Morphing Wing Controller Program was initiated.
- The value of the slider corresponding to the ETM being measured with the precision dial was adjusted.
- This value was incremented by the minimum amount until the needle on the dial moved.
- The value was then incremented backwards, and the reading was recorded.

The final value was the calibration value used to zero the deflections of their corresponding ETM. Each ETM must have its own calibration value. To calibrate each ETM, all the other ETM adjustment sliders should be set to zero, which ensures that only the tension of the measured ETM is considered when reading the dial. There should be four calibration values for the wing; however, disassembling the servo motors cancels the calibration, and for this reason, the calibration process must be repeated.

To test the Morphing Wing Controller program and make its adjustments, the wiring harness is connected to the Arduino board as shown in Figure 6.15.

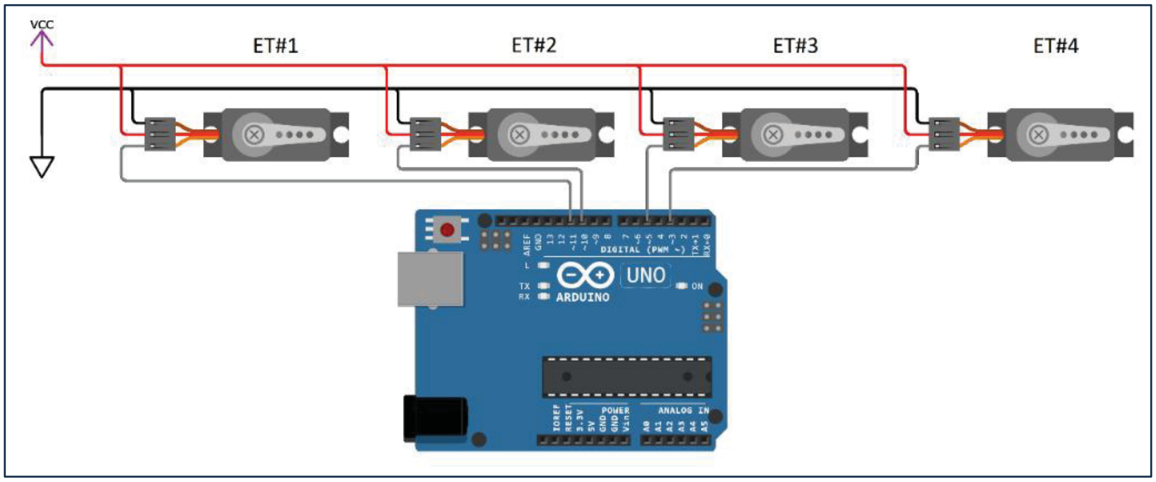

Figure 6.15 Electrical diagram of the actuation system

6.3 Results and Discussion

6.3.1 Pre-Wind Tunnel Evaluations

After the full assembly of the morphing wing, including the 3D-printed wing box, embedded ETMs, internal actuation system, and flexible skin, the feasibility of the deformation was tested for its various magnitudes. Two main goals must be achieved:1- ensuring the smooth deformation of the ETMs; and 2- maintaining the flexibility of the skin, particularly in the transition sections, where twist deformations occur.

Prior to testing the full assembly, each critical component was evaluated independently, which included examining the deformation behavior of the ETMs and the performance of the transition section. Figure 6.16 illustrates an ETM after undergoing deformation.

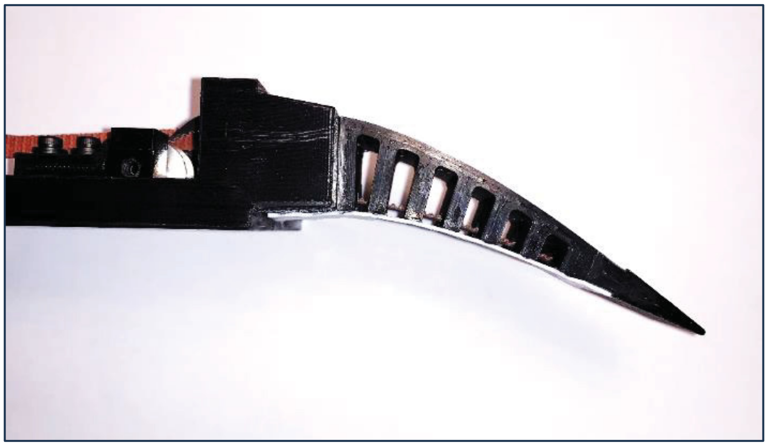

Figure 6.16 ETM after deformation

As shown in Figure 6.16, the skin deforms smoothly without any signs of buckling on the wing lower surface, which is attributed to the pre-tensioning applied to the skin prior to its attachment to ETM, as discussed in Section 6.2.5. Furthermore, the deformation of the ETM was smooth and aligns very well with the results obtained from the structural analysis presented in (Negahban et al., 2025).

Another critical component of the SMTE flap system is its transition sections. These sections were located between the solid wing box and the ETM on the left and right sides of the SMTE flap. The transition sections were covered with flexible skin, which plays a vital role in connecting the morphing section to the solid wingbox. Due to this connection, twist morphing occurred in the transition sections, making the flexible skin essential for accommodating the deformation while maintaining its structural integrity. Additionally, the twist morphing in the transition sections also affected the flaps' solid edges. To mitigate the deformation and reduce stress concentrations at the flaps' solid edges, two triangular flexible rubber components with the same cross-section as the flap edge were incorporated. These rubber components effectively moderated the deformation and enhanced the durability of the solid edges. Figure 6.17 illustrates the experimental setup for testing the transition sections, while Figure 6.18 depicts the transition sections before and after morphing.

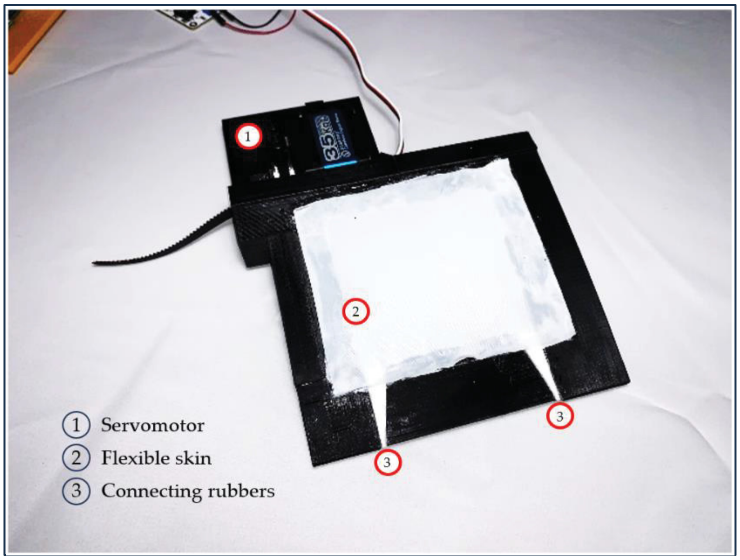

Figure 6.17 Transition section with its corresponding components

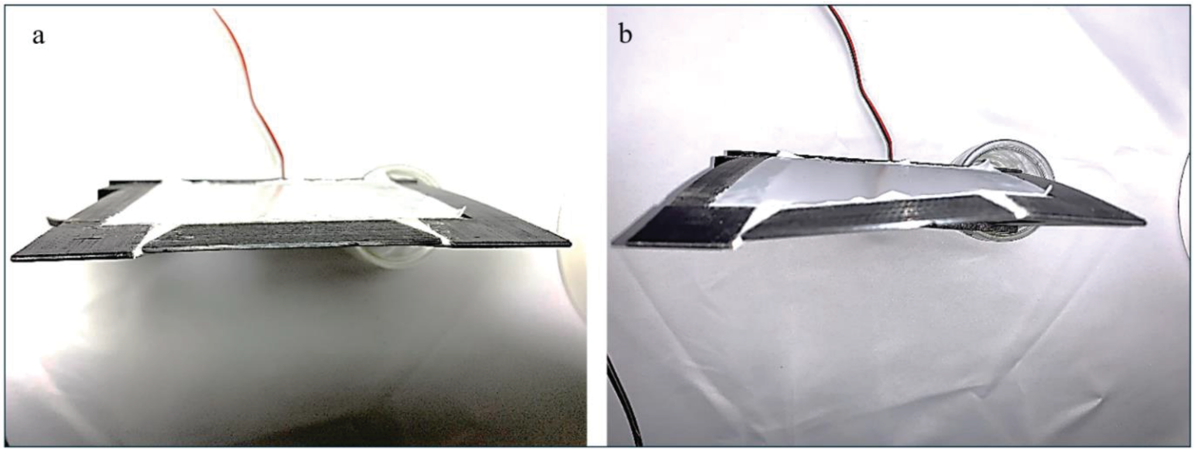

Figure 6.18 Transition section: a) before, and b) after morphing

As illustrated in Figure 6.18-a, the connecting rubber components are incorporated along the solid edge. These components effectively smooth out the deformation of the transition section, as shown in Figure 6.18-b. While a simple solid connection, over time, would increase the likelihood of failure in the transition sections, incorporating these flexible connections mitigates this risk by accommodating deformation. Furthermore, Figure 6.18-b also shows that the flexible skin exhibits smooth and consistent behavior throughout the morphing process, enhancing the overall reliability of the system.

6.3.2 Price-Païdoussis Subsonic Wind Tunnel

The final test of the complete assembly of the morphing wing was conducted using the Open Return Price-Païdoussis Subsonic Wind Tunnel at LARCASE laboratory, depicted in Figure 6.19-a. As illustrated in detail in Figure 6.19-b, the wind tunnel is composed of a centrifugal fan, a diffusing and settling chamber, a contraction section, and a test chamber or test section. Two inlets on either side of the centrifugal fan allow the air supply to enter the wind tunnel. Within the sealed section, the engine and centrifugal fan are shielded from dust particles.

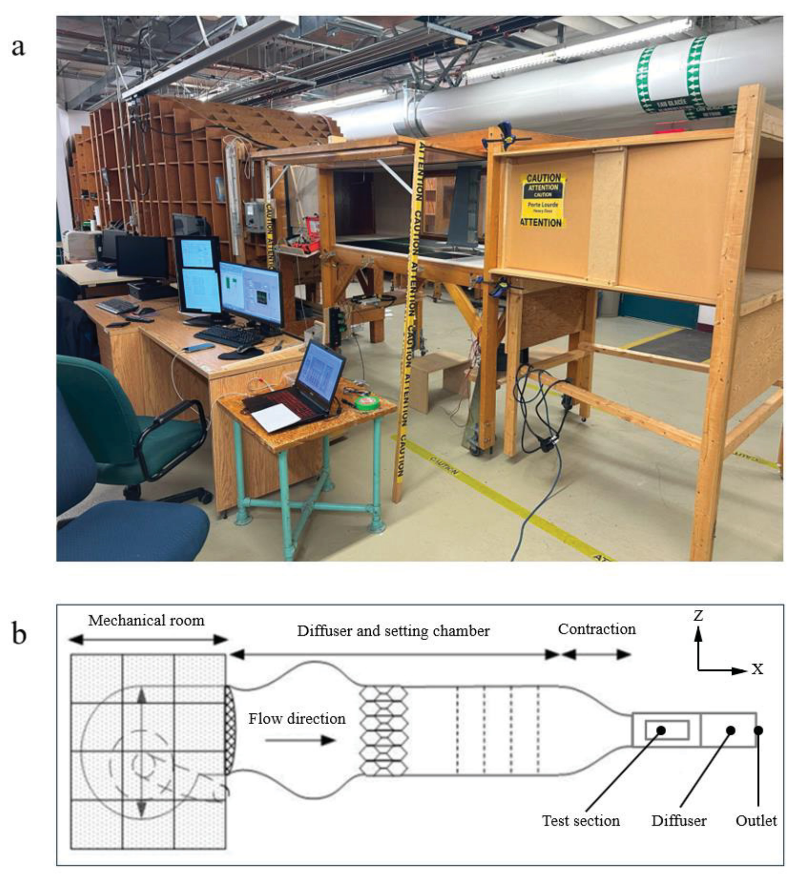

Figure 6.19 Price-Païdoussis Subsonic Wind Tunnel: a) actual model, b) schematic of sections with coordinates

6.3.3 Wind Tunnel Test Preparation

The calibration phase, which involved determining the flow parameters inside the test chamber, was a crucial step to complete prior to experimental testing. The primary parameters used to describe the flow in a wind tunnel test included the total, static, and dynamic pressures; the temperature variation during the test; the controlled flow speeds; and the Reynolds number. Temperature and pressure values are essential for calculating air density and flow rate. In the wind tunnel, temperature was measured using a Type K thermocouple sensor with an accuracy of ±0.5°C. The physical forces were digitized using a National Instruments USB-6210 multifunction data acquisition system, enabling the software to process the data.

After calibrating the wind tunnel, the prototyped morphing wing was mounted in the test section using appropriate fixations. The test section had dimensions of 0.62 m in height, 0.91 m in width, and 1.83 m in length, with a maximum speed capacity of 0.1 Mach (35 m/s). The air speed used in the previous aerodynamic study, and to be used in the wind tunnel for validation, was 28.3 m/s, well below the maximum limit of 50 m/s. Figure 6.20 shows the UAS-S45 morphing wing section installed in the wind tunnel.

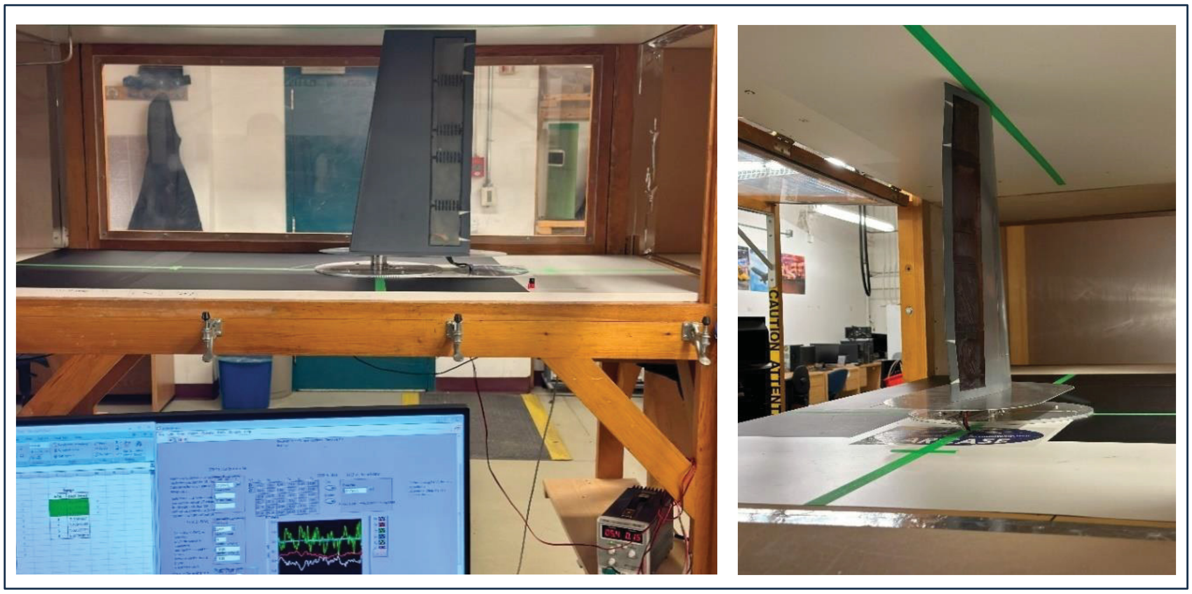

Figure 6.20 UAS-S45 morphing wing section installed in the wind tunnel test section

When models are tested in wind tunnels for performance evaluations, the airflow they encounter differs from the conditions they would experience in an open-air environment (Khalid, Juhany, & Hafez, 2018). Therefore, wind tunnel experiments have several limitations, primarily related to the thickness of the boundary layer, the scale and size of the models, obstruction effects adjustments, and levels of turbulence flow intensities, even for the same flow conditions. The two primary sources of error in subsonic flow experimentation are: (1) alterations in the flow field caused by flow confinement around the body; and (2) the flow interaction with the wind tunnel boundary (closed walls), which is represented by the obstruction, and wall interference.

The corrections of these flow effects in wind tunnel data can be addressed through various methods. To reduce uncertainties in the results, model scaling is often applied whenever is feasible to achieve a blockage area ratio of smaller than 10%. Despite the benefits of reduced-scale models for mitigating interference and blockage effects, their application can give inaccurate results. In this study, the wing was positioned at the center of the test section, as shown in Figure 6.20. The prototype model was scaled by a factor of 0.466 to accommodate the test section dimensions and the resulting blockage ratio was calculated to be 5.2%, which was below the acceptable blockage limit. Table 6.5 shows the air conditions inside the test section.

Table 6.5 Air properties inside the wind tunnel test section

Air density (Kg/m^3)	**Temperature (°C)**	**Relative humidity (%)**	**Air speed (m/s)**	**Pressure (kPa)**
1.19	22.6	34	28.3	101.6

6.3.4 Wind Tunnel Test Results-Comparison of Numerical and Experimental Data

A total of 11 distinct test sets were conducted in the wind tunnel, for various angles of attack and flap deflections. As the angle of attack increased, the deflection of the SMTE flap decreased. The flap deflection values at each angle of attack were obtained from a prior aerodynamic study. To ensure consistency of the results, Computational Fluid Dynamics (CFD) simulations were conducted using OpenFOAM, replicating the flow conditions and scaling of the wind tunnel experiments. The computational domain dimensions were selected to match the wind tunnel test section, with a height of 0.62 m, a width of 0.91 m, and a length of 1.83 m. Therefore, the effects of the tunnel walls on the flow field are inherently captured in the CFD model.

The simulations were conducted using the same free-stream velocity as in the experi-ments, 28.3 m/s, corresponding to the same Reynolds number based on the reference chord length. The fluid was modeled as incompressible, and the Reynolds-Averaged Na-vier-Stokes (RANS) equations were solved to capture the steady-state flow behavior. To account for turbulence effects, the Spalart-Allmaras turbulence model was employed. After conducting a mesh independence study, the final computational grid consisted of approximately 4,465,431 cells. Boundary conditions included uniform velocity inlet, static pressure outlet, and no-slip conditions on solid surfaces. These simulations allowed for a direct comparison between the experimental and CFD results. The results from both the wind tunnel tests and CFD simulations, along with their associated errors, are presented in Table 6.6.

Table 6.6 Comparison of wind tunnel test and CFD results

AOA (°)	**Flap Vertical Displacement (mm)**	**CFD**		**Wind tunnel**		**Error (%)**	
		C_L	**C_D**	**C_L**	**C_D**	**C_L**	**C_D**
0	30.815	0.1371	0.0110	0.1412	0.01201	3.98	7.30
1	25.132	0.1418	0.0109	0.1380	0.01103	3.03	1.20
2	20.630	0.1487	0.0108	0.1515	0.01043	1.69	3.46
3	17.594	0.1579	0.0108	0.1613	0.01047	3.91	3.02
4	15.086	0.1694	0.0109	0.1648	0.01165	2.39	6.87
5	13.405	0.1829	0.0111	0.1762	0.01144	3.40	3.04
6	11.419	0.1985	0.0113	0.2021	0.01092	4.04	3.36
7	10.734	0.2165	0.0116	0.2251	0.01195	0.88	3.02
8	10.062	0.2370	0.0120	0.2313	0.01135	1.02	5.38
9	8.030	0.2603	0.0124	0.2557	0.01320	4.06	6.45
10	5.157	0.2865	0.0128	0.2974	0.01253	2.18	2.12
11	3.048	0.3157	0.0133	0.3032	0.01258	1.93	5.40

Table 6.6 shows that the numerical and experimental results are in very good agreement for both C_L and C_D. The maximum error occurred in the C_D results, reaching up to 7.3%, while the maximum error for C_L is 4.06%. These differences arise from various uncertainty factors in the wind tunnel tests, with drag force being more affected than lift force. However, both errors for C_L and C_D remain within an acceptable range and demonstrate strong agreement with the numerical results. Figure 6.21 presents the variations of C_L and C_D with angle of attack along with their relative errors.

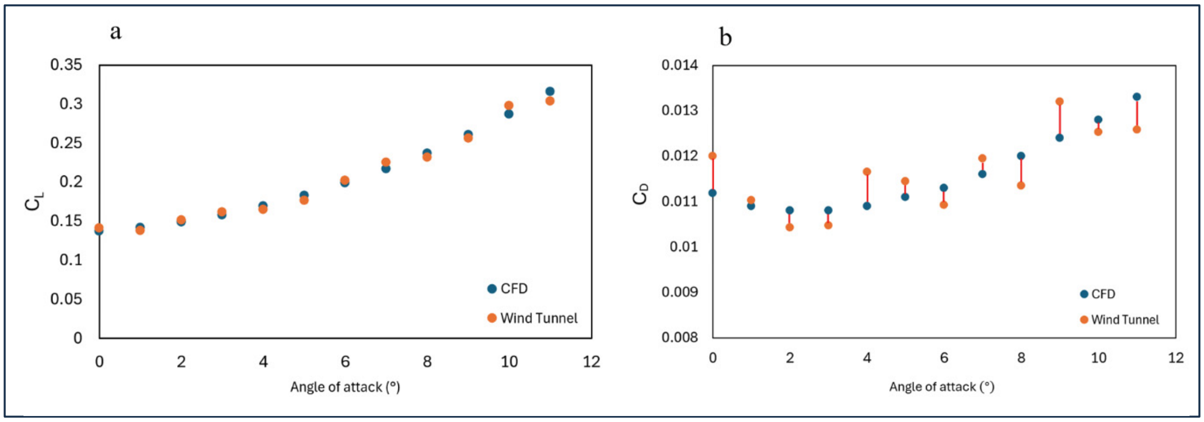

Figure 6.21 Comparison of CFD and wind tunnel results of a) lift and b) drag coefficients variations with angle of attack

As shown in Figure 6.21, both data sets exhibit an increasing trend with angle of attack. However, the rate at which C_L increases with the variation of the angle of attack is higher than that of C_D. This observation also validates the findings of our recent aerodynamic study (Negahban, Bashir, Traisnel, & Botez, 2024), which reported similar variation trends for both C_L and C_D.

6.3.5 Wind Tunnel Test Results - Structural Feasibility of ETMs and Flexible Skin

Beyond validating the numerical results, the wind tunnel tests also aimed to assess the structural integrity and feasibility of the ETMs and flexible skin for SMTE flap morphing. Throughout all 11 tests, the deformation of the ETMs and the performance of the flexible skin were carefully observed. The results of the structural analysis in (Negahban et al., 2025) showed that the ETM could achieve the minimum required deflection of 66 mm. This was confirmed by experimental tests, where the vertical flap deflection reached 30.815 mm (Table 6), which corresponds to 66.13 mm when scaled by a factor of 0.466. Figure 6.22 presents the SMTE flap after its morphing.

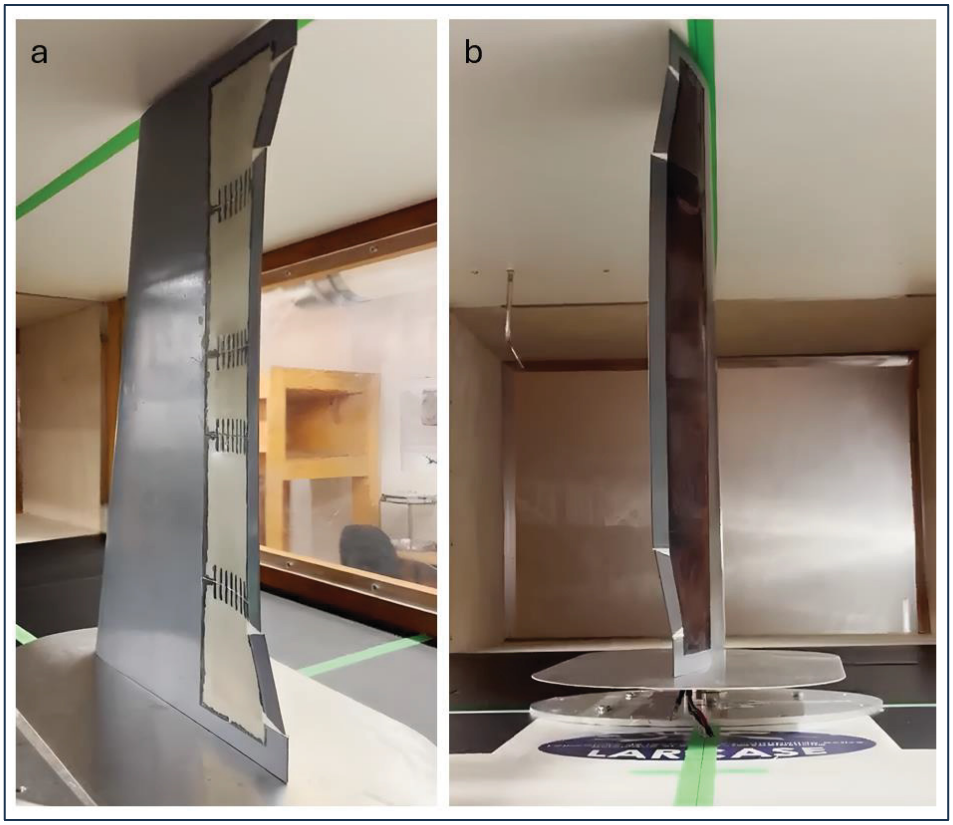

Figure 6.22 UAS-S45 wing section with SMTE flap after morphing in the wind tunnel: a) lower surface view, b) upper surface view

As mentioned in Section 6.2.5, the buckling behavior of the flexible skin was mitigated by pre-tensioning the skin before attachment to the SMTE flap's lower surface using a screw-driven pre-tensioning device. Figure 6.22-a illustrates the lower surface of the SMTE flap at its maximum deflection. As shown in this Figure, no buckling signs are present, and the skin maintains a smooth surface across the entire flap, demonstrating the effectiveness of the flexible skin. Additionally, through continuous variation of the SMTE flap deflection angle, it was confirmed that all four ETMs, along with the connecting rubbers in the transition sections, worked properly without any malfunctions (Figure 6.22-b).

6.4 Conclusion

Based on the successful aerodynamic and structural analyses conducted in previous studies, the present work aimed to experimentally validate the obtained numerical results and therefore develop a practical model of the proposed morphing designs: the Seamless Morphing Trailing Edge (SMTE) flap and the Elephant Trunk Mechanism (ETM). The final stage of this project involved prototyping and testing the feasibility of the SMTE flap and the ETM-based actuation system, resulting in the development of a morphing trailing edge flap for the UAS-S45 wing.

The prototyping process comprised multiple stages, including the 3D printing of the wingbox and the ETMs, integration of the actuation system within the wing structure, attachment of the silicone rubber flexible skin to the SMTE flap, and the development of a control system using a Graphical User Interface (GUI). A series of tests were conducted to assess the feasibility and reliability of various structural components. These tests included individual ETM evaluations, transition section tests, and flexible skin assessments prior to full-wing assembly.

Upon successful completion of these tests, the design's reliability and practicality were confirmed. The experimental results validated the smooth deformability of the ETMs and of the transition sections, aligning with the numerical findings from previous structural analyses. Additionally, a key issue identified in prior studies—skin buckling on the lower flap surface—was effectively mitigated by employing a pre-tensioning tool to stretch the skin before attachment. To further enhance the performance, flexible rubber connectors were introduced in the transition sections to minimize stress concentrations along the flap's solid edges.

Following its full assembly, the morphing wing model underwent wind tunnel testing. A total of 11 tests were conducted, varying both the angle of attack and flap deflection angles. To complement these experiments, Computational Fluid Dynamics (CFD) simulations were performed under identical flight conditions, test constraints, and parameters. The lift coefficient (CL) and drag coefficient (CD) obtained from CFD closely matched the experimental results, with maximum discrepancies of 4.06% and 7.3%, respectively. These variations are within acceptable ranges and underscore the reliability of the numerical models. This strong agreement with experimental data, confirmed the validity of the aerodynamic findings obtained in previous study.

Furthermore, the structural performance of the ETM was quantitatively validated through both numerical and experimental results. Previous structural analyses demonstrated the ETM's ability to achieve a minimum required flap tip deflection of 66 mm. In the wind tunnel experiments, the SMTE flap exhibited a vertical displacement of 30.815 mm. Given that the test model was constructed at 46.6% of the full-scale size, this measured dis-placement translates to 66.13 mm in actual scale, thereby confirming the ETM's effective-ness in achieving the target deflection range.

This research successfully validated the aerodynamic and structural performance of the proposed morphing wing model. Future studies will focus on exploring additional aerodynamic phenomena, including flow separation, transition, and dynamic stall. These aspects will be investigated in wind tunnel experiments using advanced measurement techniques, such as Particle Image Velocimetry (PIV) and smoke injection, further showing the advantages of the SMTE flap design.

CHAPTER 7

NOVEL TWIST MORPHING AILERON AND WINGLET DESIGN FOR UAS CONTROL AND PERFORMANCE

Mir Hossein Negahban[1], Musavir Bashir[2], Clovis Priolet[3], Ruxandra Mihaela Botez[4]

[1, 2, 3, 4] LARCASE Laboratory of Applied Research in Active Controls, Avionics and Aeroservoelasticity, Department of System Engineering, École de Technologie Supérieure, 1100 Notre-Dame West, Montréal, Québec, Canada H3C 1K3

Paper published in Journal of Drones, 13 August 2024
DOI : https://doi.org/10.3390/drones8080392

Résumé

Cette étude présente une nouvelle conception « d’aileron et d’ailette à morphing de torsion » pour le système d’avion sans pilote UAS-S45. Améliorer l'efficacité de roulage grâce aux ailerons à torsion et réduire la traînée induite grâce aux ailettes à torsion sont les deux principaux objectifs de cette étude. Une nouvelle conception d'aile est introduite, et une optimisation de forme aérodynamique basée sur un gradient haute-fidélité est effectuée pour les ailerons à morphing de torsion et les ailerons à morphing de torsion, séparément, avec des fonctions objectives spécifiées. L'aileron à torsion déformable est ensuite comparé à la configuration conventionnelle des ailerons articulés en termes d'efficacité de roulement et d'autres propriétés aérodynamiques, en particulier la maniabilité de l'avion. Les résultats pour les ailerons à morphing de torsion montrent que la nouvelle conception de morphing augmente l'efficacité des ailerons de 34 % par rapport à la conception conventionnelle et réduit la traînée induite de 61 %. Ensuite, les ailettes à torsion déformable sont étudiées en ce qui concerne la traînée induite dans des conditions de vol de croisière et de montée. Les résultats pour les ailettes à morphing de torsion indiquent que la nouvelle conception réduit la traînée induite de 25,7 % en vol de croisière et jusqu'à 16,51 % en montée ; il réduit également la traînée totale jusqu'à 7,5 % et augmente l'efficacité aérodynamique jusqu'à 9 %.

Abstract

This study introduces a novel “twist morphing aileron and winglet” design for the Unmanned Aircraft System UAS-S45. Improving rolling efficiency through twist-morphing ailerons and reducing induced drag through twist-morphing winglets are the two main objectives of this study. A novel wing design is introduced, and a high-fidelity gradient-based aerodynamic shape optimization is performed for twist morphing ailerons and twist morphing winglets, separately, with specified objective functions. The twist morphing aileron is then compared to the conventional hinged aileron configuration in terms of rolling efficiency and other aerodynamic properties, in particular aircraft maneuverability. The results for twist morphing ailerons show that the novel morphing design increases the aileron efficiency by 34% compared to the conventional design and reduces induced drag by 61%. Next, twist-morphing winglets are studied regarding the induced drag in cruise and climb flight conditions. The results for twist morphing winglets indicate that the novel design reduces induced drag by 25.7% in cruise flight and up to 16.51% in climb; it also decreases the total drag by up to 7.5% and increases aerodynamic efficiency by up to 9%.

7.1 Introduction

For decades, research on morphing wing technology has been proceeding at an ever-increasing pace, most of which have passed the conceptual design phase and are currently dealing with manufacturing challenges. Since this challenge is the last phase, meticulous consideration should be made concerning morphing wings development on real aircraft. Meanwhile, research on discovering other promising abilities of this technology is also ongoing. In a broad sense, morphing wing technology(Ameduri & Concilio, 2023; Dimino, Lecce, & Pecora, 2017; Pecora, 2021) replicates the flight patterns of birds, which have been optimized for millions of years, and this technology aims to discover these patterns and how to apply them on man-made flying objects. This broad field of research thus encompasses several disciplines, including aerodynamics, structures, materials, and control, making strong links and interchangeability among these disciplines essential for this field to advance.

Aerodynamic simulation is the logical first step to confirm the advantage of a morphing design. As confirmed by an aerodynamic study, morphing wing designs that underwent the manufacturing process have demonstrated their promising capabilities(Kota et al., 2009b). Numerous morphing designs have been proposed, each concerning specific mission objectives and aircraft maneuverability as demonstrated by flight patterns. Span morphing or telescopic wings (Elelwi, Botez, & Dao, 2021; Elelwi et al., 2022; Samuel & Pines, 2007), drooped nose wings (Bashir, Botez, & Wong, 2024; Bashir, Longtin-Martel, Botez, & Wong, 2022; Bashir et al., 2024) variable sweep wings (An et al., 1988), upper surface morphing (R. M. Botez et al., 2018; Botez, Molaret, & Laurendeau, 2007; Koreanschi[a] et al., 2017; Popov, Botez, & Labib, 2008) variable thickness wings (Liu et al., 2021), and variable camber wings (Negahban, Botez, & Razavi, 2022; Xiasheng et al., 2024) are among the morphing wing types on which research has been conducted. Some of these designs, such as variable camber wings or morphing trailing edge (MTE) (Pecora, Dimino, et al., 2016; Pecora et al., 2014), have garnered more attention than the others, due to their very promising potential in improving flight performance. For example, swept morphing has been used in the F-14 TOMCAT for many years, as it is considered one of the most successful morphing designs(Barbarino et al., 2011). Given that each morphing wing is mainly proposed according to its specific mission objectives, if the mission objective is to enhance flight range or endurance in cruise flight, then camber morphing would be the first design choice due to its high potential for achieving those objectives (Negahban, Bashir, Traisnel, & Botez, 2024).

The present research aims to find an appropriate morphing wing design to enhance the rolling efficiency, and to reduce downwash or induced drag. For aerodynamics researchers, the first wing components that come to mind for this mission objective are the ailerons and winglets, but the main question is related to the optimum morphing approach for this goal. So far, very few research has been done on morphing ailerons (Amendola et al., 2015)or morphing winglets (Ameduri et al., 2021) to enhance rolling efficiency or to reduce downwash. Jenett et al., in collaboration with NASA's Ames Research Center (Jenett et al., 2017), proposed a modular and reversibly assembled wing structure that can perform continuous span-wise twist deformation. Having lightweight and simple fabrication and maintenance is one of the advantages of their proposed mechanism. The purpose of this cellular composite structure morphing wing structure is to increase the roll efficiency compared to conventional aileron systems. This mechanism includes the flexible skin, wing structure, actuation, and control system. The final twist morphing wing design was attached to an arbitrary fuselage, and then tested in NASA's Langley 12-foot Low-Speed wind tunnel. The test results showed that this morphing wing model could linearly alter the yaw from adverse to proverse. The wind tunnel tests also determined that active twist morphing was able to achieve stall mitigation. Manoranjan et al. (Majji, Rediniotis, & Junkins, 2007) modeled a novel twistable morphing wing design with an elastomeric skin. The aerodynamic wing model was developed using Prandtl's Lifting Line theory, and the final design was tested in a low-speed wind tunnel equipped with flow visualization. It was found that using this method increased the range of angles of attack, a strong advantage for twisting wings. Garcia et al. (Garcia, Abdulrahim, & Lind, 2003) designed a morphing wing for a micro air vehicle to twist and perform the rolling maneuver. For twist deformation purposes, they used a series of rotating torque rods through which the twist morphing could be achieved. The flight tests showed that this type of morphing provided a substantial control authority for roll control, and that the roll rate was considerably increased proportionally to the yaw rate; in other words, it could generate pure roll and decrease the adverse yaw effect, thereby achieving an accurate flight path. An analytical solution was introduced by Phillips et al. (Phillips, Alley, & Goodrich, 2004), through which the roll response, yawing moments, lift, and induced drag of hinged and twisted ailerons could be predicted. This solution can be applied to arbitrary planform and spanwise variations of control surface deflection. They used Prandtl's classical lifting-line theory, and the Fourier coefficients followed the wing geometry. This solution can also be applied to full-span twisting wings called "twisterons". They showed that the induced drag was minimized by using a variable twist wing. Abdulrahim et al. (Abdulrahim, 2005) presented a twisting morphing wing for roll control, varying the gull wing angle to mimic bird wings in different flight patterns such as gliding and soaring. They tested their design on a micro aerial vehicle to study the effect of gull-wing morphing on flight dynamics. They concluded that twisting wingtips provide an excellent roll response and could improve the aerodynamic performance. Kaygan and Ulusoy (KAYGAN & Ulusoy, 2018) examined the twisting wing effectiveness in terms of aircraft performance and control by specifying the optimum twist angle. They used the Athena Vortex Lattice Method to predict aerodynamic performance. By considering several twisting configurations ranging from -8° to +8°, they showed that considerable aerodynamic performance could be gained from higher twist angles, which could be applied to ailerons, rudders, and elevators. A study was performed on the Airbus A320, revealing the promising benefits of twisting wings. A numerical analysis on twist-morphing wings with a high-aspect-ratios for efficient control roll maneuvers was conducted by Pecora et al. (Pecora, Amoroso, & Lecce, 2012). They compared conventional hinged aileron configurations with twisted morphing ailerons in terms of aerodynamics and aeroelasticity, including the induced roll rate and reversal speed control. This study showed that linear or quadratic twist morphing wings not only outperformed conventional ailerons by nearly 1.6 times in terms of roll control effectiveness, but also more powerful and robust roll control could be achieved. This morphing strategy was applied on the wing by varying local leading-edge angles along the entire wingspan, in contrast to conventional ailerons. Their analysis also revealed that structural weight reduction could be expected using this unconventional morphing configuration.

Rodrigue et al. (Rodrigue et al., 2016) introduced a novel twist-morphing wing in which a specified part of the wing span underwent a twist morphing, namely the wingtip, while the other part remained fixed, i.e., the part attached to the fuselage. The morphing part was composed of flexible and innovative composite materials to ensure a smooth twist. The prototype of the model was tested in a wind tunnel, and the results revealed that lift increased for angles of attack below 10 degrees. Moreover, in zero-lift conditions, the twisting part could generate lift and increase the lift-to-drag ratio by up to 13%. Ahmed et al. (Ahmed et al., 2011) established an aerodynamic shape optimization on a Micro Air Vehicle (MAV) to find the optimal configuration of an asymmetric wing twist for a better roll control and minimized induced drag. This optimization was based on a gradient-based algorithm and was applied on two cases of symmetric and asymmetric wing twist with specific objective functions. These two morphing configurations were expected to reduce induced drag and achieve better roll control. The Prandtl's Lifting Line Theory was used during the optimization process to determine the load distribution along the span. The optimization results indicated that the induced drag was minimized using optimum asymmetric twist, and a good roll response was obtained. Stanford et al. (Stanford et al., 2007) used a reference MAV with a flexible membrane wing to implement it through a torque-actuated wing structure. For this purpose, a static aeroelastic model was developed. They performed an optimization using a genetic algorithm on the proposed wing design to increase the steady-state roll rate and the lift-to-drag ratio. Using a single-torque-rod design, the roll rate was increased by up to 10% compared to its conventional wing design, while the lift-to-drag ratio was improved by up to 6.5%. Subsequently, optimizing the actuation mechanism with a multiple-torque-rod design increased the roll rate and lift-to-drag ratio by 34% and 6%, respectively, compared to the baseline design. Vos et al. (Vos, Gürdal, & Abdalla, 2010) proposed a mechanism for actively controlling wing twist based on a wrapping deformation of the skin. A structural analysis was performed on the wrapping wing using the generalized thin-walled beam theory. Numerical and analytical models, in conjunction with wind tunnel tests, showed a 0.7 increase in lift corresponding to the maximum wing twist. It was found that wing wrapping positively influenced lift-induced drag and improved the lift-to-drag ratio at lower angles of attack. Their study confirmed that actively wrapping the twisted wing could improve roll control motion by ensuring a maximized lift-to-drag ratio. Rodrigue et al. (Rodrigue et al., 2014) developed a novel actuation system for pure twist morphing wings using a smart soft composite, by which shape memory alloy wires were embedded in the structure designed in a cross-shaped matrix to produce a wing twist deformation. The results showed that the mechanism could make large twist angles with higher stability.

This paper presents a novel twist morphing aileron through which the rolling efficiency, rolling rate, and overall aerodynamic performance are investigated on the UAS-S45. The impact of morphing ailerons on induced drag is also analyzed. The UAS-S45 is used for surveillance and reconnaissance purposes and is designed and manufactured by Hydra Technologies in Mexico. The study is performed in several steps. First, asymmetric twist morphing ailerons are studied through aerodynamic shape optimization, and their obtained optimum configurations are compared with conventional hinged aileron configurations in terms of rolling efficiency and rolling rate to quantify the performance of the novel morphing design. Next, the symmetric morphing ailerons are studied in the same manner through aerodynamic optimization to evaluate the gain that can be achieved in induced drag reduction, after which the optimum design performance in terms of induced drag is compared to that of a conventional wing with winglets. The gradient-based optimization algorithm is established for all studies. Finally, the optimum morphing aileron designs for improved rolling maneuvers and reduced induced drag are presented and described in detail.

7.2 Asymmetric analysis-twist morphing ailerons

7.2.1 Implementation of a UAS-S45 wing for twist morphing

Figure 7.1 shows the baseline wing for a UAS-S45 equipped with standard and modified flattened winglets. In this study, the wingtip is designed to be feasible for twist morphing applications. Therefore, any curvature on the wingtip should be eliminated as it will be created after the twist. Two alternatives could be utilized to achieve this goal: 1- elimination of the winglet; or 2- using a flattened winglet. The first alternative would eliminate the winglet’s impact on the wing; however, if the winglet shape is implemented in a flattened form (second option), its effects will be preserved after the twisting morphing of the wingtip. Therefore, in this study, the flattened winglet will be attached to the baseline wing, and by twist morphing, the impacts of the aileron and the winglet will be combined. This effect will be further studied in symmetric wing analysis to reduce the downwash.

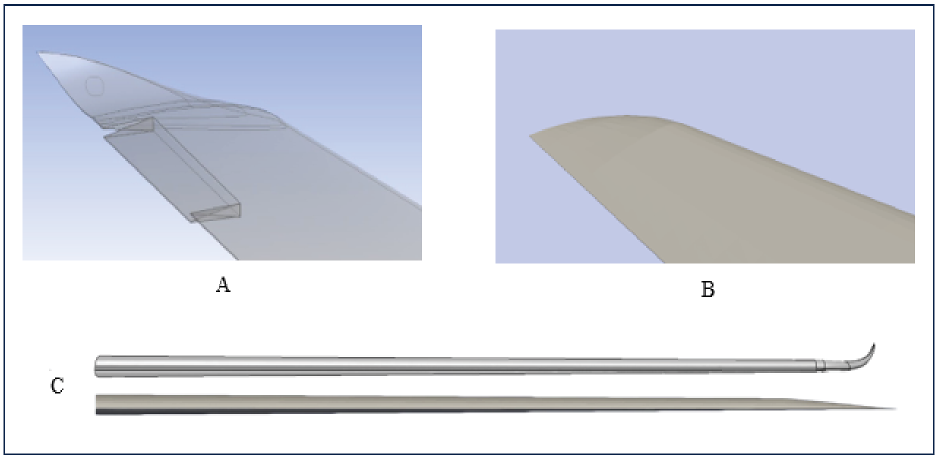

Figure 7.1 UAS-S45 baseline wing with A) its standard winglet, B) a modified flattened winglet, and C) the front view of both wingtips

7.2.2 Methodology used for asymmetric twist analysis (twist morphing ailerons)

7.2.2.1 Roll motion

Performing rolling maneuvers requires ailerons on both wings of an aircraft to deflect asymmetrically in upward and downward directions. The downward deflection increases the lift force on one wingtip, while the upward deflection on the other wing decreases the lift force as the wingtip enters the stall condition. The unequal spanwise lift distribution on both wingtips creates a moment around the roll axis which makes the aircraft roll clockwise (positive roll) or counterclockwise (negative roll) around the roll axis, depending on both left and right aileron configurations. For example, if the right aileron deflects upward and the left aileron downward, the aircraft will have a positive roll and vice versa. Figure 2 shows the UAS-S45 in a rolling maneuver.

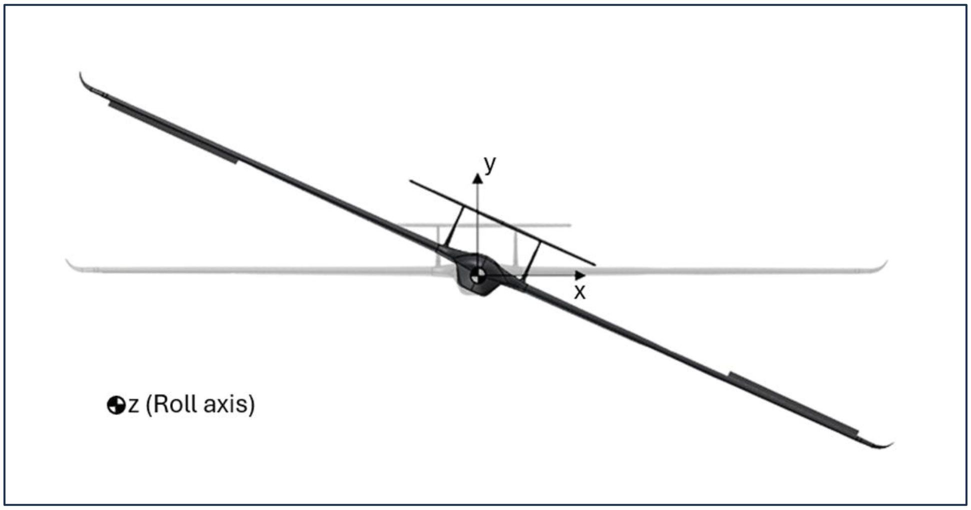

Figure 7.2 Schematics of UAS-S45 in a rolling maneuver

During a rolling maneuver, a yawing moment is also created, which makes the aircraft yaw in the opposite direction of the roll. This unwanted yawing moment is called adverse yaw; however, since it is beyond the scope of this study, only the pure rolling maneuver is investigated here. In the rolling maneuver, several criteria exist to quantify the roll's performance, including its power, rate, and efficiency. The roll control power can be obtained through strip integration (Nelson, 1998). The opposite deflection of the ailerons generates a roll moment around the roll axis that can be found by use of the following equation:

$$M_z = \Delta L . y \tag{7.1}$$

where y represents the span length of the wing.

The equation (7.1) may be expressed in coefficient form by replacing $\boldsymbol{M_z}$ with $\boldsymbol{C_{mz} Q S b}$, in which $\boldsymbol{Q}$ denotes the dynamic pressure, S the surface area and b the span length, and therefore Eq. (7.1) becomes (Nelson, 1998):

$$C_{mz} = \frac{\Delta L \, y}{QSb} = \frac{C_l Q c y dy}{QSb} = \frac{C_l c y dy}{Sb} \tag{7.2}$$

Equation (7.2), which represents the roll moment coefficient, will be used in this comparative study between hinged and morphing ailerons, as it is directly proportional to the roll efficiency and roll rate. To obtain the local lift coefficient generated on the ailerons, $\boldsymbol{C_l}$ in Eq. (7.2) is replaced by local lift coefficient ($\boldsymbol{C_l = C_{L_{\alpha_w}} \tau \delta_a}$). Therefore, Eq. (7.2) is integrated over the section of the wings containing the ailerons , which is expressed as:

$$C_{mz} = \frac{2C_{L_{\alpha_w}} \tau \delta_a}{Sb} \int_{y_1}^{y_2} cydy \tag{7.3}$$

where $C_{L_{\alpha_w}}$ is the lift curve slope, δ_a is the aileron deflection angle, and $\boldsymbol{\tau}$ denotes the derivative of the angle of attack with respect to the angle of deflection ($\boldsymbol{\frac{d\alpha}{d\delta_a}}$). Finally, by taking the derivative from Eq. (7.3) with respect to angle of deflection ($\boldsymbol{\delta_a}$), the aileron control power is obtained, as follows:

$$C_{mz_{\delta_a}} = \frac{2C_{L_{\alpha_w}} \tau}{Sb} \int_{y_1}^{y_2} cydy \tag{7.4}$$

The aileron control power ($C_{mz_{\delta_a}}$) measures the moments variations per unit of aileron deflection. It is evident that when a higher roll moment is produced, the control power is high, indicating that an aileron is more effective.

The flow solver used for all the optimizations in this study is the OpenFOAM's steady state flow solver, "simpleFoam"; therefore, only pure roll motion (no adverse yaw effect) in steady state form is formulated (as noted above). The roll motion can be written as a second-order differential equation (Nelson, 1998):

$$\sum Rolling\ moments = I_z \Delta\ddot{\phi} = \frac{\partial M_z}{\partial p} \Delta\dot{\phi} + \frac{\partial M_z}{\partial \delta_a} \Delta\delta_a \tag{7.5}$$

where ϕ denotes the roll angle about the roll axis, $\boldsymbol{p}$ is the dimensionless roll rate and $\boldsymbol{\frac{\partial M_z}{\partial \delta_a} \Delta\delta_a}$ is the roll moment created by aileron deflection. Since the roll rate ($\Delta\boldsymbol{p}$) is equal to $\boldsymbol{\Delta\dot{\phi}}$, Eq. (7.5), it can be reduced to a first-order equation as follows:

$$I_z \Delta\dot{p} = \frac{\partial M_z}{\partial p}\Delta p + \frac{\partial M_z}{\partial \delta_a}\Delta\delta_a \tag{7.6}$$

Next, by replacing ${\frac{\partial M_z}{\partial p}}\Big/{I_z}$ with M_{z_p} , ${\frac{\partial M_z}{\partial \delta_a}}\Big/{I_z}$ with $M_{z_{\delta_a}}$ and assuming $\tau = -\frac{1}{M_{z_p}}$, Eq. (7.6) is solved and the following time-dependant equation is obtained:

$$\Delta p(t) = -\frac{M_{z_{\delta_a}}}{M_{z_p}}\left(1 - e^{-t/\tau}\right)\Delta\delta_a \tag{7.7}$$

where $\boldsymbol{\tau}$ is the roll response time, and lower $\boldsymbol{\tau}$ values are interpreted as rapid roll motion. To obtain steady-state pure roll motion, $\boldsymbol{t}$ is assumed large enough $(\boldsymbol{e}^{-\boldsymbol{t}/\tau} \approx \boldsymbol{0})$ to account for steady-state solution; therefore, Eq. (7.7) will change to:

$$\omega_z = -\frac{M_{z_{\delta_a}}}{M_{z_p}}\Delta\delta_a = -\frac{2U_\infty}{b}\frac{C_{mz_{\delta_a}}}{C_{mz_p}}\Delta\delta_a \tag{7.8}$$

where ω_z is the roll rate about the z-axis, $C_{mz_{\delta_a}}$ is the aileron control power (Eq. 7.4), C_{mz_p} is the roll damping coefficient, and $\Delta\delta_a$ is the aileron deflection angle. Since C_{mz_p} is always negative, the ultimate roll rate will be positive. Therefore, Eq. (7.8) indicates that increasing roll moment not only increases aileron control power, but it also increases the roll rate.

For decades, conventional ailerons have performed rolling maneuvers through their hinged deflections, and so rolling efficiency and determining how well this maneuver was performed has been directly dependent upon aileron performance. In some aircraft, particularly commercial jets with large swept wings, since ailerons' efficiency is reduced, spoilers are used for rolling maneuvers because of their quick actuation to partially recover the reduced efficiency of ailerons. Inspired by nature and rolling maneuvers of birds, the same pattern can be implemented in aircraft, in which wingtip twist deformation could be used instead of aileron deflection. Morphing is the first technology that can lead to this objective. The rolling maneuver can be made more efficient by smoothly twisting the wingtip instead of the using discontinuous and sharp deflections of ailerons or spoilers. We present in this paper novel twist morphing ailerons that can achieve such rolling maneuvers. For this purpose, the UAS-S45 is used as the base model, for which both hinged and morphing ailerons are studied. As expressed through Eqs. (7.1) to (7.8), the roll moment coefficient is the best comparison parameter because it influences both the aileron's control power and roll rate, and it is therefore used as the primary measure in this study to compare the performance of hinged and morphing ailerons. The aerodynamic optimization is performed on the morphing of asymmetric ailerons, and then, after their optimum configurations have been obtained, their performance is compared to that of hinged ailerons.

7.2.2.2 Optimization of Asymmetric Morphing Ailerons for Rolling Maneuver

The optimization uses the DAFoam (Discrete Adjoint with OpenFOAM) optimization framework, a high-fidelity multidisciplinary optimization framework based on a gradient algorithm. Since its development in 2019 (He et al., 2020), it has been used in several benchmark studies (He et al., 2019). In the literature, most of the aerodynamic optimization frameworks use low-fidelity potential flow solvers in the optimization loop; however, DAFoam takes advantage of OpenFOAM, in which the flow is simulated through Reynolds-averaged Navier-Stokes (RANS) equations, leading to more accurate optimization results. Moreover, DAFoam is an appropriate framework for three-dimensional optimizations, in which a whole wing or aircraft is optimized, involving hundreds of design variables. This framework is explained in detail in (Negahban, Bashir, Traisnel, & Botez, 2024).

7.2.2.3 Wing Parametrization

Special considerations should be taken when large-scale optimization is performed. Parametrization or mathematical definition of a wing is a crucial step in the optimization algorithm. Since the whole wing is optimized in this study, the number of design variables is very high. ”Constructive” parametrization techniques (Sripawadkul, Padulo, & Guenov, 2010) cannot handle such a high number of design variables; therefore, the best candidates for this type of parametrization are the “deformative” parametrization techniques, in which the mathematical definition of the geometry is independent of design variables. This study uses the Free-Form Deformation technique (FFD) to handle hundreds of design variables. The initial objective for developing the FFD technique was related to its use in graphics(Sederberg & Parry, 1986). However, it is an excellent tool in engineering problems, especially in optimization. Since its development in 1986, several modifications and improvements have been made, particularly in aerodynamic optimization(Ronzheimer, 2004; Samareh, 2004) and today, it is the best parametrization technique in aircraft or wing optimization. (See (Mir Hossein Negahban, Musavir Bashir, & Ruxandra Mihaela Botez, 2023) for more details). In this parametrization technique, the geometry is embedded inside the FFD block, which has a defined number of control points; and this embedded geometry is morphed by the displacement of control points. In this study, the baseline wing design is embedded inside the FFD block. Since the objective of the optimization refers to the ailerons and wingtips, only the control points in these regions have the freedom to move. The rest of control points (around the main flaps and the wing root) are confined with zero displacements. Figure 3 illustrates both wings (right and left) inside the FFD block, where active control points are shown in green. These control points can move downwards in the left wing and upwards in the right wing. The blue FFD boxes surround the static wing section, and the red ones the wing section where its twist deformation occurs.

The number of control points directly impacts the optimization results, as shown in our previous work(Negahban, Bashir, & Botez, 2022); therefore, the optimum number of control points in this study was determined through trial and error. In this procedure, several criteria are considered to determine the optimum number of control points. These criteria include optimization convergence, computational time, optimality error, and feasibility of the deformation. Based on these criteria, different numbers of control points were examined and finally, after analyzing different numbers of control points, 64 control points were chosen for each wing model (Figure 3).

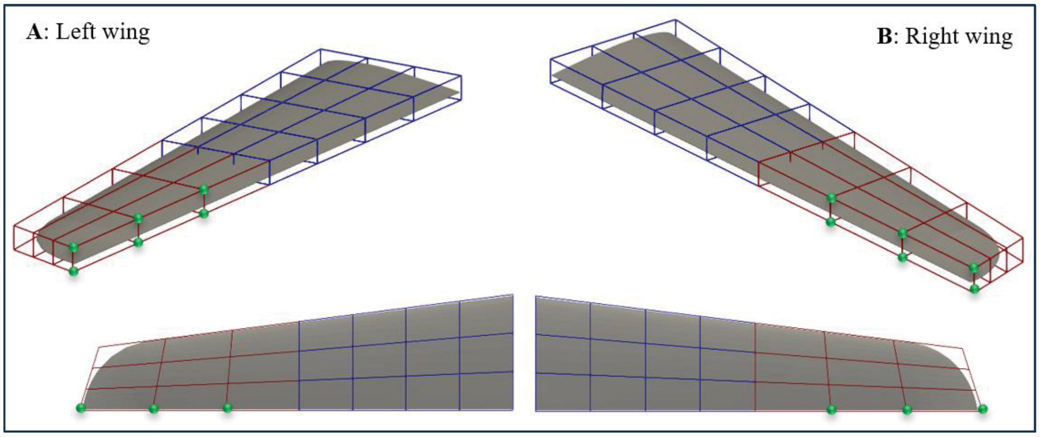

Figure 7.3 UAS-S45 wings embedded inside FFD blocks; A) left wing, B) right wing

7.2.2.4 Optimization setup

The objective in this paper is to optimize the proposed twist morphing aileron to achieve better rolling efficiency. The straightforward optimization method consists in defining the objective function in terms of rolling moment or rolling efficiency maximization; however, an alternative simple way is established in this work, in which the optimization process is divided into two separate processes, one for the left wing and the other one for the right wing. The objective function of each wing is based on the lift force on the wingtip; in one wing, the lift force is maximized, and in the other wing, it will be minimized to create an unbalanced lift distribution on the whole wingspan. While the optimization is performed for one wing, the other wing is confined with no de-formation during the optimization. The boundary condition for the opposite wing is defined in a way that the opposite wing is not deformed during the optimization by constraining the control points of FFD block to zero deflection on the opposite wing. The two optimization frameworks are shown in Table 7.1, in which the entire optimization setup, including the objective function, the constraint function, and the number of design variables are specified.

Table 7.1 Optimization setups for A) right and B) left wings

(A)

Function/variable	**Description**	**Total number**
Objective function		
max C_L	*objective function* *for left wing*	1
w.r.t:		
Y	*FFD control points*	64
T	*Twist*	1
Subject to:		
$\text{AOA}_{\text{initial}}=\text{AOA}_{\text{final}}$	*Constant Angle of Attack*	1
$V \geq V_{initial}$	*Volume constraint*	64
$-300\ mm \leq \Delta y \leq 0$	*Design variable bounds*	6
$-5° < T \leq 0$	*Twist deformation bounds*	24

(B)

Function/variable	**Description**	**Total number**
Objective function		
min C_L	*objective function* *for right wing*	1
w.r.t:		
Y	*FFD control points*	64
T	*Twist*	1
Subject to:		
$\text{AOA}_{\text{initial}}=\text{AOA}_{\text{final}}$	*Constant Angle of Attack*	1
$V \geq V_{initial}$	*Volume constraint*	64
$0 \leq \Delta y \leq 300\ mm$	*Design variable bounds*	6
$0 \leq T < 5°$	*Twist deformation bounds*	24

As seen in Table 7.1, the left wing is optimized to maximize the lift, while the right wing is optimized to minimize the lift. They have the same geometrical constraints to maintain equal deformations on both wings. The control points are confined to upward and downward displacements for minimizing and maximizing the lift force, respectively. Design variable constraint (Δy), sets the limits for these vertical displacements along the y-axis in the FFD block. The reference axis of the twist variable is at 50% of the chord, and its start point in the spanwise direction is at 50% of the wingspan, which corresponds to the start point of the ailerons in hinged configuration. Both wings follow the same optimization process as shown in Figure 7.4, except that the objective function relates to either lift maximization or minimization.

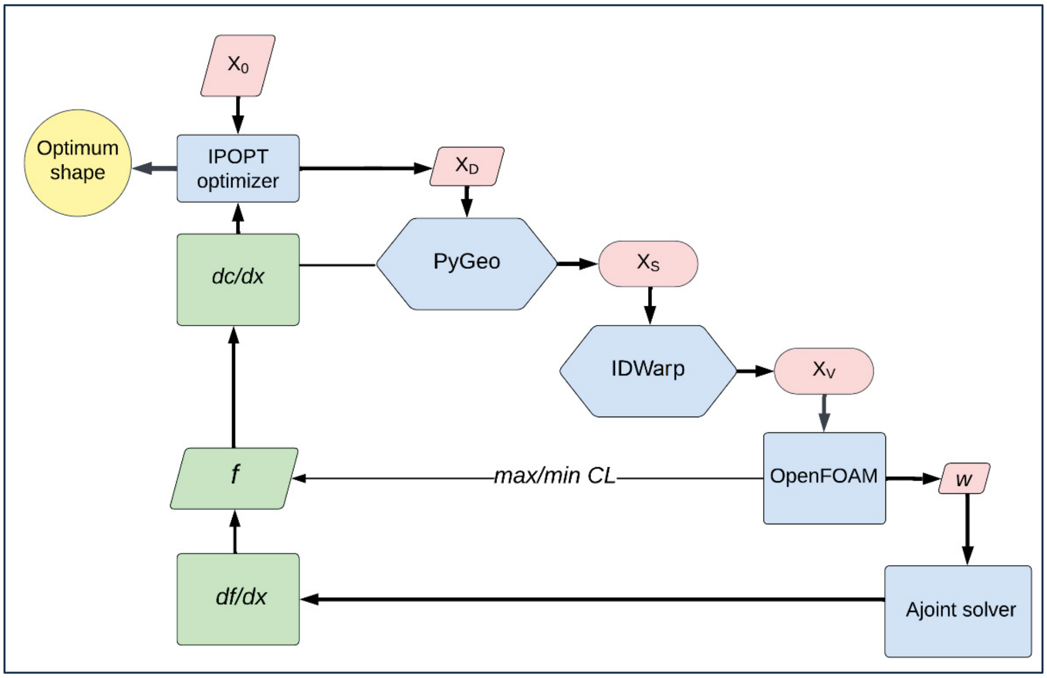

Figure 7.4 DAFoam optimization process for twist morphing aileron, X_0: initial variables, X_D: design variables, X_S: surface coordinates, X_V: volume mesh, w: state variables, *f*: objective function

As shown in Figure 7.4, the optimization is using different modules in Python. Within the PyGeo module, surface geometry parametrization is implemented through the FFD, and the constraints and their derivatives (dc/dx) are also computed within this module. Next, all changes in surface geometry are applied to the surface mesh. The volume mesh is then deformed, corresponding to these changes in the surface geometry, all of which are implemented within PyWarp (mesh morphing module). Finally, the corresponding volume mesh, X_v, is given as an input to the flow solver, OpenFOAM, to compute the specified objective function that works the best with the constraint. However, since the objective function f is dependent on both design variables x and state variables w, ($f = f(x, w)$), the discrete adjoint solver computes the total derivative of f, (df/dx), also called the sensitivity of the objective function. Similarly, the sensitivities of constraint functions are also computed and transferred to the IPOPT algorithm, that will find the solution using optimization iterations. Note that the objective function for the left wing is lift maximization, while for the right wing, it is lift minimization.

The optimization is performed in cruise flight conditions, where the cruise speed for UAS-S45 is 70 knots (28.3 m/s), the initial angle of attack is zero degrees, and the mission altitude is 15,000 ft.

7.2.3 Results and discussions for asymmetric twist analysis

7.2.3.1 Morphing ailerons

Once the optimization is performed for both right and left wings, the optimum wing configurations are attached to the fuselage to evaluate the UAS rolling efficiency. In this phase, the simulation is performed in OpenFOAM with a high number of meshes (14,199,957 elements). Since there are strong vortices and recirculation around the wing tip, finer elements are used around wing tip to have a better visualization of the airflow around morphing ailerons. This section presents only the results expressed in terms of pressure, vorticity, and velocity streamlines, while the quantitative aerodynamic properties, such as the rolling efficiency, are presented and discussed in subsequent sections, where they are compared with hinged ailerons results. Figure 7.5 illustrates the static pressure contours on the top and bottom of the UAS-S45.

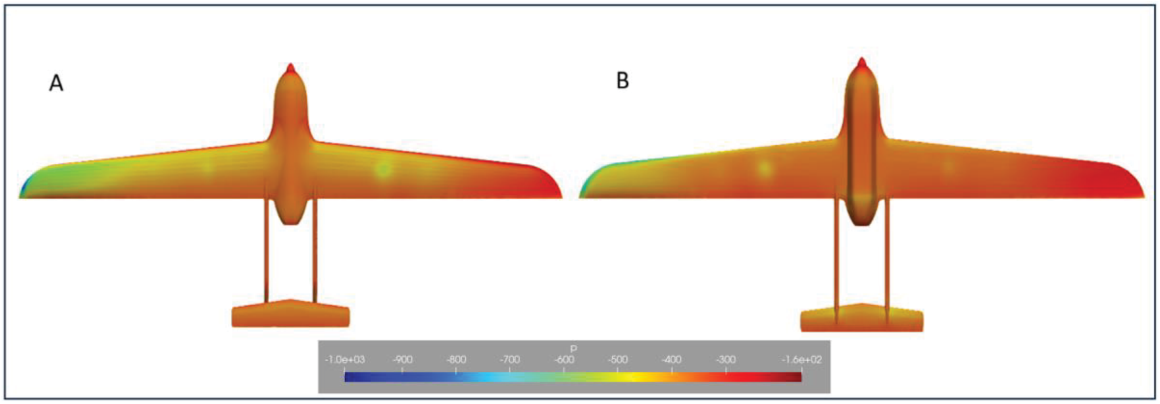

Figure 7.5 Static pressure contour on the A) upper and B) bottom surface of a UAS-S45

The static pressure contour (Fig. 7.5) clearly shows the unbalanced pressure distribution on the left and right wingtips, where the downward twist produced higher pressure on the bottom surface (left wing, Fig. 7.5-B), and the upward twist (right wing, Fig. 7.5-A) produced it on the upper surface. The advantage of morphing ailerons use is that the pressure variations on the wing surface, both in chord-wise and spanwise directions, are very smooth, so that there is no pressure peak on the transition surface from solid to twisted wing.

Very good visualization of the flow around the twisted ailerons can be captured by velocity streamlines, as shown in Figure 7.6, where the airflow recirculation and velocity magnitude variation are captured perfectly. Figures 7.6-A, 7.6-C, and 7.6-E show the downward twisted morphing aileron from its forward, isometric, and top views, respectively, and Figures 7.6-B, 7.6-D, and 7.6-F show the upward twisted morphing aileron in the same manner. Figures 7.6-G and 7.6-H illustrate the UAS-S45 equipped with morphing ailerons.

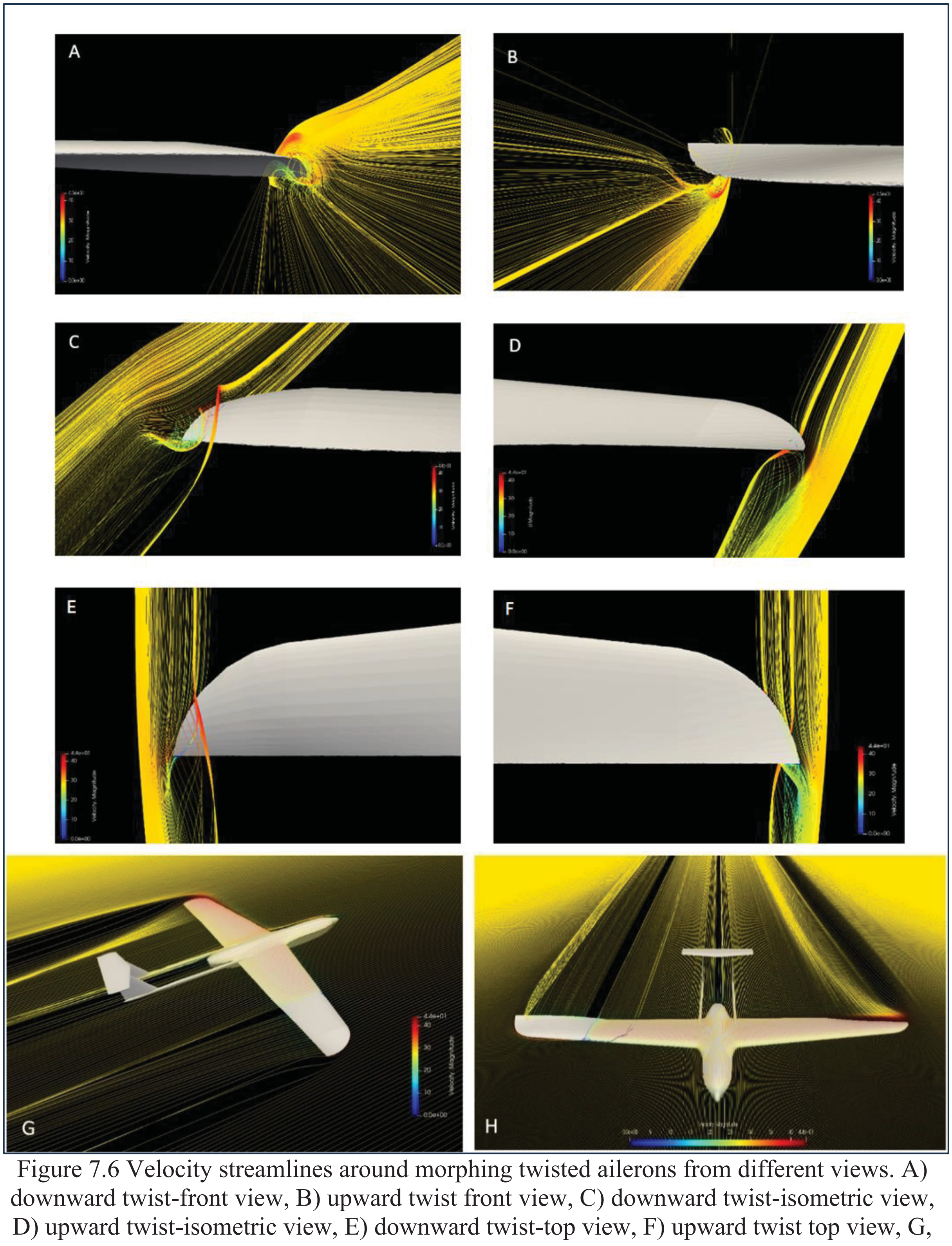

Figure 7.6 Velocity streamlines around morphing twisted ailerons from different views. A) downward twist-front view, B) upward twist front view, C) downward twist-isometric view, D) upward twist-isometric view, E) downward twist-top view, F) upward twist top view, G, H) UAS-S45 equipped with morphing ailerons

As depicted by these Figures, the only flow characteristic that makes the aircraft roll is the opposite flow distribution, wherein for a downward morphed aileron, flow is mainly concentrated on the upper surface of the wingtip, but in an upward morphed aileron, the flow concentration is mainly on the wingtips' lower surface. This opposite flow distribution creates opposite pressure distribution, as shown in the pressure contours in Figure 7.3, which leads to unequal lift distribution and the generation of roll moment. Figures 7.6-C and 7.6-D show the flow recirculation on both morphing ailerons, wherein for the downward twisted aileron, it emerges on the upper surface, and for the upward twisted aileron, it is on the lower surface. Thanks to the wingtip's circular curvature, this recirculation has a restricted propagation zone, and just past the wingtip, its magnitude approaches zero. Moreover, since there is a smooth transition between the solid and morphing parts of the wing, the flow has no turbulence at the start of the twist. (Figures 7.6-G and 7.6-H).

7.2.3.2 Hinged ailerons

To compare the morphing with the hinged ailerons, they must be simulated under the same flight conditions (speed, pressure, angle of attack, angle of deflection) with the same simulation setup (number of elements). The simulation of the hinged aileron is conducted in ANSYS Fluent, a high-fidelity flow solver similar to OpenFOAM. However, the simulation of the hinged flap does not include any optimization; it is pure aerodynamic simulation. Therefore, the morphing aileron's configuration is obtained first, through optimization, and then the corresponding data, including the optimum angle of attack and angle of deflection, are transferred to the hinged aileron simulation to determine the most accurate comparison in terms of overall aerodynamic performance, rolling efficiency, rolling moment, and rolling rate.

In a hinged flap, whether it is the main flap, an aileron, or any other control surface, the deflections are either pure upwards or downwards deflections. The only effective parameters on lift force are the geometric parameters of that control surface, such as its size and position. In (Caughey, 2011), Caughey quantified the effectiveness of a control surface by considering flap deflection magnitude and size in terms of chord length. As seen in Figure 7.7, control surface or flap effectiveness is proportional to its size.

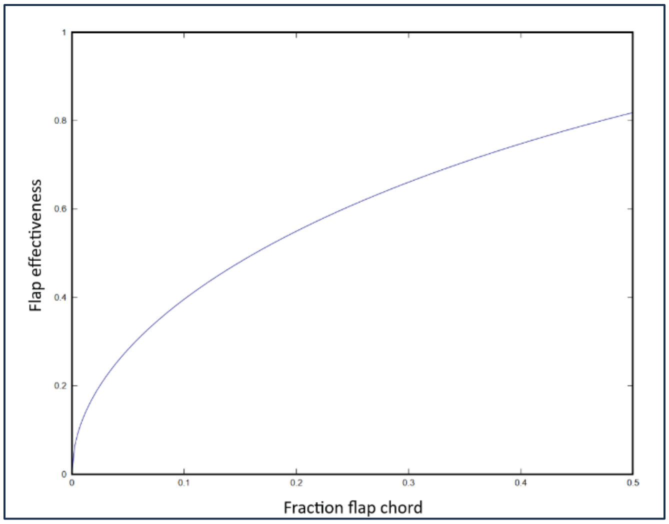

Figure 7.7 Control surface effectiveness (normalized by 2π) (Caughey, 2011)

Flap effectiveness can be directly interpreted into lift generation; in other words, according to Figure 7.7, the flap effectiveness corresponding to a flap at 25% of a chord has an efficacy of 0.6, which means that it can generate 60% of the lift force. Despite the main flap being restricted only to its upward or downward deflection, no matter whether it is morphed or hinged, since the ailerons are usually located at the wingtip, they have other forms of deformations rather than up or down, meaning that the ailerons can also have twist deformation, that can be more feasible than that of the hinged aileron. This section focuses on hinged ailerons; a thorough comparison between morphed and hinged ailerons is presented in Section 7.2.3.3.

This study investigates hinged ailerons on the UAS-S45 with its standard winglets and was performed using the Spalart-Allmaras turbulence model. The flight condition chosen for this study is the cruise flight, where the cruise speed for UAS-S45 is 70 knots, the ceiling altitude is 15,000 ft, and the effective angle of attack is zero degrees. These are the same conditions applied to morphing ailerons in the previous section (section 2.2). The hinged ailerons are deflected from 0° to 10° with increments of 2°. Within this range of deflections, aerodynamic parameters are evaluated, including lift and drag coefficients both for the whole UAV and each wing separately, rolling and pitching moments, and pressure coefficients.

Since there are tiny gaps around the hinged aileron, the convergence of the simulations is very sensitive to the element size. Therefore, special consideration was taken in the meshing part. An unstructured mesh with 10 inflation layers around the UAS surface was used with the first element size of 0.001m corresponding to Y+=50. To reduce the computational cost, a density box with finer elements was used around the UAS, making the element's size much coarser; this feature substantially reduces the computational time. Figures 7.8 and 7.9 illustrate the meshing detail.

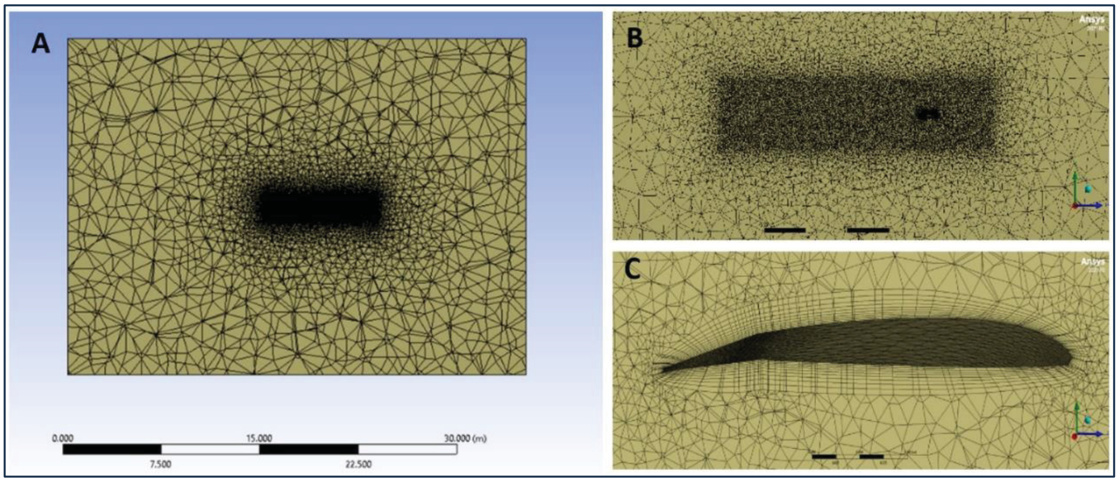

Figure 7.8 Grid sizes in A) far-field, B) density box, and C) around the UAV surface (inflation layers)

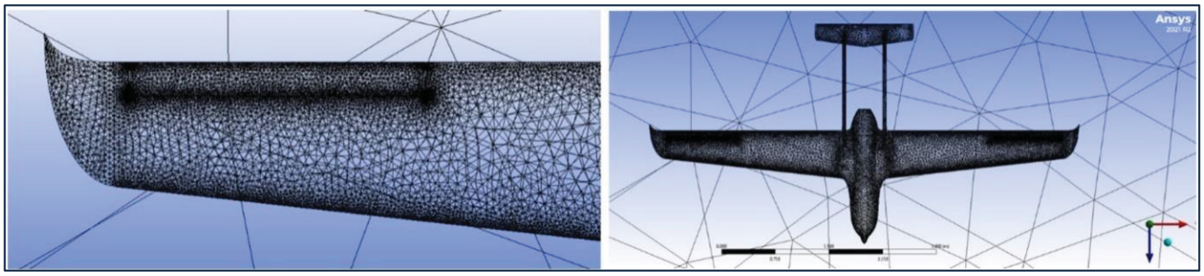

Figure 7.9 Unstructured surface mesh on the UAS-S45

As depicted in Figure 7.9, specific parts of the wings are refined to get better results. This is generally the case for the ailerons, where the gaps between them and the wing create eddies, and the simulation's convergence is highly sensitive to these discontinuous parts of the wing. It is also the case of the leading and trailing edges, as they present high pressure and velocity differences.

A mesh independence study was performed on the UAV with an 8° aileron deflection. Three different elements were evaluated for each of three meshes. Tables 7.2 and 7.3 show the numbers of elements for each of these three meshes and their corresponding error percentages, respectively.

Table 7.2 Element sizes and total number of meshes for different grid sizes

	Far-field (m)	**Density box (m)**	**Total number ($\times 10^6$)**
Mesh 1	2	0.075	4.16
Mesh 2	1.75	0.05	8.845
Mesh 3	1.75	0.045	10.52

Table 7.3 Corresponding error for different element sizes

	Cl	**Relative error (%)**	**Cd**	**Relative error (%)**
Mesh 1	0.1930	0	0.0285	5
Mesh 2	0.1930	0	0.0288	4
Mesh 3	0.1930	0	0.03	0

As seen in Table 7.3, having Mesh 3 as reference mesh, due to its accurate results and very good convergence, the relative error for each element size for the lift coefficient is zero; however, for the drag coefficient, the maximum error is 5%, by having Mesh 3 as reference mesh. The final mesh chosen for this study is Mesh 2, which has the intermediate number of elements, and an error of 4%, which is less than 5%; therefore, it lies within the acceptable range.

The simulation of hinged ailerons was done by an evaluation process of the aerodynamic parameters for different angles of deflection of ailerons. Figure 7.10 shows the variations of the lift coefficients for the right and left wings separately, as well as the total lift coefficient for the whole UAS. Note that for the left wing, the angle of deflection (AOD) is positive as it deflects downward, and for the right wing, which has an upward deflection, the AOD is negative. As seen in Figure 7.10, the lift for the left wing is increased as the AOD increases, while for the right-wing, the lift decreases due to the upward deflection, approaching zero lift conditions as the AOD increases. Nevertheless, the net lift force for the whole UAS is independent of the angle of deflection and remains constant. The linear regressions calculated for the wings are 0.963 and 0.995 for the left and right wings, respectively, values that are very close indeed. For the chosen flight condition, the net lift force for the whole UAS equals 0.29. As a result of the unequal lift distribution on left and right wings ($CL_{right\ wing} < CL_{left\ wing}$), the UAV rolls towards the right (a positive roll).

The rolling moment is obtained from the ANSYS Fluent default outputs and by manual calculation by subtracting the right wing's CL from that of the left wing. Figure 7.11 displays the results obtained by both methods, showing that they both follow the same trend, which is increasing linearly with the deflection angle. However, there is an error of less than 10% for the angles of deflections greater than 2 degrees, which is because the ANSYS Fluent considers the whole UAS in the calculation of rolling moment, while in the manual calculation, only the wings are considered.

The drag coefficient was also calculated. Figure 7.12 shows the drag variations for the whole UAS for different angles of deflection, revealing an increasing trend as the AOD increases. However, by comparing the slope of the drag coefficient with those of the lift coefficient, these slopes are 0.021 and 0.0004 for C_L and C_D, respectively, which are 98% lower than the C_L variations. Therefore, drag variations with aileron deflection are not notable compared to lift variations for the whole UAS and thus can be neglected.

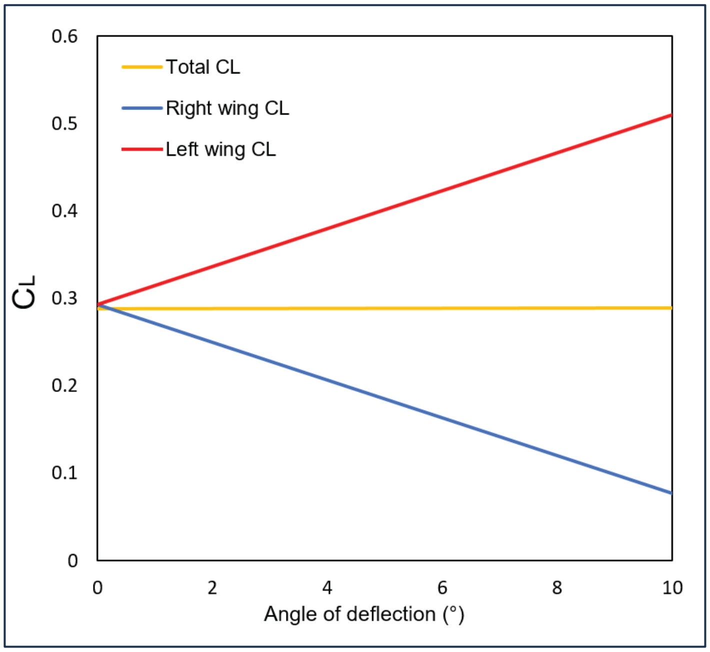

Figure 7.10 Variations of lift coefficient versus aileron angle of deflection

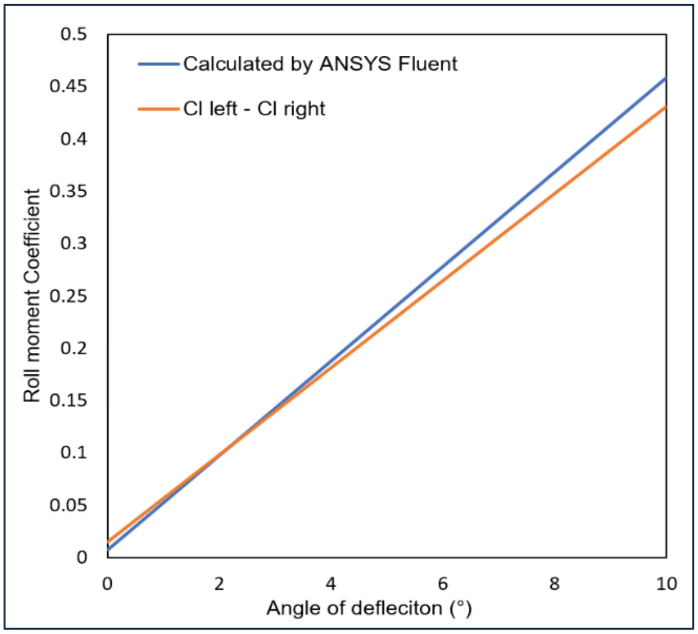

Figure 7.11 Variations of roll moment versus aileron angle of deflection

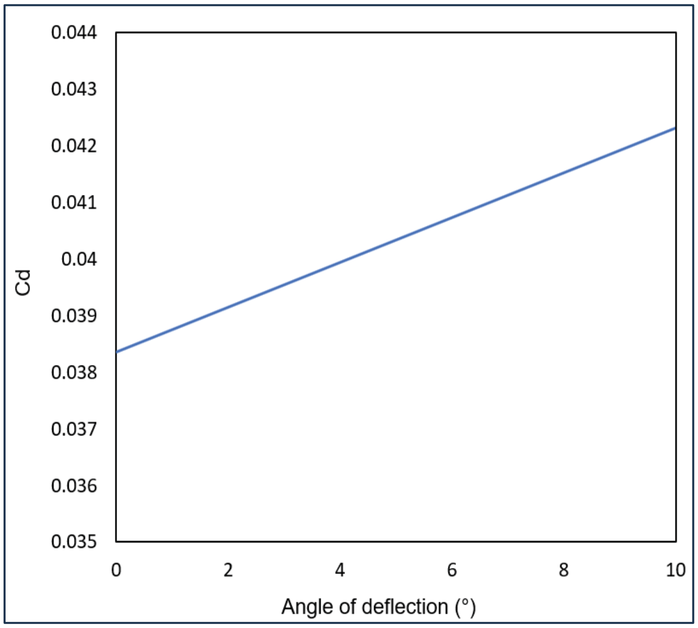

Figure 7.12 Variations of drag coefficient with the angle of deflection

The static pressure contour for the UAS with hinged ailerons is shown in Figure 7.13. The discontinuity in the gaps around the ailerons clearly shows the peak static pressure boundaries. In addition, these discontinuities also contribute to the wingtip-induced drag, as they facilitate the mixture of high-pressure flow on the lower surface and low-pressure flow on the upper surface and thus create additional vortices along with wingtip vortices. However, as observed in twist morphing ailerons (Fig. 7.5), the variation of the static pressure is smooth and coherent throughout the span; in fact, no boundaries can be determined for ailerons due to the elimination of discontinuities, and the probability of flow mixture around ailerons was zero. The pressure peaks in the hinged ailerons will be further illustrated through pressure coefficient diagrams and will be compared with those of the morphing ailerons in the next section.

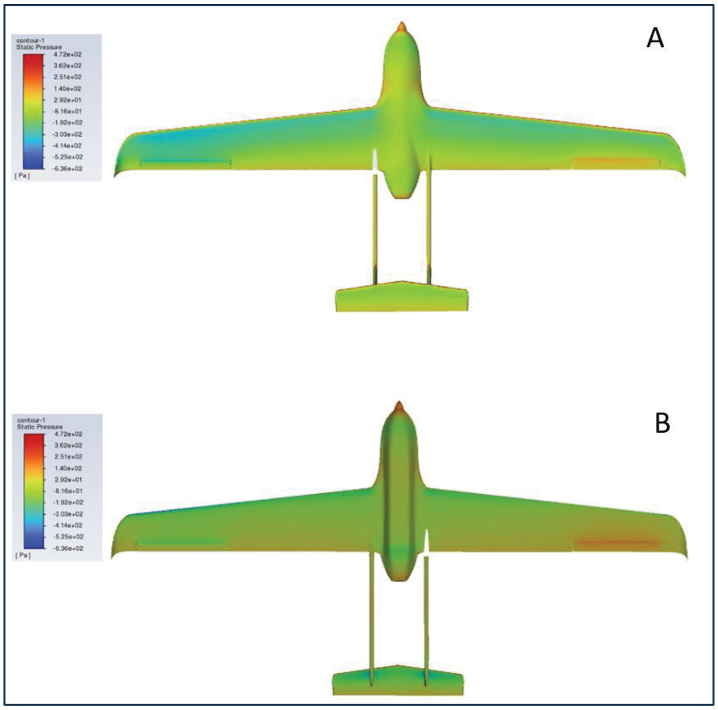

Figure 7.13 Static pressure contour for the UAS-S45 with hinged ailerons: A) upper surface, B) lower surface

7.2.3.3 Comparison of hinged and morphing ailerons

In this section, a comparison is drawn between hinged and twist morphing ailerons in terms of roll moment and overall performance. As explained earlier, the comparison of their roll moments evaluates the performance of ailerons both in terms of roll rate and control power. Table 7.4 shows the comparison of these ailerons in terms of their roll moments. Unlike hinged ailerons, the twist deformation of the morphing ailerons is not constant spanwise; therefore, the comparison is drawn by having the same vertical displacement of the ailerons edge, which is equal to ±61.2 mm both for hinged and morphing ailerons. Note that positive and negative displacements refer to upward and downward displacements, respectively.

Table 7.4 Comparison of the UAS-S45 with hinged and twist morphing ailerons

Ailerons	AOA (°)	C_L	C_D	**Roll Moment Coefficient (C_{mz})**	**Induced Drag** (C_{Di})	**(C_{mz}) variations (%)**
Hinged ailerons	0	0.289	0.0427	0.463	0.00296	-
Twist morphing ailerons	0	0.188	0.0395	0.701	0.00115	+34

By considering the roll moment coefficient as an index for aileron performance, Table 7.4 shows that using twist morphing ailerons increases the roll moment by 34 % compared to conventional hinged ailerons. According to Eq. (7.4) and Eq. (7.8), an increase in roll moment is directly interpreted as an increase in the ailerons' control power as well as in their roll rate, translating into higher aileron efficiency and rapid roll maneuver, respectively. Meanwhile, due to the elimination of the discontinuities around the ailerons in their morphing configuration, induced drag is also considerably decreased (by 61%) in morphing ailerons, which means that flow mixture and vertices due to gaps are of no concern in twist morphing ailerons.

7.3 Symmetric twist analysis (twist morphing wingtips)

7.3.1 Twist morphing wingtips

In this section, twist morphing is applied on the same wing configuration introduced in Section 7.2.1, the UAS-S45 wing with a flattened winglet. However, this section aims to reduce the induced drag under different flight conditions, including climb and cruise.

7.3.2 Induced drag

Drag force imposed on an aircraft has different components, each of which arises from a different phenomenon. In general, drag is divided into two main components: parasite (or parasitic) and induced drag. The former consists of three different types: form drag (pressure drag), skin friction and interference drag. In the form drag, the flow resistance originates mainly from an aircraft's shape, while the skin friction is due to air viscosity on an aircraft's surface, and interference drag arises from turbulent flow at different parts of aircraft, namely, the wing root. On the other hand, the induced drag arises from the generation of lift force and is directly dependent on the amount of lift produced on the wings. It is well known that the pressure gap on the upper and lower surfaces of a wing creates the lift force; however, on the wingtip, the high-pressure flow finds a way to move to the upper surface and mix with the low-pressure flow. This flow mixture at the wingtip creates wingtip vortices, where the resultant vector of these vertices is in the opposite direction of aircraft, and thus an amount of energy is lost due to the generation of these vortices, reducing aircraft aerodynamic efficiency. In addition to this adverse effect, these wingtip vortices also contribute to extra drag creation due to producing local airflow direction, meaning that when these vortices are generated, the flow circulation on the wingtip pushes the airflow downward, which is called downwash, and the wing experiences local airflow rather than free stream; therefore, the lift force direction inclines backwards, being perpendicular to local airflow, and the magnitude of the inclined lift force is equal to the induced drag magnitude (Figure 7.14).

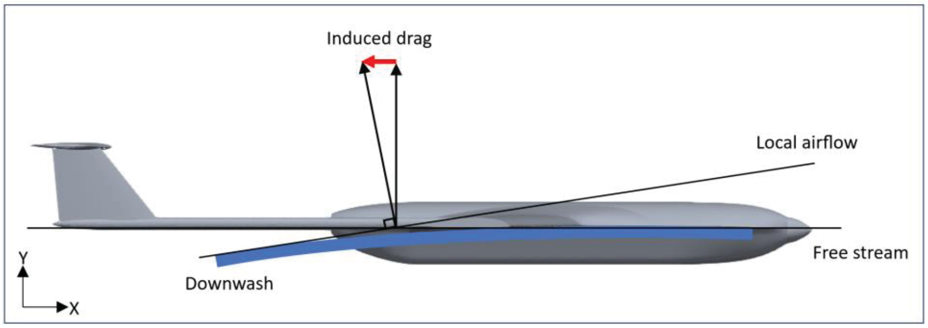

Figure 7.14 Illustration of induced drag in relation to aerodynamic forces

The induced drag is calculated from the following formula:

$$C_{Di} = \frac{C_L^2}{e \times \pi \times AR} \tag{7.9}$$

where AR is the wing aspect ratio and e is its efficiency factor, which ranges from 0.7 to 1. For a wing with an elliptic lift distribution (an ideal wing), e=1, while for a typical rectangular wing, it equals 0.7. According to Eq. (7.9), the induced drag is dependent on one aerodynamic parameter, C_L, and one geometrical factor, AR, and is reduced either by reducing the lift or by increasing the aspect ratio. In this study, both parameters are met to minimize the induced drag by keeping the total drag constant. As shown in Figure 7.1 in Section 7.2.1, the proposed wing aspect ratio is increased by 19.6% compared to the baseline wing without a winglet, and by 9% compared to the baseline wing with a standard winglet for UAS-S45. This reduces induced drag to some extent; however, since the induced drag is proportional to the square of the lift coefficient (Eq. 7.9), an infinitesimal reduction in the lift coefficient would highly reduce the induced drag.

7.3.3 Methodology used for the symmetric twist (Twist morphing wingtips)

Since the aim is to reduce the induced drag, an optimization was performed to minimize the lift coefficient while keeping the drag constant. Minimizing the lift is directly proportional to induced ag reduction according to Eq. (7.9); however, since the wingtip twist causes an increase in total drag, a constraint function is defined to keep the total drag constant during the optimization. The same optimization framework was used in the asymmetric analysis for rolling efficiency; however, in this section, the only differences are seen in the wing parametrization and in the objective function. Since this section only deals with wing tip vortices, which are the leading cause of induced drag, the FFD block is implemented according to Figure 7.15.

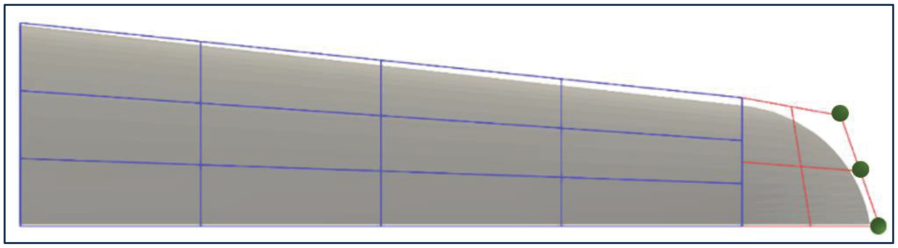
Figure 7.15 FFD blocks for twist morphing wingtip

As shown in Figure 7.15, the FFD block in blue color represents the solid part where no twist exists, and the FFD in red block shows the twisting section of the wing where the twist deformation is locally restricted to the wingtip; therefore, it will not influence the wing shape in the blue block. The active control points allowed to move upwards and downwards are located on the wingtip and shown in green. A different number of control points were established; however, considering the feasibility of deformation, 6 control points, 3 on the upper and 3 on lower wing surfaces were chosen on the wingtip. Once the optimum FFD block was determined, the optimization setup is specified according to Table 7.5.

Table 7.5 Optimization setup for a twist morphing wingtip

Function/variable		**Description**	**Total number**
Objective function			
min	C_L^2	objective function	1
w.r.t:			
	Y	*FFD control points*	52
	T	*Twist*	1
Subject to:			
$C_D \leq C_{D\ nominal}$		*Constant drag*	
AOA $_{initial}$=AOA $_{final}$		*Constant Angle of attack*	1
$V \geq V_{initial}$		*Volume constraint*	52
$-300\ mm \leq \Delta y \leq 300\ mm$		*Design variable bounds*	2
$-5° < T \leq 5°$		*Twist deformation bounds*	12

As shown in Table 7.5, the minimization of the square of the lift coefficient is constrained by the total drag coefficient; therefore, the optimum configuration will have a lower or the same total drag coefficient as that of the baseline wing drag. As the objective minimizes C_L to reduce induced drag, although this involves a slight reduction in lift, it does not significantly alter the specified flight conditions, rather, it indicates a minor adjustment to improve efficiency. By maintaining the same angle of attack and flight speed, we ensure that the overall flight conditions remain stable.

7.3.4 Results and discussion for symmetric analysis (twist morphing wingtip)

In this study, the model optimization was performed for two flight conditions: cruise and climb. Once the optimum configuration was obtained for each flight condition, it was compared with that of the baseline wing with and without winglet and with the unmorphed baseline wing in terms of induced drag. Figure 7.16 illustrates the four wings with different wingtip configurations, and Table 7.6 shows the results obtained for cruise flight conditions for these wingtip configurations.

Figure 7.16 Wingtip configurations, A) baseline wing, B) proposed wingtip (flattened winglet), C) baseline wing with standard UAS-S45 winglet, D) Twist morphing wingtip

Table 7.6 Comparison of induced drag for different wing configurations in cruise flight

Wingtip	AR	C_L	C_D	C_{Di}	C_{Di} **Variation %**
A	11.55	0.1788	0.0170	0.0012591	0.00
B	13.90	0.1894	0.0167	0.0011736	-7.28
C	12.83	0.1937	0.0169	0.0013303	+5.35
D	13.90	0.1749	0.0170	0.0010016	-25.70

As shown in Figure 7.16, three types of wingtips are investigated in this study. Model B is the wingtip attached to the baseline wing where there is no deformation on the wingtip; it is simply reduced in thickness, leading to a nearly sharp wingtip. This flattened winglet is proposed as the base model for the twist morphing wingtip, as mentioned in Section 7.2.1, and it is not the final design in this study. Wingtip Model C is the standard winglet currently used on the UAS-S45, and Model D is the proposed twist morphing wingtip design after being optimized for cruise flight condition. As depicted in Table 7.6, comparisons are drawn among these wingtip configuration performances. Wingtip models B, C and D are compared to the baseline UAS-S45 wing without winglet (A) in terms of induced-drag variations. The results indicate that the twist morphing wingtip (Model D) reduced induced drag by 25.7%, while the standard winglet (Model C) increased it by 5.35%. Moreover, when the proposed wingtip is unmorphed (model B), the induced drag is reduced by 7.28%. These improvements are primarily due to the lift coefficient reduction after the optimization, and secondarily, due to the increase of aspect ratio by 19.6%. According to Eq (7.9), C_L reduction and Aspect-ratio increase lead to reduced induced drag; however, the effect of C_L reduction is substantial compared to the AR effect. As shown in Table 7.6, the drag coefficient remains constant for both the baseline wing and the wing with a twist morphing wingtip, due to the drag coefficient constraint in the optimization (Table 7.4). Figure 7.17 shows the velocity streamlines for all four wingtip types in cruise flight.

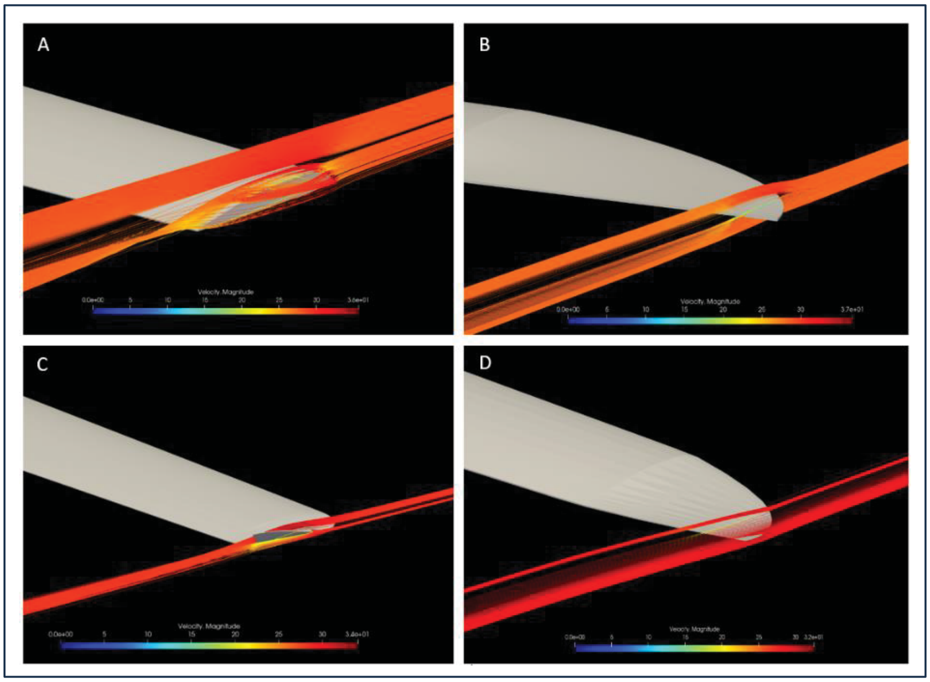

Figure 7.17 Velocity streamlines for different wingtip types: A) type A-baseline wing, B) type B-flattened wingtip, C) type C-wing with standard winglet, D) type D-twist morphing wingtip

The mixture of low-pressure flow with high-pressure flow is evident in Figure 7.17-A, where there is no winglet. Because of the turbulent flow mixture, wingtip vortices are created, leading to lift-induced-drag. However, using different types of wingtips, especially a twist morphing wingtip, the turbulent flow mixture approaches zero, which results in a noticeable reduction in induced drag.

To further examine the superior advantages of twist morphing wingtips, the study optimizes the proposed wingtip in climb flight conditions. Since a climb flight experiences higher angles of attack than a cruise flight, the effect of induced drag is more conspicuous in climb than in cruise flight. Three climb angles (5°, 8°, 10°) are studied to find the trend by which the induced drag is increased. Table 7.7 shows the flight parameters used for cruise and climb flight conditions, and Figure 7.18 shows the optimum morphed configurations for each flight condition.

Table 7.7 Flight specifications for optimizing a twist morphing wingtip in cruise and climb flight conditions

Flight condition	**Angle of attack/climb (°)**	**Airspeed (m/s)**	**Altitude (ft)**	**Air density (kg/m^3)**
Cruise	0	28.3	15,000	0.771
Climb	5, 8, 10	33.44	0	1.225

Figure 7.18 Optimum twist morphing wingtip configuration for four flight conditions: A) rear view, B) side view

As shown in Figure 7.18, as the angle of attack increases, the wingtip on the trailing edge morphs upward (Fig. 7.18-A), while the leading edge morphs downward (Fig. 7.18-B), which results in an increased twist on the wingtip as the angle of attack increases; therefore, higher twisting effect is observed in climb than in cruise flight. This observation means that the twisting impact is proportional to production of induced drag, and as more induced drag is produced, a higher twist intensity is required to reduce its impact.

Next, the optimization results are obtained for the climb flight condition. As in the case of cruise flight, the optimization for climb follows the same setup described in Table 7.5. Once the optimum configuration of a twist morphing wingtip is found, a comparison is drawn with wingtip types A, B, and C in terms of induced drag, total drag, and lift-to-drag ratio. Figures 7.19 to 7.21 show the results obtained.

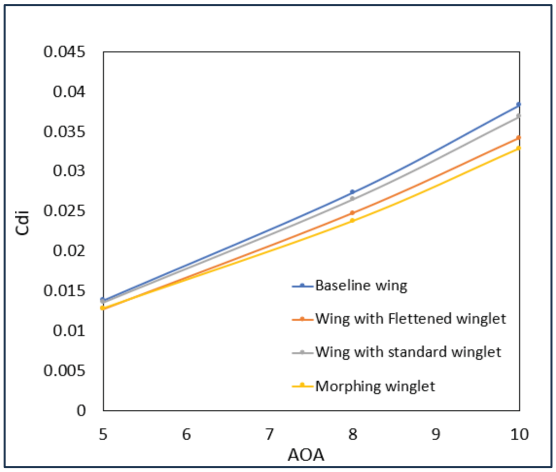

Figure 7.19 Comparison of induced drag for different wingtip configurations in climb flight conditions

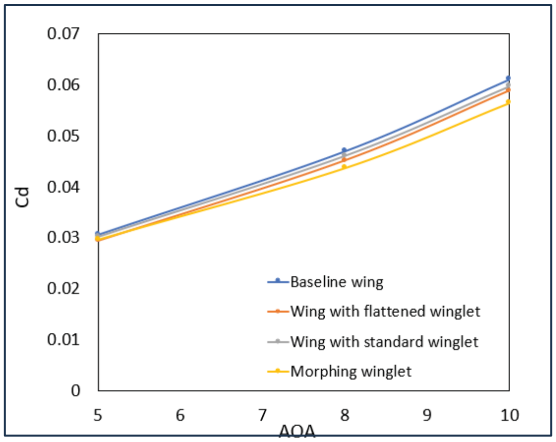

Figure 7.20 Comparison of total drag for different wingtip configurations in climb flight condition

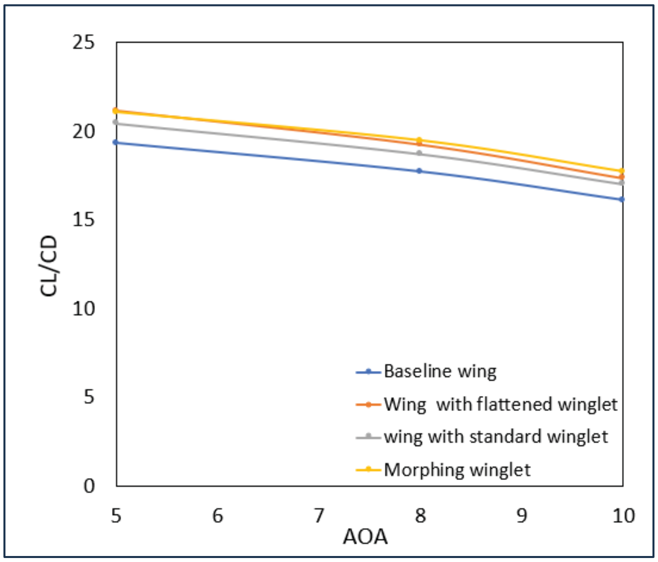

Figure 7.21 Comparison of lift-to-drag ratio for different wingtip configurations in climb flight conditions

Figures 7.19 to 7.21 clearly show the efficiency of twist-morphing wingtips through different aerodynamic parameters, including induced drag, total drag, and lift-to-drag ratio. Table 7.8 summarizes these results in terms of induced drag reduction for three wingtips compared to that of the baseline wing.

Table 7.8 Induced-drag reduction for three different wingtip types in climb flight condition

Wingtip	γ (°)	C_{Di} Reduction (%)
B	5	-8.66
	8	-10.44
	10	-12.04
C	5	-1.99
	8	-3.28
	10	-3.92
D	5	-7.90
	8	-15.10
	10	-16.51

As shown in Figure 7.19 and Table 7.8, all three wing tip configurations (types B, C, and D) reduced the induced drag for all studied angles of climb. However, the amount by which the induced drag is reduced is much greater for the twist morphing wingtip (type D), where it reduces the induced drag by up to 16.51%, while wingtip types B and C reduced it by up to 12.04% and 3.92%, respectively. In addition, Figure 7.20 shows that the total drag was also reduced by using wingtips other than baseline wings, and again, the twist morphing wingtip produced the highest total drag reduction compared to other wingtip types with a 0.16% reduction for cruise flight and 7.5% for climb. During the optimization process, the total drag was constrained to be less than or equal to the initial total drag; therefore, while minimizing C_L, the total drag was reduced as well, which contributes to the overall improvement in aerodynamic efficiency. Finally, Figure 7.21 reveals that the lift-to-drag ratio, or in other words, the aerodynamic efficiency of the wing, was also improved, and the highest aerodynamic efficiency belongs to the morphing wingtip, with a gain of up to 9% compared to the baseline model (Type A). The overall improvement in aerodynamic performance is primarily because of a reduction in total drag during the optimization. The twist morphing wingtip outperforms the other wingtip types in terms of aerodynamic efficiency, total drag, and induced drag, making it a prime candidate for both cruise and climb.

7.4 Conclusion

This study presents another of the many advantages of morphing wing technology. Twist morphing was this study's main morphing approach, and the objectives were accomplished as expected. This morphing approach was investigated on the wingtip with two main goals: 1- improving rolling maneuver by replacing hinged ailerons with twist morphing ailerons, and 2- reducing induced drag at the wingtip through twist morphing wingtips. For this purpose, a novel wingtip model was proposed as the baseline model for the twist morphing approach. The aerodynamic shape optimization was performed for both objectives to find the optimum configuration with the specified objective function. The results obtained for the twist morphing ailerons revealed that this novel morphing configuration increased the roll moment of an UAS by 34%. It was shown that any improvement in roll moment enhanced both ailerons' control power, or in other words, the ailerons' efficiency, increasing the maneuverability of the UAV by increasing the roll rate, which leads to rapid roll motion compared to conventional hinged ailerons. In addition to roll moment improvement, twist morphing ailerons decreased induced drag by 61% due to elimination of the gaps around the ailerons.

The second objective, reducing induced drag via twist morphing wingtips, was studied using the same optimization framework with the specified objective function to minimize the induced drag. Two flight conditions, cruise and climb, were studied, and optimum wingtip configurations were found for each. The optimum configuration was evaluated in terms of induced drag, total drag, and lift-to-drag ratio. The results indicated that the twist morphing wingtip reduced the induced drag by 25.7% in cruise flight and by up to 16.51% in climb compared to the baseline wing. In addition, it also reduced the total drag by up to 0.16% in cruise flight and 7.5% in climb and increased the aerodynamic efficiency by up to 9%.

The overall result indicates that from an aerodynamic point of view, the proposed twist morphing design for ailerons and winglets considerably outperforms the conventional design and could be a prime candidate for replacing current ailerons and winglets. In future studies, this proposed morphing design will be evaluated from various structural aspects by proposing a suitable actuation mechanism to increase its likelihood of being applied to next-generation aircraft.

CONCLUSION

This research was designed to contribute to the goals of green aviation by using morphing wing technology. Over the past few decades, the promising outcomes of morphing wings have guaranteed the ability to reach these goals by reducing carbon emissions and replacing the current fleet of airlines with environmentally friendly aircraft. Inspired by nature and the flight patterns of birds, the morphing wing technology attempts to mimic these patterns in modern aircraft.

Two bio-inspired morphing approaches were investigated. Firstly, a comprehensive study was conducted on a morphing trailing edge by engaging multiple disciplines, including aerodynamics, structure, and control systems. The aerodynamic study of an SMTE flap was done on the UAS-S45 wing for its entire flight envelope, including climb, cruise, and descent. A high-fidelity optimization was performed to find the optimum SMTE flap configuration for each flight condition by defining a specific objective function for each of these conditions. The objective for the climb condition was to increase the climb rate and reduce the required engine power. The results showed that the climb rate increased, and the required engine power decreased, as expected. The optimization of the morphing wing with the SMTE flap in cruise flight was designed to increase the flight range and endurance. The results of the comparison between a hinged flap wing and the morphing wing with a SMTE flap configuration confirmed the superiority of the SMTE flap over a hinged flap; not only were the range and endurance increased, but the aerodynamic performance (lift-to-drag ratio) in cruise flight was also considerably improved. Finally, the third objective was to decrease the descent rate in gliding condition. The results showed the optimum SMTE configuration for this flight condition, where the upward flap morphing reduced the descent rate as intended.

After obtaining these promising results from the aerodynamic study, the next step was to propose an actuation mechanism for the SMTE flap. For this purpose, a bio-inspired Elephant trunk Mechanism (ETM) was proposed. This proposed mechanism was analyzed using a static structural analysis by measuring its critical structural parameters, including the minimum factor of safety, its stress, strain, and maximum deformation. Our previous aerodynamic study determined the maximum deformation, and the feasibility of the proposed mechanism in providing the intended deformation was analyzed. The results obtained from the structural analysis were further improved by geometrical modification. Finally, a topology optimization was performed on the modified structure with the objective of maximizing its stiffness and minimizing its weight. The results not only indicated a notable improvement in structure stability and reliability, they also revealed a very good weight reduction on the optimized ETM. Ultimately, four ET ribs were installed on the UAS-S45 wing for further evaluation.

In the final phase of morphing wing development, having obtained the aerodynamic data for different flight conditions, and structural data for the proposed actuation mechanism, a 3D printed model of the UAS-S45 wing was prototyped, and four ETMs were embedded in the flap section with their corresponding actuation motors in the wing box. Next, the flap section was covered by a flexible skin. A graphical interface was developed to control the magnitude of the flap vertical displacement. The assembled wing was tested in a subsonic wind tunnel, with a total of 11 tests conducted for validation purposes. These tests were performed with high accuracy and without any failures, confirming the functionality of the SMTE flap and its actuation mechanism (ETM). Furthermore, the experimental results showed strong agreement with numerical predictions, with maximum relative errors of 4.1% and 6.9% for C_L and C_D, respectively.

After the development of the morphing wing with an SMTE flap, another novel morphing approach was studied, composing the final part of this research. The proposed bio-inspired morphing approach was focused on twist morphing wingtips with two objectives. The first objective was aimed at improving the rolling efficiency of the UAS-S45 by asymmetrically twisting the wingtips and replacing conventional hinged ailerons with twist morphing ailerons. The proposed twist morphing ailerons were optimized using a high-fidelity optimization framework with the aim to find the optimum configuration of the twisting wingtips during a rolling maneuver. After obtaining the optimum deformation, the aileron's efficiency was evaluated in terms of control power, rolling moment and roll rate. A comparison was drawn between conventional hinged ailerons and twist morphing ailerons in terms of rolling moments; a noticeable improvement was found by using twist morphing ailerons. The second objective was aimed at enhancing wingtip efficiency by replacing conventional winglets with symmetrically twisting morphing wingtips. This study aimed to decrease the lift-induced drag in cruise and climb flight conditions by optimizing twist morphing wingtips. The results showed that the use of twist morphing wingtips substantially reduced the adverse induced drag during cruise and climb by eliminating strong vortices and flow recirculation on the wing tip.

RECOMMENDATIONS

This thesis presents a new methodology in the development of morphing wing technology by proposing novel approaches for the high-fidelity optimization of morphing wings. This research could be continued or improved in several ways:

- This study was conducted in a steady-state regime, so that the results were not based on a dynamic flow variation. Therefore, to capture further detail on the dynamics of morphing wings during deformations, evaluations under unsteady-state regime is recommended.

- The optimization was performed using a gradient-based optimization algorithm with a high-fidelity flow solver (OpenFOAM). In future work, optimization on a 3D wing using evolutionary algorithms could be explored.

- For twist morphing aileron study, an actuation mechanism can be proposed. A structural analysis of a novel actuation mechanism for a twist morphing wing along with its experimental tests would be worthwhile to explore in future studies.

APPENDIX I

The specifications of the Unmanned Aerial System (UAS-S45) are summarized in Table AI-1, and its configuration is illustrated in Figure AI-1.

Table AI-1 Specifications of Unmanned Aerial System UAS-S45

Specification	**Value**
Wing span	6.11 m
Wing area	2.72 m²
Total length	3.01 m
Mean aerodynamic chord	0.57 m
Empty weight	57 kg
Maximum take-off Weight	79.6 kg
Loitering airspeed	55 knots
Service ceiling	17, 000 ft
Operational range	120 km

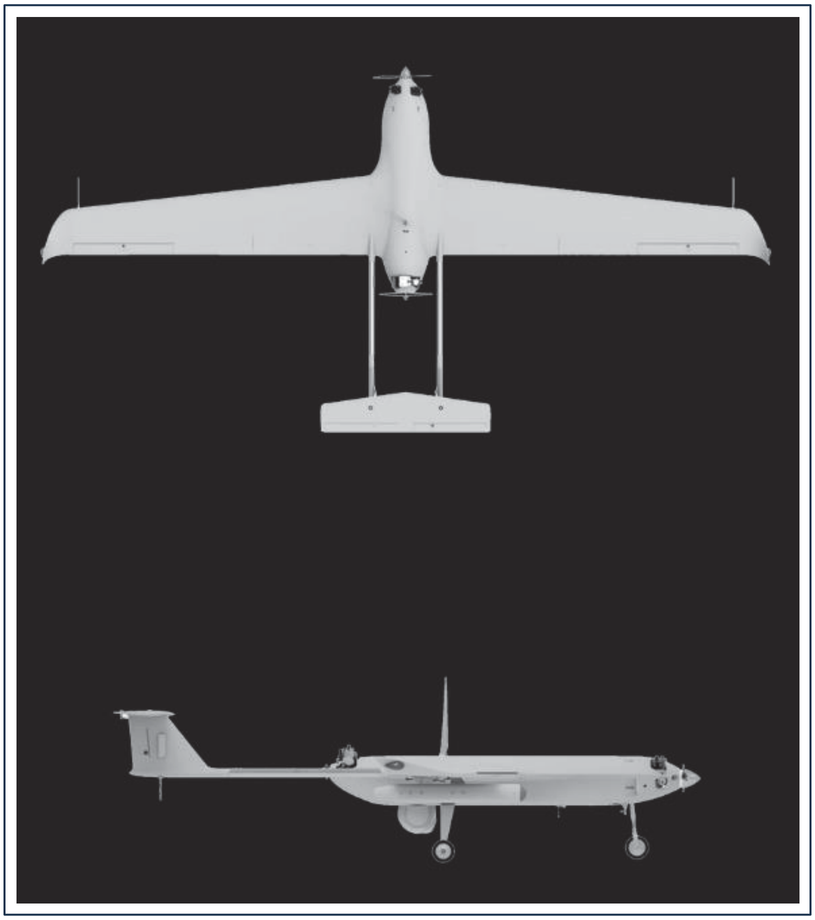

Figure AI-1 Unmanned Aerial System UAS-S45

APPENDIX II

To ensure that the numerical results were independent of the mesh resolution, a grid independence study was conducted. Several mesh configurations with varying element sizes were tested, and their effects on key parameters, such as computation time, vertical displacement, and von Mises stress were analyzed. The relative errors of these parameters were also evaluated to determine the optimal mesh density. In this study, an element size of 1 mm was considered as the reference. Table AII-1 summarizes the results of the grid independence study.

Table AII-1 Results of grid independence study

Element size (mm)	**Run time (Sec)**	**Displacement (mm)**	**Relative Error %**	**von Mises stress MPa**	**Relative Error %**
6	32	59.32	4.87	43.39	26.85
4	42	61.56	1.28	52.27	11.88
2	116	62.17	0.30	58.45	1.47
1.5	218	62.24	0.19	57.45	3.15
1.25	368	62.31	0.08	58.80	0.88
1	727	62.36	-	59.32	-

A 5% margin error was set as the maximum admissible threshold for selecting the appropriate element size. As shown in Table AII-1, when the element size exceeds 2 mm, the relative error in von Mises stress surpasses 11.88%, which is very high. To balance computational efficiency and accuracy while maintaining a relative error below 5%, an element size of 2 mm was chosen for the structural analysis of ET due to its minimal relative errors and efficient computation time.

BIBLIOGRAPHY

Abdessemed, C., Bouferrouk, A., & Yao, Y. (2022). Effects of an unsteady morphing wing with seamless side-edge transition on aerodynamic performance. *Energies*, *15*(3), 1093.

Abdessemed, C., Yao, Y., Bouferrouk, A., & Narayan, P. (2018a). Analysis of a 3D unsteady morphing wing with seamless side-edge transition. 2018 Applied Aerodynamics Conference,

Abdessemed, C., Yao, Y., Bouferrouk, A., & Narayan, P. (2018b). Morphing airfoils analysis using dynamic meshing. *International Journal of Numerical Methods for Heat & Fluid Flow*.

Abdulrahim, M. (2005). Flight performance characteristics of a biologically-inspired morphing aircraft. 43rd AIAA aerospace sciences meeting and exhibit,

Ahmed, M., Abdelrahman, M., ElBayoumi, G., & ElNomrossy, M. (2011). Optimal wing twist distribution for roll control of MAVs. *The Aeronautical Journal*, *115*(1172), 641-649.

Ajaj, R., Friswell, M., Saavedra Flores, E., Little, O., & Isikveren, A. (2012). Span morphing: a conceptual design study. 53rd AIAA/ASME/ASCE/AHS/ASC structures, structural dynamics and materials conference 20th AIAA/ASME/AHS adaptive structures conference 14th AIAA,

Ameduri, S., & Concilio, A. (2020). Morphing wings review: aims, challenges, and current open issues of a technology. *Proceedings of the Institution of Mechanical Engineers, Part C: Journal of Mechanical Engineering Science*, 0954406220944423.

Ameduri, S., & Concilio, A. (2023). Morphing wings review: Aims, challenges, and current open issues of a technology. *Proceedings of the Institution of Mechanical Engineers, Part C: Journal of Mechanical Engineering Science*, *237*(18), 4112-4130.

Ameduri, S., Concilio, A., Dimino, I., Pecora, R., & Ricci, S. (2018a). AIRGREEN2-clean sky 2 programme: Adaptive Wing technology maturation, challenges and perspectives. *Smart Materials, Adaptive Structures and Intelligent Systems*, *51944*, V001T004A023.

Ameduri, S., Concilio, A., Dimino, I., Pecora, R., & Ricci, S. (2018b). AIRGREEN2 - Clean Sky 2 Programme: Adaptive Wing Technology Maturation, Challenges and Perspectives. ASME 2018 Conference on Smart Materials, Adaptive Structures and Intelligent Systems,

Ameduri, S., Dimino, I., Concilio, A., Mercurio, U., & Pellone, L. (2021). Specific Modeling Issues on an Adaptive Winglet Skeleton. *Applied Sciences*, *11*(8), 3565.

Amendola, G., Dimino, I., Concilio, A., Pecora, R., & Amoroso, F. (2015). Actuation system design for a morphing aileron. *Applied Mechanics and Materials*, *798*, 582-588.

Amendola, G., Dimino, I., Magnifico, M., & Pecora, R. (2016). Distributed actuation concepts for a morphing aileron device. *The Aeronautical Journal*, *120*(1231), 1365-1385.

An, J., Yan, M., Zhou, W., Sun, X., Yan, Z., & Qiu, C. (1988). Aircraft dynamic response to variable wing sweep geometry. *Journal of Aircraft*, *25*(3), 216-221.

Arena, M., Amoroso, F., Pecora, R., Amendola, G., & Dimino, I. (2018). Numerical and experimental validation of a full scale servo-actuated morphing aileron model. *Smart Materials and Structures*, *27*(10), 105034.

Arena, M., Concilio, A., & Pecora, R. (2019). Aero-servo-elastic design of a morphing wing trailing edge system for enhanced cruise performance. *Aerospace Science and Technology*, *86*, 215-235.

Arena, M., Nagel, C., Pecora, R., Schorsch, O., Concilio, A., & Dimino, I. (2019). Static and dynamic performance of a morphing trailing edge concept with high-damping elastomeric skin. *Aerospace*, *6*(2), 22.

Barbarino, S., Bilgen, O., Ajaj, R. M., Friswell, M. I., & Inman, D. J. (2011). A review of morphing aircraft. *Journal of intelligent material systems and structures*, *22*(9), 823-877.

Barbarino, S., Dettmer, W. G., & Friswell, M. I. (2010). Morphing trailing edges with shape memory alloy rods. Proceeding of,

Bartley-Cho, J. D., Wang, D. P., Martin, C. A., Kudva, J. N., & West, M. N. (2004). Development of high-rate, adaptive trailing edge control surface for the smart wing phase 2 wind tunnel model. *Journal of intelligent material systems and structures*, *15*(4), 279-291.

Bashir, M., Botez, R. M., & Wong, T. (2024). Design and Optimization of Droop Nose Leading Edge (DNLE) Morphing Wing Skin for the UAS-S45. AIAA SCITECH 2024 Forum,

Bashir, M., Longtin-Martel, S., Botez, R. M., & Wong, T. (2021). Aerodynamic design optimization of a morphing leading edge and trailing edge airfoil–application on the uas-s45. *Applied Sciences*, *11*(4), 1664.

Bashir, M., Longtin-Martel, S., Botez, R. M., & Wong, T. (2022). Optimization and design of a flexible droop-nose leading-edge morphing wing based on a novel black widow optimization algorithm—Part I. *Designs*, *6*(1), 10.

Bashir, M., Longtin-Martel, S., Zonzini, N., Botez, R. M., Ceruti, A., & Wong, T. (2022). Optimization and Design of a Flexible Droop Nose Leading Edge Morphing Wing Based on a Novel Black Widow Optimization (BWO) Algorithm—Part II. *Designs*, *6*(6), 102.

Bashir, M., Longtin Martel, S., Botez, R. M., & Wong, T. (2022). Aerodynamic shape optimization of camber morphing airfoil based on black widow optimization. AIAA Scitech 2022 Forum,

Bashir, M., Negahban, M. H., Botez, R. M., & Wong, T. (2024). Numerical Simulation of the Transient Flow around the Combined Morphing Leading-Edge and Trailing-Edge Airfoil. *Biomimetics*, *9*(2), 109.

Botez, R. (2018). Morphing wing, UAV and aircraft multidisciplinary studies at the Laboratory of Applied Research in Active Controls, Avionics and AeroServoElasticity LARCASE. *Aerospace Lab*(14), 1-11.

Botez, R., Koreanschi, A., Gabor, O., Tondji, Y., Guezguez, M., Kammegne, J., Grigorie, L., Sandu, D., Mebarki, Y., & Mamou, M. (2018). Numerical and experimental transition results evaluation for a morphing wing and aileron system. *The Aeronautical Journal*, *122*(1251), 747-784.

Botez, R. M. (2022). Overview of morphing aircraft and unmanned aerial systems methodologies and results–application on the cessna citation X, CRJ-700, UAS-S4 and UAS-S45. AIAA Scitech 2022 Forum, Botez, R. M., Koreanschi, A., Gabor, O. S., Tondji, Y., Guezguez, M., Kammegne, J., Grigorie, L., Sandu, D., Mebarki, Y., & Mamou, M. (2018). Numerical and experimental transition results evaluation for a morphing wing and aileron system. *The Aeronautical Journal*, *122*(1251), 747-784.

Botez, R. M., Koreanschi, A., Oliviu, S. G., Mebarki, Y., Mamou, M., Tondji, Y., Amoroso, F., Pecora, R., Lecce, L., & Amendola, G. (2017). Numerical and experimental testing of a morphing upper surface wing equipped with conventional and morphing ailerons. 55th AIAA Aerospace Sciences Meeting,

Botez, R. M., Molaret, P., & Laurendeau, E. (2007). Laminar flow control on a research wing project presentation covering a three year period. Canadian aeronautics and space institute annual general meeting,

Bourchak, M., Ajaj, R., Flores, E. S., Khalid, M., & Juhany, K. (2015). Optimum design of a PID controller for the adaptive torsion wing. *The Aeronautical Journal*, *119*(1217), 871-889.

Bubert, E. A., Woods, B. K., Lee, K., Kothera, C. S., & Wereley, N. (2010). Design and fabrication of a passive 1D morphing aircraft skin. *Journal of intelligent material systems and structures*, *21*(17), 1699-1717.

Burdette, D. A., Kenway, G. K., Lyu, Z., & Martins, J. R. (2015). Aerostructural design optimization of an adaptive morphing trailing edge wing. 56th AIAA/ASCE/AHS/ASC Structures, Structural Dynamics, and Materials Conference,

Burdette, D. A., & Martins, J. R. (2019). Impact of morphing trailing edges on mission performance for the common research model. *Journal of Aircraft*, *56*(1), 369-384.

Burdyshaw, C. E., & Anderson, W. K. (2005). A general and extensible unstructured mesh adjoint method. *Journal of Aerospace Computing, Information, and Communication*, *2*(10), 401-413.

Campanile, L., & Sachau, D. (2000). The belt-rib concept: a structronic approach to variable camber. *Journal of intelligent material systems and structures*, *11*(3), 215-224.

Carossa, G. M., Ricci, S., De Gaspari, A., Liauzun, C., Dumont, A., & Steinbuch, M. (2015). Adaptive trailing edge: specifications, aerodynamics, and exploitation. Smart Intelligent Aircraft Structures (SARISTU) Proceedings of the Final Project Conference,

Carossa, G. M., Ricci, S., De Gaspari, A., Liauzun, C., Dumont, A., & Steinbuch, M. (2016). Adaptive trailing edge: specifications, aerodynamics, and exploitation. Smart Intelligent Aircraft Structures (SARISTU) Proceedings of the Final Project Conference,

Carrier, G., Destarac, D., Dumont, A., Meheut, M., Salah El Din, I., Peter, J., Ben Khelil, S., Brezillon, J., & Pestana, M. (2014). Gradient-based aerodynamic optimization with the elsA software. 52nd Aerospace Sciences Meeting,

Caughey, D. A. (2011). Introduction to aircraft stability and control course notes for M&AE 5070. *Sibley School of Mechanical & Aerospace Engineering Cornell University*, *15*.

Chae, E. J., Moosavian, A., Pankonien, A. M., & Inman, D. J. (2017). A comparative study of a morphing wing. Smart Materials, Adaptive Structures and Intelligent Systems,

Cheng, G., Ma, T., Yang, J., Chang, N., & Zhou, X. (2023). Design and Experiment of a Seamless Morphing Trailing Edge. *Aerospace*, *10*(3), 282.

Communier, D., Botez, R., & Wong, T. (2019). Experimental validation of a new morphing trailing edge system using Price–Païdoussis wind tunnel tests. *Chinese Journal of Aeronautics*, *32*(6), 1353-1366.

Communier, D., Botez, R. M., & Wong, T. (2020). Design and validation of a new morphing camber system by testing in the price—Païdoussis subsonic wind tunnel. *Aerospace*, *7*(3), 23.

Communier, D., Le Besnerais, F., Botez, R. M., & Wong, T. (2019). Design, manufacturing, and testing of a new concept for a morphing leading edge using a subsonic blow down wind tunnel. *Biomimetics*, *4*(4), 76.

Concilio, A., Dimino, I., Pecora, R., & Ciminello, M. (2016). Structural design of an adaptive wing trailing edge for enhanced cruise performance. 24th AIAA/AHS Adaptive Structures Conference,

Coquillart, S. (1990). Extended free-form deformation: A sculpturing tool for 3D geometric modeling. Proceedings of the 17th annual conference on Computer graphics and interactive techniques,

Daynes, S. (2023). High stiffness topology optimised lattice structures with increased toughness by porosity constraints. *Materials & Design*, *232*, 112183.

Di Luca, M., Mintchev, S., Heitz, G., Noca, F., & Floreano, D. (2017). Bioinspired morphing wings for extended flight envelope and roll control of small drones. *Interface focus*, *7*(1), 20160092.

Di Matteo, N., & Guo, S. (2011). Morphing trailing edge flap for high lift wing. 52nd AIAA/ASME/ASCE/AHS/ASC Structures, Structural Dynamics and Materials Conference 19th AIAA/ASME/AHS Adaptive Structures Conference 13t,

Dimino, I., Flauto, D., Diodati, G., Concilio, A., & Pecora, R. (2014). Actuation system design for a morphing wing trailing edge. *Recent Patents on Mechanical Engineering*, *7*(2), 138-148.

Dimino, I., Flauto, D., Diodati, G., & Pecora, R. (2014). Actuation system design for a morphing wing trailing edge. *Recent Patents on Mechanical Engineering*, *7*(2), 138-148.

Dimino, I., Galasso, B., Guida, M., Miceli, M., Riemenschneider, J., Kalow, S., & Luebker, J. (2022). Whirl Tower Demonstration of an SMA Blade Twist System., 2022, 11, 141. *DOI: https://doi. org/10.3390/act11060141*.

Dimino, I., Lecce, L., & Pecora, R. (2017). *Morphing wing technologies: Large commercial aircraft and civil helicopters*. Butterworth-Heinemann.

Du, S., & Ang, H. (2012). Design and feasibility analyses of morphing airfoil used to control flight attitude. *Strojniški vestnik-Journal of Mechanical Engineering*, *58*(1), 46-55.

Dumont, A. (2018). Adjoint-based aerodynamic shape optimization applied to morphing technology on a regional aircraft wing. In *Morphing Wing Technologies* (pp. 145-174). Elsevier.

Eguea, J. P., Bravo-Mosquera, P. D., & Catalano, F. M. (2021). Camber morphing winglet influence on aircraft drag breakdown and tip vortex structure. *Aerospace Science and Technology*, *119*, 107148.

Elelwi, M., Botez, R. M., & Dao, T.-M. (2021). Structural sizing and topology optimization based on weight minimization of a variable tapered span-morphing wing for aerodynamic performance improvements. *Biomimetics*, *6*(4), 55.

Elelwi, M., Pinto, F. S., Botez, R. M., & Dao, T.-M. (2022). Multidisciplinary optimization for weight saving in a variable tapered span-morphing wing using composite materials—Application to the UAS-S4. Actuators,

Farnell. (2025). *PLA+ Filament* Technical Data Sheet. Retrieved February 13, 2025 from https://www.farnell.com/datasheets/3775310.pdf

Federal Aviation Administration. 1970. https://www.ecfr.gov/current/title-14/part-25/section-25.303

Fengqian, H., Tao, T., Yuan, G., Yimeng, L., Shenghui, Y., & Jian, L. (2021). Continuous morphing trailing-edge wing concept based on multi-stable nanomaterial. *Chinese Journal of Aeronautics*, *34*(7), 219-231.

Fereidooni, A., Marchwica, J., Leung, N., Mangione, J., & Wickramasinghe, V. (2021). Development of a hybrid (rigid-flexible) morphing leading edge equipped with bending and extending capabilities. *Journal of intelligent material systems and structures*, *32*(9), 1024-1037.

Fonzi, N., Brunton, S. L., & Fasel, U. (2020). Data-driven nonlinear aeroelastic models of morphing wings for control. *Proceedings of the Royal Society A*, *476*(2239), 20200079.

Gabor, O. Ş., Koreanschi, A., & Botez, R. (2016). Analysis of UAS-S4 Éhecatl aerodynamic performance improvement using several configurations of a morphing wing technology. *The Aeronautical Journal*, *120*(1231), 1337-1364.

Gabor, O. Ş., Koreanschi, A., & Botez, R. M. (2016). A new non-linear vortex lattice method: Applications to wing aerodynamic optimizations. *Chinese Journal of Aeronautics*, *29*(5), 1178-1195.

Gabor, O. Ş., Simon, A., Koreanschi, A., & Botez, R. M. (2016). Improving the UAS-S4 Éhecal airfoil high angles-of-attack performance characteristics using a morphing wing approach. *Proceedings of the institution of mechanical engineers, Part G: Journal of Aerospace Engineering*, *230*(1), 118-131.

Garcia, H., Abdulrahim, M., & Lind, R. (2003). Roll control for a micro air vehicle using active wing morphing. AIAA Guidance, Navigation, and Control Conference and Exhibit,

Gebremedhin, A. H., Manne, F., & Pothen, A. (2005). What color is your Jacobian? Graph coloring for computing derivatives. *SIAM review*, *47*(4), 629-705.

Groves-Raines, M. M., Araujo-Estrada, S. A., Mohamed, A., Watkins, S., & Windsor, S. P. (2022). Wind tunnel testing of an avian-inspired morphing wing with distributed pressure sensing. 2022 International Conference on Unmanned Aircraft Systems (ICUAS),

He, P., Mader, C. A., Martins, J. R., & Maki, K. (2019). An object-oriented framework for rapid discrete adjoint development using OpenFOAM. AIAA scitech 2019 forum,

He, P., Mader, C. A., Martins, J. R., & Maki, K. J. (2018). An aerodynamic design optimization framework using a discrete adjoint approach with OpenFOAM. *Computers & Fluids*, *168*, 285-303.

He, P., Mader, C. A., Martins, J. R., & Maki, K. J. (2020). Dafoam: An open-source adjoint framework for multidisciplinary design optimization with openfoam. *AIAA journal*, *58*(3), 1304-1319.

https://abcnews.go.com/International/severe-reduction-emissions-coronavirus-mitigate-climate-change-long/story?id=69334246.

https://abcnews.go.com/International/severe-reduction-emissions-coronavirus-mitigate-climate-change-long/story?id=69334246

https://stock.adobe.com. Retrieved 5 june 2024 from https://stock.adobe.com/ca/images/ct-scan-of-an-elephants-trunk-detailing-muscular-and-tissue-structure/806136007?prev_url=detail

https://www.airbus.com/en/innovation/disruptive-concepts/biomimicry/fellofly.

Huang, J., & Ge, W. (2010). Advanced and key techniques in the adaptive wing. *Aero Weaponry*, *2*, 8-12.

Huynh, N. T., Nguyen, T. V., & Nguyen, Q. M. (2022). Optimum Design for the Magnification Mechanisms Employing Fuzzy Logic-ANFIS. *Computers, Materials & Continua*, *73*(3).

Ipopt Documentation, h. c.-o. g. i. I. https://coin-or.github.io/Ipopt/

Ismail, N., Zulkifli, A., Abdullah, M., Basri, M. H., & Abdullah, N. S. (2014). Optimization of aerodynamic efficiency for twist morphing MAV wing. *Chinese Journal of Aeronautics*, *27*(3), 475-487.

Jenett, B., Calisch, S., Cellucci, D., Cramer, N., Gershenfeld, N., Swei, S., & Cheung, K. C. (2017). Digital morphing wing: active wing shaping concept using composite lattice-based cellular structures. *Soft robotics*, *4*(1), 33-48.

Jeong, J., & Bae, J.-S. (2022). Wind tunnel & Flight Test of VCCS Morphing UAV. 2022 International Conference on Unmanned Aircraft Systems (ICUAS),

Jha, A. K., & Kudva, J. N. (2004). Morphing aircraft concepts, classifications, and challenges. Smart structures and materials 2004: industrial and commercial applications of smart structures technologies,

Jia, S., Zhang, Z., Zhang, H., Song, C., & Yang, C. (2022). Wind tunnel tests of 3D-Printed variable camber morphing wing. *Aerospace*, *9*(11), 699.

Jo, B. W., & Majid, T. (2022). Aerodynamic analysis of camber morphing airfoils in transition via computational fluid dynamics. *Biomimetics*, *7*(2), 52.

KAYGAN, E., & Ulusoy, C. (2018). Effectiveness of twist morphing wing on aerodynamic performance and control of an aircraft. *Journal of Aviation*, *2*(2), 77-86.

Kenway, G., Kennedy, G., & Martins, J. R. (2010). A CAD-free approach to high-fidelity aerostructural optimization. 13th AIAA/ISSMO multidisciplinary analysis optimization conference,

Khalid, M., Juhany, K. A., & Hafez, S. (2018). Computational modeling of the flow in a wind tunnel. *Aircraft Engineering and Aerospace Technology*, *90*(1), 175-185.

Khorrami, M. R., Lockard, D. P., Moore, J. B., Su, J., Turner, T. L., Lin, J. C., Taminger, K. M., Kahng, S. K., & Verden, S. A. (2014). Elastically deformable side-edge link for trailing-edge flap aeroacoustic noise reduction.

Khurana, M., Winarto, H., & Sinha, A. (2008). Airfoil geometry parameterization through shape optimizer and computational fluid dynamics. 46th AIAA aerospace sciences meeting and exhibit,

Koreanschi, A., Gabor, O. S., Acotto, J., Brianchon, G., Portier, G., Botez, R. M., Mamou, M., & Mebarki, Y. (2017). Optimization and design of an aircraft’s morphing wing-tip demonstrator for drag reduction at low speed, Part I–Aerodynamic optimization using genetic, bee colony and gradient descent algorithms. *Chinese Journal of Aeronautics*, *30*(1), 149-163.

Koreanschi, A., Sugar-Gabor, O., Acotto, J., Brianchon, G., Portier, G., Botez, R. M., Mamou, M., & Mebarki, Y. (2017). Optimization and design of a morphing wing tip aircraft demonstrator for drag reduction at low speeds, Part Π–Experimental validation using infra-red transition measurements during wind tunnel tests. *Chin. J. Aeronaut*, *30*, 164-174.

Koreanschi[a], A., Gabor[a], O. S., Acotto[a], J., Brianchon[a], G., Portier[a], G., Botez[a], R. M., Mamou[b], M., & Mebarki[b], Y. (2017). Optimization and Design of a Morphing Aircraft Wing Tip Demonstrator at Low Speed for Drag Reduction, Part I–Aerodynamic Optimizations Using 3 Algorithms: Genetic, Bee Colony and Gradient Descent.

Körpe, D. S. (2014). Aerodynamic modelling and optimization of morphing wings.

Kota, S., Flick, P., & Collier, F. S. (2016). Flight testing of flexfloiltm adaptive compliant trailing edge. 54th AIAA Aerospace Sciences Meeting,

Kota, S., Osborn, R., Ervin, G., Maric, D., Flick, P., & Paul, D. (2009a). Mission adaptive compliant wing–design, fabrication and flight test. RTO Applied Vehicle Technology Panel (AVT) Symposium,

Kota, S., Osborn, R., Ervin, G., Maric, D., Flick, P., & Paul, D. (2009b). Mission adaptive compliant wing–design, fabrication and flight test. RTO Applied Vehicle Technology Panel (AVT) Symposium,

Kuitche, M. A. J., & Botez, R. M. (2019). Modeling novel methodologies for unmanned aerial systems–Applications to the UAS-S4 Ehecatl and the UAS-S45 Bálaam. *Chinese Journal of Aeronautics*, *32*(1), 58-77.

Kuitche, M. A. J., Botez, R. M., Guillemin, A., & Communier, D. (2020). Aerodynamic modelling of unmanned aerial system through nonlinear vortex lattice method, computational fluid dynamics and experimental validation-application to the uas-s45 bàlaam: Part 1. *INCAS bulletin*, *12*(1), 91-103.

Lamousin, H. J., & Waggenspack, N. (1994). NURBS-based free-form deformations. *IEEE Computer Graphics and Applications*, *14*(6), 59-65.

Le Quéré, C., Jackson, R. B., Jones, M. W., Smith, A. J., Abernethy, S., Andrew, R. M., De-Gol, A. J., Willis, D. R., Shan, Y., & Canadell, J. G. (2020). Temporary reduction in daily global CO 2 emissions during the COVID-19 forced confinement. *Nature climate change*, *10*(7), 647-653.

Lebofsky, S., Ting, E., & Nguyen, N. T. (2015). Multidisciplinary drag optimization of reduced stiffness flexible wing aircraft with variable camber continuous trailing edge flap. 56th AIAA/ASCE/AHS/ASC Structures, Structural Dynamics, and Materials Conference,

Li, B., & Li, G. (2016). Analysis and optimization of a camber morphing wing model. *International Journal of Advanced Robotic Systems*, *13*(5), 1729881416664846.

Li, D., Zhao, S., Da Ronch, A., Xiang, J., Drofelnik, J., Li, Y., Zhang, L., Wu, Y., Kintscher, M., & Monner, H. P. (2018). A review of modelling and analysis of morphing wings. *Progress in Aerospace Sciences*, *100*, 46-62.

Liang, Y., McMeeking, R., & Evans, A. (2006). A finite element simulation scheme for biological muscular hydrostats. *Journal of theoretical biology*, *242*(1), 142-150.

Liauzun, C., Le Bihan, D., David, J.-M., Joly, D., & Paluch, B. (2018). Study of morphing winglet concepts aimed at improving load control and the aeroelastic behavior of civil transport aircraft. *Aerospace Lab*(14), 1-15.

Liu, W., Zhu, H., Zhou, S., Bai, Y., Wang, Y., & Zhao, C. (2013). In-plane corrugated cosine honeycomb for 1D morphing skin and its application on variable camber wing. *Chinese Journal of Aeronautics*, *26*(4), 935-942.

Liu, Z., Dai, N., Wang, H., & Wu, L. (2021). Design of Variable Thickness Wing Based on Two-way Shape Memory Alloy Drive. 2021 2nd International Conference on Intelligent Design (ICID),

Lyu, Z., Kenway, G. K., & Martins, J. R. (2015). Aerodynamic shape optimization investigations of the common research model wing benchmark. *AIAA journal*, *53*(4), 968-985.

Lyu, Z., & Martins, J. R. (2015). Aerodynamic shape optimization of an adaptive morphing trailing-edge wing. *Journal of Aircraft*, *52*(6), 1951-1970.

Majji, M., Rediniotis, O., & Junkins, J. (2007). Design of a morphing wing: modeling and experiments. AIAA Atmospheric Flight Mechanics Conference and Exhibit,

Marchman, J. F. (2004). *Aerodynamics and aircraft performance*. James F. Marchman.

Masters, D. A., Taylor, N. J., Rendall, T., Allen, C. B., & Poole, D. J. (2015). Review of aerofoil parameterisation methods for aerodynamic shape optimisation. 53rd AIAA aerospace sciences meeting,

Miller, E. J., Cruz, J., Lung, S.-F., Kota, S., Ervin, G., Lu, K.-J., & Flick, P. (2016). Evaluation of the hinge moment and normal force aerodynamic loads from a seamless adaptive compliant trailing edge flap in flight. 54th AIAA Aerospace Sciences Meeting,

Moosavian, A., Xi, F., & Hashemi, S. M. (2013). Design and motion control of fully variable morphing wings. *Journal of Aircraft*, *50*(4), 1189-1201.

Moulton, B. C. (2021). *3D-Printed Morphing Wings for Controlling Yaw on Flying-Wing Aircraft* Utah State University].

Mrazova, M. (2014). Sustainable development-the key for green aviation. *INCAS bulletin*, *6*(1), 109.

Muhammad Umer, H., Maqsood, A., Riaz, R., & Salamat, S. (2020). Stability characteristics of wing span and sweep morphing for small unmanned air vehicle: a mathematical analysis. *Mathematical Problems in Engineering*, *2020*.

Murugan, S., Woods, B., & Friswell, M. (2015). Hierarchical modeling and optimization of camber morphing airfoil. *Aerospace Science and Technology*, *42*, 31-38.

Negahban, M. H., Bashir, M., & Botez, R. M. (2022). Impact of Free-Form Deformation Control Points on the Optimization of the UAS-S45. International Symposium on Unmanned Systems and The Defense Industry,

Negahban, M. H., Bashir, M., & Botez, R. M. (2023). Aerodynamic optimization of a novel synthetic trailing edge and chord elongation morphing: Application to the UAS-S45 airfoil. AIAA SCITECH 2023 Forum,

Negahban, M. H., Bashir, M., & Botez, R. M. (2023). Free-Form Deformation Parameterization on the Aerodynamic Optimization of Morphing Trailing Edge. *Applied Mechanics*, *4*(1), 304-316.

Negahban, M. H., Bashir, M., Priolet, C., & Botez, R. M. (2024). Novel twist morphing aileron and winglet design for UAS control and performance. *Drones*, *8*(8), 392.

Negahban, M. H., Bashir, M., Traisnel, V., & Botez, R. M. (2024). Seamless morphing trailing edge flaps for UAS-S45 using high-fidelity aerodynamic optimization. *Chinese Journal of Aeronautics*, *37*(2), 12-29.

Negahban, M. H., Botez, R. M., & Razavi, S. E. (2022). New method for the flow modeling around chord-wise morphing airfoil. AIAA SCITECH 2022 Forum,

Negahban, M. H., Hallonet, A., Noupoussi Woumeni, M., Nguyen, C., & Botez, R. M. (2025). Structural and Topological Optimization of a Novel Elephant Trunk Mechanism for Morphing Wing Applications. *Aerospace*, *12*(5), 381. https://www.mdpi.com/2226-4310/12/5/381

Nelson, R. C. (1998). *Flight stability and automatic control* (Vol. 2). WCB/McGraw Hill New York.

Nguyen, N. T., Livne, E., Precup, N., Urnes, J. M., Nelson, C., Ting, E., & Lebofsky, S. (2014). Experimental investigation of a flexible wing with a variable camber continuous trailing edge flap design. 32nd AIAA Applied Aerodynamics Conference,

Nielsen, E. J., & Kleb, W. L. (2006). Efficient construction of discrete adjoint operators on unstructured grids using complex variables. *AIAA journal*, *44*(4), 827-836.

Ninian, D., & Dakka, S. M. (2017). Design, development and testing of shape shifting wing model. *Aerospace*, *4*(4), 52.

Obradovic, B., & Subbarao, K. (2011). Modeling of flight dynamics of morphing wing aircraft. *Journal of Aircraft*, *48*(2), 391-402.

Özel, C., Özbek, E., & Ekici, S. (2020). A review on applications and effects of morphing wing technology on uavs. *International Journal of Aviation Science and Technology*, *1*(01), 30-40.

Pankonien, A. M., & Inman, D. J. (2014). Aerodynamic performance of a spanwise morphing trailing edge concept. 25th International Conference on Adaptive Structures and Technologies,

Parancheerivilakkathil, M. S., Pilakkadan, J. S., AMOOZGAR, M., ASADI, D., ZWEIRI, Y., & FRISWELL, M. I. (2024). A review of control strategies used for morphing aircraft applications. *Chinese Journal of Aeronautics*.

Pecora, R. (2021). Morphing wing flaps for large civil aircraft: Evolution of a smart technology across the Clean Sky program. *Chinese Journal of Aeronautics*, *34*(7), 13-28.

Pecora, R., Amoroso, F., & Lecce, L. (2012). Effectiveness of wing twist morphing in roll control. *Journal of Aircraft*, *49*(6), 1666-1674.

Pecora, R., Amoroso, F., Magnifico, M., & Dimino, I. (2016). KRISTINA: Kinematic rib-based structural system for innovative adaptive trailing edge. Industrial and Commercial Applications of Smart Structures Technologies 2016,

Pecora, R., Dimino, I., Amoroso, F., & Ciminello, M. (2016). Structural design of an adaptive wing trailing edge for enhanced cruise performance. Proceedings of the 24th AIAA/AHS Adaptive Structures Conference,

Pecora, R., Magnifico, M., Amoroso, F., & Monaco, E. (2014). Multi-parametric flutter analysis of a morphing wing trailing edge. *The Aeronautical Journal*, *118*(1207), 1063-1078.

Phillips, W., Alley, N., & Goodrich, W. (2004). Lifting-line analysis of roll control and variable twist. *Journal of Aircraft*, *41*(5), 1169-1176.

Popov, A. V., Botez, R. M., & Labib, M. (2008). Transition point detection from the surface pressure distribution for controller design. *Journal of Aircraft*, *45*(1), 23-28.

Popov, A. V., Grigorie, L. T., Botez, R., Mamou, M., & Mebarki, Y. (2010). Closed-loop control validation of a morphing wing using wind tunnel tests. *Journal of Aircraft*, *47*(4), 1309-1317.

Popov, A. V., Grigorie, L. T., Botez, R., Mamou, M., & Mébarki, Y. (2010). Real time morphing wing optimization validation using wind-tunnel tests. *Journal of Aircraft*, *47*(4), 1346-1355.

POWERS, S., WEBB, L., FRIEND, E., & LOKOS, W. (1992). Flight test results from a supercritical mission adaptive wing with smooth variable camber. 6th AIAA Biennial Flight Test Conference,

Qiu, J., Wang, C., Huang, C., Ji, H., & Xu, Z. (2014). Smart skin and actuators for morphing structures. *Procedia Iutam*, *10*, 427-441.

Razavi, S. E., & Negahban, M. H. (2020). Numerical Investigation of Flow Behavior Around Chordwise Morphing NACA 0012. *Amirkabir Journal of Mechanical Engineering*, *51*(6), 1411-1426.

Ricci, S., De Gaspari, A., & Riccobene, L. (2016). Design, manufacturing and wind tunnel test of a morphing wing based on compliant structures. 24th AIAA/AHS adaptive structures conference,

Rivero, A. E., Fournier, S., Heeb, R. M., & Woods, B. K. (2022). Design, manufacture and wind tunnel test of a modular FishBAC wing with novel 3D printed skins. *Applied Sciences*, *12*(2), 652.

Rivero, A. E., Fournier, S., Manolesos, M., Cooper, J. E., & Woods, B. K. (2021). Experimental aerodynamic comparison of active camber morphing and trailing-edge flaps. *AIAA Journal*, *59*(7), 2627-2640.

Rodrigue, H., Cho, S., Han, M.-W., Bhandari, B., Shim, J.-E., & Ahn, S.-H. (2016). Effect of twist morphing wing segment on aerodynamic performance of UAV. *Journal of Mechanical Science and Technology*, *30*, 229-236.

Rodrigue, H., Wang, W., Bhandari, B., Han, M.-W., & Ahn, S.-H. (2014). Cross-shaped twisting structure using SMA-based smart soft composite. *International Journal of Precision Engineering and Manufacturing-Green Technology*, *1*, 153-156.

Rodriguez, D. L., Aftosmis, M. J., Nemec, M., & Anderson, G. R. (2015). Optimized off-design performance of flexible wings with continuous trailing-edge flaps. 56th AIAA/ASCE/AHS/ASC structures, structural dynamics, and materials conference,

Ronzheimer, A. (2004). Shape Parameterisation Based on Freeform Deformation in Aerodynamic Design Optimization. *ERCOFTAC Design Optimization: Methods & Applications*, *400*.

Ronzheimer, A. (2006). Prospects of geometry parameterization based on freeform deformation in mdo. ERCOFTAC 2006 International Conference. ERCOFTAC, ERCOFTAC,

Salinas, M. F., Botez, R. M., & Gauthier, G. (2023). New validation methodology of an adaptive wing for UAV S45 for fuel reduction and climate improvement. *Applied Sciences*, *13*(3), 1799.

Samareh, J. (2000). Multidisciplinary aerodynamic-structural shape optimization using deformation (MASSOUD). 8th Symposium on Multidisciplinary Analysis and Optimization, Samareh, J. (2004). Aerodynamic shape optimization based on free-form deformation. 10th AIAA/ISSMO multidisciplinary analysis and optimization conference,

Samareh, J. A. (2001). Survey of shape parameterization techniques for high-fidelity multidisciplinary shape optimization. *AIAA journal*, *39*(5), 877-884.

Samuel, J. B., & Pines, D. (2007). Design and testing of a pneumatic telescopic wing for unmanned aerial vehicles. *Journal of Aircraft*, *44*(4), 1088-1099.

Secanell, M., Suleman, A., & Gamboa, P. (2006). Design of a morphing airfoil using aerodynamic shape optimization. *AIAA journal*, *44*(7), 1550-1562.

Sederberg, T. W., & Parry, S. R. (1986). Free-form deformation of solid geometric models. Proceedings of the 13th annual conference on Computer graphics and interactive techniques,

Segui, M., Abel, F. R., Botez, R. M., & Ceruti, A. (2021). New aerodynamic studies of an adaptive winglet application on the Regional Jet CRJ700. *Biomimetics*, *6*(4), 54.

Segui, M., & Botez, R. M. (2019). Evaluation of the impact of morphing horizontal tail design of the UAS-S45 performances.

Shi, X., Yang, Y., Wang, Z., Zhang, S., Sun, X., & Feng, W. (2023). Design and shape monitoring of a morphing wing trailing edge. *Aerospace*, *10*(2), 127.

Sicim Demirci, M. S., Pecora, R., Chianese, L., Viscardi, M., & Kaya, M. O. (2024). Structural Analysis and Experimental Tests of a Morphing-Flap Scaled Model. *Aerospace*, *11*(9), 725.

Sinapius, M., Monner, H. P., Kintscher, M., & Riemenschneider, J. (2014). DLR's morphing wing activities within the European network. *Procedia Iutam*, *10*, 416-426.

Smith, K. K., & Kier, W. M. (1989). Trunks, tongues, and tentacles: moving with skeletons of muscle. *American Scientist*, *77*(1), 28-35.

Sofla, A., Meguid, S., Tan, K., & Yeo, W. (2010). Shape morphing of aircraft wing: Status and challenges. *Materials & Design*, *31*(3), 1284-1292.

Soneda, K., Yokozeki, T., Imamura, T., & Tsushima, N. (2020). Aero-structural analysis of corrugated morphing wing with spanwise camber change. AIAA Scitech 2020 Forum,

Sripawadkul, V., Padulo, M., & Guenov, M. (2010). A comparison of airfoil shape parameterization techniques for early design optimization. 13th AIAA/ISSMO multidisciplinary analysis optimization conference,

Stanford, B., Abdulrahim, M., Lind, R., & Ifju, P. (2007). Investigation of membrane actuation for roll control of a micro air vehicle. *Journal of Aircraft*, *44*(3), 741-749.

Sugar Gabor, O. (2015). *Validation of morphine wing methodologies on an unmanned aerial system and a wind tunnel technology demonstrator* École de technologie supérieure].

Takahashi, H., Yokozeki, T., & Hirano, Y. (2016). Development of variable camber wing with morphing leading and trailing sections using corrugated structures. *Journal of intelligent material systems and structures*, *27*(20), 2827-2836.

Ting, E., Chaparro, D., Nguyen, N., & Fujiwara, G. E. (2018). Optimization of variable-camber continuous trailing-edge flap configuration for drag reduction. *Journal of Aircraft*, *55*(6), 2217-2239.

Ting, E., Chaparro, D., & Nguyen, N. T. (2017). Aero-structural optimization of variable camber continuous trailing edge flap configurations using transonic and viscous potential flow method. 35th AIAA Applied Aerodynamics Conference, Towara, M., & Naumann, U. (2013). A discrete adjoint model for OpenFOAM. *Procedia Computer Science*, *18*, 429-438.

Urnes, J., & Nguyen, N. (2013). A mission adaptive variable camber flap control system to optimize high lift and cruise lift to drag ratios of future n+ 3 transport aircraft. 51st AIAA aerospace sciences meeting including the new horizons forum and aerospace exposition,

Vos, R., Gürdal, Z., & Abdalla, M. (2010). Mechanism for warp-controlled twist of a morphing wing. *Journal of Aircraft*, *47*(2), 450-457.

Wächter, A., & Biegler, L. T. (2006). On the implementation of an interior-point filter line-search algorithm for large-scale nonlinear programming. *Mathematical programming*, *106*(1), 25-57.

Wang, C.-N., Yang, F.-C., Nguyen, V. T. T., & Vo, N. T. M. (2022). CFD Analysis and Optimum Design for a Centrifugal Pump Using an Effectively Artificial Intelligent Algorithm. *Micromachines*, *13*(8), 1208. https://www.mdpi.com/2072-666X/13/8/1208

Wang, Q., Xu, Z., & Zhu, Q. (2013). Structural design of morphing trailing edge actuated by SMA. *Frontiers of Mechanical Engineering*, *8*, 268-275.

Weishuang, L., Yun, T., & Peiqing, L. (2017). Aerodynamic optimization and mechanism design of flexible variable camber trailing-edge flap. *Chinese Journal of Aeronautics*, *30*(3), 988-1003.

Wickenheiser, A. M., & Garcia, E. (2007). Aerodynamic modeling of morphing wings using an extended lifting-line analysis. *Journal of Aircraft*, *44*(1), 10-16.

Woods, B. K., Bilgen, O., & Friswell, M. I. (2014). Wind tunnel testing of the fish bone active camber morphing concept. *Journal of intelligent material systems and structures*, *25*(7), 772-785.

Woods, B. K., Parsons, L., Coles, A. B., Fincham, J. H., & Friswell, M. I. (2016). Morphing elastically lofted transition for active camber control surfaces. *Aerospace Science and Technology*, *55*, 439-448.

Woods, B. K. S., & Friswell, M. I. (2012). Preliminary investigation of a fishbone active camber concept. Smart Materials, Adaptive Structures and Intelligent Systems,

Wu, R., Soutis, C., Zhong, S., & Filippone, A. (2017). A morphing aerofoil with highly controllable aerodynamic performance. *The Aeronautical Journal*, *121*(1235), 54-72.

Xiao, K., Chen, Y., Jiang, W., Wang, C., & Zhao, L. (2019). Modeling, simulation and implementation of a bird-inspired morphing wing aircraf. 2019 3rd International Conference on Robotics and Automation Sciences (ICRAS),

Xiasheng, S., Jingfeng, X., Jin, Z., Zhigang, W., Wenjuan, W., & Zhang, M. (2024). Design and validation of a variable camber wing structure. *Chinese Journal of Aeronautics*, *37*(2), 1-11.

Yang, J., Pitarch, E. P., Potratz, J., Beck, S., & Abdel-Malek, K. (2006). Synthesis and analysis of a flexible elephant trunk robot. *Advanced Robotics*, *20*(6), 631-659.

You, H., Kim, S., Joe, W. Y., & Yun, G. J. (2019). New concept for aircraft morphing wing skin: Design, modeling, and analysis. *AIAA journal*, *57*(5), 1786-1792.

Yuzhu, L., Wenjie, G., Jin, Z., Zhang, Y., Donglai, Z., Zhuo, W., & Dianbiao, D. (2022). Design and experiment of concentrated flexibility-based variable camber morphing wing. *Chinese Journal of Aeronautics*, *35*(5), 455-469.

Zhang, Z., De Gaspari, A., Ricci, S., Song, C., & Yang, C. (2021). Gradient-based aerodynamic optimization of an airfoil with morphing leading and trailing edges. *Applied Sciences*, *11*(4), 1929.

Zhigang, W., Xiasheng, S., Yu, Y., Wenjie, G., Daochun, L., XIANG, J., Panpan, B., Qi, W., & DA RONCH, A. (2024). Design optimization and testing of a morphing leading-edge with a variable-thickness compliant skin and a closed-chain mechanism. *Chinese Journal of Aeronautics*.

Zi, K., Daochun, L., Tong, S., Xiang, J., & Zhang, L. (2020). Aerodynamic characteristics of morphing wing with flexible leading-edge. *Chinese Journal of Aeronautics*, *33*(10), 2610-2619.